Modeling Microdefects Formation in Crystalline Silicon: The Roles of Point Defects and Oxygen

by

Zhihong Wang

Submitted to the Department of Chemical Engineering in
partial fulfillment of the requirements for the degree of

Doctor of Philosophy

at the

MASSACHUSETTS INSTITUTE OF TECHNOLOGY

December 2002

Author ....
Department of Chemical Engineering
December 23, 2002

Certified by ....
Robert A. Brown
Provost and Warren K. Lewis Professor of Chemical Engineering
Thesis Supervisor

Accepted by ....
Daniel E. Blankschtein
Professor of Chemical Engineering
Chairman, Committee for Graduate Students

Modeling Microdefects Formation in Crystalline Silicon: The Roles of Point Defects and Oxygen

by

Zhihong Wang

Abstract

Most microelectronic devices are fabricated on single crystalline silicon substrates that are grown from the melt by the Czochralski crystal growth method. There is an ever increasing demand for control of size and density of microdefects in the silicon for control of quality and uniformity of the fabricated microelectronic devices. This thesis is aimed at developing a fundamental understanding of the mechanisms for formation of such micro-defects through the development of models, theoretical analysis and large-scale simulation. Two major problems have been addressed. First, following the work of T. Sinno [150] and T. Mori [108], models have been developed for the transport, reaction and aggregation of native point defects — self-interstitials (I's) and vacancies (V's) — in crystalline silicon, so as to explain the dynamics of void formation (aggregation of V's) and stacking faults (aggregation of I's). Second, the model of point defect and cluster dynamics has been extended to include oxygen, the most common impurity in silicon, and to model oxide precipitation, an important step in silicon wafer preparation and device processing.

The models of microdefect formation begin with transport equations for native point defects that include transport by diffusion and convection (crystal motion), recombination of I's and V's, and the loss of point defects to clusters. Cluster formation is modeled by a combination of discrete rate equations for small-sized clusters (less than 100) and continuous Fokker-Planck equations for large cluster sizes. Simulation methods are developed for calculating, in time, space and cluster size, the evolution of point defect and cluster profiles, as a function of the temperature distribution in the crystal.

Considerable effort has been devoted to analysis of the critical operating conditions that divide the crystal into V-rich and I-rich regions. As analyzed by Sinno [151], these radial regions of a CZ-grown silicon crystal are distinguished by a critical value of $V/G=(V/G)_{crit}$, where V is the crystal pull rate and G is a measure of the axial temperature gradient at the melt/crystal interface. Numerical simulations identify that the evolution of microdefects at an axial slice of the crystal can be divided into three regions: (1) the region of rapid point defect dynamics near the melt-crystal interface, (2) a region of intermediate point defect concentrations where the crystal to too hot for these concentrations to become super-saturated, and (3) the nucleation and growth of point defect clusters caused by homogeneous nucleation and super-saturation.

Asymptotic analysis of void formation is carried out in each of these regions and linked by point defect conservation to give predictions for a number of very important val-

ues, including $(V/G)_{crit}$, the intermediate vacancy concentration, the void nucleation temperature, the total void concentration in the crystal and the average void size. These results agree remarkably well with simulations. Moreover, the asymptotic results give the foundation for creating a simple simulation tool for prediction of the dependence of these parameters on operating conditions.

The framework for microdefect formation is extended to oxygen precipitation by including oxygen dynamics and precipitation in the model for point defect dynamics in a self-consistent manner. The model is complicated by the fact that oxide precipitation creates elastic stress in crystalline silicon because the density of silicon oxide is roughly half that of the silicon lattice. The level of this stress is dependent on the morphology (shape) of the precipitate and is largest with spherical shaped and less for disk-shaped precipitates. Stress relief during oxide growth is modeled by either allowing V absorption into the precipitate to create free-volume, or I injection in to the silicon matrix. Hence point defect dynamics is directly coupled to oxide precipitation. Oxide morphology is modeled by accounting for the evolution of size distributions of both spherical and disk-shaped oxide precipitates and allowing the competition between their respective growth rates of these distributions to determined which morphology will be observed.

Numerical simulations using this self-consistent model show the important coupling of oxide growth rate and morphology to the point defect dynamics. For example, when excess V's are present (as is the case after a high temperature first annealing step and fast cooling rate after it), spherical oxide precipitates grow fastest because of V absorption. Without V's present the growth rate of spherical precipitates slows because of the slow process of I injection and disk-shaped precipitates, which have lower stress levels and thus require lower injection levels, dominate. This is the case at lower nucleation temperatures.

Simulations are used to model the oxide densities created during classical High-Low-High wafer annealing as a function of the nucleation temperature ($T_{nucl}=T_{low}$) and the nucleation time and are compared to experimental results from the literature. The simulations demonstrate the peak in oxide density at an intermediate value of T_{nucl}, in a quantitative agreement with experiment. The only discrepancy is the under-prediction of oxide densities at very low values of T_{nucl}. The reason for this difference is not known.

The simulations also successfully predict the large variation in oxide density caused by using rapid thermal processing (RTP) in the high temperature step, the so-called MDZ or Magic Denuded Zone process. Here the vacancy distribution implanted in the wafer by the RTP step supplies the free-volume for very rapid oxide nucleation.

The modeling and analysis demonstrated in this thesis gives a self-consistent framework for further study of the dynamics of microdefect formation in silicon processing and in other important crystalline semiconductor materials.

Thesis Supervisor: Robert A. Brown
Title: Provost and Warren K. Lewis Professor of Chemical Engineering

Acknowledgments

Time passed so quickly and I can't believe that I have already been here for five years and a half and I am close to finish my Ph.D thesis. When I look back my stay at MIT, I really have a lot to say, and also a lot of thanks to people who make it possible for me to come this far.

First of all, I would like to take this opportunity to express my great thank to my advisor, Professor Robert A. Brown, for his encourage, support, input, and superior guidance. He is a great advisor. From him I learned not only technical skills such as finite element method (I still feel lucky to take his last 10.34 class and his perspective of finite element provided me deep insight into this method). Most importantly, he taught me how to be a engineer scientist who thinks engineer problem as a scientist, how to frame and analyze hard problem, how to be precise, and how to be rigorous. All of these will definitely influence me for the rest of my life. I would also like to thank the members of my thesis committee, Professors Klavs F. Jensen, Lionel C. Kimerling, and Bernhardt L. Trout, for their support and valuable comments.

I would also like to thank MEMC Electronic Materials, Inc., Shin-Etsu Handotai Co., Ltd., and Wacker Siltronic AG for their financial support and their valuable input on my research.

Many thanks go to my friends and colleagues in Viscoelastic and Crystal Growth groups, Howard Covert, Talid Sinno, Nina Shapely, Mark Smith, Tony Caola, Garrett Sin, Tatsuo Mori, Indranil Ghosh, Jason Suen, Scott Phillips, Irina Elkin, Yong Lak Joo, Aleksey Lipchin, Yoo Cheol Won, Wei Wang, Arvind Gopinath, and Pengfei Wei. Thank Carol

Table of Contents

List of Figures

List of Tables

Chapter 1

Introduction

Today the manufacturing of microelectronics is one of the world's largest industries and has a critical impact on our society. Most microelectronics devices are manufactured on substrates or wafers made of single-crystalline silicon. The fabrication of electronic devices and circuits on silicon wafers entails a complex series of physical and chemical processes. Two realms, wafer preparation and device fabrication (device processing), can be used to classify these processes [128]. Wafer preparation includes high purity polysilicon manufacture, single silicon crystal growth, slicing of the single-crystal ingot into wafers and wafer annealing. Device processing includes oxidation, epitaxy, etching and many other processes.

Two trends dominate wafer manufacturing: increasing wafer size and decreasing defect size and density on the wafer. Because many devices are made on a single wafer and all devices from a particular wafer are manufactured and processed simultaneously at each stage in the device manufacturing process, larger size wafers allow for greater yield from the same semiconductor manufacturing process and allow semiconductor manufacturers to spread their fixed costs of production over a larger volume of product. Today's silicon wafers are mainly 300 mm in diameter while the next generation of wafers will be 450 mm. More powerful electronic device will rely on packing more transistors into the same space, so each component in the device will be smaller. To do this, the design rule, a set of rules establishing minimum dimensions of a transistor and minimum spacing between adjacent components, is being decreased. Today device processing typically uses a 0.13 micron design rule as the state-of-the-art technique, while 0.1 micron processes will be possible in the near future. The size of the characteristic design feature sets the tolera-

ble levels and sizes of defects in the crystal. For example, the 0.13 micron process requires that defect concentrations are less than 0.12 cm^{-2} for defects 0.09 μm or larger; for the 0.1 micron process wafers should contain areal densities no more than 0.1 cm^{-2} of defects 0.05 μm or larger [75].

The key to increase the quality of silicon wafers is to understand the mechanisms of defects formation, to link operating conditions of processes to characteristics of the defects, and to use these relationships to control defects formation. During high temperature wafer processing, metallic impurities are introduced onto the wafer surface and can result in harmful near surface defects [25]. Oxygen precipitates and related defects serve as effective gettering sites for removing metallic contaminants and may be concentrated in the middle of the wafer, leaving a defect-free surface section or denuded zone (DZ) where devices can be fabricated [165]. Oxygen in silicon also has other beneficial effects. For example oxygen enhances resistance of the wafer to warpage [163]. As a result, oxygen is one of the most important impurities in silicon and in last two decades a great deal of attention has been devoted to the behavior of oxygen in silicon. However, there is still not a quantitative model for successfully predicting the distribution of oxygen precipitates and related defects in silicon.

This thesis is devoted to the understanding of microdefects formation mechanism in crystalline silicon by both theoretical approach and numerical simulations. The processes studied in this thesis include crystal growth and wafer annealing, and microdefects include vacancy, self-interstitial, oxygen and all their clusters. The modeling strategy here is self-consistent: a single set of physical parameters are used for all the processes; simulations are from crystal growth through wafer annealing.

1.1 Crystal Growth Techniques

The many technological innovations in melt crystal growth of semiconductor materials build on the two basic concepts of confined and meniscus defined crystal growth [14]. Figure 1.1a is an example of confined crystal growth systems and Figure 1.1b and Figure 1.1c are two examples of meniscus defined crystal growth systems. Confined melt growth systems are used primarily for laboratory purposes. The advantage of meniscus defined crystal growth is that the cooling crystal is free to expand and so is less likely to generate large thermoelastic stresses that lead to defect and dislocation generation. However, active control is needed for control of crystal diameter in a meniscus-controlled crystal growth system.

(a)Vertical Bridgman-Stockbarger method   (b)Czochralski method   (c)Small-scale floating zone method
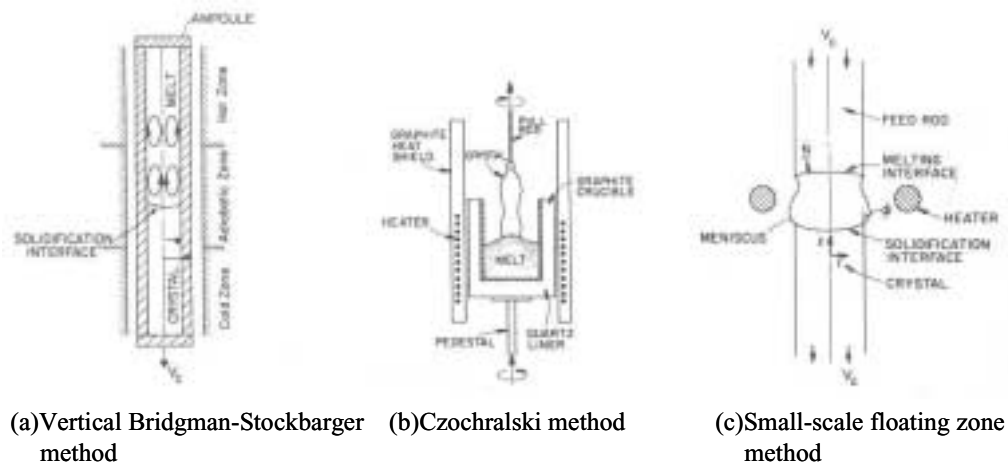
Figure 1.1: Commonly used systems for melt crystal growth of electronic materials (taken from[14]).

Although a variety of techniques can be used in crystal growth of semiconductor materials, only two methods are commonly utilized in industry; these are the Czochralski (CZ) and floating zone (FZ) meniscus-defined crystal growth systems. Of these two methods, CZ is most widely used, with over 95% of commercial silicon being grown by this technique [3].

In the CZ process, polycrystalline silicon is melted in a quartz crucible. A seed single crystal with the required crystallographic orientation is dipped into the pool and then pulled slowly from the melt to form an ingot. The CZ process is illustrated in Figure 1.2. The temperature of the melt and the pulling rate govern the diameter of the ingot. These parameters are related by the heat balance at the melt/crystal interface [94]. Although the seed crystal is normally dislocation-free, when it is dipped into melt dislocations are always generated between melt and crystal due to temperature shock. These dislocation are propagated into the growing crystal particularly if the crystal has large diameter. The larger the diameter, the more heat is trapped in inner part, therefore the higher radical temperature gradient. And strain which occurs as a result of high radical temperature gradient is probably the main reason for the dislocation movement [209]. It is the Dash's necking process that makes it possible to grow large diameter dislocation-free crystals [26]. In this process, the strain in the crystal is reduced by lowing the crystal diameter to about 3 mm. As a result new dislocations are not generated and movement of existing dislocations is slower than the crystal growth rate, therefore a dislocation-free silicon crystal is created. Once formed, the diameter of the crystal is increased to the desired diameter by slowing the growth rate. In order to prevent new dislocations from forming the thermal environment of the crystal is controlled with carefully placed heat shields which reduce surface cooling rates and create a more nearly radially uniform temperature field.
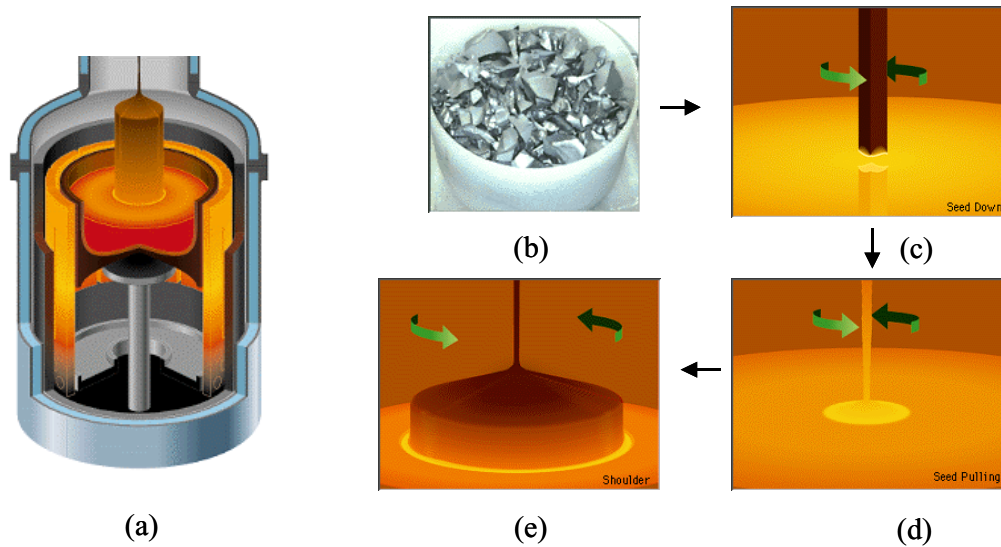
Figure 1.2: Czochralski single silicon crystal growth (a) Czochralski furnish; (b) poly-crystalline silicon hold in crucible; (c) seed down; (d) seed pulling; (e) shoulder formation [60].

In FZ crystal growth, a polycrystalline rod of silicon is converted into a single crystal by moving a molten zone of silicon from one end of the rod to the other, and the initial zone is created by contact with a single crystal seed. The advantage of FZ growth lies in the ability to produce high purity silicon, as a result of the absence of a container contacting the silicon melt. Impurities from the crucible in CZ silicon crystal growth lead to crystals that are seldom grown at resistivity much higher than 25 $\Omega \cdot cm$. Alternatively, FZ crystals can be grown over a wide range of resistivity up to 200 $\Omega \cdot cm$ [128]. The disadvantage of FZ growth comes from the difficulty of growing large diameter crystals [86].

Silicon crystals grown by the CZ method contain high oxygen concentrations caused by contaminating of the melt by the quartz crucible. Improvement of the electrical and mechanical properties of silicon wafers caused by appropriate oxygen precipitation make CZ silicon wafers more favorable than FZ silicon wafers in the fabrication of most integrated circuits.

It is also worth emphasizing that besides polished CZ wafers there are also epitaxial wafer and silicon-on-insulator (SOI) wafers. In epitaxial wafers, on top of a polished CZ wafer an epitaxial silicon layer is deposed by either chemical vapor deposition (CVD) or molecular bean epitaxy (MBE) [19,126], therefore epitaxial wafers have much lower defect density than polished CZ wafers. SOI wafers have an insulator layer such as SiO_2 underneath a thin surface silicon layer, and can be realized by several processing techniques, such as SIMOX, BESOI and Smart-Cut [93, 118]. These wafers have the advantage of low parasitic capacitance and as a result, high speed circuit [117]. However both epitaxial wafer and SOI wafers are much more expensive than polished CZ wafers. Unless the costs of these two special wafers are significantly reduced polished CZ wafers will still dominate the wafer market.

1.2 Wafer Annealing Process

All microelectronic devices are only fabricated on the thin surface layer of silicon wafer. In order to have high quality chips and high yield, defects in the surface region have to be decreased as low as possible. However, defects are not always harmful. Well-controlled defects could be very useful for device fabrication. For example, oxides or oxygen precipitates with appropriate size and density in the middle section of wafer can serve as gettering sites for metallic impurities which are introduced during fabrication processes [161]. Different metals require different minimal density of oxygen precipitates in order to achieve efficient gettering. For examples, the threshold level of oxygen precipitates for efficient Ni gettering is as low as $10^8 cm^{-3}$, while for Cu it could be $2 \times 10^9 cm^{-3}$ [56].

A three-step thermal cycle called Hi-Low-Hi wafer annealing is commonly applied to form the denuded zone in the near surface region of a wafer and have oxygen precipitates in the middle of wafer [99,124,148]. The denuded zone and the oxygen precipitates underneath it are shown in Figure 1.3. During the first step at high temperature (T>1100°C), the

denuded zone is formed at the surface of the wafer due to oxygen out-diffusion. There are

two mechanisms for oxygen out-diffusion to the wafer surface [208]. One is the out-diffu-

sion due to evaporation of oxygen in form of volatile silicon monoxide at high tempera-

ture when the silicon wafer is annealed in an inert atmosphere. The other mechanism

occurs under an oxidizing atmosphere in which a very thin surface oxide layer is formed

and serves as sink for oxygen in the bulk. In this case, even though the oxygen concentra-

tion in the wafer is in the order of $10^{18} cm^{-3}$, the oxygen concentration in the very thin

surface oxide layer could be higher than $10^{21} cm^{-3}$ (see Figure 1.4) because this layer is

oxide rather than silicon.
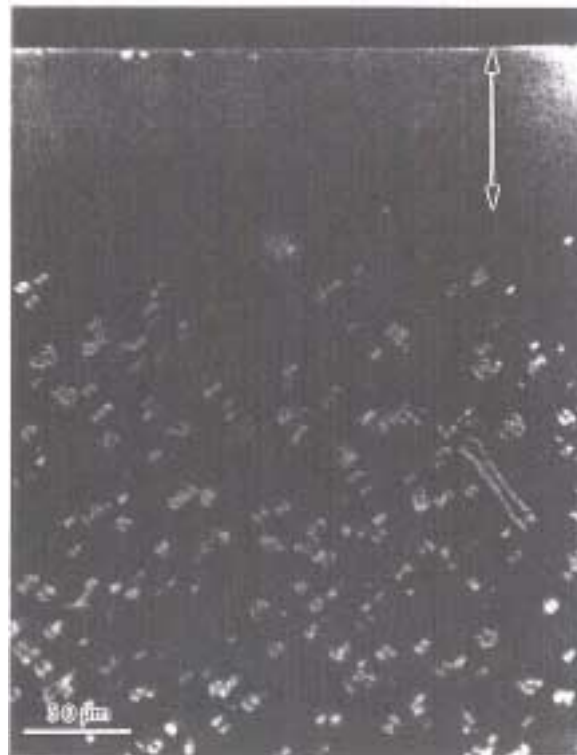
Figure 1.3: Cross section of wafer with denuded zone (marked by a double arrow) in the
near surface region and oxygen precipitates underneath it [10].
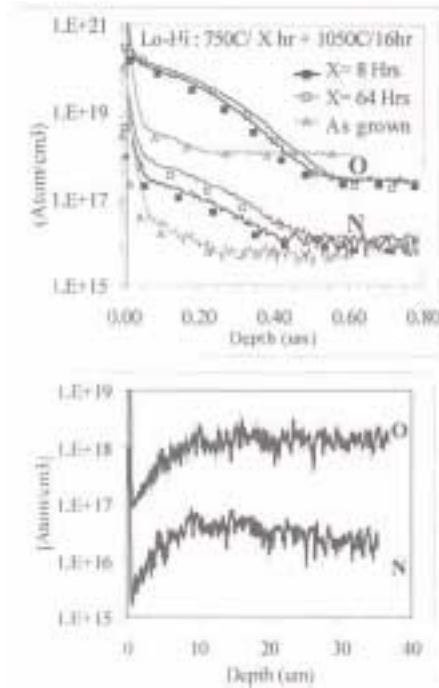
Figure 1.4: SIMS measurement of oxygen concentration near the wafer surface [83].

The second step is nucleation of oxygen precipitates at a low temperature (600-750°C). At this low temperature, small nuclei are generated by the high super-saturation of oxygen in the middle section of the wafer, but it is difficult for nuclei to grow because the temperature is too low for oxygen diffusion. The last step is growth of the oxygen pre-cipitates at high temperature (1000-1100°C). At this stage, nuclei generated under the low temperature grow rapidly [5,120].

The temperature and duration at each step can be controlled to obtain wafers with dif-ferent oxygen precipitates profiles. Many different ambient environments during wafer annealing, including O_2, O_2 with *HCl*, H_2, N_2, *Ar*, have been used. High temperature treatments in H_2, N_2 and *Ar* ambients produce erosion of the wafer surface [48,124]. Peibst [124] reported that by annealing in O_2 with a few percent *HCl* the denuded zone was thicker and could be achieved in shorter time compared with annealing in a pure O_2

atmosphere. Gräf [48] reported that high temperature annealing results in pronounced oxygen out-diffusion in H_2 and Ar ambient but significant lower out diffusion in an oxygen ambient.

Rapid thermal annealing (RTA) has been introduced in the wafer annealing process in recent years [37,39,116,178]. Only the first high temperature step of conventional Hi-Low-Hi wafer annealing is replaced by high temperature RTA. Typically the wafer is heated to $1200°C$ from room temperature at a rate about $50°C/s$. After $10s$ at $1200°C$, it is cooled to room temperature at a rate about $100°C/s$. During the RTA cycle, there is no oxygen out-diffusion since the duration of the cycle is too short for oxygen to diffuse. There is only time for the small oxygen precipitates generated during crystal growth to dissolve. After RTA cycle the high vacancy concentration established at high temperature is maintained in the bulk of wafer while the vacancy concentration is low near the surface. This is because the cooling rate is so fast that only vacancy near the surface can diffuse out. With the assistance of vacancy incorporation, nucleation of oxygen precipitates occurs preferentially in the bulk of wafer, leaving the surface of the wafer essentially free of oxygen precipitates, although with a high oxygen concentration. However, it is not very clear how this high oxygen super-saturation in the surface denuded zone will behave during device processing.

1.3 Defects in Crystalline Silicon

Types of defects in silicon are shown schematically in Figure 1.5 and listed in Table 1.1. Point defects can be separated into two categories: native point defects and impurity point defects [35]. Vacancies and self-interstitials are two fundamental native point defects. A vacancy is an empty crystal site, and self-interstitial is a silicon atom that resides in one of the interstices in the silicon lattice. Impurity point defects can occupy either a silicon lattice site (substitutional) or an off-lattice position (interstitial). When present in super-satu-

ration, point defects tend to form a variety of larger, more complex defects. Dislocations which are a kind of one-dimensional defects, impurity precipitates, vacancy clusters and interstitial clusters are each illustrated in Figure 1.5. Stacking faults are two-dimensional lattice defects of limited extent, preferentially formed on [111] planes by taking out a [111] lattice plane or inserting a [111] lattice plane into the crystal [209].

Geometry	Defects

Point (zero dimension)	Intrinsic point defect
	    Vacancy[a]
	    Self-interstitial[b]
	Extrinsic point defect
	    Substitutional impurity atom[c]
	    Interstitial impurity atom[d]

Line (one dimension)	Dislocation
	    Edge dislocation[e]
	    Screw dislocation
	Dislocation loops (extrinsic type[f] and intrinsic type[g])

Plane (two dimension)	Stacking fault (extrinsic type and intrinsic type) Twin Grain boundary
Volume (three dimension)	Precipitate[h] Void[i] Interstitial agglomerate[j]

Table 1.1: List of defects in single crystal silicon, classified by their geometry. Superscripts correspond to the indices in Figure 1.5 [108,145].
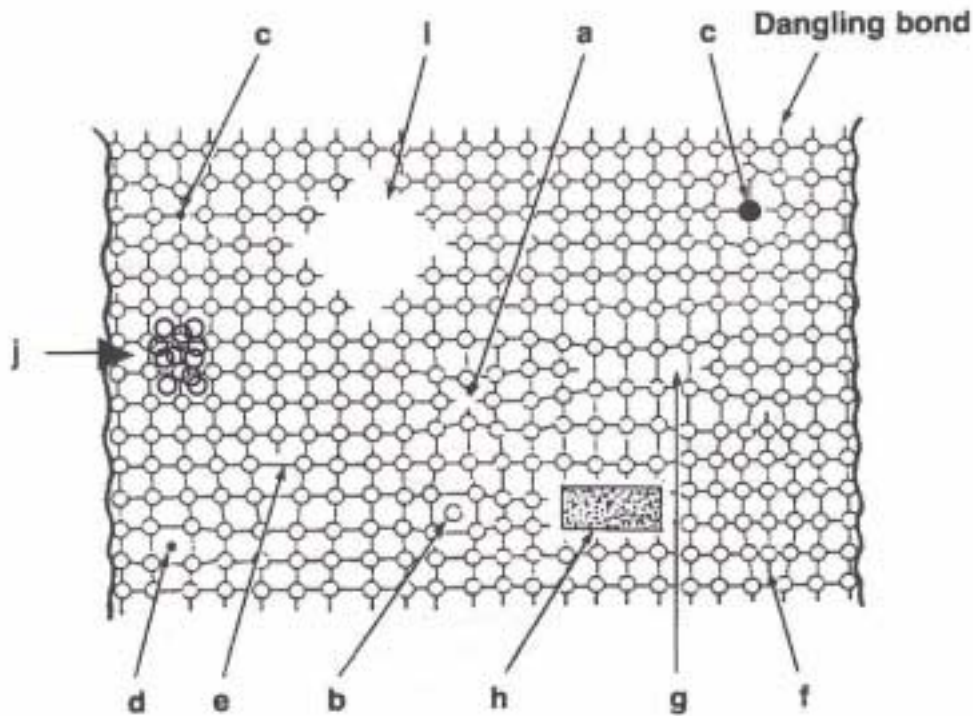
Figure 1.5: Schematic diagram of defects in single crystal silicon. Indices correspond to the superscripts in Table 1.1 [108,145].

1.3.1 Native point defects and their related defects

At finite temperature thermodynamics dictates the existence of equilibrium concentrations of native point defects within the crystal, with concentrations that are determined so that the free energy of the system is a minimum [47]. The dependence of diffusivity on concentration for phosphorus in silicon has the parabolic nature [80]. This is an indication that there exist charge state native point defects in the extrinsic or doped silicon. Many research had been done to identify different vacancy charge states and their energy levels at cryogenic temperature [89,90,157,194,195]. However it is not clear whether these charge state point defects by irradiation at low temperature are the same point defects thermally created at high temperature. Even if they are the same defects, it is still a question whether their properties at low temperature and in highly excited nonequilibrium states

are the same as these at high temperature [68]. Moreover, at the melt/crystal interface where native point defects are incorporated, silicon crystal is intrinsic even if it is doped. This is because the intrinsic carrier concentration at melting temperature is about 10^{20} cm^{-3} [117], and in order for silicon to be extrinsic the doping concentration has to be greater than 10^{20} cm^{-3} which is not practical for a silicon ingot.

At the melt/crystal interface, vacancies and self-interstitials are incorporated into a silicon crystal with their respective equilibrium concentrations at melt temperature. Vacancies and self-interstitials then diffuse, convect, and react, leaving one specie dominate beyond a thin boundary layer adjacent to the melt/crystal interface [151]. There exists an annular ring where the Oxidation-induced Stacking Faults ring (OSF-ring) can form. Vacancies dominate inside the ring while interstitials dominate outside the ring. Both experimental analysis and theory [28,151]showed that the radial location of the OSF-ring $(r = R_{OSF})$ correlates as

$$\frac{V}{G(R_{OSF})} \cong 1.34 \times 10^{-3} \quad cm^2 min^{-1} K^{-1} \tag{1.1}$$

where V is the crystal pull rate and $G(R_{OSF})$ is the estimate for the axial temperature gradient at the melt/crystal interface and at the radial location $(r = R_{OSF})$ of the OSF-ring. The OSF-ring and $V/G(R_{OSF})$ will be discussed in detail in section 2.2.

The native point defect that results from this initial dynamics near melt/crystal interface becomes the reservoir for clustering. Voids form by vacancy clustering in the vacancy-rich core; stacking faults and dislocation loops form in the interstitial-rich outer region. All commercial CZ crystals are grown today with the OSF-ring at the periphery of the crystals.

The vacancy clusters inside OSF-ring are called D-defects. It has been reported that D-defects degrade the Gate Oxide Integrity (GOI) of electronic devices [134,78,201].

Because of this phenomenon, D-defects also are called GOI defects. The gate oxide integrity of wafer is measured by fabricating many MOS capacitors with a gate oxide layer (prepared by dry O_2 oxidation) and a poly-Si gate layer on a wafer. The GOI yield is defined as the percentage of the MOS capacitors whose breakdown voltages are larger than a specific value. Correlations show that the more dense the D-defects, the more likely that there is GOI failure and therefore low GOI yield [202].

Many measurements have been used to investigate the origin of D-defects and many names for crystalline defects have evolved from these measurements. Crystal-originated particles (COP's) are counted as particles by laser particle counter after repeated cleaning of the wafer surface using a NH_4OH /H_2O_2 solution (SC-1) [132,105,202]. After the wafer is preferentially etched with the Secco etchant, wedge-shaped etched patterns termed flow patterns defects (FPD's) are revealed. These etchpits are observed at the apex of the wedge shape. Defects detected by laser scattering tomography are called LSTD's [44]. The species COP's, FPD's and LSTD's are all D-defects and are characterized microscopically as an octahedral void surrounded by SiO_2 film [85,172,203,114]. These voids often occur as twins or triples with total size of 100-300nm and concentration of $O(10^6)cm^{-3}$, with a 2-nm-thick layer of oxides on the side wall of the void [85,172]. Twin and triple voids are shown in Figure 1.6. The facets of void always are oriented along the <111> planes of the crystal.
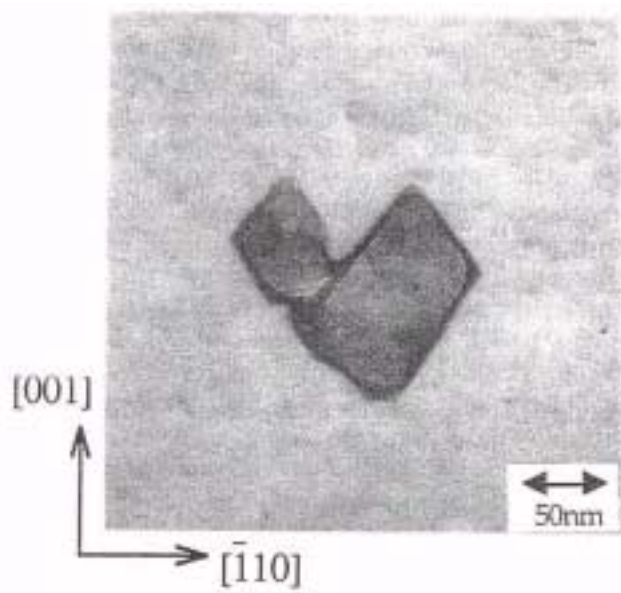
(a)
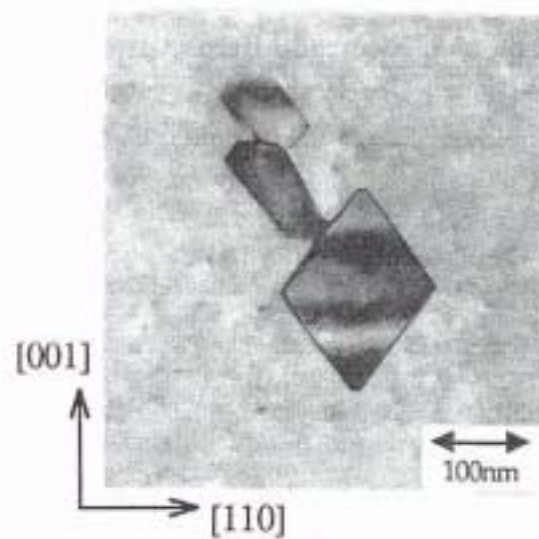
(b)

Figure 1.6: TEM image of (a) twin void and (b) triple void [85].

1.3.2 Oxygen and its related defects

One of the important features of CZ silicon is the high oxygen concentration in the crystal,

caused by the dissolution of the quartz (SiO_2) crucible used to hold the melt. Some of the

oxygen in the melt evaporates from the melt surface as volatile SiO, and some is incorporated into the silicon crystal [12]. The incorporation behavior of oxygen into silicon crystal is the result of complex interplay between the crucible dissolution, surface evaporation, thermal and forced convection in the melt, and oxygen segregation into the melt/crystal interface [95]. The strongest influence on the oxygen content in silicon crystal is exerted by the crystal and crucible rotation rates, which drive different flow patterns in the melt [209].

Oxygen is typically incorporated in the crystal at concentrations of $O(10^{18}) atoms/cm^3$ and it mainly occupies interstitial positions in the silicon lattice. When the crystal cools, the oxygen becomes supersaturated and may precipitate. Oxygen related defects include oxygen precipitates [43,73], dislocations and stacking faults associated with the precipitates [141], and thermal donors and new donors [104]. Oxygen in its usual interstitial configuration in silicon is electrically inactive. But small clusters of oxygen atoms, silicon atoms and point defects result in electrically active donor configurations within the silicon lattice. There are two kinds of thermally activated donors. Thermal Donors (TD) are formed upon heat treatment in the temperature range 300-500°C and rapidly annihilated above 600°C. New Donors (ND) are formed in the temperature range 650-850°C [104,25]. Although TD and ND have been extensively studied for several decades, the atomic structures and the formation mechanisms of these defects are not well understood.

The morphology of oxygen precipitates depends on the annealing temperature. Three temperature regimes may be distinguished [67]. Ribbon-like defects have been observed below 800°C. If the annealing is in the temperature range 800-1050°C, disk-shaped precipitates are dominant. Octahedral precipitates are formed above 1050°C. Disk-shaped precipitates are most likely cristobalite and octahedral precipitates are amorphous SiO_2

[141]. There may be considerable overlap in these three regimes and all morphologies may be observed in a single wafer. Bergholz gave a more detail summary with five temperature regimes: ribbon shape below $550°C$, mixture of ribbon and disk-shaped shapes between 550 and $700°C$, disk-shaped shape between 700 and $900°C$, octahedral shape between 900 and $1100°C$, polyhedral or nearly spherical shape above $1100°C$ [10]. Various forms of oxygen precipitates are shown in Figure 1.7.
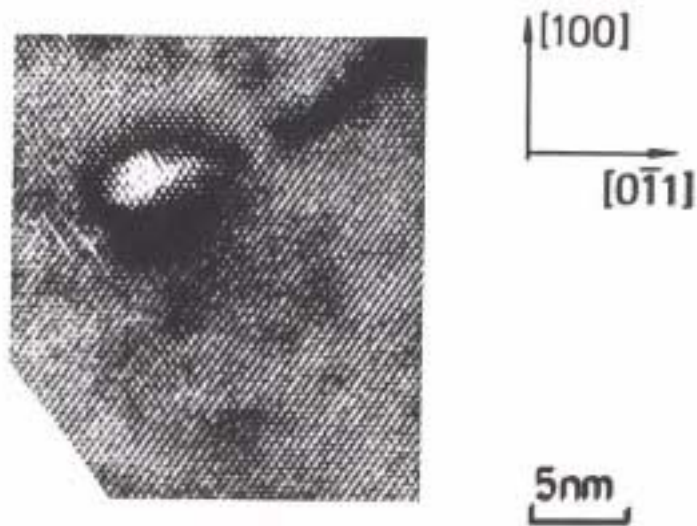
(a)
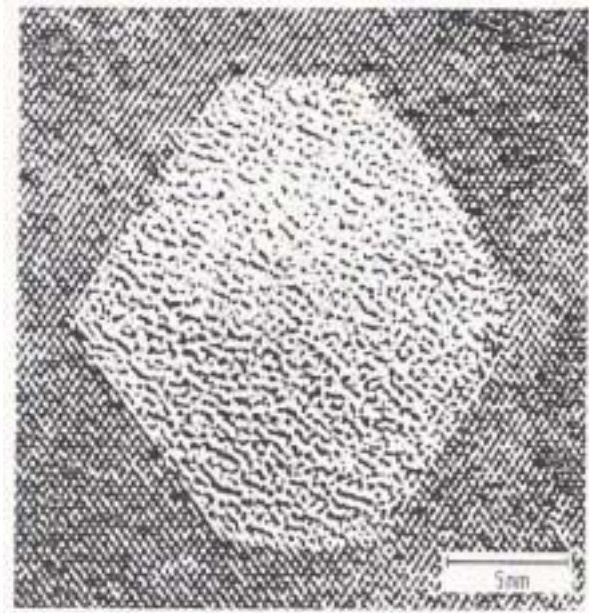
(b)
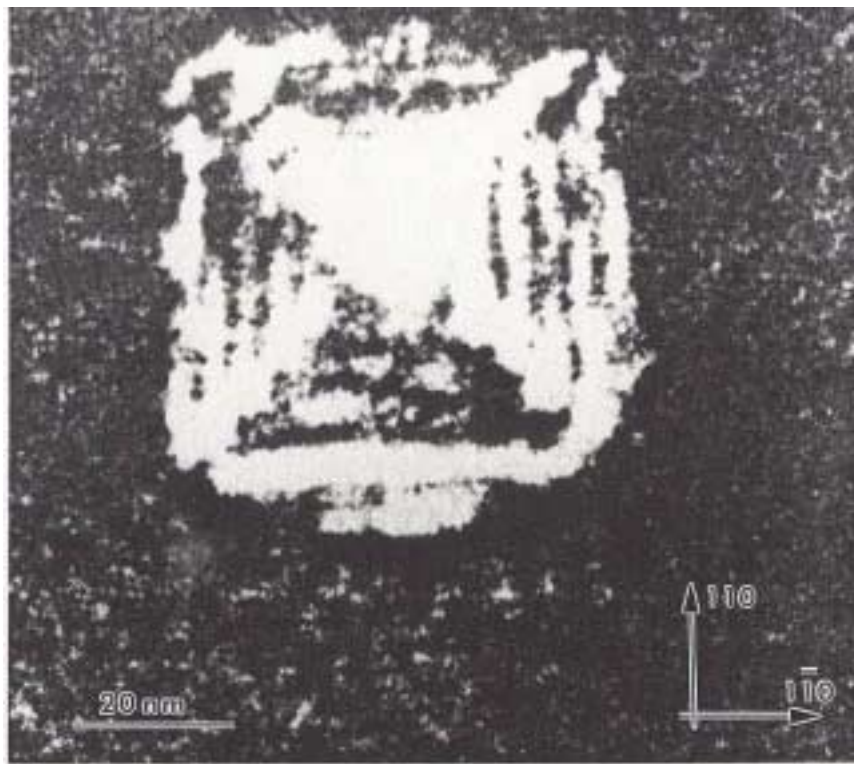
(c)
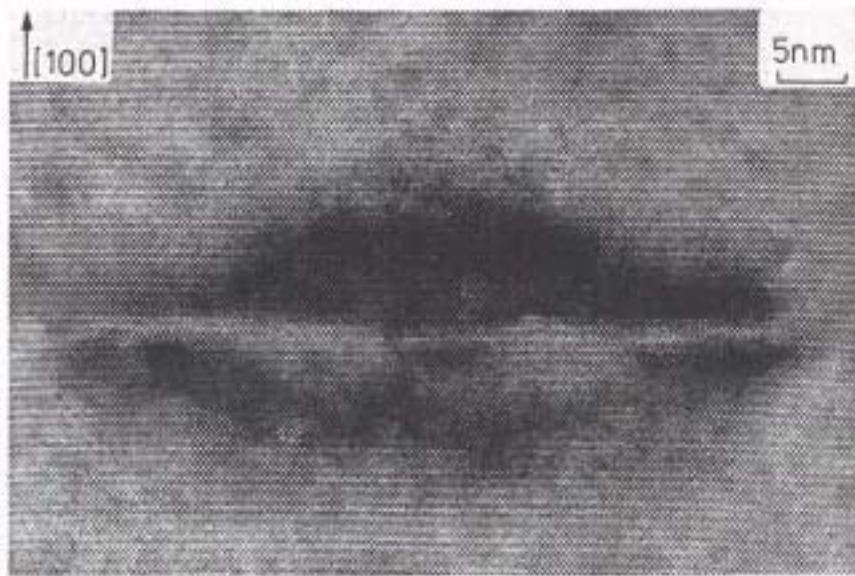
(d)

(e)

Figure 1.7: HRTEM direct lattice images (except c) of (a) a spherical amorphous oxygen precipitate; (b) a polyhedral amorphous oxygen precipitate; (c) a weak-beam TEM image of an octahedral amorphous oxygen precipitate; (d) a disk-shaped amorphous oxygen precipitate; (e) a cross section of a ribbonlike crystalline oxygen precipitate [10].

Oxygen precipitates were first considered as contaminants in silicon and considerable research were done to reduce oxygen concentration in CZ silicon. With the development of intrinsic/internal gettering (IG), oxygen precipitates and some related defects became considered as an effective means to getter impurity in silicon. In contrast to internal gettering is extrinsic/external gettering (EG), which involves the introduction of gettering sinks at the back surface region of a silicon wafer. There are at least two disadvantages of external gettering [148]. One is that external gettering process can introduce additional contamination. The other is that the diffusion path for the impurity from the front surface to gettering sinks at the back surface is relatively long.

During high temperature wafer processing, metallic impurities are introduced onto the wafer surface which can result in harmful near surface defects [25]. Oxygen precipitates and related defects may be concentrated in the wafer middle section, leaving a defect-free surface section or denuded zone (DZ) where devices can be fabricated. The volume of a SiO_2 precipitate is about two times that of Si atom. This expansion leads to strain between the precipitate and the silicon matrix and to the formation of dislocation loops and stacking faults with oxygen precipitates to release this strain. The dislocation loops and stacking faults associated with oxygen precipitates are shown in Figure 1.8 and Figure 1.9. These dislocation loops and stacking faults can act as effective sinks for harmful metallic impurities [165], as can be explained by the Cottrell effect, in which the solubility of a foreign atom will be greater in the vicinity of a dislocation [113]. Dangling bonds introduced by dislocations or stacking faults also are effective gettering sites for impurities [146]. Oxygen precipitates alone also can act as gettering sinks for iron [46]. For example, metallic impurities in silicon preferentially precipitated in the middle of the wafer where oxygen precipitates and related defects serve as low energy nucleation sites, while no metal precipitates occur in the denuded zone.
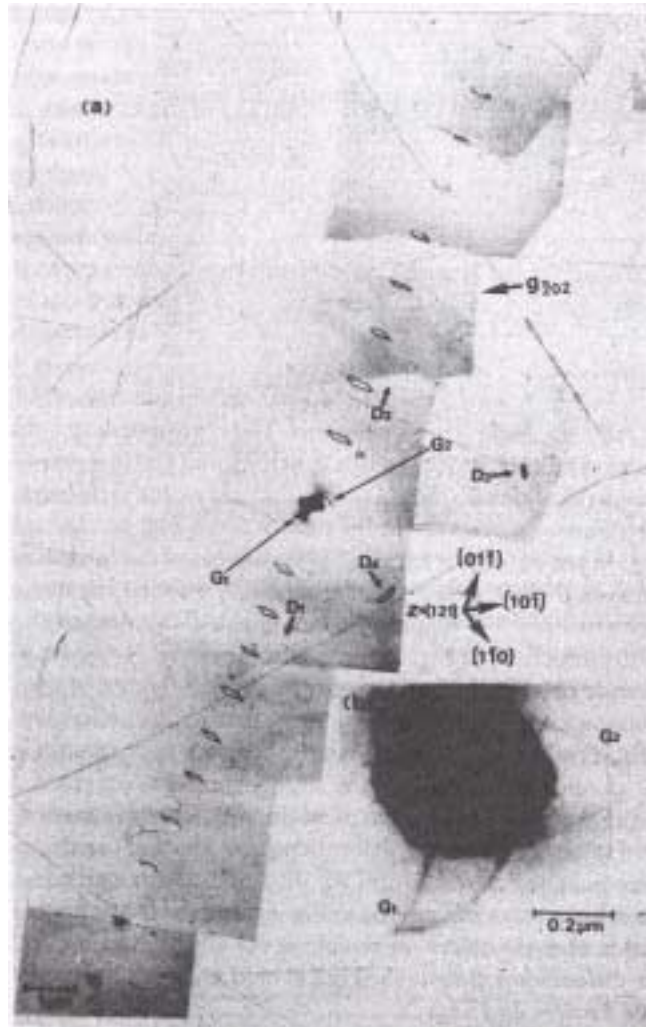
Figure 1.8: Regular octahedral precipitate and punched-out dislocations: G_1, G_2 = generator dislocation; D_1, D_2, D_3, D_4 = punched-out dislocation row [140].
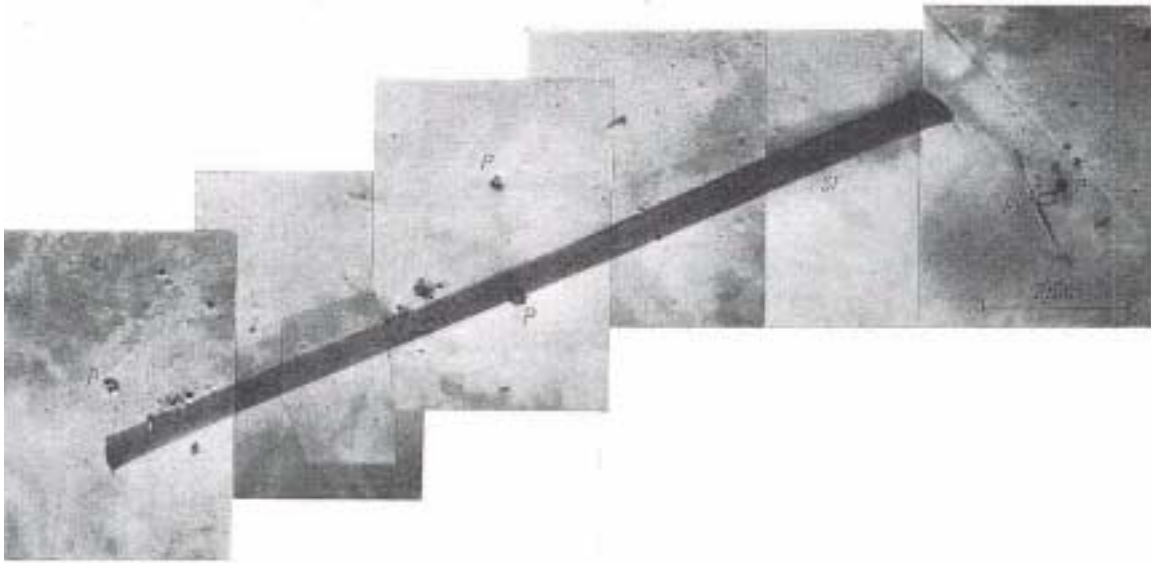
Figure 1.9: Oxygen precipitates (P), a stacking fault (SF), and prismatic dislocation loops (PL) [205].

Dislocations may be saturated with impurities [165], implying that internal gettering has limited capacity to getter impurities. The more oxygen precipitates, the more impurities they can getter. However very high concentration of oxygen precipitates can lead to the disappearance of the denuded zone and to the degradation of mechanical properties of the wafer [147]. Oxygen precipitation must be well controlled. For charge-coupled device (CCD), bipolar, dynamic random access memory (DRAM) or complementary metal-oxide-semiconductor (CMOS) devices the optimum amount of precipitated oxygen and depth of the denuded zone for the best efficiency of gettering and yield have been reported [79].

Oxygen in silicon has other beneficial effects. For example, CZ wafers with high oxygen concentration have been shown to have higher resistance to warpage than FZ wafers during wafer processing [163]. The effect of oxygen on mechanical properties of silicon wafer can be understood in terms of how oxygen affects dislocation processes [102]. Oxygen effectively suppresses the dislocation generation and retards the dislocation motion,

therefore results in high yield strength. But oxygen precipitates can degrade the mechanical properties since dislocations are punched out during precipitation. So if oxygen precipitates too much, the yield strength of wafer will be greatly reduced.

1.3.3 Other impurities-B, C, and N

Boron is a widely used p-type dopant. It is mainly substitutional and replaces a silicon atom in silicon crystal to contribute a hole. Boron concentration in silicon has wide range which is from 10^{15} to 10^{20} cm^{-3} for various application. It was found that when concentration is higher than $10^{17} cm^{-3}$, boron has significant effect on OSF-ring position and critical V/G. Specifically OSF-ring is shifted toward center and critical V/G increases with boron concentration [1]. Some impurity effects on OSF-ring position are illustrated in Figure 1.10. Quantitative prediction of model developed by Sinno et al. agreed with experiments [29,153]. The free formation energies of different defect complexes in the model were based on the work by Clancy et al. [98,123]. Small complexes BI and B_2I play important role here. Extra interstitials are stored in BI and B_2I with their equilibrium concentrations at melt/crystal interface, and then released as the interstitial concentration decreases due to recombination near the melt/crystal interface. These extra interstitials shift the balance between vacancy and interstitial more favorable for interstitial, therefore shrink the vacancy-dominated core region and increase the critical V/G. Voronkov proposed another mechanism for the effect of boron on critical V/G [187,188]. As discussed in section 1.3.1, a silicon crystal at the melt/crystal interface is intrinsic even with boron doping. The Fermi level shifted by boron is small, therefore changes of charged native point defects are relative small compared with neutral native point defects. However critical V/G is very sensitive to total native point defect which includes neutral point defect and all charged point defects at melt/crystal interface. Even though the change of total native point defect due to boron is small, it may still have significant effect on critical V/G.

If this mechanism is right, we would expect exactly the same critical *V/G* change for all p-type silicon with the same doping level, and the same thing is true for all n-type silicon but in the different direction. In other word, for silicon with different dopants such as *B*, *Ga*, *P*, and *As*, as long as the doping levels are the same the critical *V/G* changes are the same for *B* and *Ga*, and exactly the same but in the other direction for *P* and *As*. This kind of experiment is still needed to be done to prove the mechanism above.
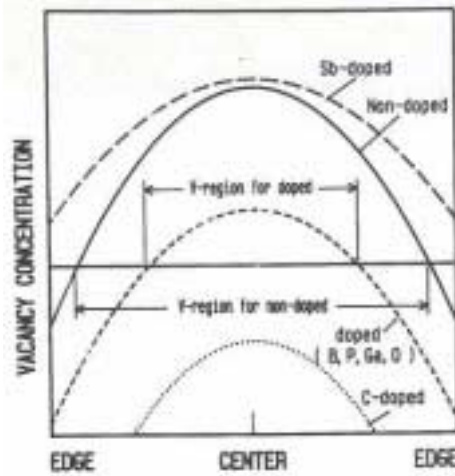
Figure 1.10: Schematic impurity effect on the position of OSF-ring [1].

Carbon is a substitutional impurity and has the similar effect on OSF-ring position and critical *V/G* as Boron. However the OSF-ring position and the critical value of *V/G* are much more sensitive to carbon. A vacancy rich core region could disappears even at carbon concentration as low as $5 \times 10^{16} cm^{-3}$ [1]. Although the carbon concentration in commercial CZ silicon crystal is less than the ion detect limit, which is about $10^{15} cm^{-3}$, it still could have non-negligible effects on silicon crystal. It is well known that there exists a critical *V/G*. However, as pointed out by Bullis [17], its value still varies from manufacturer to manufacturer and is in the range from 1.3×10^{-3} to $2.0 \times 10^{-3} cm^2 min^{-1} K^{-1}$. A very possible explanation is that they actually have different carbon concentrations in sili-

con crystal, and therefore different critical *V/G*. Free formation energies of various carbon defects are needed to prove this. Unfortunately there are only formation enthalpies available in the literature [171], and there is no too much information about formation entropies. Carbon is known to enhance oxygen precipitation in silicon crystal [144,147]. Lattice contraction due to the smaller atomic radius of carbon (0.77Å) compared with that of silicon (1.18Å) may attract interstitial oxygen atoms.

Recently nitrogen has drawn much attention because of its potential to realize the increasing demand for 'defect-free' or 'perfect' silicon in semiconductor industry. The nitrogen doping can be achieved by adding N_2 gas to the growth chamber for FZ crystal [181], or by putting silicon wafers with Si_3N_4 film into silicon melt for CZ crystal [4]. It was found that nitrogen can suppress both vacancy and interstitial related microdefects in FZ silicon crystal [2]. von Ammon [181] reported that for FZ crystal with diameter of 100 *mm* and pull rate of 2.5 *mm/min*, vacancy related D-defects disappear in the center of the crystal at nitrogen concentration of $8 \times 10^{13} cm^{-3}$, and interstitial related A-defects disappear at nitrogen concentration of $1.35 \times 10^{14} cm^{-3}$. This effect is significantly suppressed in CZ crystal due to high oxygen concentration and reaction between oxygen and nitrogen [180]. Nitrogen is also known to enhance oxygen precipitation in silicon crystal [4,143]. However, nitrogen is still very helpful for CZ crystal since it can widen the operating window for 'perfect' silicon [72]. Many researchers proposed different mechanisms to address the effect of nitrogen on FZ and CZ silicon, and there is still no agreement. Kageshima et al. [82] carried out first-principles calculations and showed that N_2V_2 is the most stable specie. Two reactions, $N_i + V \leftrightarrow N_s$ and $N_s + I \leftrightarrow N_i$ (i and s represent interstitial and substitutional respectively), were proposed to explain simultaneous suppression of D-defects and A-defects in FZ crystal [72]. von Ammon et al. [181] further proposed reactions $2N_i \leftrightarrow N_2$ and $N_2 + V \leftrightarrow N_2V$ for the suppression of D-defects, reactions

$N_s + N_i \leftrightarrow N_2 V$ and $N_2 V + I \leftrightarrow N_2$ for the suppression of A-defects without oxygen. With the present of oxygen as in CZ crystal, an additional reaction $2NO \leftrightarrow N_2 + 2O$ is proposed to take oxygen into account by shifting the formation of N_2. Apparently a lot of effort is still needed to understand the nitrogen in silicon and take full advantage of nitrogen.

1.4 Thesis Objectives and Outline

The goal of this thesis is to develop theoretical analysis which can help us understand the physics of microdefect formation and computational models which have quantitative prediction. These schemes can reduce number of expensive experiments in research and development, and eventually help to optimize operating conditions and system design for single crystal growth and wafer annealing process.

Theoretical analysis on native point defects and their clusters during CZ crystal growth is discussed in Chapter 2. OSF-ring dynamics and critical *V/G* are first reviewed. The asymptotic analysis of critical *V/G*, intermediate point defect concentration and the effect of impurity on critical *V/G* are then performed. Further theoretical analysis on the governing equations leads to important scalings for void formation and quantitative estimations of essential variables such as void aggregation temperature, total void density, and average void size.

The role of oxygen in crystalline silicon is discussed in Chapter 3. It includes a detailed description of the model for oxygen precipitation, enhanced oxygen precipitation due to grown-in spatial inhomogeneities in oxygen distribution, simulation of perfect silicon, and simulation of wafer annealing compared with experimental results.

Some directions of further research are discussed in Chapter 4.

Chapter 2

Theoretical Analysis on Native Point Defects and Point Defect Clusters

2.1 Overview

Most modern microelectronics devices are manufactured on substrates or wafers made of single-crystalline silicon which is mainly produced by the Czochralski (CZ) crystal growth system. The quality of microelectronics devices greatly relies on the defect control in the single crystal silicon. Understanding of the defect formation in silicon crystal is therefore very crucial.

The Oxidation-Induced Stacking Fault Ring or OSF-ring has received an enormous amount of attention as a defect structure in CZ-grown silicon. The ring is detectable by X-ray tomography of wafers after wet oxidation. It is composed by extrinsic (interstitial-type) stacking faults that lay in the <111> crystallographic planes and that grow isotropically from small oxide precipitates [160]. It is thought that the self-interstitials are supplied by injection during the wet oxidation and collected on stacking faults that are already formed during oxide precipitation during crystal growth [54]. The structure of the OSF-ring detected by X-ray is shown in Figure 2.1, which is taken from [59]. The ring separates the vacancy-rich core, which is populated by voids, from the self-interstitial-rich outer annulus, which contains stacking faults. Interestingly, there is a finer structure. Just outside the OSF-ring there is a annular region of almost microdefect-free crystal, as shown in Figure 2.1. This region has received much attention [185,186] because its existence is an indication of the crystal growth conditions where almost perfect silicon can be grown. Simulation of the perfect silicon will be discussed in Section 3.4.
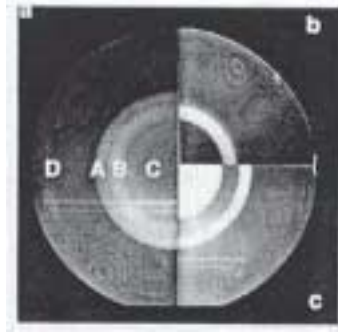
Figure 2.1: X-Ray topograph of radial cross section of CZ crystal showing the vacancy-rich core (C), the OSF-ring (B), the nearly defect free ring outside the OSF-ring (A), and the self-interstitial rich outer ring (D).

The linkage between the radius of the OSF-ring and CZ processing conditions (pull rate and the temperature field in the crystal) have been well established [29,154,183]. The most important empirical observation of the OSF-Ring was reported by Dornberger et al. [28] who demonstrated that the radius of the ring could be correlated by the simple expression

$$\frac{V}{G(R_{OSF})} \cong 1.34 \times 10^{-3} \quad cm^2 min^{-1} K^{-1} \tag{2.1}$$

where V is the pull rate and $G(R_{OSF})$ is the axial temperature gradient in the crystal measured at the melt/crystal interface and at the radial location $r = R_{OSF}$.

Voronkov was the first to connect theoretically point defect dynamics and crystal growth operating conditions, such as pull rate and temperature field, with observable transitions in microdefect structures during crystal growth. His landmark paper in 1982 [183] pioneered comprehensive modeling of point defect dynamics.

Brown et al. [15] and then Sinno et al. [151] put forward the hypothesis that the approximate location of the OSF-ring could be predicted as the location of the neutral zone where neither native point defect reached sufficient super-saturation to allow nucle-

ation and growth of the corresponding aggregates. For temperatures in the crystal much below the melting point (where the equilibrium point defect concentrations are much lower than the typical values in the crystal), this condition is expressed in terms of the excess concentration $\Delta(r, z) \equiv C_I(r, z) - C_V(r, z)$ as

$$\Delta(R_{OSF}, z) \cong 0 \tag{2.2}$$

where R_{OSF} is the approximate location of the OSF-ring according to this criterion. Here it is assumed that the axial location is far enough from the solidification interface that the crystal has cooled sufficiently so that axial diffusion of point defects is no longer important. Sinno et al. [151] further assumed that the location $r = R_{OSF}$ can be predicted solely from point defect dynamics, i.e. by solving the reaction-diffusion equations for native point defects without accounting for cluster formation. His simulations of the dynamics of the OSF-Ring with crystal pull rate V and axial temperature gradient G at melt/crystal interface well agree with experimental results for a wide range of operating conditions when point defect thermophysical properties (equilibrium concentrations and diffusivities) are fit to a single set of experimental data.

The separation between the vacancy-rich core and the self-interstitial-rich outer ring is shown schematically in Figure 2.2. Sinno et al. [151] postulated there is a region near the melt/crystal interface where the high temperature of the crystal makes the point defects so mobile that the dynamics is dominated by diffusion, convection, and point defect recombination. As a result, intermediate, almost axially constant concentrations of point defects are established with the absolute concentrations depending on a delicate balance of axial diffusion, convection, and reaction at different radial locations across the crystal. As the crystal cools, these point defects may become super-saturated and nucleate clusters at nucleation temperatures that depend on the intermediate point defect concentrations. As is

experimentally well known, voids and self-interstitial defects nucleate at different temperatures. Actually, the nucleation temperatures are not constants, but depend on the intermediate point defect concentrations that supply the driving forces for clustering. The radial dependence of the temperature field and of these vacancy and self-interstitial concentrations cause radial variation of the nucleation region.
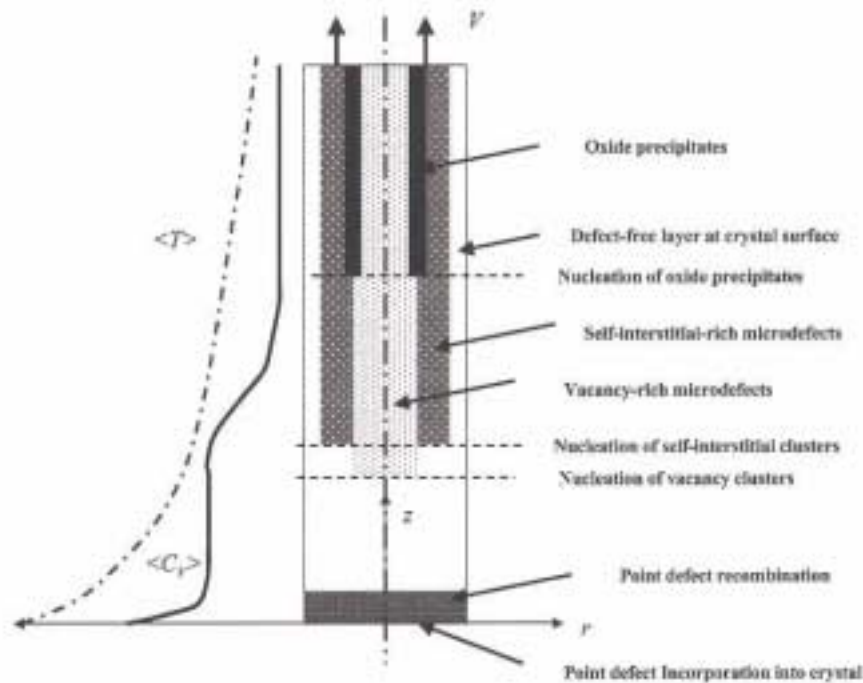
Figure 2.2: Schematic diagram of regions for point defect reaction and formation of vacancy, self-interstitial and oxygen precipitates as a function of axial and radial location in the crystal.

Finally, at a yet lower temperature, oxide precipitates begin to form from the supersaturated oxygen concentration in the crystal. These precipitates preferentially form in a region of the crystal where the residual vacancy concentration exists to supply the needed free volume for precipitate growth to relieve strain energy during precipitation. The oxygen precipitation is the subject of Chapter 3, and the details of the model and simulation results are referred to that chapter.

Sinno [150,151,152] and Mori [108] had successfully developed a framework for modeling and numerical simulation of native point defects - vacancies and self-interstitials, and point defect clusters - voids and self-interstitial clusters during the CZ crystal growth. The model was built on the dynamics of native point defects, growth and dissolution of point defect clusters. The dynamics of native point defects include diffusion, convection and recombination of vacancies and self-interstitials. Growth and dissolution of voids and self-interstitial clusters are modeled by a diffusion-limited aggregation process with a phenomenological model for the Gibbs free energies of cluster formation. Sinno developed some numerical methods based on the standard Galerkin method with artificial diffusivities for clusters and CC70 [20,31,32,121,122] finite difference method for cluster size space. Mori further developed a time-dependent simulator with operating splitting for time integral, the discontinuous Galerkin (DG) [21,81] method for clusters, and the local discontinuous Galerkin (LDG) [7,22] method for native point defects. The two-dimensional numerical simulation results of vacancies, interstitials, voids and interstitial clusters during the CZ crystal growth prove the physical picture shown in Figure 2.2 and provide physical insight for the theoretical analysis in this Chapter.

Some theoretical analysis also had been done on the native point defects during crystal growth. Voronkov derived a theoretical expression for critical V/G which separates the vacancy-rich core from the self-interstitial-rich outer ring [183]. Sinno tried to analyze the recombination region near the melt/crystal interface and get the expression for critical V/G rigorously by asymptotic analysis [151]. Even though Sinno's approach is correct and followed in the analysis of recombination region in this Chapter, his result is wrong.

In this Chapter, a comprehensive theoretical analysis will be done on the native point defects and formation of their clusters during crystal growth. First, rigorous asymptotic analysis is performed to get the expression for critical V/G which is the same as

Voronkov's final result [183]. This analysis is then extended to the intermediate point defect concentration at arbitrary V/G and the effect of impurity such as Boron on the critical V/G. The cluster formation is further analyzed by examining discrete and continuous forms of rate equations to get useful scalings and quantitative prediction of important variables such as aggregation temperature, total void density, and average size of void. All these theoretical analysis greatly improve the understanding of physics of defect formation during the silicon crystal growth.

The details of physical models for native point defects and point defect clusters during CZ crystal growth are discussed first in Section 2.2. One-dimensional simulation results of point defects and their clusters during crystal growth are then illustrated to provide physical insight for this process and introduce some important concepts in Section 2.3. Theoretical analysis on the model described in Section 2.2 is then performed. The recombination region is analyzed in Section 2.4 and the cluster formation is analyzed in Section 2.5. This Chapter is concluded by the summary in Section 2.6.

2.2 Physical Models for Native Point Defects and Point Defect Clusters during CZ Crystal Growth

2.2.1 Governing Equations

The mathematical model for native point defects and point defect clusters during CZ crystal growth developed in this section is the basis for both the numerical simulation and theoretical analysis in this chapter. The reactions associated with vacancies, interstitials and their clusters in crystal growth include

Recombination of vacancies and interstitials:

$$I + V \leftrightarrow perfect\ crystal \tag{2.3}$$

Growth and dissolution of interstitial clusters:

$$I_n + I \leftrightarrow I_{n+1} \qquad n = 1, 2, 3, \ldots \tag{2.4}$$
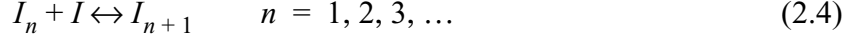
Growth and dissolution of voids (vacancy clusters):

$$V_n + V \leftrightarrow V_{n+1} \qquad n = 1, 2, 3, \ldots \tag{2.5}$$
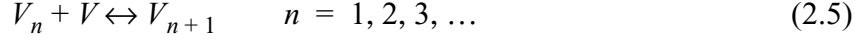
where I and V represent self-interstitial and vacancy, I_n and V_n represent interstitial cluster and void of size n. Here the clusters can only grow or dissolve by addition or subtraction of monomer since generally the clusters are immobile in solid state. However it is found that small point defect clusters such as dimer may be mobile [11,71,92,125]. Both molecular dynamics simulations and experimental results give a migration energy of about $1.35eV$ for vacancy dimer in silicon [71,125]. Pellegrino et al. reported that the maximum value of pre-exponential factor for the diffusivity of vacancy dimer is about $1 \times 10^{-1}cm^2/s$ [125]. So the diffusivity of vacancy calculated from eq. (2.31) is higher than that of the vacancy dimer in the whole temperature range of the silicon crystal growth. Fortunately the model based on reactions (2.4) and (2.5) is still valid unless the diffusivity of dimer is much higher than that of monomer. The explanation for this will be provided in Section 2.5.4 after the theoretical analysis of cluster formation.

Based on the reactions above, the dynamics of native point defects (vacancies and self-interstitials) and their clusters (voids and self-interstitial clusters) is described by the following three sets of basic conservation equations [15,108,150,152]. The time-dependent conservation equations for vacancies and self-interstitials are

$$\underbrace{\left(\frac{\partial}{\partial t} + V\frac{\partial}{\partial z}\right)}_{(A) \quad (B)} C_I + \nabla \bullet \left(\underbrace{-D_I(T)\nabla C_I}_{(C)} + \underbrace{\frac{D_I(T)C_I Q_I^{*'}}{kT^2}\nabla T}_{(D)}\right)$$

$$k_{IV}(T)(C_I C_V - C_I^{eq}(T)C_V^{eq}(T)) + \left(\frac{\partial}{\partial t} + V\frac{\partial}{\partial z}\right)\left(\sum_{n=2}^{n_{match}-1} nC_{nI} + \int_{n_{match}}^{\infty} nf_I dn\right) = 0 \tag{2.6}$$

47

$$(E) \qquad\qquad\qquad (F) \quad\ (G)$$

$$\left(\frac{\partial}{\partial t} + V\frac{\partial}{\partial z}\right)C_V + \nabla \bullet \left(-D_V(T)\nabla C_V + \frac{D_V(T)C_V Q_V^{*\prime}}{kT^2}\nabla T\right)$$

$$(A) \quad\ (B) \qquad\qquad\qquad (C) \qquad\qquad (D)$$

$$k_{IV}(T)(C_I C_V - C_I^{eq}(T)C_V^{eq}(T)) + \left(\frac{\partial}{\partial t} + V\frac{\partial}{\partial z}\right)\left(\sum_{n=2}^{n_{match}-1} nC_{nV} + \int_{n_{match}}^{\infty} nf_V\,dn\right) = 0 \quad (2.7)$$

$$(E) \qquad\qquad\qquad (F) \quad\ (G)$$

where V is crystal pulling rate, $(D_i,\ C_i,\ C_i^{eq},\ C_{ni},\ f_i,\ Q_i^{*\prime})$ are the (diffusivity, concentra-tion, equilibrium concentration, discrete cluster concentration, continuous cluster concen-tration, reduced heat of transport for the thermodiffusion) and the subscripts $i = I$ and $i = V$ represent self-interstitial and vacancy respectively, k_{IV} is the rate coefficient of recombination, k is Boltzmann constant, T is temperature, and n is the size of clusters.

A special case is the steady state when point defects concentrations don't change with time and time-dependent terms (A) and (F) vanish. The terms (B) and (G) are the convec-tion terms due to crystal pulling. The term (C) is the Fick diffusion term.

The term (D) is the thermodiffusion of point defects driven by the temperature gradi-ent. There is no reliable estimation for the reduced heat of transport for point defects. The thermodiffusion was assumed to play a small role in the point defect dynamics and the reduced heat of transport was neglected in Sinno and Mori's simulations [108,150]. This assumption was justified by the sensitivity analysis of the reduced heat of transport on the point defect dynamics in silicon crystal growth [151]. It was also shown asymptotically that thermodiffusion of point defects is much less than the Fick diffusion given an upper bound on the magnitude of the reduced heats of transport [151]. In this thesis, the ther-modiffusion will also be neglected.

The term (E) is the recombination of vacancy and interstitial with the law of mass action. The rate coefficient k_{IV} is modeled by diffusion-limited reaction with the activation energy and is written as [35]

$$k_{IV}(T) = \frac{4\pi a_r}{\Omega c_s}[D_I(T) + D_V(T)]\exp\left(-\frac{\Delta G_{IV}}{kT}\right) \tag{2.8}$$

where $a_r = 10\overset{\circ}{A}$ is the effective capture radius, $\Omega = a^3/8$ is the atomic volume of a silicon atom with lattice constant $a = 5.43095\overset{\circ}{A}$, $c_s = 5\times10^{22}cm^{-3}$ is the atomic density of silicon. The activation energy barrier $\Delta G_{IV} \equiv \Delta H_{IV} - T\Delta S_{IV}$ consists of enthalpic and entropic contributions. The value of activation energy barrier is given in eq. (2.34).

The last two terms (F) and (G) are the source or sink terms for vacancy and interstitial due to their clusters. The summation and the integral in the bracket are the total point defects consumed by point defect clusters. n_{match} is the matching point between the discrete rate equations and Fokker-Planck equations which will be discussed next. The summation from 2 to $n_{match} - 1$ is the point defects consumed by point defect clusters of size 2 to $n_{match} - 1$ in discrete form. The integral from n_{match} to infinite is the point defects consumed by point defect clusters bigger than size n_{match} in continuous form.

The second set of equations are discrete rate equations for small voids and interstitial clusters from dimer to cluster of size $n_{match} - 1$ which has $n_{match} - 1$ monomers in it.

$$\left(\frac{\partial}{\partial t} + V\frac{\partial}{\partial z}\right)C_{nI} = J_{n,I} - J_{n+1,I}, \qquad n = 2, ...n_{match} - 1 \tag{2.9}$$

$\quad (A) \quad (B) \qquad\quad (C) \quad (D)$

$$\left(\frac{\partial}{\partial t} + V\frac{\partial}{\partial z}\right)C_{nV} = J_{n,V} - J_{n+1,V}, \qquad n = 2, ...n_{match} - 1 \tag{2.10}$$

$\quad (A) \quad (B) \qquad\quad (C) \quad (D)$

49

where fluxes $J_{n,I}$ and $J_{n,V}$ are defined as

$$J_{n,X} = g_X(n-1)C_{n-1,X} - d_X(n)C_{n,X}, \qquad X = I, V \qquad (2.11)$$

C_{nI} and C_{nV} are the concentration of interstitial cluster and void of size n, g_X is the growth rate, and d_X is the dissolution rate. The growth rate and dissolution rate will be discussed in Section 2.2.2. The terms (A) and (B) in eqs. (2.9) and (2.10) are concentration changes of clusters of size n with time and position, and the right side (C)-(D) is the net flux of clusters of size n. All clusters are assumed to be immobile so diffusion of clusters is ignored. It is already discussed in the description of reactions (2.4) and (2.5) that they are still valid even if the mobility of small cluster is considered. Therefore the net flux (C)-(D) on the right side of eqs. (2.9) and (2.10) also is valid even if small clusters are mobile. However there should be a diffusion term in eqs. (2.9) and (2.10) for small clusters if their mobilities are considered. Fortunately eqs. (2.9) and (2.10) are still good approximates for small clusters in this case because their diffusivities are small. For example, estimation of diffusivity of vacancy dimer at $T = 1000°C$, which is about the void aggregation temperature where significant voids can form, gives $D_{V_2} = 4.5 \times 10^{-7} cm^2/s$ based on [125]. This corresponds to $Pe = VL/D_{V_2} = 2.2 \times 10^3$ with length scale $L = 1 cm$ and a typical pull rate $V = 1 \times 10^{-3} cm/s$. High Pe indicates that diffusion is not important compared with convection which is represented by term (B) in eqs. (2.9) and (2.10). J_n is the net flux from size n-1 cluster to size n cluster, so the net reaction rate to form the cluster of size n is the difference between J_n and J_{n+1} based on reactions (2.4) and (2.5).

The last set of equations are Fokker-Planck equations for clusters bigger than n_{match}.

$$\left(\frac{\partial}{\partial t} + V\frac{\partial}{\partial z}\right)f_I = -\frac{\partial}{\partial n}\left(A_I(n)f_I - B_I(n)\frac{\partial f_I}{\partial n}\right) \qquad (2.12)$$

$$\left(\frac{\partial}{\partial t} + V\frac{\partial}{\partial z}\right)f_V = -\frac{\partial}{\partial n}\left(A_V(n)f_V - B_V(n)\frac{\partial f_V}{\partial n}\right) \tag{2.13}$$

where f_I and f_V are continuous form of interstitial cluster and void concentrations, and the coefficients A and B are defined as

$$A_X(n) = g_X(n) - d_X(n) - \frac{\partial}{\partial n}B_X(n), \qquad X = I, V \tag{2.14}$$

$$B_X(n) = \frac{1}{2}(g_X(n) + d_X(n)), \qquad X = I, V \tag{2.15}$$

Fokker-Planck equation is basically a kind of Taylor expansion of the discrete rate equation, and is employed here because the maximum cluster size could be as big as 10^{10} and if discrete rate equations are extended to maximum cluster size we would end up with solving equations with order of 10^{10} unknowns which is a extremely difficult job. The detail of the derivation of Fokker-Planck equation from the discrete rate equation will be discussed in Section 2.2.3. At n_{match} both the cluster concentration and the nucleation flux are matched to the discrete rate equations. n_{match} is chosen as 10 to get size distribution with enough accuracy [108,150].

The computational domain is shown in Figure 2.3. The boundary conditions for vacancy and interstitial are their equilibrium concentrations at melt temperature for melt/crystal interface, and no-flux boundary conditions on other three boundaries. The boundary conditions for point defect clusters are zero concentration for all the clusters at melt/crystal interface.
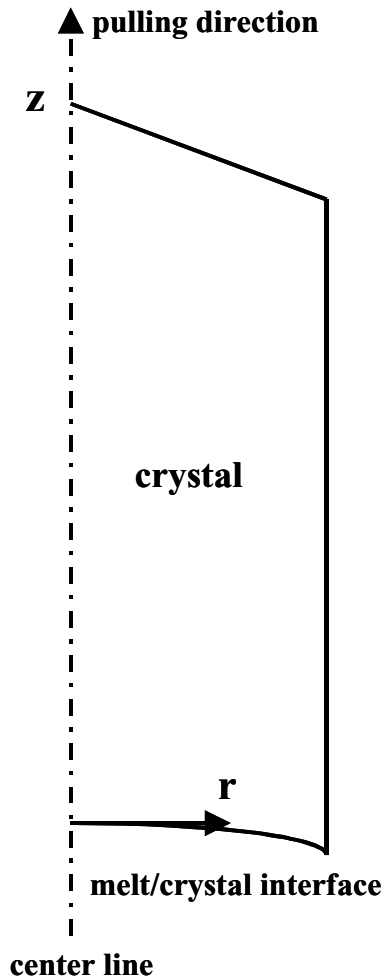
Figure 2.3: Computational domain for CZ crystal growth.

2.2.2 Growth and Dissolution Rates

The growth rate g_X and dissolution rate d_X are two important variables in the mathematical model developed in the previous section. This section is devoted to the calculation of these two variables.

Vacancy clusters in silicon crystal are characterized microscopically as octahedral voids which are shown in Figure 1.6 [85,172]. The octahedral shape in the anisotropic silicon crystal is equivalent to the spherical shape in an isotropic environment. So for the simplicity morphology of void in this thesis is taken as sphere, and it is validated by the

fact that both void aggregation temperature and void size distribution predicted by model based on spherical void well agree with experimental observation [108,182]. The interstitial clusters are assumed to be spherical, and it may need further improvement because of the existence of non-spherical interstitial clusters such as stacking-faults and dislocation loops. This work hasn't been done because the only experimental data available to compare with simulation results for interstitial clusters is the aggregation temperature of interstitial clusters and there is no enough information about interstitial cluster size distribution and their density during the crystal growth in the literature.

The Gibbs free energy of formation for void and interstitial cluster is expressed as

$$G_X(n) = -nkT\ln\frac{C_X}{C_X^{eq}} + G_X^f(n), \qquad X = I, V \tag{2.16}$$

and

$$G_X^f(n) = 4\pi r^2 \sigma_X + \frac{4}{3}\pi r^3 \Delta G_X^{Vol}, \qquad X = I, V \tag{2.17}$$

where X represents self-interstitial (I) and vacancy (V), C_X and C_X^{eq} are concentration and equilibrium concentration of point defects, and r is the radius of the cluster of size n. The free energy of formation $G_X(n)$ includes configurational part $-nkT\ln(C_X/C_X^{eq})$ and non-configurational part $G_X^f(n)$ which is consist of surface ($\propto r^2$ or $n^{2/3}$) and volume ($\propto r^3$ or n) contributions. σ_X is surface energy per surface area, and ΔG_X^{Vol} is the volume contribution per volume for Gibbs free energy. The volume contribution ΔG_X^{Vol} is related to stress energy, and it is reasonable to assume that for void $\Delta G_V^{Vol} = 0$ because any stress can be easily released through the free volume provided by void. Mori did sensitivity analysis of the aggregation temperature of spherical interstitial cluster on the volume contribution, and found out that zero volume contribution $\Delta G_I^{Vol} = 0$ gives the best estimation for interstitial cluster aggregation temperature [108]. This is consistent with the

low stress energy associated with the spherical interstitial clusters, which can not be observed by transmission electron microscopy (TEM). The surface energy for point defect clusters are chosen as

$$\sigma_I = 1.2 \ J/m^2 \tag{2.18}$$

$$\sigma_V = 0.9 \ J/m^2 \tag{2.19}$$

The growth rate $g_X(n)$ and dissolution rate $d_X(n)$ for cluster of size n are [108,138,150,152]

$$g_X(n) = k_r(n)C_X^{if}(n) \tag{2.20}$$

$$d_X(n) = k_r(n)C_X^{eq}(n) \tag{2.21}$$

where $C_X^{eq}(n)$ is the point defect equilibrium concentration for cluster of size n. $C_X^{eq}(n)$ is related to bulk point defect equilibrium concentration C_X^{eq} as

$$C_X^{eq}(n) = C_X^{eq}\exp\left(\frac{\Delta G_{X,\,n\to n+1}^{f}}{kT}\right) \tag{2.22}$$

where $\Delta G_{X,\,n\to n+1}^{f}$ is the difference of the non-configurational part of free formation energy between point defect cluster of size n and $n+1$. The cluster surface reaction rate $k_r(n)$ is given as [138]

$$k_r(n) = \frac{4\pi r^2 D_X}{\delta}\exp\left(-\frac{\Delta G_{X,\,n\to n+1}}{kT}\right) \tag{2.23}$$

where D_X is the diffusivity of point defect, δ is the lattice spacing or 0.235 nm in silicon, $\Delta G_{X,\,n\to n+1}$ is the difference of the free formation energy between point defect cluster of size n and $n+1$. $C_X^{if}(n)$ is the point defect concentration at the surface of point defect cluster of size n, and is determined by mass balance at the surface.

$$\textit{Point Defect Diffusion Flux at Surface} = g_X(n) - d_X(n) \tag{2.24}$$

The point defect diffusion flux at the surface of point defect cluster is obtained by solving the following differential equation for point defect

$$\nabla^2 C = 0 \tag{2.25}$$

with the boundary conditions

$$C_X(\infty) = C_X \tag{2.26}$$

$$C_X(r) = C_X^{if}(n) \tag{2.27}$$

where C_X is the bulk point defect concentration. The solution of eqs. (2.25)-(2.27) in the spherical coordinate together with eq. (2.24) give

$$C_X^{if}(n) = \frac{k_r(n)C_X^{eq}(n) + k_d(n)C_X}{k_r(n) + k_d(n)} \tag{2.28}$$

where

$$k_d(n) = 4\pi r D_X \tag{2.29}$$

There has been enormous work on the thermophysical properties of point defect and there is still significant discrepancy on their values [155]. The values of these parameters used in this chapter are taken from [150] and they were obtained by molecular dynamics and then fitting some parameters with experimental data on the dependence of the OSF-Ring radius on growth rate and temperature gradient. This yielded

$$D_I = 0.242 \exp\left(-\frac{0.937 eV}{kT}\right) \ cm^2/s \tag{2.30}$$

$$D_V = 1.0 \times 10^{-3} \exp\left(-\frac{0.457 eV}{kT}\right) \ cm^2/s \tag{2.31}$$

$$C_I^{eq} = 2.97 \times 10^{23} \exp\left(1.40 + 3.85 \times 10^{-3} T - \frac{(3.46 + 3.08 \times 10^{-4} T)eV}{kT}\right) \ cm^{-3} \quad (2.32)$$

$$C_V^{eq} = 4.97 \times 10^{22} \exp\left(-3.70 + 3.53 \times 10^{-3} T - \frac{(2.48 + 2.33 \times 10^{-4})eV}{kT}\right) \ cm^{-3} \quad (2.33)$$

$$k_{IV} = 1.2 \times 10^{-6} (D_I + D_V) \exp\left(2.30 - 7.38 \times 10^{-3} T - \frac{0.61 eV}{kT}\right) \ cm^3/s \quad (2.34)$$

2.2.3 Fokker-Planck Equation and Zeldovich Equation

As mentioned in section 2.2.1, the Fokker-Planck equation is a Taylor expansion of the discrete rate equation. The details of derivation from discrete rate equation to continuous form of rate equation such as Fokker-Planck equation and Zeldovich equation are discussed in this section. The Zeldovich and Fokker-Planck equations are also the basis for the theoretical analysis of the rate equations in Section 2.5.

The discrete rate equation can be written as

$$\frac{\partial C_n}{\partial t} = J_n - J_{n+1} \quad (2.35)$$

where

$$J_n = g_{n-1} C_{n-1} - d_n C_n \quad (2.36)$$

$$J_{n+1} = g_n C_n - d_{n+1} C_{n+1} \quad (2.37)$$

For steady-state CZ crystal growth at pull rate V, the axial position z and time t are related by $z = Vt$. The physics of discrete rate equations is illustrated in Figure 2.4. The change of cluster of size n is equal to the difference between net flux J_n from cluster of size n-1 to cluster of size n and net flux J_{n+1} from cluster of size n to cluster of size n+1. The net flux J_n also is the difference in the growth and dissolution rates between cluster of size n-1 and cluster of size n. Equation (2.37) gives a similar relationship for the net flux J_{n+1}. In the discrete rate equations, clusters of size n are always coupled with clusters of size n-

1 and size $n+1$. If only discrete rate equations are employed for the nucleation and aggregation of clusters with maximum size 10^{10}, the size of the matrix need to be solved would be as big as 10^{10} which is extremely difficult. The way to overcome this problem is to transform eq. (2.35) to a continuous form by truncating Taylor expansion at n. Different expansions could lead to different continuous approximations. Fokker-Planck equation and Zeldovich equation are two of them [84].
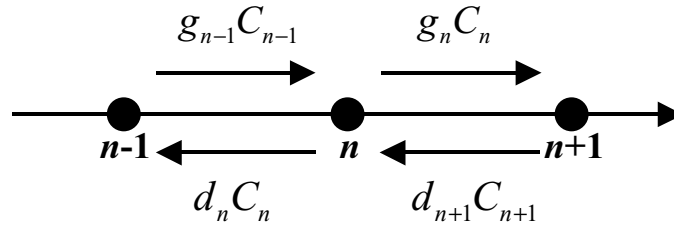
Figure 2.4: Physics of discrete rate equations.

Truncate Taylor expansion to second order for $g_{n-1}C_{n-1}$ at n in eq. (2.36)

$$J_n = g_{n-1}C_{n-1} - d_n C_n$$

$$\approx g_n C_n + \left[\frac{\partial}{\partial n}(gC)\right]\bigg|_n (n-1-n) + \frac{1}{2}\left[\frac{\partial^2}{\partial n}(gC)\right]\bigg|_n (n-1-n)^2 - d_n C_n \tag{2.38}$$

Truncate Taylor expansion to second order for $d_{n+1}C_{n+1}$ at n in eq. (2.37)

$$J_{n+1} = g_n C_n - d_{n+1}C_{n+1}$$

$$\approx g_n C_n - \left(d_n C_n + \left[\frac{\partial}{\partial n}(dC)\right]\bigg|_n (n+1-n) + \frac{1}{2}\left[\frac{\partial^2}{\partial n}(dC)\right]\bigg|_n (n+1-n)^2\right) \tag{2.39}$$

Substituting eqs. (2.38) and (2.39) into eq. (2.35)

$$\frac{\partial C_n}{\partial t} = -\frac{\partial}{\partial n}\left((g-d)C - \frac{1}{2}\frac{\partial}{\partial n}[(g+d)C]\right)\bigg|_n \tag{2.40}$$

f is used to represent continuous cluster concentration, and eq. (2.40) can be written in another form

$$\frac{\partial f}{\partial t} = -\frac{\partial}{\partial n}\left(Af - B\frac{\partial f}{\partial n}\right) \tag{2.41}$$

where

$$A = g - d - \frac{1}{2}\frac{\partial}{\partial n}(g + d) \tag{2.42}$$

$$B = \frac{1}{2}(g + d) \tag{2.43}$$

Eq. (2.41) is the so called Fokker-Planck equation [84]. A is drift velocity, B is diffusion coefficient, and $Af - B\frac{\partial f}{\partial n}$ is the net flux.

Zeldovich equation can be obtained by introducing quasi-equilibrium cluster concentrations and eliminating dissolution rates in the discrete rate equations [84]. Quasi-equilibrium cluster concentrations are defined as

$$g_n C_n^* - d_{n+1} C_{n+1}^* = 0 \qquad for \qquad n = 1, 2, 3 \ldots \tag{2.44}$$

and

$$C_1^* = C_1 \tag{2.45}$$

For any give monomer concentration C_1, the whole quasi-equilibrium cluster distribution can be determined by the definition above. It is called quasi because in eq. (2.45) monomer concentration can be any value and not necessarily the equilibrium monomer concentration. It is called equilibrium because eq. (2.44) means zero flux between any adjacent clusters. Substituting the definition above into eq. (2.35) to eliminate dissolution rates

$$\frac{\partial C_n}{\partial t} = g_{n-1} C_{n-1}^* \left(\frac{C_{n-1}}{C_{n-1}^*} - \frac{C_n}{C_n^*} \right) - g_n C_n^* \left(\frac{C_n}{C_n^*} - \frac{C_{n+1}}{C_{n+1}^*} \right) \qquad (2.46)$$

Truncate Taylor expansion to the first order in the first bracket at $n-1$, and in the second bracket at n,

$$\frac{\partial C_n}{\partial t} = -g_{n-1} C_{n-1}^* \left[\frac{\partial}{\partial n} \left(\frac{C}{C^*} \right) \right] \bigg|_{n-1} + g_n C_n^* \left[\frac{\partial}{\partial n} \left(\frac{C}{C^*} \right) \right] \bigg|_n \qquad (2.47)$$

Truncate Taylor expansion to the first order again at n

$$\frac{\partial C_n}{\partial t} = \frac{\partial}{\partial n} \left(g C^* \frac{\partial}{\partial n} \left(\frac{C}{C^*} \right) \right) \bigg|_n \qquad (2.48)$$

Again f is used to represent continuous cluster concentration, and eq. (2.48) can be rewritten as

$$\frac{\partial f}{\partial t} = -\frac{\partial}{\partial n} \left(vf - g \frac{\partial f}{\partial n} \right) \qquad (2.49)$$

where

$$v = \frac{g}{kT} \left[\frac{\partial}{\partial n} (kT \ln C^*) \right] \qquad (2.50)$$

where k is Boltzmann constant and T is temperature. Eqs. (2.48) and (2.49) are two forms of so called Zeldovich equation [84]. v is drift velocity, g is diffusion coefficient, and $vf - g \frac{\partial f}{\partial n}$ is the net flux. By comparing eqs. (2.41) and (2.49), it is very clear that Zeldovich equation and Fokker-Planck equation are different. Essentially they are two different approximations of the same rigorous discrete rate equations since different truncation schemes are used to obtain them. Among growth rate g, dissolution rate d and the quasi-equilibrium concentration C^*, only two of them are independent. For the Fokker-Planck equation (2.41), g and d are chosen as independent variables. While for the Zeldovich

equation (2.49), g and C^* are chosen as independent variables. In Section 2.5, both Fokker-Planck equation and Zeldovich equation are analyzed. Fokker-Planck equation is analyzed in order to compare with simulation results and verify the theoretical analysis since Fokker-Planck equation is the equation employed in simulation. The model for g and d is also consistent between theoretical analysis and simulation for Fokker-Planck equation. Zeldovich equation is analyzed because of its neat form. Even though Fokker-Planck equation and Zeldovich equation are not same, they lead to the same scalings which will be proved in section 2.5.2.

2.3 One Dimensional Simulation Results for Native Point Defects and Point Defect Clusters during CZ Crystal Growth

The model described in Section 2.2 is too complex to have analytical solutions. Numerical simulation is the only way to get the solutions. Sinno and Mori [108,150] already successfully developed hybrid numerical methods to solve the model for native point defects and point defect clusters during the crystal growth. In this section, one-dimensional simulation results are illustrated to draw some important concepts and verify the strategy for theoretical analysis of defect formation in the following sections.

The typical one-dimensional steady-state results of point defects and point defect clusters in vacancy dominated region are shown in Figure 2.5. The domain of this one-dimensional simulation corresponds to the axial direction at a certain radial position inside the OSF-Ring shown in Figure 2.2. Pulling rate is $1.5 \times 10^{-3} cm/s$. The profiles of vacancy, interstitial, temperature, and total void concentration are shown in Figure 2.5a. The void size distribution on the top of the crystal is shown in Figure 2.5b. The total void concentration is nothing but the total concentration of voids bigger than $5nm$ in diameter. It is basically the integral of void size distribution from $5nm$ in diameter to infinite. In vacancy concentration profile, apparently there are three regions. In the first region near melt/crys-

tal interface, vacancy concentration decreases dramatically due to rapid recombination near melt/crystal interface. Under this particular operating condition, self-interstitial is depleted after recombination while there is some residual vacancy left. The second region is the plateau region where the vacancy concentration is the residual vacancy concentration after the recombination. This residual vacancy concentration, which is the reservoir for void formation, is also called intermediate vacancy concentration. Void nucleation occurs in this region, but the total vacancies consumed by voids are too small to have significant effect on intermediate vacancy concentration. In the last region, vacancy concentration decreases significantly due to the growth of the voids. The temperature at the turning point between the last two regions is called void aggregation temperature. Around aggregation temperature, total void concentration increases dramatically. And then it becomes flat in the whole last region. This is an indication that in the last region, there is no more nucleation of voids and there is only growth of voids already formed. Simulation result only for point defects and without any clustering is also shown for comparison. Before aggregation temperature which is much lower than melt temperature, point defect clustering essentially has no effect on point defect concentrations because point defects consumed by their clusters are very small compared with point defect concentration. The physical explanation is that only at lower temperature super-saturation of point defect is high enough to drive significant clustering. This validates the 'two phases' approach in this chapter. In the first phase, intermediate vacancy concentration is determined by analyzing point defects balance in the boundary layer near melt/crystal interface without any clustering. In the second phase, void nucleation is then analyzed based on the intermediate vacancy concentration and temperature field around aggregation temperature. These two phases are the objectives of Section 2.4 and 2.5 respectively.
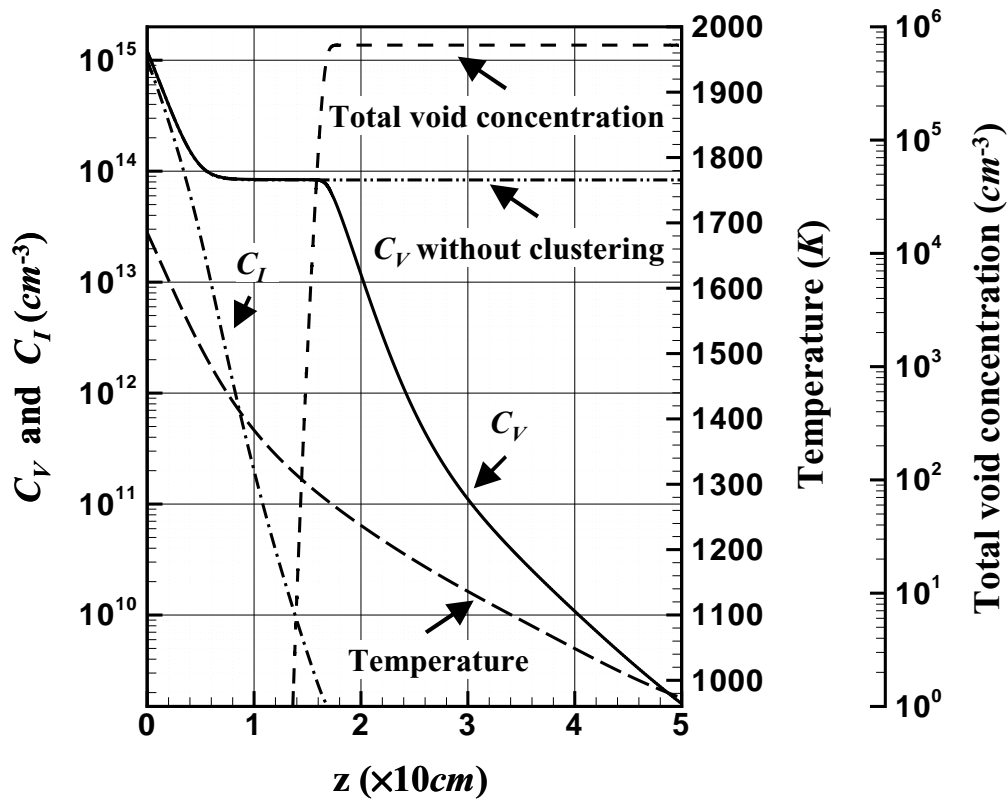
(a)
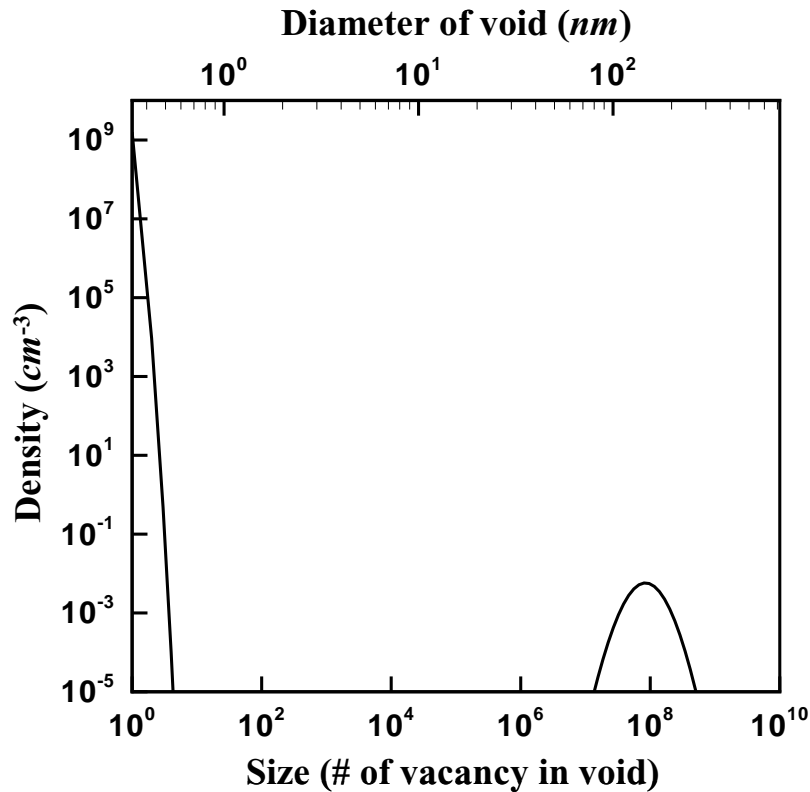
(b)

Figure 2.5: One-dimension steady-state results in vacancy rich region: (a) profiles of vacancy, interstitial, temperature and total void concentration; (b) void size distribution at top of the crystal.

2.4 Asymptotic Analysis on Recombination Region

As discussed in the previous section, the very first step to analyze the point defects and their clusters during crystal growth is the asymptotic analysis of point defects without any clusterings on the recombination region near the melt/crystal interface. The intermediate point defect concentration obtained from this analysis can then be used in the analysis of point defect cluster formation afterward.

Voronkov derived a theoretical expression for critical V/G which separates the vacancy-rich core from the self-interstitial-rich outer ring [183]. Sinno tried to analyze the recombination region near the melt/crystal interface and get the expression for critical V/G

rigorously by asymptotic analysis [150,151]. Even though Sinno's approach is correct and followed in this section, his result is wrong because of mistakes on some scales.

In this section rigorous asymptotic analysis is first performed to get the expression for critical *V/G* which is the same as Voronkov's final result [183]. This analysis is then extended to the intermediate point defect concentration at arbitrary *V/G* and the effect of impurity such as Boron on the critical *V/G*

2.4.1 Critical V/G

A series of one-dimensional results of vacancies and interstitials without any clusterings during the CZ crystal growth for varying *V/G* are shown in Figure 2.6. Vacancies dominate after the recombination for high *V/G*, and interstitials dominate after the recombination for low *V/G*. These results are also consistent with the physical picture shown in Figure 2.2 where *V/G* has highest value at the center and lowest at the periphery of the crystal. The *V/G* corresponding the transition point between vacancy-rich region and interstitial-rich region is the critical *V/G*. Therefore under the critical *V/G*, vacancies and interstitials recombine exactly with each other and neither of them survives beyond the recombination region.

(a)

0.47(V/G)$_{\text{crit}}$

0.93(V/G)$_{\text{crit}}$

1.004(V/G)$_{\text{crit}}$

0.99(V/G)$_{\text{crit}}$

1.05(V/G)$_{\text{crit}}$

1.75(V/G)$_{\text{crit}}$

C_I (cm^{-3})

z (×10cm)
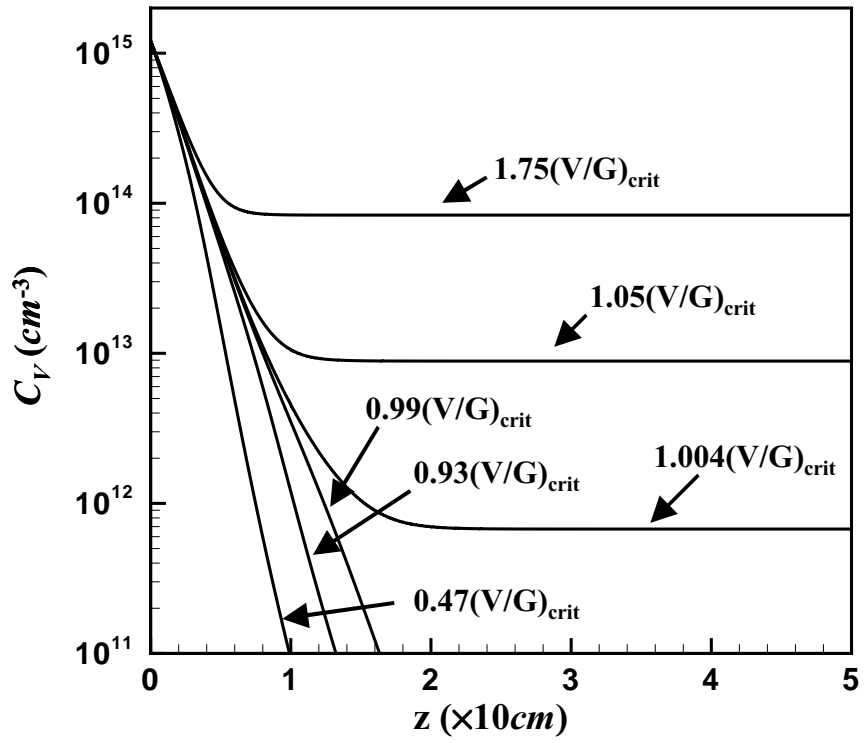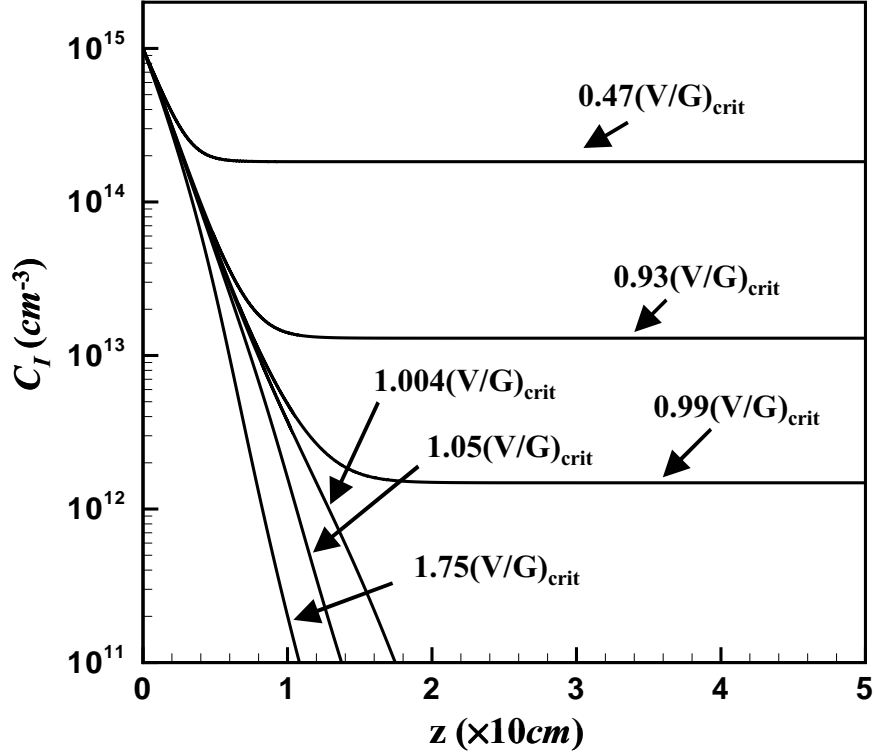
(b)

Figure 2.6: Profiles of vacancy and self-interstitial in the crystal growth for different *V/G* (a) vacancy profiles, (b) interstitial profiles.

The dynamics of point defects in the recombination region near melt/crystal interface includes convection, diffusion, recombination, but no clustering. So the governing equations are the similar as eqs. (2.6) and (2.7) except that there are no source or sink terms due to clusterings and there are no time-dependent terms since it is steady-state.

$$V\frac{\partial C_I}{\partial z} + \nabla \bullet (-D_I(T)\nabla C_I) + k_{IV}(T)(C_I C_V - C_I^{eq}(T)C_V^{eq}(T)) = 0 \qquad (2.51)$$

$$V\frac{\partial C_V}{\partial z} + \nabla \bullet (-D_V(T)\nabla C_V) + k_{IV}(T)(C_I C_V - C_I^{eq}(T)C_V^{eq}(T)) = 0 \qquad (2.52)$$

In cylindrical coordination the governing equations above are written as

$$V\frac{\partial C_I}{\partial z} - \frac{\partial}{\partial z}\left(D_I\frac{\partial C_I}{\partial z}\right) - \frac{1}{r}\frac{\partial}{\partial r}\left(rD_I\frac{\partial C_I}{\partial r}\right) + k_{IV}(T)(C_I C_V - C_I^{eq}(T)C_V^{eq}(T)) = 0 \qquad (2.53)$$

$$V\frac{\partial C_V}{\partial z} - \frac{\partial}{\partial z}\left(D_V\frac{\partial C_V}{\partial z}\right) - \frac{1}{r}\frac{\partial}{\partial r}\left(rD_V\frac{\partial C_V}{\partial r}\right) + k_{IV}(T)(C_I C_V - C_I^{eq}(T)C_V^{eq}(T)) = 0 \qquad (2.54)$$

These equations are transformed to dimensionless form by introducing a couple dimensionless variables and scales. The length scale used in radical direction is R, the radius of crystal, and the length scale in axial direction L is determined as part of the analysis. And the ratio of these two scales is defined as ω, or

$$\hat{z} \equiv \frac{z}{L}, \quad \hat{r} \equiv \frac{r}{R}, \quad \omega \equiv \frac{L}{R} \qquad (2.55)$$

The temperature is scaled with the melting temperature of silicon T_m so that

$$\Theta \equiv \frac{T}{T_m} \qquad (2.56)$$

Many variables such as equilibrium concentration and diffusivity are exponential function of temperature. The high activation energy (for example, based on eq. (2.32) the formation enthalpy of interstitial is about $3.5eV$ compared with $kT_m \approx 0.15eV$) leads to very fast decrease of these variables even with small temperature drop. This characteristic together with very high recombination rate near the melting temperature T_m make the recombination region a thin boundary layer near the melt/crystal interface. Therefore only the temperature field near the melt/crystal interface matters for analysis of the recombination region, and it is approximately linear in axial direction.

$$T = T_m - G^* g(\hat{r})z \qquad (2.57)$$

where G^* is the scale of temperature gradient and $g(\hat{r})$ is the dimensionless radial-dependence temperature gradient. Based on the scales above, the dimensionless temperature field is written as

$$\Theta(\hat{r}, \hat{z}) = 1 - \frac{G^* L}{T_m} g(\hat{r})\hat{z} \tag{2.58}$$

For a typical physical parameter Q in the analysis temperature dependence is written in Arrhenius form as

$$Q(T) = Q_0 \exp\left(-\frac{\gamma}{kT}\right) \tag{2.59}$$

where Q_0 and γ are constants. The dimensionless activation energy in eq. (2.59) is defined as

$$\gamma^* = \frac{\gamma}{kT_m} \tag{2.60}$$

From eq. (2.58), $G^* L / T_m$ is the order of the dimensionless temperature drop in the length scale L for the recombination region. With high activation energy γ, Q decrease dramatically within small temperature drop. Q is rewritten with the scales above and by taking the limit $G^* L / T_m \ll 1$

$$Q(\Theta) = Q_0 \exp\left(-\frac{\gamma^*}{\Theta}\right) = Q_0 \exp\left(-\frac{\gamma^*}{1 - \frac{G^* L}{T_m} g\hat{z}}\right) \approx Q_0 \exp(-\gamma^*) \exp\left(-\frac{\gamma^* G^* L}{T_m} g\hat{z}\right) \tag{2.61}$$

The axial length scale L is defined as the length scale for the axial temperature gradient reduced by a high dimensionless activation energy

$$L = \frac{T_m}{\gamma^* G^*} \tag{2.62}$$

so that the temperature dependent variable Q in eq. (2.61) can be written as

$$Q(\Theta) = Q_0 \exp(-\gamma^*) \exp(-g\hat{z}) = Q(1) \exp(-g\hat{z}) \tag{2.63}$$

γ is chosen to be the formation enthalpy of interstitial H_I^f which is about 3.5eV based on

eq. (2.32). For a typical Czochralski crystal growth conditions, $G^* = 80K/cm$ and $R = 10cm$ [150]. Therefore $L = 0.88cm$ and the ratio of axial length scale to radial length scale is

$$\omega \equiv \frac{L}{R} = 0.088 \ll 1 \tag{2.64}$$

This confirms that the recombination region is only confined in a thin layer near the melt/crystal interface, and the axial length scale L defined by high activation energy is much smaller than the radial length scale R. Therefore one limit $\omega \ll 1$ in the asymptotic analysis below is valid.

The concentrations and diffusivities are scaled with equilibrium concentration and diffusivity of interstitial at melting temperature respectively. The scale of recombination rate is the recombination rate at melting temperature.

$$a(\Theta) \equiv \frac{C_I(\Theta)}{C_I^{eq}(1)}, \quad b(\Theta) \equiv \frac{C_V(\Theta)}{C_I^{eq}(1)}, \quad a^{eq}(\Theta) \equiv \frac{C_I^{eq}(\Theta)}{C_I^{eq}(1)}, \quad b^{eq}(\Theta) \equiv \frac{C_V^{eq}(\Theta)}{C_I^{eq}(1)} \tag{2.65}$$

$$d_I(\Theta) \equiv \frac{D_I(\Theta)}{D_I(1)}, \quad d_V(\Theta) \equiv \frac{D_V(\Theta)}{D_I(1)} \tag{2.66}$$

$$K(\Theta) \equiv \frac{k_{IV}(\Theta)}{k_{IV}(1)} \tag{2.67}$$

Two important dimensionless groups, the Peclet number and Damkohler number, are defined as

$$Pe \equiv \frac{VL}{D_I(1)} \equiv \frac{VT_m}{D_I(1)\gamma^* G^*} \tag{2.68}$$

$$Da \equiv \frac{L^2 k_{IV}(1) C_I^{eq}(1)}{D_I(1)} \equiv \frac{T_m^2 k_{IV}(1) C_I^{eq}(1)}{\gamma^{*2} G^{*2} D_I(1)} \tag{2.69}$$

For the thermophysical properties given by eqs. (2.30) - (2.34) these parameters are

$$Pe = O(1), \quad Da = O(10^6) \tag{2.70}$$

The definition of the Peclet number in eq. (2.68) is rewritten as

$$\frac{V}{G^*} = Pe\frac{D_I(1)\gamma^*}{T_m} \tag{2.71}$$

Therefore the Peclet number is a dimensionless form of V/G.

With these scales and dimensionless groups, the governing equations (2.53) and (2.54) are rewritten in dimensionless form as

$$\frac{1}{Da}\left[-Pe\frac{\partial a}{\partial \hat{z}} + \frac{\partial}{\partial \hat{z}}\left(d_I\frac{\partial a}{\partial \hat{z}}\right) + \omega^2\frac{1}{\hat{r}}\frac{\partial}{\partial \hat{r}}\left(\hat{r}d_I\frac{\partial a}{\partial \hat{r}}\right)\right] = K(ab - a^{eq}b^{eq}) \tag{2.72}$$

$$\frac{1}{Da}\left[-Pe\frac{\partial b}{\partial \hat{z}} + \frac{\partial}{\partial \hat{z}}\left(d_V\frac{\partial b}{\partial \hat{z}}\right) + \omega^2\frac{1}{\hat{r}}\frac{\partial}{\partial \hat{r}}\left(\hat{r}d_V\frac{\partial b}{\partial \hat{r}}\right)\right] = K(ab - a^{eq}b^{eq}) \tag{2.73}$$

Equations (2.72) and (2.73) are complicate non-linear differential equations and there are no analytical solutions available. However due to two important characteristics (large Da and small ω which are estimated in eqs. (2.64) and (2.70)) about the CZ silicon crystal growth, the asymptotic solutions for $Da \gg 1$ and $\omega \ll 1$ are constructed by expanding $a(\hat{r}, \hat{z})$ and $b(\hat{r}, \hat{z})$ as Taylor series in both parameters as

$$a(\hat{r}, \hat{z}) = a_{00}(\hat{r}, \hat{z}) + \varepsilon a_{10}(\hat{r}, \hat{z}) + \omega a_{01}(\hat{r}, \hat{z}) + O(\varepsilon^2, \omega^2, \varepsilon\omega) \tag{2.74}$$

$$b(\hat{r}, \hat{z}) = b_{00}(\hat{r}, \hat{z}) + \varepsilon b_{10}(\hat{r}, \hat{z}) + \omega b_{01}(\hat{r}, \hat{z}) + O(\varepsilon^2, \omega^2, \varepsilon\omega) \tag{2.75}$$

where $\varepsilon \equiv Da^{-1/2}$. Substituting eqs. (2.74) and (2.75) into eqs. (2.72) and (2.73) gives

$$-\varepsilon^2 Pe\frac{\partial(a_{00} + \varepsilon a_{10} + \omega a_{01})}{\partial \hat{z}} + \varepsilon^2\frac{\partial}{\partial \hat{z}}\left(d_I\frac{\partial(a_{00} + \varepsilon a_{10} + \omega a_{01})}{\partial \hat{z}}\right)$$

$$+\varepsilon^2\omega^2\frac{1}{\hat{r}}\frac{\partial}{\partial \hat{r}}\left(\hat{r}d_I\frac{\partial(a_{00} + \varepsilon a_{10} + \omega a_{01})}{\partial \hat{r}}\right)$$

70

$$= K[(a_{00} + \varepsilon a_{10} + \omega a_{01})(b_{00} + \varepsilon b_{10} + \omega b_{01}) - a^{eq}b^{eq}] \tag{2.76}$$

$$- \varepsilon^2 Pe \frac{\partial(b_{00} + \varepsilon b_{10} + \omega b_{01})}{\partial \hat{z}} + \varepsilon^2 \frac{\partial}{\partial \hat{z}}\left(d_V \frac{\partial(b_{00} + \varepsilon b_{10} + \omega b_{01})}{\partial \hat{z}}\right)$$

$$+ \varepsilon^2 \omega^2 \frac{1}{\hat{r}} \frac{\partial}{\partial \hat{r}}\left(\hat{r} d_V \frac{\partial(b_{00} + \varepsilon b_{10} + \omega b_{01})}{\partial \hat{r}}\right)$$

$$= K[(a_{00} + \varepsilon a_{10} + \omega a_{01})(b_{00} + \varepsilon b_{10} + \omega b_{01}) - a^{eq}b^{eq}] \tag{2.77}$$

At *O(1)* in the expansions (2.74) and (2.75), subtracting eq. (2.76) from (2.77) leads to

$$Pe \frac{\partial a_{00}}{\partial \hat{z}} - \frac{\partial}{\partial \hat{z}}\left(d_I \frac{\partial a_{00}}{\partial \hat{z}}\right) = Pe \frac{\partial b_{00}}{\partial \hat{z}} - \frac{\partial}{\partial \hat{z}}\left(d_V \frac{\partial b_{00}}{\partial \hat{z}}\right) \tag{2.78}$$

Two important points arise from eq. (2.78). First, at leading order the radial contribution of the diffusion is negligible, this feature is a direct result of $\omega \ll 1$. Second, eq. (2.78) is valid for any value $\hat{z}$ at leading order. Therefore the boundary conditions for leading order are

$$a_{00}(\hat{r}, 0) = 1, \quad b_{00}(\hat{r}, 0) = \frac{C_V^{eq}(1)}{C_I^{eq}(1)} \tag{2.79}$$

and

$$\frac{\partial a_{00}(\hat{r}, \infty)}{\partial \hat{z}} = 0, \frac{\partial b_{00}(\hat{r}, \infty)}{\partial \hat{z}} = 0 \tag{2.80}$$

Equation (2.78) also can be written as

$$\frac{\partial}{\partial \hat{z}}\left(Pe a_{00} - d_I \frac{\partial a_{00}}{\partial \hat{z}}\right) = \frac{\partial}{\partial \hat{z}}\left(Pe b_{00} - d_V \frac{\partial b_{00}}{\partial \hat{z}}\right) \tag{2.81}$$

Because diffusion is negligible for $\hat{z} \gg 1$, eq. (2.81) reduces to

$$Pe(a_{00} - a_{00}^\infty) - d_I \frac{\partial a_{00}}{\partial \hat{z}} = Pe(b_{00} - b_{00}^\infty) - d_V \frac{\partial b_{00}}{\partial \hat{z}} \tag{2.82}$$

where $a_{00}^{\infty} \equiv a_{00}(\hat{r}, \infty)$ and $b_{00}^{\infty} \equiv b_{00}(\hat{r}, \infty)$.

At leading order both eqs. (2.76) and (2.77) reduce to

$$a_{00}b_{00} - a^{eq}b^{eq} = 0 \tag{2.83}$$

Equations. (2.82) and (2.83) together with boundary condition (2.79) are the dimensionless governing equations that define $a_{00}(\hat{r}, \hat{z})$ and $b_{00}(\hat{r}, \hat{z})$. Generally analytical solutions for a_{00} and b_{00} are not available for any arbitrary Peclet number. However, there are analytical solutions for critical value of *Pe* which corresponds to $a_{00}^{\infty} = b_{00}^{\infty} = 0$. Approximate solutions are constructed for values of *Pe* close to critical *Pe*.

The equilibrium concentrations and diffusivities are expanded in the same manner as outlined for the temperature dependent variable Q in eq. (2.61).

$$a^{eq}(\Theta) = \exp(-\hat{\delta}\hat{z}) \quad b^{eq}(\Theta) = \frac{C_V^{eq}(1)}{C_I^{eq}(1)}\exp(-\hat{\phi}\hat{z}) \tag{2.84}$$

$$d_I(\Theta) = \exp(-\hat{\mu}\hat{z}) \quad d_V(\Theta) = \frac{D_V(1)}{D_I(1)}\exp(-\hat{v}\hat{z}) \tag{2.85}$$

where $\hat{\delta}$, $\hat{\phi}$, $\hat{\mu}$, and $\hat{v}$ are defined as

$$\hat{\delta} \equiv \frac{\overset{*}{\gamma}_{If}}{\overset{*}{\gamma}}g(\hat{r}) \quad \overset{*}{\gamma}_{If} \equiv \frac{H_I^f}{kT_m} \tag{2.86}$$

$$\hat{\phi} \equiv \frac{\overset{*}{\gamma}_{Vf}}{\overset{*}{\gamma}}g(\hat{r}) \quad \overset{*}{\gamma}_{Vf} \equiv \frac{H_V^f}{kT_m} \tag{2.87}$$

$$\hat{\mu} \equiv \frac{\overset{*}{\gamma}_{Im}}{\overset{*}{\gamma}}g(\hat{r}) \quad \overset{*}{\gamma}_{Im} \equiv \frac{H_I^m}{kT_m} \tag{2.88}$$

$$\hat{v} \equiv \frac{\overset{*}{\gamma}_{Vm}}{\overset{*}{\gamma}}g(\hat{r}) \quad \overset{*}{\gamma}_{Vm} \equiv \frac{H_V^m}{kT_m} \tag{2.89}$$

where γ_{If}^* and γ_{Vf}^* are the dimensionless enthalpies of formation for interstitial and vacancy, γ_{Im}^* and γ_{Vm}^* are the dimensionless migration energies for interstitial and vacancy. Based on thermophysical properties given by eqs. (2.30) to (2.34), $(\gamma_{If}^*, \gamma_{Vf}^*, \gamma_{Im}^*, \gamma_{Vm}^*) = (3.46, 2.48, 0.937, 0.457)$; hence $\hat{\delta}$ and $\hat{\phi}$ are $O(1)$, but $\hat{\mu}$ and $\hat{\nu}$ can be assumed to be $O(10^{-1})$. Therefore in the recombination region $z = O(L)$ or $\hat{z} = O(1)$, $d_I = 1$ and $d_V = D_V(1)/D_I(1)$, and eq. (2.82) can be rewritten as

$$Pe(a_{00} - a_{00}^\infty) - \frac{\partial a_{00}}{\partial \hat{z}} = Pe(b_{00} - b_{00}^\infty) - \frac{D_V(1)}{D_I(1)}\frac{\partial b_{00}}{\partial \hat{z}} \tag{2.90}$$

For $Pe = Pe_{crit}$, $a_{00}^\infty = b_{00}^\infty = 0$, and a_{00} and b_{00} must have exponential forms which satisfy the boundary conditions (2.79)

$$a_{00}(\hat{r}, \hat{z}) = \exp(-\hat{\alpha}\hat{z}) \tag{2.91}$$

$$b_{00}(\hat{r}, \hat{z}) = \frac{C_V^{eq}(1)}{C_I^{eq}(1)}\exp(-\hat{\beta}\hat{z}) \tag{2.92}$$

Substituting eqs. (2.91) and (2.92) into eqs. (2.83) and (2.90) to determine $\hat{\alpha}$, $\hat{\beta}$ and Pe_{crit} gives

$$\hat{\alpha} + \hat{\beta} = \hat{\delta} + \hat{\phi} \tag{2.93}$$

$$(Pe_{crit} + \hat{\alpha})\exp(-\hat{\alpha}\hat{z}) = \frac{C_V^{eq}(1)}{C_I^{eq}(1)}\left(Pe_{crit} + \frac{D_V(1)}{D_I(1)}\hat{\beta}\right)\exp(-\hat{\beta}\hat{z}) \tag{2.94}$$

The solutions are

$$\hat{\alpha} = \hat{\beta} = \frac{(\hat{\delta} + \hat{\phi})}{2} \tag{2.95}$$

$$Pe_{crit} = \frac{\hat{\delta}+\hat{\phi}}{2} \frac{1 - \dfrac{C_V^{eq}(1)D_V(1)}{C_I^{eq}(1)D_I(1)}}{\dfrac{C_V^{eq}(1)}{C_I^{eq}(1)} - 1} \tag{2.96}$$

The fact that there are solutions for eqs. (2.93) and (2.94) verifies that the supposed exponential forms (2.91) and (2.92) with $\hat{\alpha}$ and $\hat{\beta}$ determined by eq. (2.95) is the real solution for Pe_{crit} which is determined by eq. (2.96).

Equation (2.96) is the dimensionless expression for the critical V/G. Transforming eq. (2.96) back to dimensional form to get the expression for the critical V/G

$$\left[\frac{V}{G}\right]_{crit} = \frac{\gamma_{If}^* + \gamma_{Vf}^*}{2T_m} \cdot \left[\frac{C_I^{eq}(T_m)D_I(T_m) - C_V^{eq}(T_m)D_V(T_m)}{C_V^{eq}(T_m) - C_I^{eq}(T_m)}\right] \tag{2.97}$$

With the point defects properties given by eqs. (2.30) to (2.33), theoretical prediction of critical V/G by expression above is $1.28 \times 10^{-3}\ cm^2 min^{-1} K^{-1}$ which is in excellent agreement with the experimental value of $1.34 \times 10^{-3}\ cm^2 min^{-1} K^{-1}$ [28]. Voronkov already gave this theoretical expression for critical V/G in 1982 [183]. However, it is derived more rigorously from the governing equations here. And it will also be extended to the intermediate vacancy and interstitial concentrations in next section.

2.4.2 Intermediate Vacancy Concentration
Most silicon crystals are grown under the condition of $Pe > Pe_{crit}$ or $V/G > (V/G)_{crit}$. So after the recombination near the melt/crystal interface there are some residual vacancies or intermediate vacancies left which play an important role in the void formation or oxygen precipitation at lower temperature. Therefore it is very crucial to understand the relationship between the intermediate vacancy concentration and operating condition. The approach is the same as that used to obtain Pe_{crit} or $(V/G)_{crit}$ in the previous section.

Generally there are no analytical solutions for eqs. (2.83) and (2.90) for value of Pe other than Pe_{crit}. However, there are approximate solutions for a_{00} and b_{00} for $|Pe - Pe_{crit}| \ll 1$. For the case $Pe > Pe_{crit}$ which corresponds to the vacancy-rich region of the crystal,

$$a_{00}^{\infty} = 0 \tag{2.98}$$

$$b_{00}^{\infty} = b^{int} \tag{2.99}$$

Assuming a_{00} and b_{00} have the forms

$$a_{00}(\hat{r}, \hat{z}) = \exp(-\hat{\alpha}\hat{z}) \tag{2.100}$$

$$b_{00}(\hat{r}, \hat{z}) = \left(1 - \frac{C_I^{eq}(T_m)}{C_V^{eq}(T_m)} b^{int}\right) \frac{C_V^{eq}(T_m)}{C_I^{eq}(T_m)} \exp(-\hat{\beta}\hat{z}) + b^{int} \tag{2.101}$$

where

$$\hat{\alpha} = \hat{\beta} = \frac{(\hat{\delta} + \hat{\phi})}{2} \tag{2.102}$$

Equations. (2.100) and (2.101) are approximate solutions for eq. (2.83) if $b^{int} \ll 1$ which is true since normally $C_V^{int} < 10^{14} cm^{-3}$ and $C_I^{eq}(T_m) \approx 1 \times 10^{15} cm^{-3}$. Equations. (2.100) and (2.101) exactly satisfy eq. (2.90). Substituting eqs. (2.100) and (2.101) into eq. (2.90) gives the relationship between Pe and b^{int} as

$$Pe + \hat{\alpha} = Pe \frac{C_V^{eq}(T_m)}{C_I^{eq}(T_m)}\left(1 - \frac{C_I^{eq}(T_m)}{C_V^{eq}(T_m)} b^{int}\right) + \frac{D_V(T_m)}{D_I(T_m)} \frac{C_V^{eq}(T_m)}{C_I^{eq}(T_m)} \hat{\beta}\left(1 - \frac{C_I^{eq}(T_m)}{C_V^{eq}(T_m)} b^{int}\right) \tag{2.103}$$

For Pe_{crit}, $b^{int} = 0$ or

$$Pe_{crit} + \hat{\alpha} = Pe_{crit} \frac{C_V^{eq}(T_m)}{C_I^{eq}(T_m)} + \frac{D_V(T_m)}{D_I(T_m)} \frac{C_V^{eq}(T_m)}{C_I^{eq}(T_m)} \hat{\beta} \tag{2.104}$$

Equation (2.104) is identical to eq. (2.96). Combining eqs. (2.103) and (2.104) gives the expression for the dimensionless intermediate vacancy concentration

$$b^{int} = \frac{\left(\dfrac{C_V^{eq}(T_m)}{C_I^{eq}(T_m)} - 1\right)\left(1 - \dfrac{Pe_{crit}}{Pe}\right)}{1 + \dfrac{D_V(T_m)}{D_I(T_m)}\dfrac{\hat{\beta}}{Pe}}$$

(2.105)

The second term in the denominator on the right side of eq. (2.105) is negligible since

$$\frac{D_V(T_m)}{D_I(T_m)}\frac{\hat{\beta}}{Pe} < \frac{D_V(T_m)}{D_I(T_m)}\frac{\hat{\beta}}{Pe_{crit}} = O(10^{-2})$$

(2.106)

Therefore eq. (2.105) reduces to a simple express for the dimensionless intermediate vacancy concentration

$$b^{int} = \left(\frac{C_V^{eq}(T_m)}{C_I^{eq}(T_m)} - 1\right)\left(1 - \frac{Pe_{crit}}{Pe}\right)$$

(2.107)

Transforming eqs. (2.105) and (2.107) back to dimensional forms to get expression for intermediate vacancy concentration as

$$C_V^{int} = f(Pe, Pe_{crit}) = \frac{[C_V^{eq}(T_m) - C_I^{eq}(T_m)][1 - Pe_{crit}/Pe]}{1 + \dfrac{(\gamma_{If}^* + \gamma_{Vf}^*)D_V(T_m)g}{2\gamma^* D_I(T_m)Pe}}$$

$$= \frac{[C_V^{eq}(T_m) - C_I^{eq}(T_m)][1 - (V/G)_{crit}/(V/G)]}{1 + \dfrac{(\gamma_{If}^* + \gamma_{Vf}^*)D_V(T_m)}{2T_m(V/G)}}$$

(2.108)

Or simply

$$C_V^{int} = f(Pe, Pe_{crit}) = [C_V^{eq}(T_m) - C_I^{eq}(T_m)][1 - Pe_{crit}/Pe]$$

$$= [C_V^{eq}(T_m) - C_I^{eq}(T_m)][1 - (V/G)_{crit}/(V/G)]$$

(2.109)

The correlations of C_V^{int} and Pe are plotted in Figure 2.7. The predictions of intermediate vacancy concentration in vacancy-rich region by eqs. (2.108) and (2.109) agree well with the simulation results of point defects dynamics described by eqs. (2.51) and (2.52).
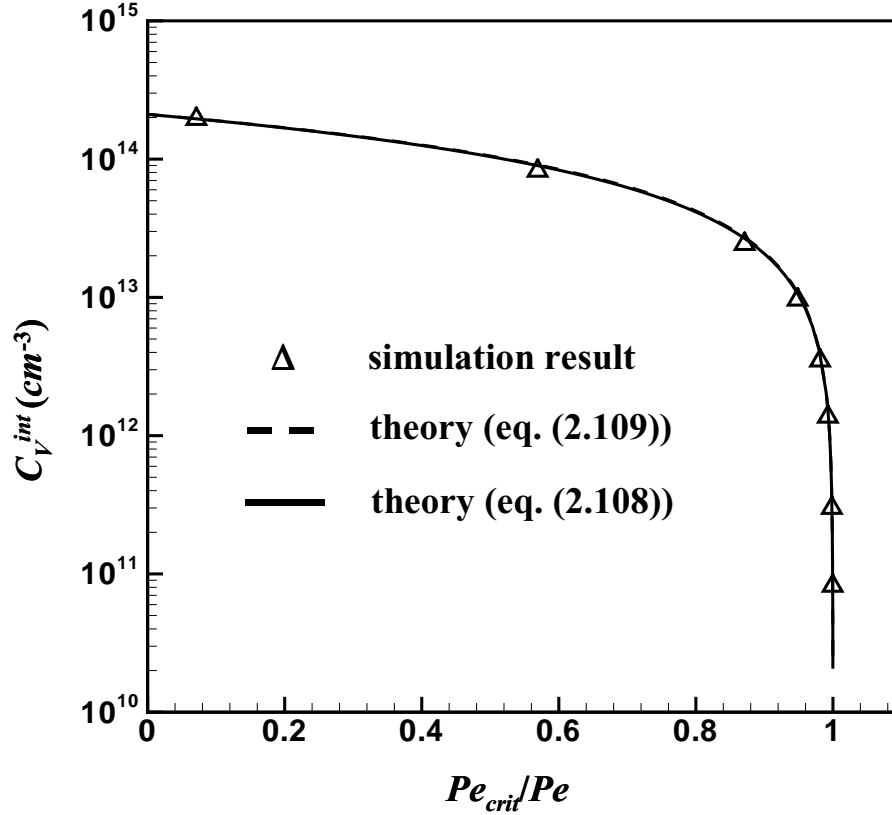
Figure 2.7: Intermediate vacancy concentrations under different Pe.

The same derivation can be applied to intermediate interstitial concentration in interstitial-rich region. In interstitial-rich region which corresponds $Pe < Pe_{crit}$,

$$a_{00}^{\infty} = a^{int} \tag{2.110}$$

$$b_{00}^{\infty} = 0 \tag{2.111}$$

Assume a_{00} and b_{00} have the forms

$$a_{00} = (1 - a^{int})\exp(-\hat{\alpha}\hat{z}) + a^{int} \qquad (2.112)$$

$$b_{00} = \frac{C_V^{eq}(T_m)}{C_I^{eq}(T_m)}\exp(-\hat{\beta}\hat{z}) \qquad (2.113)$$

where

$$\hat{\alpha} = \hat{\beta} = \frac{(\hat{\delta} + \hat{\phi})}{2} \qquad (2.114)$$

Substituting eqs. (2.112) and (2.113) into eq. (2.90) gives the relationship between Pe and a^{int}

$$Pe\frac{C_V^{eq}(T_m)}{C_I^{eq}(T_m)} + \hat{\beta}\frac{D_V(T_m)}{D_I(T_m)}\frac{\overset{\wedge}{C_V^{eq}(T_m)}}{C_I^{eq}(T_m)} = Pe(1 - a^{int}) + \hat{\alpha}(1 - a^{int}) \qquad (2.115)$$

Combining eqs. (2.104) and (2.115) gives the expression for the dimensionless intermediate interstitial concentration

$$a^{int} = \frac{\left(\dfrac{C_V^{eq}(T_m)}{C_I^{eq}(T_m)} - 1\right)\left(\dfrac{Pe_{crit}}{Pe} - 1\right)}{1 + \dfrac{\hat{\alpha}}{Pe}} \qquad (2.116)$$

Unlike the intermediate vacancy concentration described by eq. (2.105), neglecting the second term in the denominator on the right side of equation above introduces errors of more than 20% because

$$\frac{\hat{\alpha}}{Pe} > \frac{\hat{\alpha}}{Pe_{crit}} \approx 0.25 \qquad (2.117)$$

Transforming eq. (2.116) to dimensional form gives an expression for the intermediate interstitial concentration as

$$C_I^{int} = f(Pe, Pe_{crit}) = \frac{[C_V^{eq}(T_m) - C_I^{eq}(T_m)][Pe_{crit}/Pe - 1]}{1 + \dfrac{(\gamma_{If}^* + \gamma_{Vf}^*)g}{2\gamma^* Pe}}$$

$$= \frac{[C_V^{eq}(T_m) - C_I^{eq}(T_m)][(V/G)_{crit}/(V/G) - 1]}{1 + \frac{(\gamma_{If}^* + \gamma_{Vf}^*)D_I(T_m)}{2T_m(V/G)}} \tag{2.118}$$

The correlations of C_I^{int} and Pe are plotted in Figure 2.8. Again the predictions of intermediate interstitial concentration in the interstitial-rich region by eq. (2.118) agree well with the simulation results of point defects dynamics described by eqs. (2.51) and (2.52).
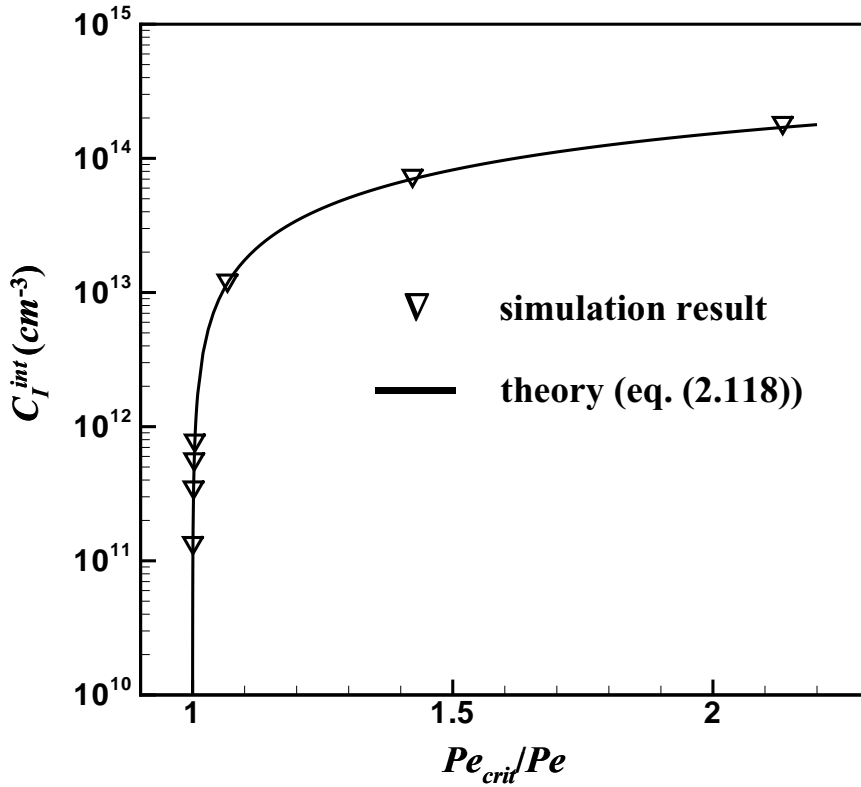
Figure 2.8: Intermediate interstitial concentrations under different Pe.

It is worth emphasizing the limitations of eqs. (2.108) and (2.118). These results are valid only for $|Pe - Pe_{crit}| \ll 1$, and will not be accurate for either limit $Pe \ll 1$ or $Pe \gg 1$. For $Pe \gg 1$ diffusion can be ignored, and recombination is negligible if $Pe/Da \gg 1$. In

this latter limit, the intermediate vacancy concentration becomes the equilibrium vacancy concentration $C_V^{eq}(T_m)$ which is the vacancy concentration at melt/crystal interface. While the prediction of eq. (2.108) is the difference between equilibrium concentrations of vacancy and interstitial at melt temperature. Fortunately the operating conditions for normal silicon crystals are not near either of these two extremes. Figure 2.7 and Figure 2.8 show that eqs. (2.108) and (2.118) are valid at least for the range between $0.5Pe_{crit}$ and $15Pe_{crit}$ which covers the normal operating conditions. In other words, predictions by eqs. (2.108) and (2.118) are good enough to understand the point defects behavior under normal operating conditions. It is not surprising because for high quality silicon crystal the intermediate point defect concentration has to be controlled to a relative low level compared with equilibrium interstitial concentration at silicon melting temperature to ensure less point defects available for the point defect clustering. This is just the condition under which the asymptotic analysis for the intermediate point defect is hold.

2.4.3 Effect of Impurity on Critical V/G

Even though the single crystal silicon is the purest material in the world, there are still impurities in it: some are intentional such as boron, a widely used p-type dopant; some are unintentional such as carbon. The effects of different impurities on OSF-ring position are illustrated in Figure 1.10 [1]. Both carbon and boron can increase the critical *V/G*, therefore shift OSF-ring position inward. These effects must relate to the point defect balance modified by the impurities.

The OSF-ring position and critical *V/G* are very sensitive to carbon. Vacancy rich core region could disappears even at carbon concentration as low as $5 \times 10^{16} cm^{-3}$ [1]. Although carbon concentration in commercial CZ silicon crystal is less than detecting limit which is about $10^{15} cm^{-3}$, it still could have non-negligible effects on silicon crystal. It is well known that there exists a critical *V/G*, but its value still varies from manufacturer

to manufacturer [17]. A very possible explanation is that even though under the detecting limit they actually have different carbon concentrations in silicon crystal, and therefore different critical *V/G*. The free formation energies of various carbon defects are needed to prove this. Unfortunately there are only formation enthalpies available in the literature [171], and there is no too much information about formation entropies.

For boron, both systematic experimental data on the effect of boron on the critical *V/G* and reliable physical parameters on various boron defects are available [29,98,123]. This section is devoted to the asymptotic analysis on the recombination region to take the boron effect on the critical *V/G* into account.

Dornberger et al. did systematic experiment to investigate the effect of boron on the location of OSF-Ring [29]. Three different crystal growth systems - 125, 150, and 200 *mm* diameter crystal - were investigated with the boron concentrations in the range of $1 \times 10^{15} - 2 \times 10^{19} cm^{-3}$. The critical *V/G* was measured at the location of OSF-Ring under different growth conditions and with different boron concentrations. The critical *V/G* as a function of boron concentration are shown in Figure 2.9 for three different crystal growth systems. The overlap of the data between three growth systems indicates that the critical *V/G* is only a function of boron concentration and it is independent on the other operating condition. A linear fit of these experimental data gives

$$\left[\frac{V}{G}\right]_{crit}(C_B) = 1.34 \times 10^{-3}(cm^2 min^{-1} K^{-1}) + 1.2 \times 10^{-22}(cm^5 min^{-1} K^{-1})C_B \quad (2.119)$$

where $\left[\frac{V}{G}\right]_{crit}(C_B)$ is the critical *V/G* with boron concentration C_B.
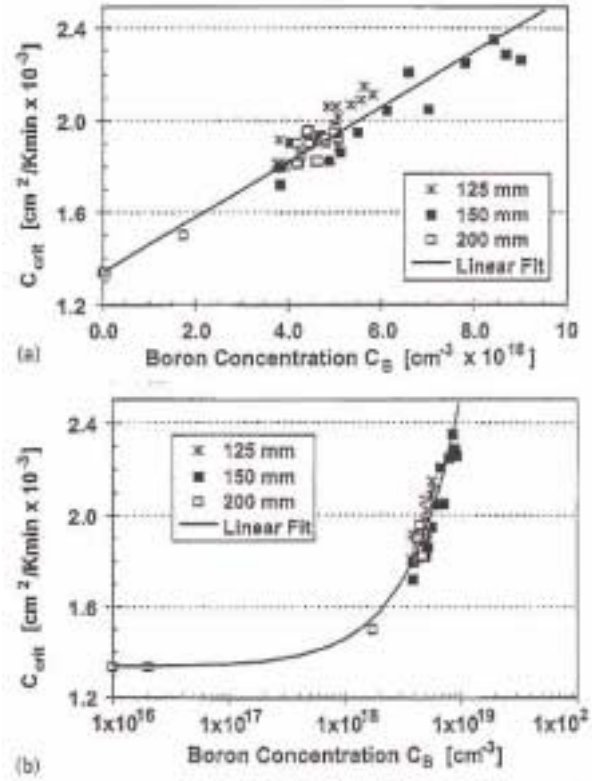
Figure 2.9: Dependence of the critical V/G on boron concentration, (a) linear, (b) logarithmic representation [29].

Sinno et al. [153,164] tried to explain the experimental results above by numerical simulation. They developed a model based on the following reactions

$$I + V \leftrightarrow perfect\ crystal \tag{2.120}$$

$$B + B \leftrightarrow B_2 \tag{2.121}$$

$$B + I \leftrightarrow BI \tag{2.122}$$

$$B + V \leftrightarrow BV \tag{2.123}$$

$$BI + V \leftrightarrow B \tag{2.124}$$

$$B_2 + I \leftrightarrow B_2 I \tag{2.125}$$

where B represent a substitutional boron atom. The governing equations for the species (I,

V, B, B_2, BI, BV, B_2I) are therefore written as

$$V\frac{\partial C_i}{\partial z} + \nabla \bullet (-D_i \nabla C_i) + R_{ij} = 0 \tag{2.126}$$

where

$$R_{ij} = \Lambda_{ij} k_{ij} \left(C_i C_j - \frac{C_{ij}}{K_{ij}} \right) \tag{2.127}$$

$$k_{ij} = \frac{4\pi a_r}{\Omega c_s}(D_i + D_j) \exp\left(-\frac{\Delta G_{ij}}{kT}\right) \tag{2.128}$$

$$K_{ij}^{eq} = \frac{\theta_{ij}}{c_s} \exp(S_{ij}^b) \exp\left(\frac{E_{ij}^b}{kT}\right) \tag{2.129}$$

where i and j range over the species (I, V, B, B_2, BI, BV, B_2I). The $\{\Lambda_{ij}\}$ are the stochio-metric coefficients for each reaction among eqs. (2.120) - (2.125). The reaction rate constant k_{ij} is modeled by diffusion-limited reaction with the activation energy ΔG_{ij}, and its physics is already described in eq. (2.8). The native point defects properties are already listed in eqs. (2.30) - (2.34). Several literature sources [36,103,119,174,200] are used to estimate the average diffusivity of different boron defect complexes.

$$D_B = 1.89 \exp\left(-\frac{3.54 eV}{kT}\right) \ cm^2/s \tag{2.130}$$

$$D_{BI} = 3.32 \times 10^{-2} \exp\left(-\frac{2.42 eV}{kT}\right) \ cm^2/s \tag{2.131}$$

$$D_{BV} = 4 \times 10^{-6} \exp\left(-\frac{3.54 eV}{kT}\right) \ cm^2/s \tag{2.132}$$

B_2 and B_2I are assumed to be immobile. In the equilibrium constant K_{ij}^{eq}, θ_{ij} is the orientational degeneracy, S_{ij}^b and E_{ij}^b are binding entropy and binding enthalpy. θ_{ij}, S_{ij}^b and E_{ij}^b based on the atomistic simulation results are listed in Table 2.1 for different boron defect

complexes [98,123]. The enthalpy calculations using an empirical tight-binding method have uncertainties about $\pm 0.2 eV$, while the entropy calculations using the empirical Stillinger-Weber potential contain much larger uncertainties. For this reason, the binding entropies of BI and B_2I were considered as adjustable parameters to fit experimental data. Sinno et al. [153,164] were able to numerically solve the model above, and their simulation results of normalized OSF-Ring position as function of boron concentration are shown in Figure 2.10 and well agree with the experimental results. The crystal growth systems HS1/6, HS2/6, and HS3/5 Figure 2.10 correspond the three systems with 125, 150, and 200mm diameter crystal in Figure 2.9. Two parameters - binding entropies of BI and B_2I - are fitted to the set of experimental data for growth system HS1/6. The predictions of OSF-Ring position with boron concentration based on these adjusted parameters are excellent for the other two growth systems.

Property	Original value	Adjusted value in simulations by Sinno et al.	Adjusted value in asymptotic analysis in this thesis
$S_{B_2}^b$	2.75k	2.75k	2.75k
$E_{B_2}^b$	0.8eV	0.8eV	0.8eV
θ_{B_2}	2	2	2
S_{BI}^b	-5.98k	0.31k	0.09k
E_{BI}^b	0.88eV	0.88eV	0.88eV
θ_{BI}	4	4	4
$S_{B_2I}^b$	-6.33k	-3.00k	-6.33k
$E_{B_2I}^b$	1.18eV	1.18eV	1.18eV

Table 2.1: Binding entropy, binding enthalpy, and orientational degeneracy for B_2, BI, B_2I, BV: original values are based on the atomistic simulation results [98,123]; Sinno et al. [153,164] adjusted two parameters - S_{BI}^b and S_{B2I}^b- to fit the experimental results; one parameter - S_{BI}^b - is adjusted to fit the experimental observations in this thesis.

Property	Original value	Adjusted value in simulations by Sinno et al.	Adjusted value in asymptotic analysis in this thesis
θ_{B_2I}	4	4	4
S_{BV}^b	1.05k	1.05k	1.05k
E_{BV}^b	0.57eV	0.57eV	0.57eV
θ_{BV}	4	4	

Table 2.1: Binding entropy, binding enthalpy, and orientational degeneracy for B_2, BI, B_2I, BV: original values are based on the atomistic simulation results [98,123]; Sinno et al. [153,164] adjusted two parameters - S_{BI}^b and S_{B2I}^b - to fit the experimental results; one parameter - S_{BI}^b - is adjusted to fit the experimental observations in this thesis.
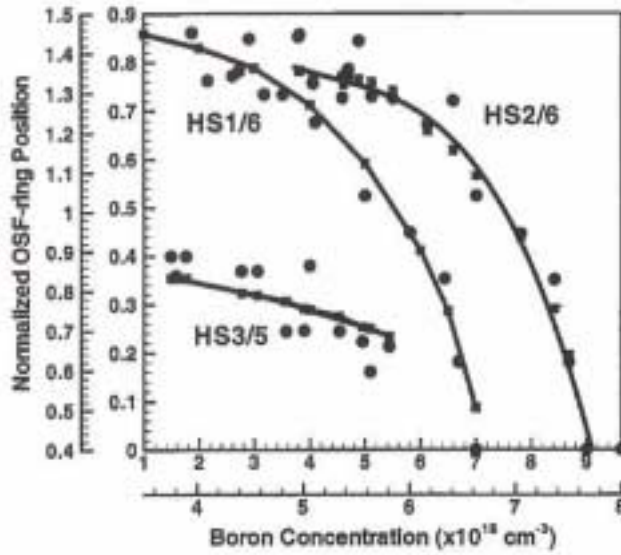
Figure 2.10: Experimental and simulation results for different crystal growth systems HS1/6, HS2/6 and HS3/5. "•" represents experimental results, and "-" represents simulation results [153].

The boundary conditions for I, V, B, B_2, BI, BV, B_2I at the melt/crystal interface in the simulations above by Sinno et al. are

$$C_I(z{=}0) = C_I^{eq}(T_m) \tag{2.133}$$

$$C_V(z{=}0) = C_V^{eq}(T_m) \tag{2.134}$$

$$C_B(z=0) + 2C_{B_2}(z=0) = C_B^{Total} \quad with \quad C_{B_2}(z=0) = [C_B(z=0)]^2 K_{BB}^{eq}(T_m) \quad (2.135)$$

$$C_{BI}(z=0) = 0 \quad (2.136)$$

$$C_{BV}(z=0) = 0 \quad (2.137)$$

$$C_{B_2I}(z=0) = 0 \quad (2.138)$$

where C_B^{Total} is the total concentration of p-type dopant boron which exists in forms of B and B_2, $K_{BB}^{eq}(T_m)$ is the equilibrium constant of reaction $B + B \leftrightarrow B_2$ at T_m. However at melt/crystal interface, with the present of boron and equilibrium concentrations of I and V, more appropriate boundary conditions for BI, BV and B_2I are their equilibrium concentrations for given C_B^{Total}.

$$C_I(z=0) = C_I^{eq}(T_m) \quad (2.139)$$

$$C_V(z=0) = C_V^{eq}(T_m) \quad (2.140)$$

$$C_B(z=0) + 2C_{B_2}(z=0) = C_B^{Total} \quad with \quad C_{B_2}(z=0) = [C_B(z=0)]^2 K_{BB}^{eq}(T_m) \quad (2.141)$$

$$C_{BI}(z=0) = K_{BI}^{eq}(T_m)C_B(z=0)C_I^{eq}(T_m) \quad (2.142)$$

$$C_{BV}(z=0) = K_{BV}^{eq}(T_m)C_B(z=0)C_V^{eq}(T_m) \quad (2.143)$$

$$C_{B_2I}(z=0) = K_{B_2I}^{eq}(T_m)C_{B_2}(z=0)C_I^{eq}(T_m) \quad (2.144)$$

Strictly speaking the boundary condition (2.141) should be replaced by

$$C_B(z=0) + C_{BI}(z=0) + C_{BV}(z=0) + 2C_{B_2}(z=0) + 2(C_{B_2I}(z=0)) = C_B^{Total} \quad (2.145)$$

C_B^{Total} is in the order of $10^{18} cm^{-3}$, and equilibrium concentrations of BI, BV and B_2I are at most in the order of $10^{14} cm^{-3}$ (for example at $C_B = 2 \times 10^{18} cm^{-3}$, $C_{BI}^{eq}(T_m) = 9.3 \times 10^{13} cm^{-3}$, $C_{B_2I}^{eq}(T_m) = 8.3 \times 10^{12} cm^{-3}$, and $C_{BV}^{eq}(T_m) = 2.8 \times 10^{13} cm^{-3}$ based on adjusted parameters used by Sinno et al. in Table

2.1) and their consumption of boron is negligible, so the boundary condition (2.141) is still valid. The boundary conditions (2.133) - (2.138) have different impact on the modification of point defect balance by boron compared with boundary conditions (2.139) - (2.144) which are used in this thesis. This is because the equilibrium concentration of BI at T_m could be in the order of $10^{14} cm^{-3}$ and the I stored in BI is comparable with $C_V^{eq}(T_m) - C_I^{eq}(T_m) \approx 2 \times 10^{14} cm^{-3}$. The situation for boundary conditions of boron defect complexes is different from that for point defect clusters. As discussed in Section 2.2.1, in the model for native point defects and their clusters, zero concentration for all the clusters are imposed at melt/crystal interface. Zero concentration is valid boundary condition for all point defect clusters because at melt/crystal interface vacancy and interstitial are not supersaturated and the concentrations of all clusters are very small. The binding entropy of BI in the following theoretical analysis is fitted to the experimental observation described by eq. (2.119). Other parameters keep their original values [98,123]. All these parameters are listed in Table 2.1. The original binding entropy of BI is -5.98k, the adjusted value in the work of Sinno et al. is 0.31k, and the adjusted value in this thesis is 0.09k.

The physical mechanism for the boron effect on point defect balance is different between the boundary conditions (2.133) - (2.138) and (2.139) - (2.144). For boundary conditions (2.139) - (2.144), the extra vacancies and interstitials needed to modify the point defect balance are mainly from the convection of BI, B_2I, and BV at melt/crystal interface due to their equilibrium concentrations at T_m. Extra interstitials are stored in BI and B_2I with their equilibrium concentrations at melt/crystal interface, and then released as the interstitial concentration decreases due to recombination near the melt/crystal interface. The similar physics is true for vacancies and BV. But the concentration of the extra interstitials in BI and B_2I is higher than that of the extra vacancies in BV. These extra net interstitials shift the balance between vacancy and interstitial more favorable for intersti-

tial, therefore shrink the vacancy-dominated core region and increase the critical V/G. For boundary conditions (2.133) - (2.138), the convection has no contribution to the extra vacancies and interstitials since the concentrations of BI, B_2I, and BV at melt/crystal interface are zeros. In a very thin layer near the melt/crystal interface, the concentrations of BI, B_2I, and BV quickly increase to their equilibrium concentrations. More interstitial related boron defect complexes (BI and B_2I) are formed than vacancy related boron defect complex (BV). The net effect is the higher increase in the gradient of interstitial near the melt/crystal interface due to more consumption of interstitials by BI and B_2I. This leads to more diffusion of interstitials at the melt/crystal interface, and therefore shifts the balance between vacancy and interstitial more favorable for interstitial.

Among BI, B_2I, and BV, only BI and BV are important. This can be proved by the comparison of equilibrium concentrations of BI, B_2I, and BV at melting temperature. Based on the parameters used for the asymptotic analysis in Table 2.1, at $C_B = 2 \times 10^{18} cm^{-3}$, $C_{BI}^{eq}(T_m) = 7.5 \times 10^{13} cm^{-3}$, $\qquad C_{B_2I}^{eq}(T_m) = 3.0 \times 10^{11} cm^{-3}$, $\qquad$ and $C_{BV}^{eq}(T_m) = 2.8 \times 10^{13} cm^{-3}$. The equilibrium concentration of B_2I at melting temperature is about two order-of magnitude lower than these of BI and BV, so BI and BV are the dominate species to modify the point defects balance. From eq. (2.131), $D_{BI}(T_m) = 1.9 \times 10^{-9} cm^2/s$ which is about five order-of-magnitude lower than that of self-interstitial. This corresponds to $Pe = VL/D_{BI} = 5 \times 10^5$ with length scale $L = 1 cm$ and a typical pull rate $V = 1 \times 10^{-3} cm/s$. The high Pe with respect to $D_{BI}(T_m)$ justifies the ignorance of the diffusion of BI in the following analysis. For the same reason, the diffusion of B and BV can be also ignored since $D_B(T_m) = 4.9 \times 10^{-11} cm^2/s$ and $D_{BV}(T_m) = 5.9 \times 10^{-10} cm^2/s$.

Since only *BI* and *BV* are important among the boron complexes, the governing equations in the following asymptotic analysis for the boron effect on the critical *V/G* are based on reactions (2.120) - (2.123).

$$V\frac{\partial C_I}{\partial z} + \nabla \bullet (-D_I \nabla C_I) + k_{IV}(C_I C_V - C_I^{eq} C_V^{eq}) + k_{BI}\left(C_B C_I - \frac{C_{BI}}{K_{BI}^{eq}}\right) = 0 \qquad (2.146)$$

$$V\frac{\partial C_V}{\partial z} + \nabla \bullet (-D_V \nabla C_V) + k_{IV}(C_I C_V - C_I^{eq} C_V^{eq}) + k_{BV}\left(C_B C_V - \frac{C_{BV}}{K_{BV}^{eq}}\right) = 0 \qquad (2.147)$$

$$V\frac{\partial C_B}{\partial z} + k_{BI}\left(C_B C_I - \frac{C_{BI}}{K_{BI}^{eq}}\right) + k_{BV}\left(C_B C_V - \frac{C_{BV}}{K_{BV}^{eq}}\right) + 2k_{BB}\left(C_B^2 - \frac{C_{B_2}}{K_{BB}^{eq}}\right) = 0 \qquad (2.148)$$

$$V\frac{\partial C_{B_2}}{\partial z} - k_{BB}\left(C_B^2 - \frac{C_{B_2}}{K_{BB}^{eq}}\right) = 0 \qquad (2.149)$$

$$V\frac{\partial C_{BI}}{\partial z} - k_{BI}\left(C_B C_I - \frac{C_{BI}}{K_{BI}^{eq}}\right) = 0 \qquad (2.150)$$

$$V\frac{\partial C_{BV}}{\partial z} - k_{BV}\left(C_B C_V - \frac{C_{BV}}{K_{BV}^{eq}}\right) = 0 \qquad (2.151)$$

where (k_{BI}, K_{BI}^{eq}), (k_{BV}, K_{BV}^{eq}), and (k_{BB}, K_{BB}^{eq}) are reaction rate and equilibrium constant of reactions $B + I \leftrightarrow BI$, $B + V \leftrightarrow BV$, and $B + B \leftrightarrow B_2$. The diffusivities of B, B_2, *BI*, and *BV* are so small that their diffusions are not included in the conservation equations above. The boundary conditions at melt/crystal interface are eqs. (2.139) - (2.143). The governing equations (2.146) - (2.151) can be transformed to the dimensionless form in cylindrical coordination by introducing a couple dimensionless variables and scales in the same way as the asymptotic analysis in Section 2.4.1.

$$\hat{z} \equiv \frac{z}{L}, \quad \hat{r} \equiv \frac{r}{R}, \quad \omega \equiv \frac{L}{R}, \quad L \equiv \frac{T_m}{\gamma^* G^*} \tag{2.152}$$

$$\Theta \equiv \frac{T}{T_m}, \quad \Theta(\hat{r}, \hat{z}) = 1 - \frac{G^* L}{T_m} g(\hat{r})\hat{z} \tag{2.153}$$

$$a(\Theta) \equiv \frac{C_I(\Theta)}{C_I^{eq}(1)}, \quad b(\Theta) \equiv \frac{C_V(\Theta)}{C_I^{eq}(1)}, \quad a^{eq}(\Theta) \equiv \frac{C_I^{eq}(\Theta)}{C_I^{eq}(1)}, \quad b^{eq}(\Theta) \equiv \frac{C_V^{eq}(\Theta)}{C_I^{eq}(1)} \tag{2.154}$$

$$\rho_B(\Theta) \equiv \frac{C_B(\Theta)}{C_I^{eq}(1)}, \quad \rho_{B_2}(\Theta) \equiv \frac{C_{B_2}(\Theta)}{C_I^{eq}(1)}, \quad \rho_{BI}(\Theta) \equiv \frac{C_{BI}(\Theta)}{C_I^{eq}(1)}, \quad \rho_{BV}(\Theta) \equiv \frac{C_{BV}(\Theta)}{C_I^{eq}(1)} \tag{2.155}$$

$$d_I(\Theta) \equiv \frac{D_I(\Theta)}{D_I(1)}, \quad d_V(\Theta) \equiv \frac{D_V(\Theta)}{D_I(1)} \tag{2.156}$$

$$\psi_{IV}(\Theta) \equiv \frac{k_{IV}(\Theta)}{k_{IV}(1)}, \quad \psi_{BB}(\Theta) \equiv \frac{k_{BB}(\Theta)}{k_{BB}(1)}, \quad \psi_{BI}(\Theta) \equiv \frac{k_{BI}(\Theta)}{k_{BI}(1)}, \quad \psi_{BV}(\Theta) \equiv \frac{k_{BV}(\Theta)}{k_{BV}(1)} \tag{2.157}$$

$$\Psi_{BB}(\Theta) \equiv K_{BB}^{eq}(\Theta)C_I^{eq}(1), \quad \Psi_{BI}(\Theta) \equiv K_{BI}^{eq}(\Theta)C_I^{eq}(1), \quad \Psi_{BV}(\Theta) \equiv K_{BV}^{eq}(\Theta)C_I^{eq}(1) \tag{2.158}$$

$$Pe \equiv \frac{VL}{D_I(1)} \equiv \frac{VT_m}{D_I(1)\gamma^* G^*} \tag{2.159}$$

$$Da^{IV} \equiv \frac{L^2 k_{IV}(1)C_I^{eq}(1)}{D_I(1)}, Da^{BB} \equiv \frac{L^2 k_{BB}(1)C_I^{eq}(1)}{D_I(1)} \tag{2.160}$$

$$Da^{BI} \equiv \frac{L^2 k_{BI}(1)C_I^{eq}(1)}{D_I(1)}, Da^{BV} \equiv \frac{L^2 k_{BV}(1)C_I^{eq}(1)}{D_I(1)} \tag{2.161}$$

where ρ_i $(i = B, B_2, BI, BV)$ are dimensionless concentrations of B, B_2, BI, and BV. ψ_i and Ψ_i $(i = IV, BB, BI, BV)$ are dimensionless reaction rates and equilibrium constants of reactions (2.120) - (2.123). Da^i $(i = IV, BB, BI, BV)$ are Damkohler numbers based on these reactions. The detail description of other dimensionless variables and scales are referred to Section 2.4.1. For the physical properties given in eqs. (2.30) - (2.34) and Table 2.1

$$Pe = O(1) \tag{2.162}$$

$$Da^{IV} = O(10^6), Da^{BB} = O(10^{-1}), Da^{BI} = O(10^6), Da^{BV} = O(10^6) \tag{2.163}$$

With these scales and dimensionless groups, the governing equations are rewritten in dimensionless form in cylindrical coordination as

$$\frac{1}{Da^{IV}}\left[-Pe\frac{\partial a}{\partial \hat{z}} + \frac{\partial}{\partial \hat{z}}\left(d_I\frac{\partial a}{\partial \hat{z}}\right) + \omega^2\frac{1}{\hat{r}}\frac{\partial}{\partial \hat{r}}\left(\hat{r}d_I\frac{\partial a}{\partial \hat{r}}\right)\right]$$

$$= \psi_{IV}(ab - a^{eq}b^{eq}) + \frac{Da^{BI}}{Da^{IV}}\psi_{BI}\left(\rho_B a - \frac{\rho_{BI}}{\Psi_{BI}}\right) \tag{2.164}$$

$$\frac{1}{Da^{IV}}\left[-Pe\frac{\partial b}{\partial \hat{z}} + \frac{\partial}{\partial \hat{z}}\left(d_V\frac{\partial b}{\partial \hat{z}}\right) + \omega^2\frac{1}{\hat{r}}\frac{\partial}{\partial \hat{r}}\left(\hat{r}d_V\frac{\partial b}{\partial \hat{r}}\right)\right]$$

$$= \psi_{IV}(ab - a^{eq}b^{eq}) + \frac{Da^{BV}}{Da^{IV}}\psi_{BV}\left(\rho_B b - \frac{\rho_{BV}}{\Psi_{BV}}\right) \tag{2.165}$$

$$-Pe\frac{\partial \rho_B}{\partial \hat{z}} = 2Da^{BB}\psi_{BB}\left(\rho_B^2 - \frac{\rho_{B_2}}{\Psi_{BB}}\right) +$$

$$Da^{BI}\psi_{BI}\left(\rho_B a - \frac{\rho_{BI}}{\Psi_{BI}}\right) + Da^{BV}\psi_{BV}\left(\rho_B b - \frac{\rho_{BV}}{\Psi_{BV}}\right) \tag{2.166}$$

$$Pe\frac{\partial \rho_{B_2}}{\partial \hat{z}} = Da^{BB}\psi_{BB}\left(\rho_B^2 - \frac{\rho_{B_2}}{\Psi_{BB}}\right) \tag{2.167}$$

$$\frac{Pe}{Da^{IV}}\frac{\partial \rho_{BI}}{\partial \hat{z}} = \frac{Da^{BI}}{Da^{IV}}\psi_{BI}\left(\rho_B a - \frac{\rho_{BI}}{\Psi_{BI}}\right) \tag{2.168}$$

$$\frac{Pe}{Da^{IV}}\frac{\partial \rho_{BV}}{\partial \hat{z}} = \frac{Da^{BV}}{Da^{IV}}\psi_{BV}\left(\rho_B b - \frac{\rho_{BV}}{\Psi_{BV}}\right) \tag{2.169}$$

Equations (2.164) - (2.165) - (2.168) + (2.169) gives

$$Pe\frac{\partial(a + \rho_{BI})}{\partial \hat{z}} - \frac{\partial}{\partial \hat{z}}\left(d_I\frac{\partial a}{\partial \hat{z}}\right) - \omega^2\frac{1}{\hat{r}}\frac{\partial}{\partial \hat{r}}\left(\hat{r}d_I\frac{\partial a}{\partial \hat{r}}\right) =$$

$$Pe\frac{\partial(b + \rho_{BV})}{\partial \hat{z}} - \frac{\partial}{\partial \hat{z}}\left(d_V\frac{\partial b}{\partial \hat{z}}\right) - \omega^2\frac{1}{\hat{r}}\frac{\partial}{\partial \hat{r}}\left(\hat{r}d_V\frac{\partial b}{\partial \hat{r}}\right) \tag{2.170}$$

Because of large Da^i ($i = IV, BI, BV$) and small ω in the system, asymptotic solution for $Da^i \gg 1$ ($i = IV, BI, BV$) and $\omega \ll 1$ are constructed as

$$a(\hat{r}, \hat{z}) = a_{00}(\hat{r}, \hat{z}) + O(\varepsilon_{IV}, \varepsilon_{BI}, \varepsilon_{BV}, \omega) \tag{2.171}$$

$$b(\hat{r}, \hat{z}) = b_{00}(\hat{r}, \hat{z}) + O(\varepsilon_{IV}, \varepsilon_{BI}, \varepsilon_{BV}, \omega) \tag{2.172}$$

$$\rho_B(\hat{r}, \hat{z}) = \rho_{B\,00}(\hat{r}, \hat{z}) + O(\varepsilon_{IV}, \varepsilon_{BI}, \varepsilon_{BV}, \omega) \tag{2.173}$$

$$\rho_{B_2}(\hat{r}, \hat{z}) = \rho_{B_2\,00}(\hat{r}, \hat{z}) + O(\varepsilon_{IV}, \varepsilon_{BI}, \varepsilon_{BV}, \omega) \tag{2.174}$$

$$\rho_{BI}(\hat{r}, \hat{z}) = \rho_{BI00}(\hat{r}, \hat{z}) + O(\varepsilon_{IV}, \varepsilon_{BI}, \varepsilon_{BV}, \omega) \tag{2.175}$$

$$\rho_{BV}(\hat{r}, \hat{z}) = \rho_{BV00}(\hat{r}, \hat{z}) + O(\varepsilon_{IV}, \varepsilon_{BI}, \varepsilon_{BV}, \omega) \tag{2.176}$$

where $\varepsilon_i = (Da^i)^{-1/2}$ ($i = IV, BI, BV$). At $O(1)$ in the expansions above, substituting eqs (2.171) - (2.176) into (2.165) - (2.170) gives the governing equations at leading order

$$-Pe\frac{\partial \rho_{B\,00}}{\partial \hat{z}} = 2Da^{BB}\psi_{BB}\left(\rho_{B\,00}^2 - \frac{\rho_{B_2\,00}}{\Psi_{BB}}\right) \tag{2.177}$$

$$Pe\frac{\partial \rho_{B_2\,00}}{\partial \hat{z}} = Da^{BB}\psi_{BB}\left(\rho_{B\,00}^2 - \frac{\rho_{B_2\,00}}{\Psi_{BB}}\right) \tag{2.178}$$

$$Pe\frac{\partial(a_{00} + \rho_{BI00})}{\partial \hat{z}} - \frac{\partial}{\partial \hat{z}}\left(d_I\frac{\partial a_{00}}{\partial \hat{z}}\right) = Pe\frac{\partial(b_{00} + \rho_{BV00})}{\partial \hat{z}} - \frac{\partial}{\partial \hat{z}}\left(d_V\frac{\partial b_{00}}{\partial \hat{z}}\right) \tag{2.179}$$

$$a_{00}b_{00} - a^{eq}b^{eq} = 0 \tag{2.180}$$

$$\rho_{B00}a_{00} - \frac{\rho_{BI00}}{\Psi_{BI}} = 0 \tag{2.181}$$

$$\rho_{B00}b_{00} - \frac{\rho_{BV00}}{\Psi_{BV}} = 0 \tag{2.182}$$

Because diffusion is negligible for $\hat{z} \gg 1$, equation (2.179) reduces to

$$Pe(a_{00} - a_{00}^{\infty}) + Pe(\rho_{BI00} - \rho_{BI00}^{\infty}) - d_I \frac{\partial a_{00}}{\partial \hat{z}} =$$

$$Pe(b_{00} - b_{00}^{\infty}) + Pe(\rho_{BV00} - \rho_{BV00}^{\infty}) - d_V \frac{\partial b_{00}}{\partial \hat{z}} \qquad (2.183)$$

where $\quad a_{00}^{\infty} = a_{00}(\hat{r}, \infty), \qquad b_{00}^{\infty} = b_{00}(\hat{r}, \infty), \qquad \rho_{BI00}^{\infty} = \rho_{BI00}(\hat{r}, \infty), \qquad$ and $\rho_{BV00}^{\infty} = \rho_{BV00}(\hat{r}, \infty)$.

$a^{eq}(\Theta)$, $b^{eq}(\Theta)$, $d_I(\Theta)$, and $d_V(\Theta)$ are defined in eqs. (2.84) - (2.89). Ψ_{BB}, Ψ_{BI}, and Ψ_{BV} are defined as

$$\Psi_{BB}(\Theta) = \Psi_{BB}(1)\exp(-\hat{\varphi}_{BB}\hat{z}) \qquad (2.184)$$

$$\Psi_{BI}(\Theta) = \Psi_{BI}(1)\exp(-\hat{\varphi}_{BI}\hat{z}) \qquad (2.185)$$

$$\Psi_{BV}(\Theta) = \Psi_{BV}(1)\exp(-\hat{\varphi}_{BV}\hat{z}) \qquad (2.186)$$

and

$$\hat{\varphi}_{BB} \equiv \frac{\overset{*}{\gamma}_{BB}}{\overset{*}{\gamma}} \qquad \overset{*}{\gamma}_{BB} \equiv \frac{-E_{BB}^b}{kT_m} \qquad (2.187)$$

$$\hat{\varphi}_{BI} \equiv \frac{\overset{*}{\gamma}_{BI}}{\overset{*}{\gamma}} \qquad \overset{*}{\gamma}_{BI} \equiv \frac{-E_{BI}^b}{kT_m} \qquad (2.188)$$

$$\hat{\varphi}_{BV} \equiv \frac{\overset{*}{\gamma}_{BV}}{\overset{*}{\gamma}} \qquad \overset{*}{\gamma}_{BV} \equiv \frac{-E_{BV}^b}{kT_m} \qquad (2.189)$$

where E_i^b ($i = BB, BI, BV$) are the binding enthalpies of B_2, BI, and BV. Since $(\overset{*}{\gamma}_{If}, \overset{*}{\gamma}_{Vf}, \overset{*}{\gamma}_{Im}, \overset{*}{\gamma}_{Vm}, \overset{*}{\gamma}_{BB}, \overset{*}{\gamma}_{BI}, \overset{*}{\gamma}_{BV}) = (3.46, 2.48, 0.937, 0.457, 0.8, 0.88, 0.57)$ based on thermophysical properties given in eqs (2.30) to (2.34) and Table 2.1, $\hat{\delta}$ and $\hat{\varphi}$ are $O(1)$, and $\hat{\mu}$, $\hat{\nu}$ and $\hat{\varphi}_i$ ($i = BB, BI, BV$) are all $O(10^{-1})$. Therefore in the region $z = O(L)$ or $\hat{z} = O(1)$, $d_I = 1$, $d_V = D_V(1)/D_I(1)$ and $\Psi_i = \Psi_i(1)$ ($i = BB, BI, BV$).

Boron can only have significant effect on Pe_{crit} at level higher than $O(10^{18})$ cm^{-3}, while the concentrations of I, V, BI and BV are less than $O(10^{15})$ cm^{-3}. So the effect of

interaction between boron and point defects on boron concentration is negligible. In the region $z = O(L)$ or $\hat{z} = O(1)$, equilibrium constant of reaction $B + B \leftrightarrow B_2$ $\Psi_{BB} = \Psi_{BB}(1)$. Therefore the constant concentrations of B and B_2, $\rho_{B\,00} = \rho_B(\hat{z}{=}0)$ and $\rho_{B_2\,00} = \rho_{B_2}(\hat{z}{=}0)$, are the solution of eqs. (2.177) and (2.178) in the region $z = O(L)$ or $\hat{z} = O(1)$. $\rho_B(\hat{z}{=}0)$ and $\rho_{B_2}(\hat{z}{=}0)$ are determined by equations $\rho_{B_2}(\hat{z}{=}0) = \rho_B^2(\hat{z}{=}0)\Psi_{BB}(1)$ and $2\rho_{B_2}(\hat{z}{=}0) + \rho_B(\hat{z}{=}0) = \rho_B^{Total}$ which are the dimensionless form of eq. (2.141).

For critical Peclet number which corresponds to $a_{00}^\infty = b_{00}^\infty = \rho_{BI\,00}^\infty = \rho_{BV\,00}^\infty = 0$, substituting eqs. (2.181) and (2.182) into eq. (2.183) gives

$$Pe_{crit}a_{00}(1 + \rho_B\Psi_{BI}(1)) - \frac{\partial a_{00}}{\partial \hat{z}} = Pe_{crit}b_{00}(1 + \rho_B\Psi_{BV}(1)) - \frac{D_V(1)}{D_I(1)}\frac{\partial b_{00}}{\partial \hat{z}} \qquad (2.190)$$

Equation (2.190) together with eq. (2.180) are the governing equations for a_{00} and b_{00}. a_{00} and b_{00} are assumed to have the exponential forms

$$a_{00}(\hat{r}, \hat{z}) = \exp(-\hat{\alpha}\hat{z}) \qquad (2.191)$$

$$b_{00}(\hat{r}, \hat{z}) = \frac{C_V^{eq}(1)}{C_I^{eq}(1)}\exp(-\hat{\beta}\hat{z}) \qquad (2.192)$$

Substituting eqs. (2.191) and (2.192) into governing equations and (2.190) gives $\hat{\alpha}$, $\hat{\beta}$ and $Pe_{crit}(\rho_B)$ as

$$\hat{\alpha} = \hat{\beta} = \frac{(\hat{\delta} + \hat{\phi})}{2} \qquad (2.193)$$

$$Pe_{crit}(\rho_B) = \frac{\hat{\delta} + \hat{\phi}}{2}\frac{1 - \dfrac{C_V^{eq}(1)D_V(1)}{C_I^{eq}(1)D_I(1)}}{\dfrac{C_V^{eq}(1)(1 + \rho_B\Psi_{BV}(1))}{C_I^{eq}(1)} - (1 + \rho_B\Psi_{BI}(1))} \qquad (2.194)$$

94

Equation (2.194) is the expression for critical Pe with the present of boron. Combining eq. (2.194) with eq. (2.96) gives the relationship between the critical Pe with and without boron as

$$Pe_{crit}(\rho_B) = Pe_{crit}^0 \frac{1}{1-x} \tag{2.195}$$

where $Pe_{crit}^0 = Pe_{crit}(\rho_B = 0)$ and

$$x \equiv \frac{\Psi_{BI}(1)C_I^{eq}(1) - \Psi_{BV}(1)C_V^{eq}(1)}{C_V^{eq}(1) - C_I^{eq}(1)} \rho_B \tag{2.196}$$

Transforming eq. (2.194) back to dimensional form gives the expression for critical V/G with boron concentration C_B

$$\left[\frac{V}{G}\right]_{crit}(C_B) = \frac{\gamma_{If}^* + \gamma_{Vf}^*}{2T_m} \cdot \frac{C_I^{eq}(T_m)D_I(T_m) - C_V^{eq}(T_m)D_V(T_m)}{[C_V^{eq}(T_m) + C_{BV}^{eq}(T_m)] - [C_I^{eq}(T_m) + C_{BI}^{eq}(T_m)]} \tag{2.197}$$

where $C_{BI}^{eq}(T_m) = K_{BI}^{eq}(T_m)C_I^{eq}(T_m)C_B$ and $C_{BV}^{eq}(T_m) = K_{BV}^{eq}(T_m)C_V^{eq}(T_m)C_B$.

The physical mechanism for the modification of the location of the OSF-Ring caused by adding boron is clear from eq. (2.197). The complex BI forms at high temperature near the melt/crystal interface but dissociates into B and I at lower temperature as the self-interstitial concentration is depleted because of recombination of vacancies and interstitials. Near the melt/crystal interface, the number of self-interstitial convected into the crystal is effectively given by the sum of the equilibrium concentration of I and BI at $T = T_m$; therefore, the $C_I^{eq}(T_m)$ term in the denominator of eq. (2.97) should be replaced by $(C_I^{eq}(T_m) + C_{BI}^{eq}(T_m))$ to take into account boron effect due to boron complex BI. For the same reason, $C_V^{eq}(T_m)$ term in the denominator of eq. (2.97) should be replaced by $(C_V^{eq}(T_m) + C_{BV}^{eq}(T_m))$.

Transforming eqs. (2.195) and (2.196) back to dimensional form gives the relationship between the critical V/G with and without boron as

$$\left[\frac{V}{G}\right]_{crit}(C_B) = \left[\frac{V}{G}\right]_{crit}^0 \frac{1}{1-x} \qquad (2.198)$$

where $\left[\frac{V}{G}\right]_{crit}^0 = \left[\frac{V}{G}\right]_{crit}(C_B = 0)$ and

$$x \equiv \frac{K_{BI}^{eq}(T_m)C_I^{eq}(1) - K_{BV}^{eq}(T_m)C_V^{eq}(1)}{C_V^{eq}(1) - C_I^{eq}(1)} C_B \qquad (2.199)$$

At melt/crystal interface significant boron exists in the form of B_2 which does not contribute to x in eq. (2.196). The experimentally measured boron concentration is the total boron concentration which includes concentration of both B and B_2. The actual boron concentration at melt/crystal interface are determined by eq. (2.141) as

$$C_B^{Total} = C_B + 2C_{B_2} = C_B + 2K_{B_2}(T_m)C_B^2 \qquad (2.200)$$

C_B is then applied in eqs. (2.198) and (2.199) to predict critical V/G. The critical V/G as function of total boron concentration predicted by eqs. (2.198) - (2.200) is plotted in Figure 2.11. The binding entropy of BI, S_{BI}^b, is fitted to get the same linear fit as the experimental results described in (2.119). The curve is approximately linear and the best linear fit across the $\left[\frac{V}{G}\right]_{crit}^0$, which is $1.34 \times 10^{-3} cm^2 min^{-1} K^{-1}$, is

$$\left[\frac{V}{G}\right]_{crit}(C_B) = 1.34 \times 10^{-3}(cm^2 min^{-1}K^{-1}) + 1.2 \times 10^{-22}(cm^5 min^{-1}K^{-1})C_B^{Total} \qquad (2.201)$$

C_B^{Total} in eq. (2.201) is the same thing as C_B in eq. (2.119). The fitted binding entropy of BI is $S_{BI}^b = 0.09k$. The dependence of the critical V/G is sensitive to S_{BI}^b. For the value of $S_{BI}^b = 0.31k$, the best linear fit for the critical V/G as function of total boron concentration is

$$\left[\frac{V}{G}\right]_{crit}(C_B) = 1.34 \times 10^{-3}(cm^2 min^{-1}K^{-1}) + 2.3 \times 10^{-22}(cm^5 min^{-1}K^{-1})C_B^{Total} \quad (2.202)$$
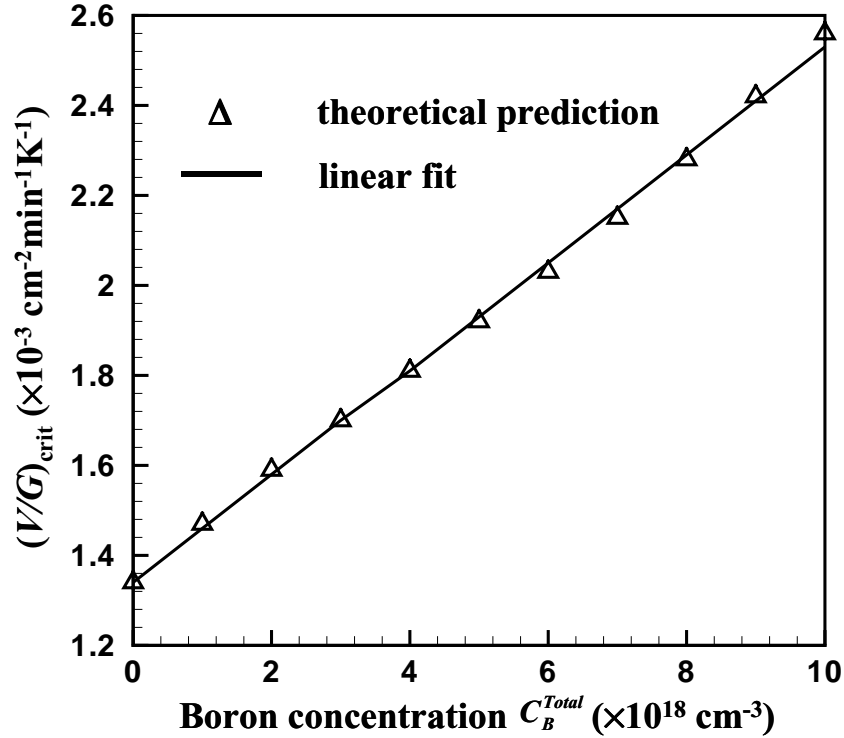
Figure 2.11: Dependence of critical *V/G* on boron concentration.

It should be pointed out that Voronkov proposed another mechanism for the effect of boron on critical *V/G* [187,188]. As discussed in section 1.3.1, silicon crystal at melt/crystal interface is intrinsic even with boron doped. The Fermi level shifted by boron is small, therefore changes of charged native point defects are relative small compared with neutral native point defects. However critical *V/G* is very sensitive to total native point defect which includes neutral point defect and all charged point defects at melt/crystal interface. Even though the change of total native point defect due to boron is small, it may still have significant effect on critical *V/G*. If this mechanism is right, we would expect exactly the same critical *V/G* change for all p-type silicon with the same doping level, and the same

97

thing is true for all n-type silicon but in the different direction. In other word, for silicon with different dopants such as *B*, *Ga*, *P*, and *As*, as long as the doping levels are the same the critical *V/G* changes are the same for *B* and *Ga*, and exactly the same but in the other direction for *P* and *As*. This kind of experiment is still needed to be done to prove the mechanism above proposed by Voronkov.

2.5 Theoretical Analysis on Void Formation

As discussed in Section 2.3, near the melt/crystal interface vacancies and self-interstitial convect, diffuse, and recombine with each other, leaving residual vacancies when *V/G* is higher than critical *V/G*. There is essentially no void formation in the recombination region near the melt/crystal interface since there is no enough super-saturation for the driving force. So the residual vacancy concentration can be determined by the asymptotic analysis of vacancies and self-interstitials without any clustering in the recombination region. The asymptotic results for the residual vacancy or intermediate vacancy concentration are described in eqs. (2.105) - (2.109). This is the first step in the comprehensive theoretical analysis on the point defects and point defect clusters during the CZ crystal growth. The intermediate vacancies are the reservoir for void formation at lower temperature. So the next step is to analyze the void formation using the intermediate vacancy concentration and temperature field around aggregation temperature as inputs. The void formation is governed by the rate equations (either discrete or continuous) and constrained by the con-servation of vacancy. In this section, the continuous form of rate equation is first analyzed to give physical insight for the void formation in silicon crystal growth. Specifically the size space of the rate equation can be divided into two regions; small clusters are governed by 'inner equation' and big clusters are governed by 'outer equation'. The analytical solu-tion of the outer equation leads to two important scalings for void formation. The analyti-cal solutions of discrete inner equation and continuous outer equation together with the

vacancy conservation equation give accurate predictions of important variables such as void aggregation temperature, total void density, and average void size.

2.5.1 Inner Equation and Outer Equation

The Zeldovich equation derived in Section 2.2.3 is a continuous rate equation and can be written in dimensionless form by introducing a couple scaled variables. The temperature field near the aggregation temperature is approximate

$$T = T^* - \langle G \rangle V t \tag{2.203}$$

where T^* is approximately the nucleation temperature, $\langle G \rangle$ is temperature gradient in this region of the crystal, and V is the crystal pull rate. The typical values for $\langle G \rangle$ and V are 20 *K/cm* and 10^{-3} *cm/s* respectively. A characteristic value of $T^* = 1200K$. Using these scales a characteristic time scale for the residence of the crystal in this temperature range is

$$t^* \equiv \frac{T^*}{\langle G \rangle V} = 6 \times 10^4 s \tag{2.204}$$

The cluster size is scaled by the value

$$n^* = 10^8 \tag{2.205}$$

and scales for v and g are taken as their values at n^* or

$$v^* = v(n^*) \tag{2.206}$$

$$g^* = g(n^*) \tag{2.207}$$

Based on eqs. (2.204) - (2.207) dimensionless variables are defined as

$$F \equiv \frac{f}{C_1^{eq}(T_m)}, \quad \eta \equiv \frac{n}{n^*}, \quad \hat{t} \equiv \frac{t}{t^*}, \quad \hat{v} \equiv \frac{v}{v^*}, \quad \hat{g} \equiv \frac{g}{g^*} \tag{2.208}$$

and dimensionless Zeldovich equation is written as

$$Q\frac{\partial F}{\partial \hat{t}} = -\frac{\partial}{\partial \eta}(\hat{v}F) + \frac{1}{P}\frac{\partial}{\partial \eta}\left(\hat{g}\frac{\partial F}{\partial \eta}\right) \tag{2.209}$$

where

$$Q \equiv \frac{\overset{*}{n}}{\overset{*}{t}\,\overset{*}{v}} \tag{2.210}$$

$$P \equiv \frac{\overset{*}{n}\,\overset{*}{v}}{\overset{*}{g}} \tag{2.211}$$

In this form P scales the importance of the diffusion-like term on the evolution of the size distribution. The magnitude of P can be evaluated with the aid of eq. (2.50) in which quasi-equilibrium cluster concentration C_n^* must be calculated first. As described in [84], C_n^* is related to monomer concentration by the following expression.

$$C_n^* = C_1 \exp\left(\frac{-(G(n) - G(1))}{kT}\right) \tag{2.212}$$

where G is Gibbs free formation energy. For void formation, the free energy of formation is given by eq. as

$$G = -nkT\ln\left(\frac{C_1}{C_1^{eq}}\right) + 4\pi r^2 \sigma \tag{2.213}$$

where r and σ are radius and surface energy of the void respectively. The first term in eq. (2.213) is the contribution from the monomer super-saturation and the second term is the surface energy of a spherical void. Substituting eq. (2.213) into eq. (2.212) gives

$$C_n^* = C_1 \exp\left[(n-1)\ln\left(\frac{C_1}{C_1^{eq}}\right) - \frac{a\sigma}{kT}\left(n^{\frac{2}{3}} - 1\right)\right] \tag{2.214}$$

where

$$a \equiv (36\pi b^2)^{\frac{1}{3}} \tag{2.215}$$

and b is the volume of the monomer. Substituting eq. (2.214) into eq. (2.50) gives an expression for the drift velocity as

$$v = g\left(\ln \frac{C_1}{C_1^{eq}} - \frac{2a\sigma}{3kT} n^{-1/3} \right) \tag{2.216}$$

Near the aggregation temperature T^*, the monomer concentration is always highly supersaturated, or two to three orders-of-magnitude higher than the equilibrium concentration at $T = T^*$. The typical values of parameters in eq. (2.216) are $b = 2 \times 10^{-29} m^3$, $\sigma = 1.0 J/m^2$, and $T = 1200 K$, and lead to the coefficient value $((2a\sigma)/(3kT)) = 14.3$. Hence, for large n, the second term in eq. (2.216) is small compared with the first term, so the drift velocity is simply

$$v = g\ln \frac{C_1}{C_1^{eq}} \tag{2.217}$$

and the parameter P is

$$P = \frac{n^* v^*}{g^*} = n^* \ln\left(\frac{C_1}{C_1^{eq}} \right) \gg 1 \tag{2.218}$$

Because $P \gg 1$, the diffusion term in the Zeldovich equation (2.209) can be ignored so that eq. (2.209) reduces to

$$Q\frac{\partial F}{\partial \hat{t}} = -\frac{\partial}{\partial \eta}(\hat{v}F) \tag{2.219}$$

Equation (2.219) is referred to as 'outer equation' in this thesis, where 'outer' implies it is valid for $n \gg 1$. Because the Zeldovich equation is a second order differential equation for n and the outer equation is first order in n, eq. (2.219) can not be valid through the

whole domain $n_{match} < n < n_{max}$. There must be at least one more region where a different approximation is needed and the second order term is retained. In order to retain the second order term, n or its dimensionless variable η has to be rescaled. Consider the scaling

$$\xi \equiv P\eta \tag{2.220}$$

With this new variable, equation (2.209) becomes

$$\frac{Q}{P}\frac{\partial F}{\partial \hat{t}} = -\frac{\partial}{\partial \xi}(\hat{v}F) + \frac{\partial}{\partial \xi}\left(\hat{g}\frac{\partial F}{\partial \xi}\right) \tag{2.221}$$

From eqs. (2.210) and (2.211)

$$\frac{Q}{P} = \frac{g^*}{t^* v^{*2}} \tag{2.222}$$

For diffusion-limited growth, the growth rate g is written as [84]

$$g = 4\pi r D C_1 \tag{2.223}$$

This is nothing but the monomer diffusion flux to a spherical cluster with radius r under the bulk monomer concentration C_1. It can be obtained by solving differential equation $\nabla^2 C = 0$ in the spherical coordination. Since the cluster size n is related to radius r by $\frac{4}{3}\pi r^3 = nb$, g is rewritten as

$$g = 4\pi r D C_1 = K n^{1/3} \tag{2.224}$$

where

$$K = (48\pi^2 b)^{1/3} D C_1 \tag{2.225}$$

Near the nucleation temperature $T^* = 1200K$ $D_V = 1.2 \times 10^{-5} cm^2/s$, and the monomer concentration C_V is typically between 10^{13} and $10^{14} cm^{-3}$. The constant Q/P can be evaluated from eqs. (2.217) and (2.224) as

$$\frac{Q}{P} = \frac{1}{t^* K n^{*1/3}\left(\ln\dfrac{C_1}{C_1^{eq}}\right)^2} \ll 1 \tag{2.226}$$

Because $Q/P \ll 1$, the left side in eq. (2.221) can be ignored and the dimensionless Zeldovich reduces to

$$-\frac{\partial}{\partial\xi}(\hat{v}F) + \frac{\partial}{\partial\xi}\left(\hat{g}\frac{\partial F}{\partial\xi}\right) = 0 \tag{2.227}$$

Because $P \gg 1$, eq. (2.220) implies that eq. (2.227) is only valid for very small n or $\xi = O(1)$. Hence eq. (2.227) is referred to as the 'inner equation' in this thesis. A stationary solution is defined as the solution which satisfies $J_n = J_{n+1}$ in the discrete form (see eq. (2.35)) and $\partial(vf - g\partial f/\partial n)/\partial n = 0$ in continuous form (see eq. (2.49)). Hence, the inner equation is stationary.

To summarize, the cluster size distribution $F(n, t)$ modeled by the Zeldovich equation can be divided into two regions. In the region of small n, the time-dependent term can be ignored, and the distribution can be described by inner equation eq. (2.227), and the result is the stationary solution. In the region of $n = O(n^*)$, the diffusion term in eq. (2.209) can be ignored and the size distribution can be described by the outer equation eq. (2.219). There is a matching point between the inner and outer equation.

The Zeldovich equation is one representation of the evolution of void size distribution. So the characteristics of the Zeldovich equation in the two regions reveal the basic physics of the void formation. For void formation, the time scale to reach the stationary size distribution for small n is much smaller than the system time scale t^*, and the time-dependent term is negligible. While for $n \gg 1$, the cluster size distribution propagate with a drift velocity, and the diffusion in size space is negligible.

Since the Fokker-Planck equation derived in Section 2.2.3 is just another representation for the void formation. Due to the nature of the void formation just discussed, in the Fokker-Planck equation for void formation, the time-dependent term can be ignored for small n, and the diffusion term in n can be ignored for big n. Therefore the dimensional outer equation for Fokker-Planck equation is

$$\frac{\partial f}{\partial t} = -\frac{\partial}{\partial n}(Af) \tag{2.228}$$

where

$$A = g - d - \frac{1}{2}\frac{\partial}{\partial n}(g + d) \tag{2.229}$$

In the following sections, dimensional inner and outer equations are used instead to save the conversion back to dimensional results.

Sample steady-state simulation results for void size distributions at different axial positions are shown in Figure 2.12. The governing equations used in these simulation are eqs. (2.6) - (2.15). The axial position is interchangeable with the pulling time ($z=Vt$) which is defined as the time needed to pull crystal from melt/crystal interface to a certain axial position. The evolution of the void size distribution is clearly shown. Void aggregation temperature under these particular operating conditions occurs at about $z = 1.7$. When the temperature is higher than the aggregation temperature or $z < 1.7$, the size distribution void concentration decreases dramatically when n is small, and then decrease more gradually for $n \gg 1$. The transition point between these two regions occurs approximately between $n=20$ to $n=100$ in Figure 2.12. The size distribution for $n \ll n^*$ is the stationary solution, as will be discussed in Section 2.4.3. In the region for $n \gg 1$, the void concentration is proportional to $n^{-1/3}$ which is the scaling of the solution of the outer equation, as will be proved in Section 2.4.2. Near the aggregation temperature, the total

number vacancies consumed by all voids become significant compared with the intermediate vacancy concentration which is the finite reservoir for void formation. Therefore, the vacancy concentration begins to decrease significantly at $T = T^*$. This leads to the decrease in the concentration of void in the region for small n, while large voids continue to grow. This mechanism leaves a peak at large n in the size distribution. Hence the finite reservoir of monomer is the real reason why there is a peak in the final void size distribution. Below the aggregation temperature the total void concentration no longer changes (see Figure 2.5) because there is essentially no further nucleation and only the growth of large clusters which are already formed.
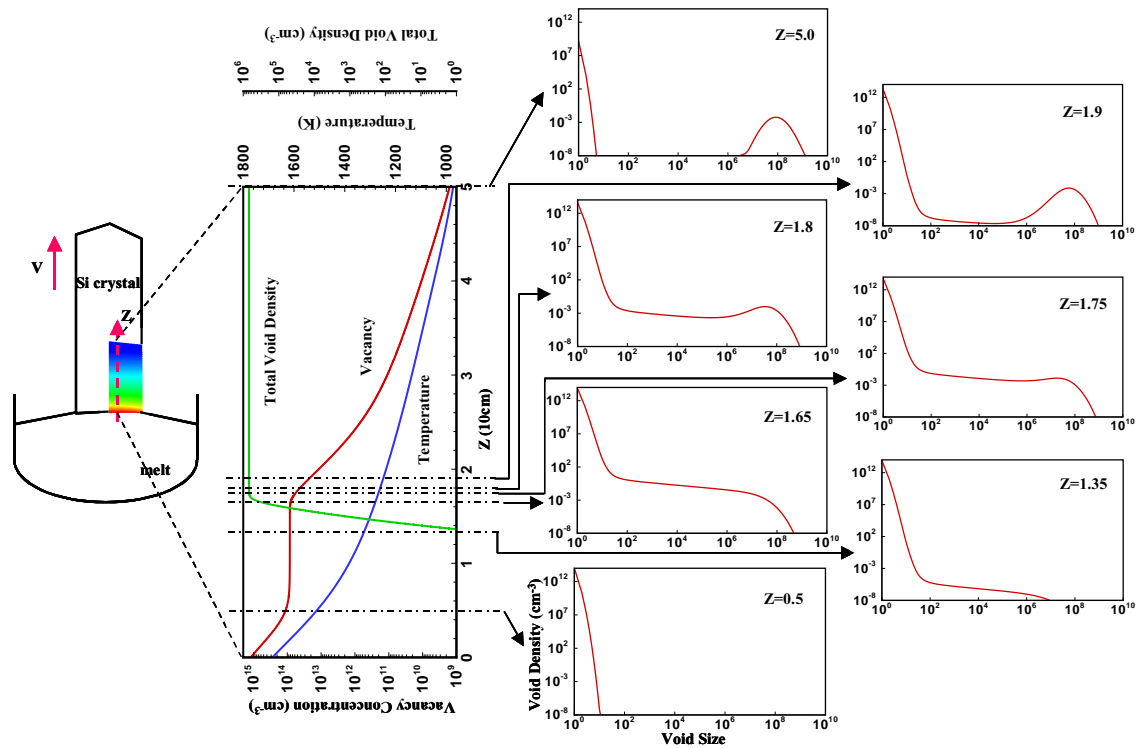
Figure 2.12: Void size distribution at different axial positions (Pe=1.75Pe_{crit}).

2.5.2 Scalings for Void Formation

Voronkov used a classical nucleation model to get two scalings for void formation [185]. Total void concentration is proportional to $\langle G \rangle^{3/2} (C_V^0)^{-1/2}$ and the average void size is

proportional to $(C_V^0 / \langle G \rangle)^{3/2}$ where $\langle G \rangle$ is the temperature gradient around void aggregation temperature and C_V^0 is the vacancy concentration at the onset of void formation. Mori et al. confirmed these scalings by the numerical simulations of point defects and their clusters during the CZ crystal growth [107]. In this section, these two scalings are rigorously derived from the governing equations for void formation.

The concentration of the total vacancies consumed in the voids is

$$C_V^{Total} = \int_2^\infty nf dn \qquad (2.230)$$

The void concentration decreases dramatically with n when $n \ll n^*$. While for $n \gg 1$, both n and dn are big. So only in the outer region is the void size distribution significant in eq. (2.230). Therefore only the outer equation is used in this section to derive the scalings for void formation, particularly the dependence of total void concentration N_{Total} and average void size n_{avg} on the intermediate concentration and temperature gradient near the aggregation temperature $T = T^*$. From eqs. (2.217) and (2.224), the drift velocity v for $n \gg 1$ and diffusion-limited void growth is written as

$$v = L_Z n^{1/3} \qquad (2.231)$$

where the subscript Z represents Zeldovich and the constant L_Z is

$$L_Z = (48\pi^2 b)^{1/3} D_V C_V^{int} \ln \frac{C_V^{int}}{C_V^{eq}} \qquad (2.232)$$

and C_V^{int} is the intermediate vacancy concentration which is the reservoir for void formation. The constant D_V and C_V^{eq} are vacancy diffusivity and equilibrium concentration respectively. Using the expression for drift velocity in eq. (2.231), the dimensional outer equation, boundary condition, and initial condition are described as

$$\frac{\partial f}{\partial t} = -L_Z \frac{\partial}{\partial n}(n^{1/3}f)$$ (2.233)

with boundary condition

$$f(n^0, t) = f^0 \quad for \quad t > t^0$$ (2.234)

and initial condition

$$f(n, t^0) = 0 \quad for \quad n \geq n^0$$ (2.235)

where n^0 is the matching point between the inner equation and the outer equation, and $f^0 = f(n^0, t^0)$. Equation (2.233) is a first-order partial differential equation and can be solved by the method of characteristics [206]. The solution is

$$f = \begin{cases} f^0\left(\dfrac{n^0}{n}\right)^{1/3} & when \quad n^{2/3} < (n^0)^{2/3} + \dfrac{2}{3}L_Z(t - t^0) \\ 0 & when \quad n^{2/3} \geq (n^0)^{2/3} + \dfrac{2}{3}L_Z(t - t^0) \end{cases}$$ (2.236)

The result above indicates that in the outer region, the void concentration is proportional to $n^{-1/3}$, as observed in the numerical simulations.

We can proceeded further to get some useful scalings for void formation. A reasonable assumption for void formation is that at the aggregation temperature $T = T^*$ the concentration of the total vacancies consumed by the voids is equal to the intermediate vacancy concentration. As discussed at the beginning of this section, only the outer region plays an important role in determining the total vacancy stored in the voids. This assumption is restated as

$$C_V^{int} = \int_2^\infty nf dn \approx \int_{n^0}^\infty nf dn$$ (2.237)

substituting eq. (2.236) into eq. (2.237) gives

$$C_V^{int} = \int_{n^0}^{\left((n^0)^{2/3} + \frac{2}{3}L_Z\tilde{t}\right)^{3/2}} nf^0\left(\frac{n^0}{n}\right)^{1/3} dn = \frac{3}{5}f^0(n^0)^{1/3} n^{5/3}\Big|_{n^0}^{\left((n^0)^{2/3} + \frac{2}{3}L_Z\tilde{t}\right)^{3/2}}$$

$$= \frac{3}{5}f^0(n^0)^{1/3}\left[\left((n^0)^{2/3} + \frac{2}{3}L_Z\tilde{t}\right)^{5/2} - (n^0)^{5/3}\right] \qquad (2.238)$$

where $\tilde{t} \equiv t - t^0$, and it is the residence time of a void near the aggregation temperature where significant vacancies are consumed by voids. Accordingly D_V and C_V^{eq} in eq. (2.232) are evaluated at void aggregation temperature. Assuming that n^0, which is matching point between inner and outer equation, is very small compared with the maximum non-zero void size $\left((n^0)^{2/3} + \frac{2}{3}L_Z\tilde{t}\right)^{3/2}$ at $T = T^*$ and also is an extreme small contribution to the maximum non-zero void size. Therefore eq. (2.238) is simplified to

$$C_V^{int} = \frac{3}{5}f^0(n^0)^{1/3}\left(\frac{2}{3}L_Z\tilde{t}\right)^{5/2} \qquad (2.239)$$

The total void concentration is defined as the summation of all voids larger than n^0 or

$$N_{Total} = \int_{n^0}^{\infty} f\,dn = \int_{n^0}^{\left((n^0)^{2/3} + \frac{2}{3}L_Z\tilde{t}\right)^{3/2}} f^0\left(\frac{n^0}{n}\right)^{1/3} dn = f^0(n^0)^{1/3}L_Z\tilde{t} \qquad (2.240)$$

This integral is actually insensitive to the lower bound because the contribution around lower limit to the integral is not significant. The average void size is defined as the ratio of total vacancies consumed by voids to the total voids concentration. Using eqs. (2.237), (2.239), and (2.240), the average void size is written as

$$n_{avg} = \frac{\int_{n^0}^{\infty} nf\,dn}{\int_{n^0}^{\infty} f\,dn} = \frac{C_V^{int}}{N_{Total}} = \frac{3}{5}\left(\frac{2}{3}\right)^{5/2}(L_Z\tilde{t})^{3/2} \qquad (2.241)$$

This expression can be simplified by examining the dependence of eq. (2.232) on C_V^{int}. Hence $L_Z \propto C_V^{int}$. The residence time $\tilde{t}$ of clusters near $T = T^*$ is inverse proportional to the temperature gradient $\langle G \rangle$, or $\tilde{t} \propto \frac{1}{\langle G \rangle}$ as given in eq. (2.204). Use these two scalings, the average void size can be approximated as.

$$n_{avg} \propto \left(\frac{C_V^{int}}{\langle G \rangle} \right)^{3/2} \tag{2.242}$$

The scaling of total voids concentration is obtained by combining eqs. (2.241) and (2.242).

$$N_{Total} = \frac{C_V^{int}}{n_{avg}} \propto \langle G \rangle^{3/2} (C_V^{int})^{-1/2} \tag{2.243}$$

The scalings above are direct results of $n^{-1/3}$ dependence of void concentration on the void size in the outer region. The simulation results of void size distribution in the outer region are shown in Figure 2.13. In the log plot, the curve is linear except for very large n and for the matching point for small n. The scaling $n^{-1/3}$ also is very accurate.
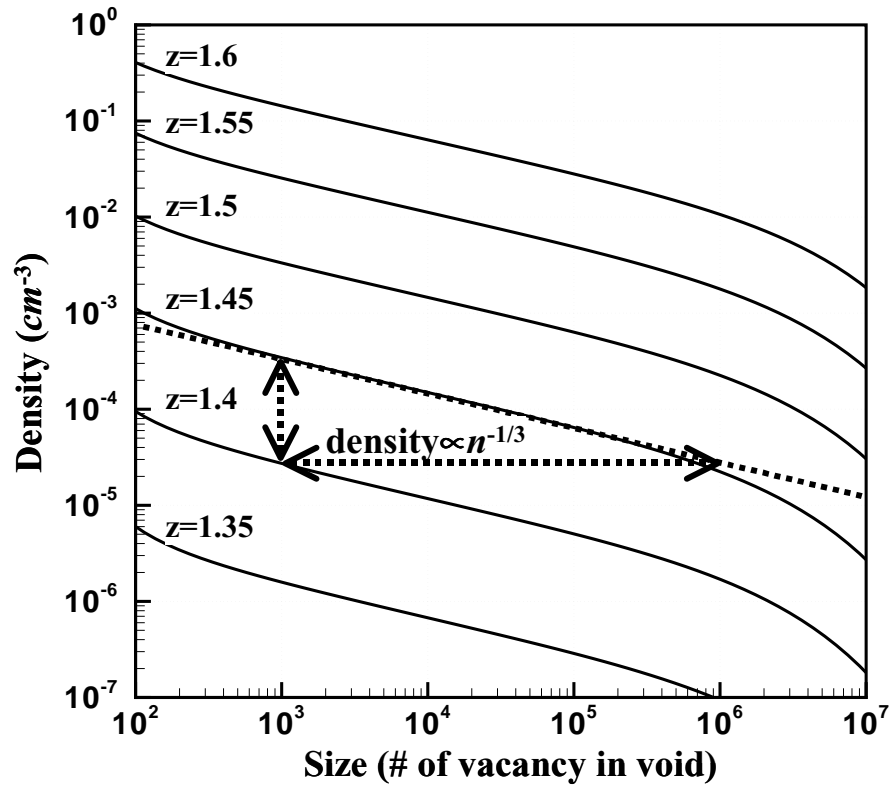
Figure 2.13: Outer region of void size distribution at different axial positions.

As discussed in Section 2.2.1, the Fokker-Planck equations (2.12) and (2.13), and the model for g and d (eqs. (2.20) and (2.21)) are used in the simulation. A similar theoretical analysis on the Fokker-Planck equation with g and d from eqs. (2.20) and (2.21) also leads to the same scalings above. The void drift velocity of the outer equation (2.228) for Fokker-Planck equation is $A = g - d - \frac{1}{2}\frac{\partial}{\partial n}(g + d)$. g is determined by eqs. (2.20) as

$$g = \frac{4\pi D_V}{\delta}\frac{C_V}{C_V^{eq}}r^2\exp\left(-\frac{2b\sigma}{rkT}\right)\frac{\frac{r}{\delta}C_V + C_V}{\frac{r}{\delta}\frac{C_V}{C_V^{eq}}\exp\left(-\frac{2b\sigma}{rkT}\right) + 1} \tag{2.244}$$

d is determined by eq. (2.21) as

$$d = \frac{4\pi r^2 D_V C_V}{\delta} \tag{2.245}$$

where b is the volume of monomer as used in eq. (2.215). Near the aggregation temperature $T = T^*$ and for $n \gg 1$ ($r \gg \delta$)

$$\frac{r}{\delta}\frac{C_V}{C_V^{eq}}\exp\left(-\frac{2b\sigma}{rkT}\right) \gg 1 \tag{2.246}$$

Therefore with the relationship between cluster size n and radius r, $\frac{4}{3}\pi r^3 = nb$, the void drift velocity for Fokker-Planck equation is written as

$$A = g - d - \frac{1}{2}\frac{\partial}{\partial n}(g + d) = 4\pi\lambda D_V C_V n^{1/3}\left(1 - \frac{2\lambda}{3\delta}n^{-2/3} - \frac{1}{6}n^{-1}\right) \tag{2.247}$$

where $\lambda = \left(\frac{3b}{4\pi}\right)^{1/3}$ is the radius of monomer, and it is the same order with δ which is the lattice spacing in silicon crystal. For $n \gg 1$, eq. (2.247) reduces to

$$drift\ velocity = A = g - d - \frac{1}{2}\frac{\partial}{\partial n}(g + d) = L_{FP}n^{1/3} \tag{2.248}$$

where the subscript FP represents Fokker-Planck equation and the constant L_{FP} is

$$L_{FP} = (48\pi^2 b)^{1/3} D_V C_V^{int} \tag{2.249}$$

Hence, the drift velocity for the outer equation of the Fokker-Planck equation has the same $n^{1/3}$ dependence as that for Zeldovich equation, and L_{FP} is proportional to C_V^{int}. So with exactly the same analysis for the outer equation of Zeldovich equation, the Fokker-Planck equation used in simulation also leads to the same scalings described by eqs. (2.242) and (2.243).

The scalings for total voids concentration and average void size provide their important dependences on $\langle G \rangle$ and C_V^{int} which is related to operating conditions by eq. (2.109). However, the aggregation temperature, the absolute values of total void concentration and average void size must still be determined. In the following section, the outer equation (2.228) with the drift velocity defined by eq. (2.248) will be used in order to quantitatively compare theoretical estimations with simulation results.

2.5.3 Estimations of Aggregation Temperature, Total Void Concentration and Average Void Size

In the previous section, only the solution of the outer equation was considered, and was enough to obtain the scalings because the void concentration at matching point n^0 $f^0(n^0, t)$ does not influence these results. However, in order to get absolute values for the total void concentration and the average void size instead of just scalings, f^0 has to be determined. Therefore, the inner equation must be analyzed.

As discussed in section 2.3, continuous equations such as Fokker-Planck equation and Zeldovich equation are only approximations of the rigorous discrete rate equation. Unfortunately they are only good for big clusters, and they introduce significant error for small clusters. The steady-state simulation results of void size distributions with different matching points are shown in Figure 2.14. They are the results of the same governing equations under the same operating conditions but with different matching points between

111

discrete rate equations and Fokker-Planck equations. Three curves correspond to matching points at 3, 10 and 100 respectively. The curves for $n_{match} = 10$ and $n_{match} = 100$ almost overlap with each other and the connections at n_{match} are very smooth for both curves. However, the results for $n_{match} = 3$ over predict the cluster density, and the connection at n_{match} is very abrupt. This is an indication that discrete rate equations at small n can not be replaced by their continuous approximations. The reason is that void concentrations decrease dramatically at small n and are far from linear so that the second order Taylor expansions which are used to get continuous forms do not hold. The n_{match} between discrete rate equations and Fokker-Planck equations in void formation can be set as 10 to yield reasonable results.
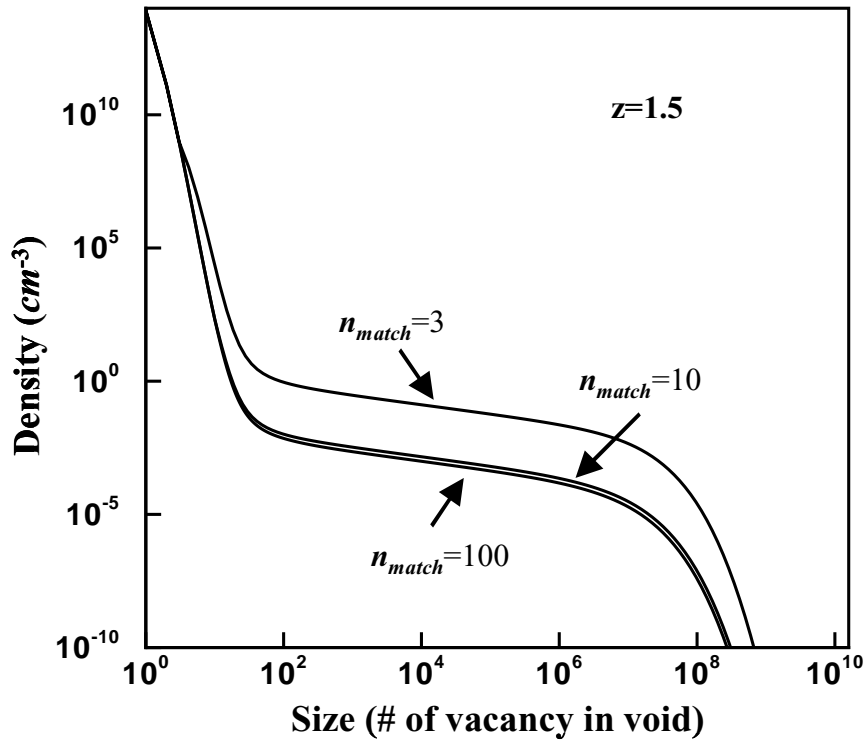
Figure 2.14: Void size distributions with different matching points between discrete rate equations and Fokker-Planck equations.

In the inner region for small n, the discrete rate equations have to be used instead of the continuous inner equation eq. (2.227). However the conclusion in section 2.4.1 that the time-dependent term can be ignored in the inner region is still valid. In other words, the concentration of small voids can be determined by the discrete form of inner equation or stationary solution. The stationary discrete rate equations are

$$J_n - J_{n+1} = 0 \qquad n = 2, 3, 4\ldots \qquad (2.250)$$

where

$$J_n = g_{n-1}C_{n-1} - d_n C_n \qquad (2.251)$$

$$J_{n+1} = g_n C_n - d_{n+1}C_{n+1} \qquad (2.252)$$

A special case is the quasi-equilibrium void concentration when $J_n = 0$ for all n. The quasi-equilibrium cluster concentrations are defined in eqs. (2.44) and (2.45), and are written in the following form.

$$C_n^* = C_V \frac{\displaystyle\prod_{m=1}^{n-1} g_m}{\displaystyle\prod_{m=2}^{n} d_m}, \qquad n = 2, 3, 4\ldots \qquad (2.253)$$

The discrete form of the inner equation or stationary solution with boundary conditions can be written as

$$J_n - J_{n+1} = 0 \qquad n = 2, \ldots, M-1 \qquad (2.254)$$

where

$$J_n = g_{n-1}C_{n-1} - d_n C_n \qquad (2.255)$$

with the boundary conditions

$$C_1 = C_V \tag{2.256}$$

$$C_M = f_M \tag{2.257}$$

The equations above have M-2 equations and M-2 unknowns (from C_2 to C_{M-1}), so this problem is well imposed. In order to solve these equations, another unknown - the stationary flux J_S - is introduced and the eqs. (2.254) and (2.255) are rearranged as

$$J_S = g_{n-1}C_{n-1} - d_n C_n \qquad n = 2, \ldots, M \tag{2.258}$$

with the same boundary conditions (2.256) and (2.257). This new form of stationary solution has M-1 equations and M-1 unknowns (J_S, C_2, C_3, ..., C_{M-1}). With the help of quasi-equilibrium void concentrations defined by eq. (2.44), eq. (2.258) is rearranged as [84]

$$\frac{J_S}{g_{n-1}C_{n-1}^*} = \frac{C_{n-1}}{C_{n-1}^*} - \frac{C_n}{C_n^*} \qquad n = 2, \ldots, M \tag{2.259}$$

Note that the monomer concentration C_1 appears only in the equation for $n = 2$. The summation of the M-1 equations represented by eq. (2.259) gives

$$J_S \left[\sum_{m=1}^{M-1} \frac{1}{g_m C_m^*} \right] = 1 - \frac{f_M}{C_M^*} \tag{2.260}$$

The summation of some equations (from n+1 to M) gives

$$J_S \left[\sum_{m=n}^{M-1} \frac{1}{g_m C_m^*} \right] = \frac{C_n}{C_n^*} - \frac{f_M}{C_M^*} \tag{2.261}$$

Combining eqs (2.260) and (2.261) to remove the stationary flux J_S gives

$$C_n = C_n^* \left(\left(1 - \frac{f_M}{C_M^*} \right) \left[\sum_{m=1}^{M-1} \frac{1}{g_m C_m^*} \right]^{-1} \sum_{m=n}^{M-1} \frac{1}{g_m C_m^*} + \frac{f_M}{C_M^*} \right) \qquad (2.262)$$

which is the general solution to the discrete rate equation. A special solution when $f_M = 0$ is

$$C_n = C_n^* \left[\sum_{m=1}^{M-1} \frac{1}{g_m C_m^*} \right]^{-1} \sum_{m=n}^{M-1} \frac{1}{g_m C_m^*} \qquad (2.263)$$

The stationary solutions described by eq. (2.263) with different values of M are plotted in Figure 2.15 to compare with the simulation result of void size distribution. The stationary solutions match the simulation result except in the small tail around $n = M$. This comparison verifies that the discrete form of the inner equation or stationary solution is a good approximation to the dynamics void calculation for small n.

The void concentration at the matching point $n = n^0$ between the inner and outer regions of cluster size is determined by matching the flux between the two regions. Set $M = n^0$ in eq. (2.260) and consider $f_M = f^0$ as the unknown to be determined. At the matching point $M = n^0$, the discrete form of the stationary flux J_S in the inner region is equal to the continuous form of the flux in the outer region at $n = n^0$; hence,

$$J_S = L_{FP}(n^0)^{1/3} f^0 \qquad (2.264)$$

from eq. (2.260) or

$$J_S = \left(1 - \frac{f^0}{C_{n^0}^*} \right) \left[\sum_{m=1}^{n^0-1} \frac{1}{g_m C_m^*} \right]^{-1} \qquad (2.265)$$

The value of the cluster size at $M = n^0$, f^0, is found by solving eqs. (2.264) and (2.265). The selection of the matching point $n = n^0$ is arbitrary as long as n^0 is large enough to

be in the outer region. Interestingly, the outer equation eq. (2.236) automatically satisfies the condition that derivative of net flux is zero, which is the continuous form of stationary solution. The simulation results shown in Figure 2.15 also exhibit this property. Our experience indicated that when $n > 75$, the void size distribution is in the outer region, where the cluster concentration is proportional to $n^{-1/3}$.

When the temperature is higher than the aggregation temperature ($T > T^*$) the void size distribution still agrees with the stationary solution with a moving 'front' (maximum cluster size with non-zero concentration). However the outer equation is still essential for two reasons. First, the quasi-equilibrium cluster concentration C_n^* increase exponentially for large n, so the stationary solution (2.262) can not be used for n larger than 10^3. Secondly, the velocity of the moving 'front' at large n must be determined from the outer equation. The general solution for $T > T^*$ is described below.
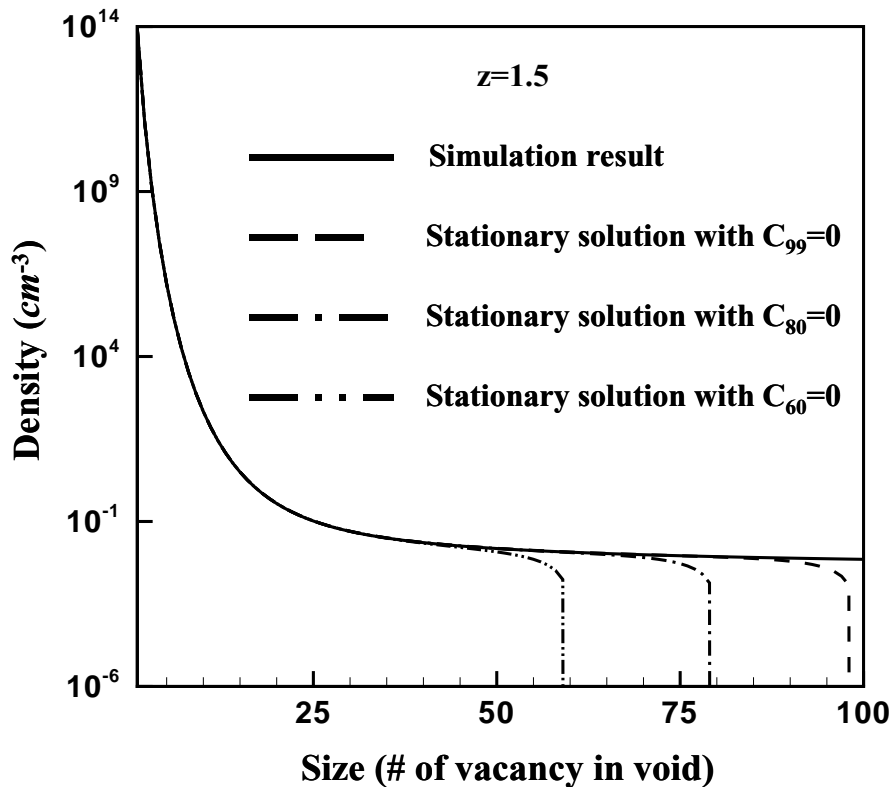
Figure 2.15: Stationary solutions for different maximum cluster size with non-zero concentration.

A general outer equation (2.233) with time varying boundary condition is

$$\frac{\partial f}{\partial t} = -L_{FP}(t)\frac{\partial}{\partial n}(n^{1/3}f) \tag{2.266}$$

with the boundary condition

$$f(n^0, t) = f^0(t) \quad for \quad t > t^0 \tag{2.267}$$

and initial condition

$$f(n, t^0) = 0 \quad for \quad n \geq n^0 \tag{2.268}$$

The problem (2.266) - (2.268) is solved by the method of characteristics to give

$$f = \begin{cases} f^0(t'(n, t))\left(\dfrac{n^0}{n}\right)^{1/3} & when \quad n^{2/3} < (n^0)^{2/3} + \dfrac{2}{3}\int_{t^0}^{t}L_{FP}(t)dt \\[4mm] 0 & when \quad n^{2/3} \geq (n^0)^{2/3} + \dfrac{2}{3}\int_{t^0}^{t}L_{FP}(t)dt \end{cases} \tag{2.269}$$

where $t'(n, t)$ is determined by

$$n^{2/3} = (n^0)^{2/3} + \frac{2}{3}\int_{t'}^{t}L_{FP}(t)dt \quad when \quad n^{2/3} < (n^0)^{2/3} + \frac{2}{3}\int_{t^0}^{t}L_{FP}(t)dt \tag{2.270}$$

The matching condition is applied between the inner equation (2.262) and outer equation (2.269) -(2.270). The value of the stationary flux is equal to the continuous form of the flux in the outer region at $n = n^0$

$$J_S(t) = L_{FP}(t)(n^0)^{1/3}f^0(t) \tag{2.271}$$

where $J_S(t)$ is determined from eq. (2.260) as

$$J_S(t) = \left(1 - \frac{f^0(t)}{C^*_{n^0}}\right)\left[\sum_{m=1}^{n^0-1} \frac{1}{g_m C^*_m}\right]^{-1} \tag{2.272}$$

When $n^0 > 100$, $C^*_{n^0}$ is large enough so that the second term in the first bracket can be ignored because the quasi-equilibrium cluster concentration C^*_n increases exponentially with n. Therefore $J_S(t)$ is explicitly calculated as

$$J_S(t) = \left[\sum_{m=1}^{n^0-1} \frac{1}{g_m C^*_m}\right]^{-1} \tag{2.273}$$

The total concentration of vacancies consumed by voids under a fix intermediate vacancy concentration C_V^{int} is obtained from eqs. (2.269) - (2.273) as the integral

$$C_V^{Total}(t) = \int_{n^0}^{\infty} nf\,dn = \int_{n^0}^{\left((n^0)^{2/3} + \frac{2}{3}\int_{t^0}^{t} L_{FP}(t)dt\right)^{3/2}} n\frac{J_S(t'(n,t))}{L_{FP}(t'(n,t))n^{1/3}}\,dn \tag{2.274}$$

Again for steady-state crystal growth, time t is related to the axial position z and pull rate by $z = Vt$. Hence $C_V^{Total}(t)$ monotonically increases with t (or z) and can be explicitly computed. The aggregation temperature is determined by the intersection of C_V^{Total} (under a fix intermediate vacancy concentration C_V^{int}) and the intermediate vacancy concentration, or $C_V^{Total}(t^a) = C_V^{int}$. We assume that the temperature at $t^a = z^a/V$ is the aggregation temperature. The total void concentration is evaluated at $t = t^a$ as

$$N_{Total} = \int_{n^0}^{\infty} f\,dn = \int_{n^0}^{\left((n^0)^{2/3} + \frac{2}{3}\int_{t^0}^{t^a} L_{FP}(t)dt\right)^{3/2}} \frac{J_S(t'(n,t))}{L_{FP}(t'(n,t))n^{1/3}}\,dn \tag{2.275}$$

and the average void size is calculated as

$$n_{avg} = \frac{C_V^{int}}{N_{total}} \tag{2.276}$$

Under the operating conditions used in the simulation shown in Figure 2.5, $C_V^{int} = 8.4 \times 10^{13} cm^{-3}$. Since vacancies are only consumed significantly by void formation in a narrow temperature range near the aggregation temperature, the value of L_{FP} described by eq. (2.249) doesn't change significantly near the aggregation temperature. In this case, the vacancy diffusivity D_V is evaluated at temperature $T(z = 1.7) = 1273 K$, and $L_{FP} = 276 \ s^{-1}$. With this constant L_{FP}, eqs. (2.274) and (2.275) are simplified to

$$C_V^{Total}(t) = \int_{n^0}^{\infty} nf dn = \int_{n^0}^{\infty} n \frac{\left((n^0)^{2/3} + \frac{2}{3}L_{FP}(t-t^0)\right)^{3/2} J_S\left(t - \frac{n^{2/3} - n_0^{2/3}}{2L_{FP}/3}\right)}{L_{FP} n^{1/3}} dn \qquad (2.277)$$

$$N_{Total}(t) = \int_{n^0}^{\infty} f dn = \int_{n^0}^{\infty} \frac{\left((n^0)^{2/3} + \frac{2}{3}L_{FP}(t-t^0)\right)^{3/2} J_S\left(t - \frac{n^{2/3} - n_0^{2/3}}{2L_{FP}/3}\right)}{L_{FP} n^{1/3}} dn \qquad (2.278)$$

It should be pointed out that the simplification above based on constant L_{FP} is not necessary, it just makes the calculation much simple. The calculations using eqs. (2.277) and (2.278) under the fix vacancy concentration C_V^{int} are listed in Table 2.2 and shown in Figure 2.16. At $z = 1.74$, C_V^{Total} is approximately equal to C_V^{int}, therefore the aggregation temperature is around $z = 1.74$ which agrees with the simulation results shown in Figure 2.5a and Figure 2.17. However, N_{Total} at $z = 1.74$ is $5.54 \times 10^6 cm^{-3}$ which is about one order-of-magnitude higher than the value of $6.89 \times 10^5 cm^{-3}$ from the simulation.

This difference is explained by the actual change of the vacancy concentration. The stationary flux J_S increases with monomer concentration, and near the aggregation temperature the vacancy concentration already decreases significantly by void formation. While in the calculation above the fix vacancy concentration is used, therefore it will overestimate total void concentration N_{Total}. The way to overcome this problem is to impose conservation of vacancy instead of the fix vacancy concentration.

Under the fix vacancy concentration C_V^{int}, we only need to calculate the cluster concentration $f(C_V^{int}, t)$ from eq. (2.269). With the conservation of vacancy, we must also calculate vacancy concentration from

$$\frac{dC_V}{dt} = -\frac{d}{dt}\int_{n^0}^{\infty} nf(C_V, t)dn \tag{2.279}$$

where $f(C_V, t)$ is determined by eq. (2.269). The conservation equation (2.279) can be also written as

$$C_V(t) + C_V^{Total}(t) = C_V^{int} \tag{2.280}$$

where

$$C_V^{Total}(t) = \int_{n^0}^{\infty} nf(C_V, t)dn \tag{2.281}$$

The results with the conservation of vacancy are listed in Table 2.2 and shown in Figure 2.17. The aggregation temperature is approximately $z = 1.74$ and the total vacancy concentration is $7.22 \times 10^5 cm^{-3}$. These results agree with the simulation results shown in Figure 2.5a and Figure 2.17. The average void size is estimated by eq. (2.276), as $n_{avg} = 1.16 \times 10^8 atoms$ which corresponds to a void of 164 nm in diameter. The theoretical prediction and simulation result of void size distribution also show reasonable agreement as shown in Figure 2.18. The evolution of void size distribution from $z = 1.76$ to $z = 1.8$ predicted by the theoretical analysis almost matches that from $z = 1.8$ to $z = 1.9$ predicted by the numerical simulations.

z	results under fix vacancy concentration C_V^{int}		results with the conservation of vacancy $(C_V + C_V^{Total} = C_V^{int})$	
	$C_V^{ToTal}(cm^{-3})$	$N_{Total}(cm^{-3})$	$C_V^{ToTal}(cm^{-3})$	$N_{Total}(cm^{-3})$
1.66	4.65E12	4.04E5	4.65E12	4.04E5
1.68	9.64E12	8.05E5	8.71E12	5.48E5
1.70	1.95E13	1.57E6	1.44E13	6.57E5
1.72	3.85E13	2.98E6	2.15E13	7.07E5
1.74	7.46E13	5.54E6	2.98E13	7.21E5
1.76	1.41E14	1.01E7	3.92E13	7.22E5
1.78	2.62E14	1.81E7	4.95E13	7.22E5
1.80	4.78E14	3.17E7	6.06E13	7.22E5

Table 2.2: Theoretical results of C_V^{Total} and N_{Total} with axial position z.
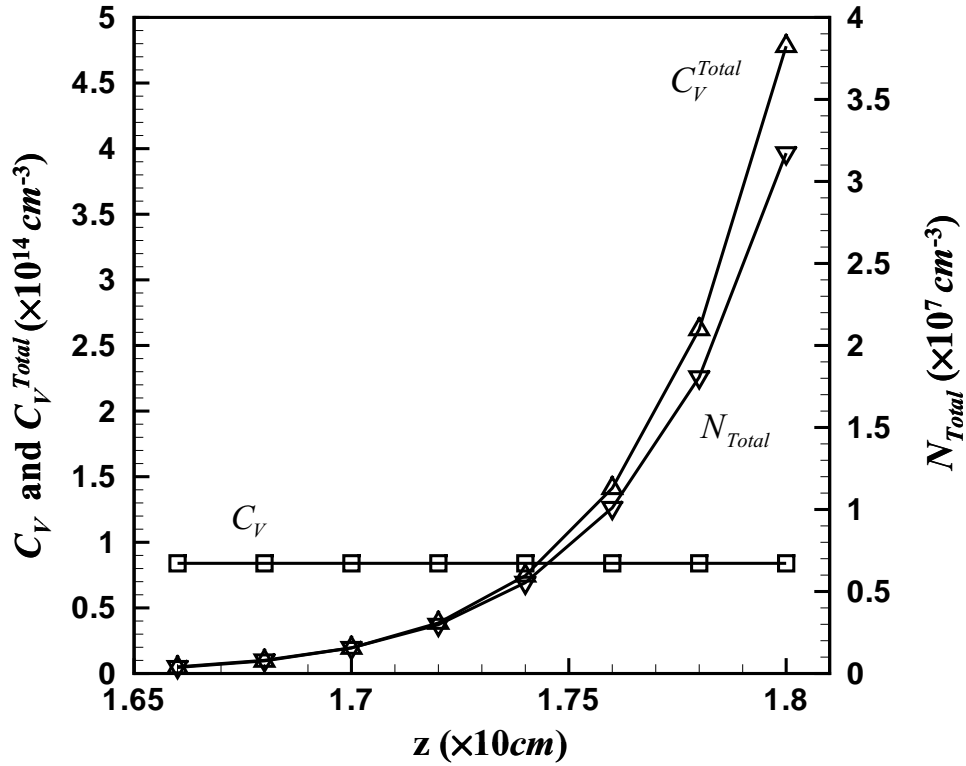
Figure 2.16: Theoretical results using fix vacancy concentration C_V^{int}.
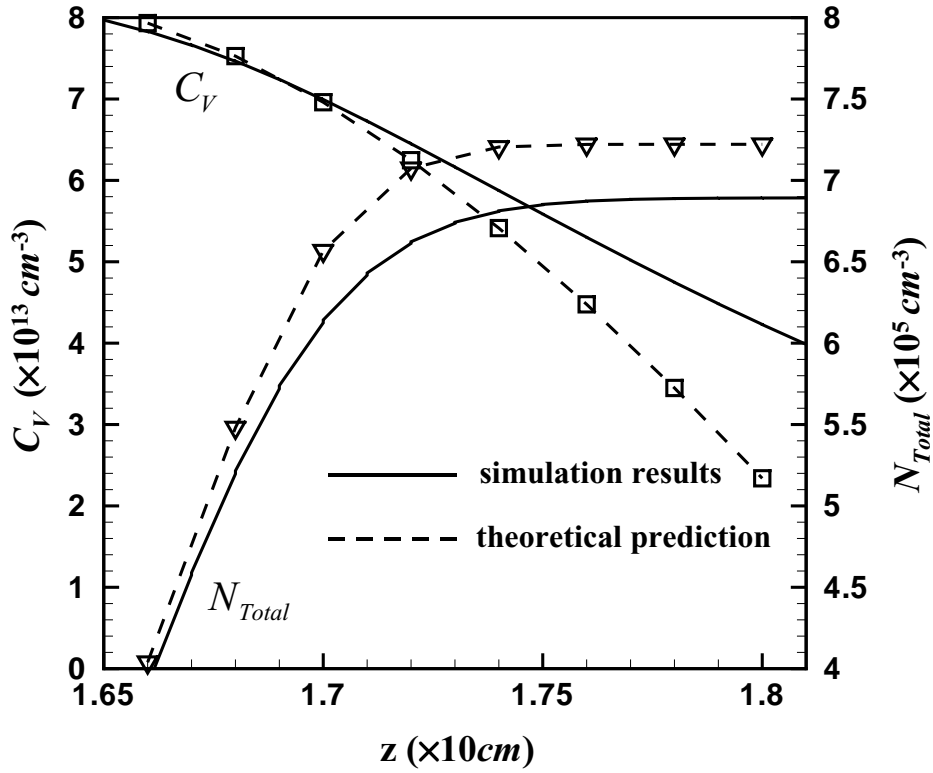
Figure 2.17: Theoretical results with the conservation of vacancy ($C_V + C_V^{Total} = C_V^{int}$) compared with simulation results (expansion from Figure 2.5a).
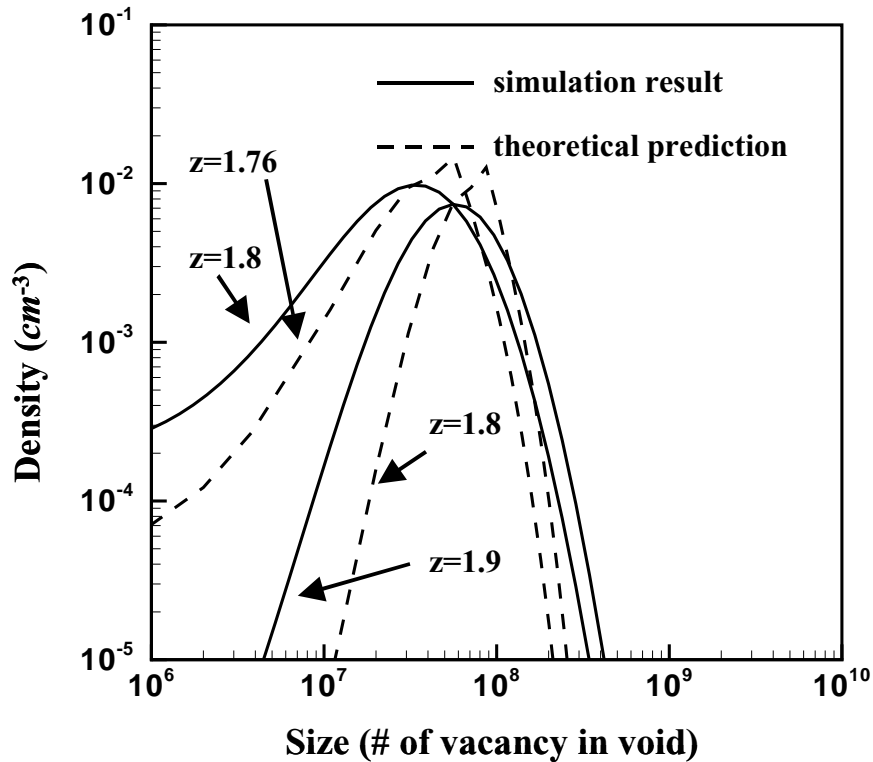
Figure 2.18: Theoretical prediction and simulation result of void size distribution.

2.5.4 Mobility of Vacancy dimer

As mentioned in the model description in Section 2.2.1, the physical model employed in this chapter is based on one important assumption that the clusters can only grow or dissolve by the addition or subtraction of monomer, and the mobility of any cluster is negligible. However it is found that small point defect clusters such as dimer may be mobile [11,71,92,125]. Both molecular dynamics simulations and experimental results give a migration energy of about $1.35 eV$ for vacancy dimer in silicon [71,125]. Pellegrino et al. reported that the maximum value of pre-exponential factor for the diffusivity of vacancy dimer is about $1 \times 10^{-1} cm^2/s$ [125]. All these demonstrate that vacancy dimer is mobile but with diffusivity smaller than vacancy diffusivity in the whole temperature range of the silicon crystal growth. Fortunately unless diffusivity of vacancy dimer is much higher than

vacancy diffusivity, the mobility of vacancy dimer essentially has no effect on the void formation and all the theoretical and simulation results in this Chapter are valid.

The theoretical analysis in section 2.5.1 shows that for small n it is in the region of inner equation where time dependent terms can be ignored. The solution is stationary solution which depends on equilibrium solution. Or put it precisely, the time needed to reach stationary state is very small (in order of second). So in the region for small n, it is really equilibrium or stationary state that matters, dynamics doesn't matter.

Considering mobility of vacancy dimers will only change the dynamics, but not equilibrium or stationary state. This can be proved by considering the concept of independent reactions. If the mobility of clusters is negligible, the cluster can only grow or dissolve by addition or subtraction of monomer. Therefore for the void formation, the first three reactions are

$$V + V \leftrightarrow V_2 \tag{2.282}$$

$$V_2 + V \leftrightarrow V_3 \tag{2.283}$$

$$V_3 + V \leftrightarrow V_4 \tag{2.284}$$

where V_2, V_3, and V_4 represent vacancy clusters with 2, 3, and 4 vacancies in it. Given the vacancy concentration and temperature, the stationary solutions of V_2, V_3, and V_4 can be determined. Another reaction has to be added in order to take the mobility of vacancy dimers into account. It is

$$V_2 + V_2 \leftrightarrow V_4 \tag{2.285}$$
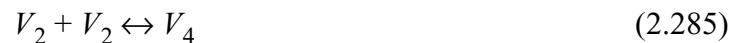
But this reaction is not an independent reaction of the first three reactions. In other words, reaction (2.285) = reaction (2.283) + reaction (2.284) - reaction (2.282). This means that considering reaction (2.285) will not change equilibrium or stationary state at all, it will only decrease the time needed to reach equilibrium or stationary state which is already so

small that only equilibrium or stationary state matters. Therefore the mobility of vacancy dimer will not change results for small n, and the boundary for the outer equation.

For big cluster, concentration of cluster size n-1 has the same order of magnitude or almost same with that of cluster size n because change of cluster concentration is at most five order of magnitude over big size change which is much more than 10^3. But concentration of vacancy is several order of magnitude higher than that of vacancy dimer. The growth rate is proportional to the concentration of cluster, the diffusivity and concentration of mobile species. So among the three reactions

$$V_n + V \leftrightarrow V_{n+1} \tag{2.286}$$

$$V_n + V_2 \leftrightarrow V_{n+2} \tag{2.287}$$

$$V_{n-1} + V_2 \leftrightarrow V_{n+1} \tag{2.288}$$

the first reaction definitely dominates and the effect of mobility of vacancy dimer is negligible unless the diffusivity of vacancy dimer is several order of magnitude higher than that of vacancy which is apparently not the case.

2.6 Conclusion

The void formation in Czochralski crystal growth is an extremely complex process. And the model for this process is also too complex to have analytical solutions. Numerical simulation is the only way to get the solutions. These numerical simulations can be considered as virtual experiments. Verified relations between operating conditions and model predictions can be used to reduce number of expensive experiments, and optimize operating conditions and system design. Another important aspect of numerical simulation is that it can help to get physical insight of the process, valid the appropriate assumptions and further develop theoretical analysis and useful scalings. This is the strategy of theoretical analysis in this chapter.

The asymptotic analysis on critical *V/G*, intermediate vacancy concentration, intermediate interstitial concentration, and effect of boron on critical *V/G* are performed first in the region close to the melt/crystal interface. The asymptotic analysis is based on two important characteristics - large *Da* and small ω - about the CZ silicon crystal growth. The large *Da* is due to the high recombination rate near the melt/crystal interface and leads to mass law for vacancies and interstitials. The small ω is due to the high activation energy for the equilibrium concentrations of native point defects and leads to a thin recombination layer near the melt/crystal interface and negligible radial contribution of diffusion.

At lower temperature or the region away from the melt/crystal interface, void formation is modeled by combination of discrete rate equation for small *n* and its continuous representation for big *n* with matching between them. The discrete rate equation can not be used alone because of computational difficulty. And its continuous representation can not be used alone because it is not accurate for small *n*. Fokker-Planck equation and Zeldovich equation are two different continuous approximations of the same rigorous discrete rate equation.

The analysis on various scales shows that for small *n*, the time-dependent term in the governing equation can be ignored and the corresponding equation is called inner equation. While for big *n*, the second order terms for *n* can be ignored and the corresponding equation is called outer equation. The discrete form of inner equation is employed since continuous form is not valid for small *n*. The inner equation is also called stationary solution because there is no time-dependent term. The outer equation has continuous form and it is basically a first order partial derivative equation. At matching point, both concentration and flux are matched. Interestingly, as long as matching point is in the outer region, the choice of matching point is arbitrary. The reason is the unique property of the outer

equation. The outer equation automatically satisfies the continuous form of inner equation or stationary solution. Actually the void size distribution is approximately stationary solution with a moving 'front' (maximum cluster size with non-zero concentration). However outer equation is still essential because of two reasons. First, the quasi-equilibrium cluster concentration used in the results of inner equation increases exponentially for big n, so practically the results of stationary solution can not be used for n more than a couple hundred. Second, the drift velocity of the moving 'front' is still needed to be determined by the outer equation.

Based on the analysis of the inner and outer equations with the appropriate model for growth rate and dissolution rate, two important scalings for total void concentration and average void size are obtained. Total void concentration is proportional to $\langle G \rangle^{3/2} (C_V^{int})^{-1/2}$ and the average void size is proportional to $(C_V^{int}/\langle G \rangle)^{3/2}$. The quantitative theoretical estimations of void aggregation temperature, total void concentration, and average void size also reasonably agree with the simulation results. Some important physical insights are also obtained. As discussed in section 2.4.1, for a homogenous nucleation without initial seeds, the real reason for the peak in the size distribution is the finite source of monomer.

It is worth to point out that the theoretical approach and the results in this chapter are rather general and relatively insensitive to the physical parameters chosen for the system. The same kind of results can be easily extended to the formation of interstitial cluster. It can be also extended to other system with different growth mechanism. For example, two important scalings in this chapter are direct results of $n^{1/3}$ dependence of drift velocity on cluster size which corresponds to the diffusion limited growth. For a system with surface reaction limited growth, the drift velocity is proportional to $n^{2/3}$. With the same deriva-

tion in this chapter, total cluster concentration is proportional to $\langle G \rangle^2 / C_1$ and the average cluster size is proportional to $(C_1 / \langle G \rangle)^2$.

Chapter 3

The Role of Oxygen

3.1 Overview

One important characteristic of CZ silicon is the high oxygen concentration in the crystal, which typically reaches concentrations of $O(10^{18})$ atoms/cm^3 compared to the solubility of oxygen in silicon at $650°C$ of 3.6×10^{15} atoms/cm^3. This super-saturation is the source of oxygen precipitation during crystal growth and subsequent processing of the wafer. The source of this oxygen is the dissolution of the quartz (SiO$_2$) crucible used to hold the melt in the CZ method. As described by the modeling of Kinney and Brown [91] and Lipchin and Brown [96,97] this oxygen is convected to the gas in the CZ chamber as SiO or incorporated into the crystal at the solidification interface. At the interface, oxygen typically is incorporated into the crystal as an interstitial impurity.

The history of the understanding of oxygen in silicon has been reviewed by Hu [68]. The interest in oxygen in silicon first appeared in the mid-1950's, and then almost disappeared by the end of the 1960's. Around 1970, it was found that the integrated circuits made out of the seed-end of CZ silicon crystals tended to have higher yield than those from tail-end of the crystal. It turned out that differences in oxygen concentration mainly contributed to this phenomena; it was known that oxygen had the highest concentration in the seed-end and lowest in the tail-end of the crystals of that day. The benefit of oxygen has two fold: oxygen atoms effectively suppressed dislocation generation and retarded dislocation motion, therefore resulting in high mechanical strength [163]. Also oxygen precipitates and associated stacking faults and dislocation loops, if confined well below the wafer surface region, could serve as effective gettering sites for metallic contaminants introduced during device fabrication [165]. Unfortunately oxygen precipitates also can

degrade the mechanical properties of the wafer since the dislocations are created during precipitation. Too much oxygen precipitates greatly reduces the strength of the wafer.

As a result the oxygen and oxygen precipitates in silicon wafers have to be well controlled both in space within the wafer and in total concentration. The density of oxygen precipitates has to be high enough to enhance gettering, while being not too high, in order to avoid degradation of the mechanical properties of the wafer. Oxygen precipitates also have to be confined to the middle of the wafer leaving a low defect surface region where devices can be fabricated.

One important feature of oxygen precipitates is the dependence of morphology of the precipitates on annealing temperature. Hu [67] gave a rough classification of the morphology in three temperature regimes. These precipitates are ribbon shaped below $800°C$, disk shaped between 800 and $1050°C$, and octahedral shape above $1050°C$. There may be considerable overlap in these three regimes. Bergholz [10] gave a more detail classification with five temperature regimes: ribbon shaped below $550°C$, a mixture of ribbon and disk shaped between 550 and $700°C$, disk shaped between 700 and $900°C$, octahedral shape between 900 and $1100°C$, polyhedral or nearly spherical shaped precipitates above $1100°C$. It should be emphasized that there is controversy on the identification of ribbon-shaped or rod-shaped oxygen precipitates. Bourret [13] identified these ribbon-shaped precipitates as hexagonal silicon. Roughly oxygen precipitates may take the shape of disk up to $900°C$, and be octahedral or spherically shaped above $900°C$. See Figure 3.1 for a pictorial representation of this data.
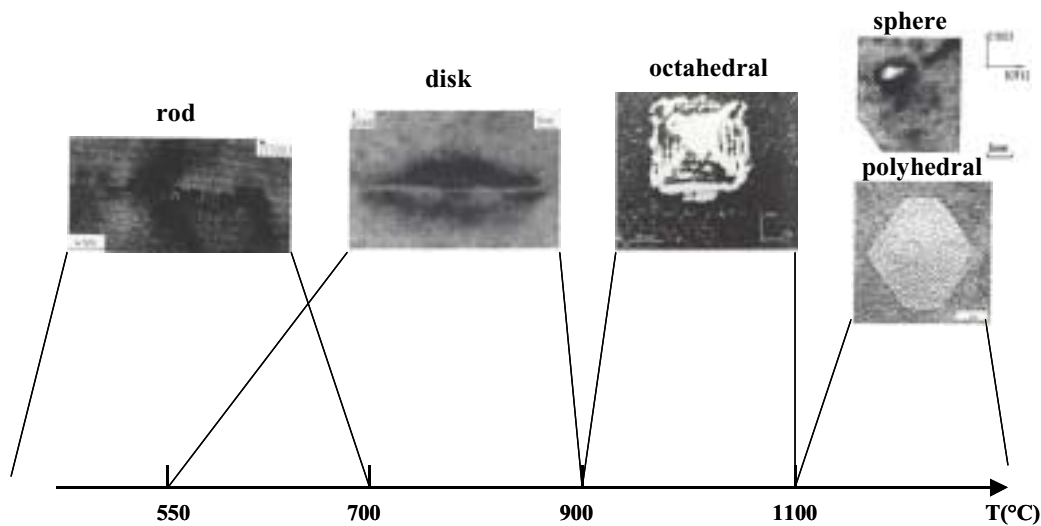
Figure 3.1: Morphology of oxygen precipitates under different nucleation temperature taken from [10].

The volume of solid SiO_2 is about two times that of silicon. This volume difference results in stress in the lattice and stress energy for oxygen precipitates. It was well known that stress energy or elastic energy is the largest for sphere and the smallest for disk [112] while surface energy is the smallest for sphere. The stress energy, surface energy, and total free energy of a spheroidal precipitate with a given volume as a function of the ratio between equatorial and polar diameters are schematically illustrated in Figure 3.2. Sin [149] formulated free boundary problem for the equilibrium shape of an individual misfitting precipitate. The shape of the precipitate is described by a Gibbs Thomson boundary condition that describes the relative contributions of elastic energy and surface energy in determining the equilibrium morphology of the precipitate. When elastic energy is the main contribution and the precipitate is elastically softer than the matrix, the equilibrium shape or energy minimizing shape is either a rod or a disk.
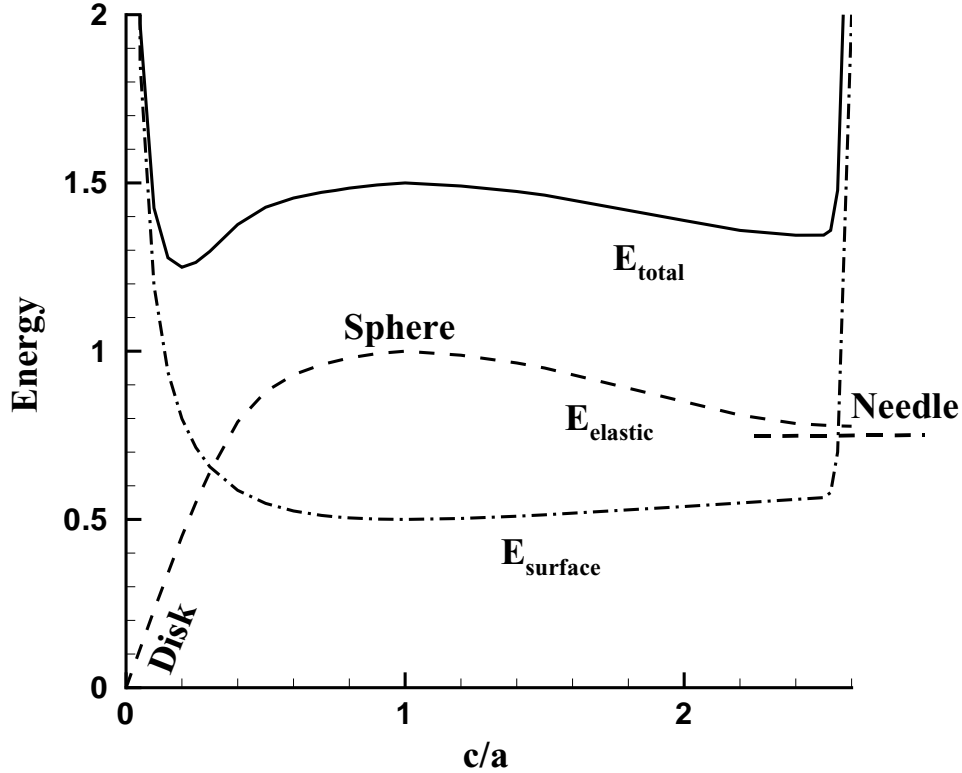
Figure 3.2: Elastic energy, surface energy, and total free energy of a spheroidal precipitate (elastic energy curve is taken from Nabarro [112]).

The free volume needed to release the stress energy of oxygen precipitates could be provided by either vacancy absorption into the precipitate or interstitial ejection. However, unless there exists a pre-existing high vacancy concentration in the silicon, vacancy absorption is not an option simply because there are not enough vacancies. As will be discussed in details in Section 3.5.3, because of the low self-diffusion (the product of diffusivity and equilibrium concentration, $D_I C_I^{eq}$) of interstitials at low temperature, both diffusion of interstitials to the wafer surface and removal of interstitials by the formation of stacking faults or dislocation loops are ineffective to remove the interstitials ejected by oxygen precipitates. In a word, the stress energy of oxygen precipitates normally can not be released through interactions with native point defects at low temperature. Therefore

during low temperature annealing the stress energy plays an important role and the oxygen precipitates are likely to take shapes that have low stress energy, or disk shaped with negligible emission of interstitials. This explanation is supported by experimental observations of strain contrast surrounding disk-shaped oxygen precipitates at low temperature [68]. Only during high temperature annealing can the stress energy be released through interactions with native point defects, and oxygen precipitates may take low surface energy shape - polyhedral or spherical shape. A high-resolution lattice image (Figure 1.7b) of a polyhedral oxygen precipitate produced after annealing for 64 hours at $1175°C$ shows no visible strain contrast.

For some special wafer annealing processes such as MDZ (Magic Denuded Zone) discussed in Section 1.2, the concentration of vacancies established after the first rapid thermal treatment is so high that the stress energy of oxide nuclei created at low temperatures can be released by vacancy incorporation. Oxide nucleation through vacancy absorption occurs quickly because it has lower energy barrier. The stress energy is low because of free volume provided by vacancies, and the configurational free energy also is low because of high super-saturation of vacancies. The details of the free energy of formation for oxygen precipitates with different morphology will be discussed in Section 3.5.

3.2 Literature Review on Modeling of Oxygen Precipitation

Oxygen and oxygen precipitates in silicon crystal are so technologically important that much effort have been devoted to their understanding. Kashchiew [84] wrote an excellent book on the nucleation theory in general which is already referred several times in Chapter 2. Schrems [138] summarized a variety of physical models applied in the simulation of oxygen precipitation. All phenomenological models fall into four categories which are listed in Table 3.1.

Models	Researchers	Capabilities	Limitations
I: Classical nucleation model	Kashchiev [84], Freeland [43], Inoue [74], Voronkov [185].	nucleation flux and total oxide density	no conservation for oxygen and no size information
II: Growth law	Ham [52,53], Hu [66,67], Wada [189,190], Sueoka [159], Vanhellemont [176].	growth rate of individual oxide particles	no conservation for oxygen and no total density information
III: Combination of model I and model II	Usami [173], Yang [204], Isomae [76].	nucleation flux, growth rate of oxide, and conservation for oxygen	no dissolution of oxides and no evolution of size distribution
IV: Model based on rate equations	Schrems [135,136,137,138], Esfandyari [33,34], Kelton [87], Wei [196], Sueoka [162].	evolution of size distribution	much more computational time

Table 3.1: Four types of phenomenological models for oxygen precipitation.

In the so-called classical nucleation model, only the stationary rate of nucleation is calculated. The exact form of stationary rate of nucleation is already described in Section 2.5.3. A simpler and physically more revealing form with reasonable approximation can be written as [84]

$$J_0 = Zg^* C^*$$

(3.1)

where g^* is frequency of monomer attachment for cluster of critical size, C^* is the equilibrium concentration for cluster of critical size n^*, and Z is the Zeldovich factor. The critical size is defined as the size which satisfies $dG(n)/dn = 0$ where $G(n)$ is the Gibbs

free energy of formation for cluster size n. The Zeldovich factor is given by [84]

$$Z = \frac{2\beta}{\pi^{1/2}\{1 - erf[\beta(1 - n^*)]\}} \qquad (3.2)$$

where β captures the curvature of the $G(n)$ at $n = n^*$

$$\beta = \left(-\frac{d^2G}{dn^2}\bigg|_{n = n^*} / (2kT)\right)^{1/2} \qquad (3.3)$$

Even though the Zeldovich factor can be theoretically determined, it was treated as a fitting parameter by many researchers [74,76,173,204]. Inoue et al. obtained $Z = 0.2$ by fitting experimental nucleation rate [74].

Under the conditions of constant temperature and super-saturation in the system, the total cluster density may be determined by eq. (3.1) with reasonable accuracy. However, the stationary rate of nucleation is very sensitive to monomer concentration or super-saturation, and with eq. (3.1) alone mass balance can not be done to calculate the monomer change. Therefore eq. (3.1) can not be used alone to get total cluster concentration for the system with changing super-saturations.

One important assumption for stationary nucleation flux described in eq. (3.1) is that the stationary size distribution is already established beyond the critical size n^*. However a considerable time maybe needed to reach this state, especially for oxygen precipitation because of low diffusivity of oxygen. Practically this effect on the nucleation rate can be modeled by introducing an exponential term in nucleation time [74]

$$J = J_0 \exp(-\tau / t) \qquad (3.4)$$

where J is the nucleation rate, J_0 is the stationary nucleation rate determined by eq. (3.1), t is the nucleation time, and the induction time τ is a constant which is given by

$$\tau = \frac{(n^*)^2}{g^*} \tag{3.5}$$

The value of the induction time experimentally obtained by fitting oxygen nucleation rate is about two orders-of-magnitude higher than the prediction by eq. (3.5) [74]. This is another indication that the classical nucleation model is not a rigorous approach to model oxygen precipitation.

Another model is the deterministic growth model which is also called the growth law. The growth law is obtained by solving diffusion equation for a single precipitate within the surrounding media. Ham's theory of diffusion-limited precipitation belongs to this category [52,53]. Wada et al. reported that the growth rate of platelet oxygen precipitate followed a 3/4 power law in time [189] and later provided a rigorous calculation for diffusion-limited growth of a disk with constant thickness to verify their experimental observation [190]. The experimental results by Sueoka et al. [159] showed a 1/2 power law for the growth of disk-shaped oxide. Sueoka et al. [159] and Vanhellemont [176] theoretically proved that diffusion-limited growth of a disk with constant aspect ratio follows a 1/2 power law. The growth law for disk-shaped oxide greatly depends on the growth conditions. Hu [66,67] derived a 2/3 power law for a disk with changing thickness and changing aspect ratio which is determined by minimizing total energy. Vanhellemont [176] summarized the experimental results by many researchers on the growth rate of oxide. However, as Sin [149] pointed out, an unambiguous growth law for oxide is impossible due to the scatter in the experimental data.

With the knowledge of monomer concentration, the growth law can provide the information about the change of precipitate size with time. However the total cluster density can not be determined by this growth law. And like the classical nucleation model, the growth law alone can not be used to calculate monomer change by mass balance.

Fortunately the two models above have deficiencies which complement each other. A combination of the classical nucleation model and the growth law together with mass balances can provide the change of the total cluster density, cluster size and monomer concentration with time. Many researchers [76,173,204] employed this approach and gave reasonable predictions for certain set of experimental data. However the dissolution of cluster is not taken into account in this combined model. Therefore this description can not explain the Ostwald ripening where large clusters grow at the expense of the dissolution of smaller clusters [6].

A major deficiency of the models discussed above is the lack of the evolution of size distribution of oxygen precipitates. Therefore some important factors such as the ramping process, especially between the nucleation step and the growth step, can not be captured by these models. A much more rigorous approach is to solve the rate equations (for example, discrete rate equations for small clusters and Fokker-Planck equations for big clusters) together with conservations of monomers, which are discussed in Section 2.4.1 and 3.3.1 [108,150,152]. This kind of models are capable to simulate the evolution of the oxide size distribution.

Schrems, Esfandyari, and their coworkers applied this framework to spherical oxygen precipitation together with formation of stacking faults as sinks for interstitials ejected by spherical oxygen precipitates to release stress energy [33,34,135,136,137,138]. However, no stacking faults were formed in their simulation especially during the low temperature annealing [33], which implies that any interstitial ejected by spherical oxygen precipitates could not be removed. The configurational free energy due to interstitial ejection for the growth of oxygen precipitates is $kT\ln(C_I/C_I^{eq})$ where C_I and C_I^{eq} are concentration and equilibrium concentration of interstitial (for example, $C_I^{eq}(650°C) = 1. \times 10^5 cm^{-3}$). This means that unless the ejected interstitials could be removed to maintain low intersti-

tial super-saturation in the bulk, interstitial ejection is not energetically favorable. Therefore in these simulations the high stress energy of spherical oxygen precipitates could not be released efficiently through the interactions with native point defects and it would be very difficult for spherical oxides to nuclear during low temperature annealing.

Kelton et al. [87,196] used the similar approach to spherical oxygen precipitation. In their model, discrete rate equations are used for small clusters and a growth model is used for big clusters, the matching point is about two or three times critical size. They also introduced a couple-flux model for nucleation that links the interfacial and long-range diffusive fluxes. However, there is no interaction between oxide formation and point defects, and the stress energy is assumed to be fully released at no expense.

Sueoka et al. [162] also applied the rate equations to the formation of oblate spheroidal oxides. They assumed equilibrium size distribution for oxides smaller than the critical size, and used Fokker-Planck equations for clusters bigger than the critical size. However, as discussed in Section 2.5, the size distribution for small clusters is stationary rather than equilibrium. And the stationary size distribution is different from the equilibrium size distribution [84]. Moreover, a complicate temperature dependent parameter (different exponential functions of temperature in four temperature ranges) was introduced to fit experimental data. And the physics of this fitting parameter was not discussed.

In this Chapter, a basic comprehensive framework for modeling of oxygen precipitation is proposed. This framework is self-consistent and the key elements include vacancy absorption, interstitial ejection, diffusion-limited reaction and free energy of formation for different morphologies of the oxygen precipitates. The model captures the right physics and simulation results reasonably agree with a variety of experimental data.

3.3 Governing Equations and Boundary Conditions

3.3.1 Governing Equations

The stress energy associated with oxygen precipitations could be released by either vacancy absorption or interstitial ejection. A general model for oxygen precipitation in silicon should include vacancies, interstitials, oxygen and the dynamics to form their clusters. Like the governing equations for native point defects and their clusters in Section 2.4.1, the first set of equations are equations for vacancy, interstitial and oxygen concentration, respectively. These are written as

$$\left(\frac{\partial}{\partial t} + V\frac{\partial}{\partial z}\right)C_I + \nabla \bullet (-D_I(T)\nabla C_I) + k_{IV}(T)(C_I C_V - C_I^{eq}(T)C_V^{eq}(T))$$

$$+ \left(\frac{\partial}{\partial t} + V\frac{\partial}{\partial z}\right)\int_2^\infty n(f_I - \gamma_I f_O)dn = 0 \tag{3.6}$$

$$\left(\frac{\partial}{\partial t} + V\frac{\partial}{\partial z}\right)C_V + \nabla \bullet (-D_V(T)\nabla C_V) + k_{IV}(T)(C_I C_V - C_I^{eq}(T)C_V^{eq}(T))$$

$$+ \left(\frac{\partial}{\partial t} + V\frac{\partial}{\partial z}\right)\int_2^\infty n(f_V + \gamma_V f_O)dn = 0 \tag{3.7}$$

$$\left(\frac{\partial}{\partial t} + V\frac{\partial}{\partial z}\right)C_O + \nabla \bullet (-D_O(T)\nabla C_O) + \left(\frac{\partial}{\partial t} + V\frac{\partial}{\partial z}\right)\int_2^\infty n f_O dn = 0 \tag{3.8}$$

where V is crystal pulling rate when applied to crystal growth and equal to zero when applied to wafer annealing, (D, C, C^{eq}, f) are the (diffusivity, concentration, equilibrium concentration, cluster concentration), subscripts (I, V, O) represent (self-interstitial, vacancy, oxygen), k_{IV} is the recombination rate, and n is the size of the clusters. A special case in this model is the steady-state analysis for crystal growth where point defects concentrations don't change with time. The third term describes Fick diffusion term. The fourth term in eqs. (3.6) and (3.7) describes the recombination of vacancies and interstitials. The last two terms are the source or sink terms for vacancy, interstitial and oxygen due to cluster formations. The coefficients γ_I and γ_V are for interstitials ejected and

vacancies absorbed by oxygen precipitates. The calculation of γ_I and γ_V is discussed in Section 3.5.

The second set of equations are the discrete rate equations for small voids, interstitial clusters and oxygen precipitates from dimer to cluster of size $n_{match} - 1$. These equations are

$$\left(\frac{\partial}{\partial t} + V\frac{\partial}{\partial z}\right)C_{n,I} = J_{n,I} - J_{n+1,I}, \qquad n = 2, \dots n_{match} - 1 \qquad (3.9)$$

$$\left(\frac{\partial}{\partial t} + V\frac{\partial}{\partial z}\right)C_{n,V} = J_{n,V} - J_{n+1,V}, \qquad n = 2, \dots n_{match} - 1 \qquad (3.10)$$

$$\left(\frac{\partial}{\partial t} + V\frac{\partial}{\partial z}\right)C_{n,O} = J_{n,O} - J_{n+1,O}, \qquad n = 2, \dots n_{match} - 1 \qquad (3.11)$$

where the fluxes $J_{n,I}$, $J_{n,V}$ and $J_{n,V}$ are defined as

$$J_{n,X} = g_X(n-1)C_{n-1,X} - d_X(n)C_{n,X}, \qquad X = I, V, O \qquad (3.12)$$

where C_n is the concentration of size n cluster, g is the growth rate, and d is the dissolution rate. The first two terms in eqs. (3.9) - (3.11) describe changes in cluster concentration, and the other terms are net reaction rates to form the clusters. All clusters are assumed to be immobile so that cluster diffusion is neglected. The net flux from cluster of size n-1 to size n is J_n, so the net reaction rate to form the cluster is the difference between J_n and J_{n+1}. The discrete cluster concentration C_n describes cluster of size 2 to $n_{match} - 1$. The term C_n is used to replace continuous cluster concentration f in the integrals in eqs. (3.6) - (3.8).

The last set of equations are Fokker-Planck equations for clusters of $n > n_{match}$. These equations are

$$\left(\frac{\partial}{\partial t} + V\frac{\partial}{\partial z}\right)f_I = -\frac{\partial}{\partial n}\left(A_I(n)f_I - B_I(n)\frac{\partial f_I}{\partial n}\right) \tag{3.13}$$

$$\left(\frac{\partial}{\partial t} + V\frac{\partial}{\partial z}\right)f_V = -\frac{\partial}{\partial n}\left(A_V(n)f_V - B_V(n)\frac{\partial f_V}{\partial n}\right) \tag{3.14}$$

$$\left(\frac{\partial}{\partial t} + V\frac{\partial}{\partial z}\right)f_O = -\frac{\partial}{\partial n}\left(A_O(n)f_O - B_O(n)\frac{\partial f_O}{\partial n}\right) \tag{3.15}$$

where A and B are the drift velocity and diffusion coefficient respectively [84], and are defined as

$$A_X(n) = g_X(n) - d_X(n) - \frac{\partial}{\partial n}B_X(n), \qquad X = I, V, O \tag{3.16}$$

$$B_X(n) = \frac{1}{2}(g_X(n) + d_X(n)), \qquad X = I, V, O \tag{3.17}$$

The Fokker-Planck equation is a Taylor expansion of the discrete rate equation. The details about why the Fokker-Planck equations are used for large clusters and how to get the Fokker-Planck equation from the discrete rate equation are discussed in Sections 2.2.1 and 2.2.3.

The growth rate g and dissolution rate d for voids and interstitial clusters are already discussed in Section 2.4.1. The growth rate and dissolution rate for oxygen precipitates will be discussed in Section 3.4 and 3.5.

The parameters for interstitial, vacancy and their clusters are listed from eqs. (2.30) through (2.34). The oxygen equilibrium concentration in silicon crystal is taken from [167].

$$C_O^{eq} = 1.53 \times 10^{21} \exp\left(-\frac{1.03\,eV}{kT}\right) \ cm^{-3} \tag{3.18}$$

The oxygen diffusivity at high temperatures ($T > 750°C$) is taken from [24] as

$$D_O = 0.23 \exp\left(-\frac{2.56\,eV}{kT}\right) \; cm^2/s \qquad (3.19)$$

However it is commonly believed [115] that the effective oxygen diffusivity at low temperature is much higher than the values predicted by eq. (3.19). Many aspects of oxygen diffusion have been discussed in a general review paper by Newman et al. [115]. The enhancement of oxygen diffusion at low temperature could involve interactions of oxygen atom with other species which may be point defects, metallic impurity such as copper and iron, nonmetallic impurity such as carbon and nitrogen, and even a second oxygen atom. Although the mechanism of the faster oxygen diffusion at low temperature is still not clear, it has been established by various experiments that the effective activation energy of oxygen diffusion for $T < 750°C$ is 1.55 eV versus the value of 2.56 eV in eq. (3.19) [139]. The oxygen diffusivity for $T < 750°C$ is taken from [139] as

$$D_O = 2.16 \times 10^{-6} \exp\left(-\frac{1.55\,eV}{kT}\right) \; cm^2/s \qquad (3.20)$$

The oxygen diffusivity as a function of temperature is shown in Figure 3.3. The solid line with a kink around $750°C$ represents the effective oxygen diffusivity employed in this Chapter.
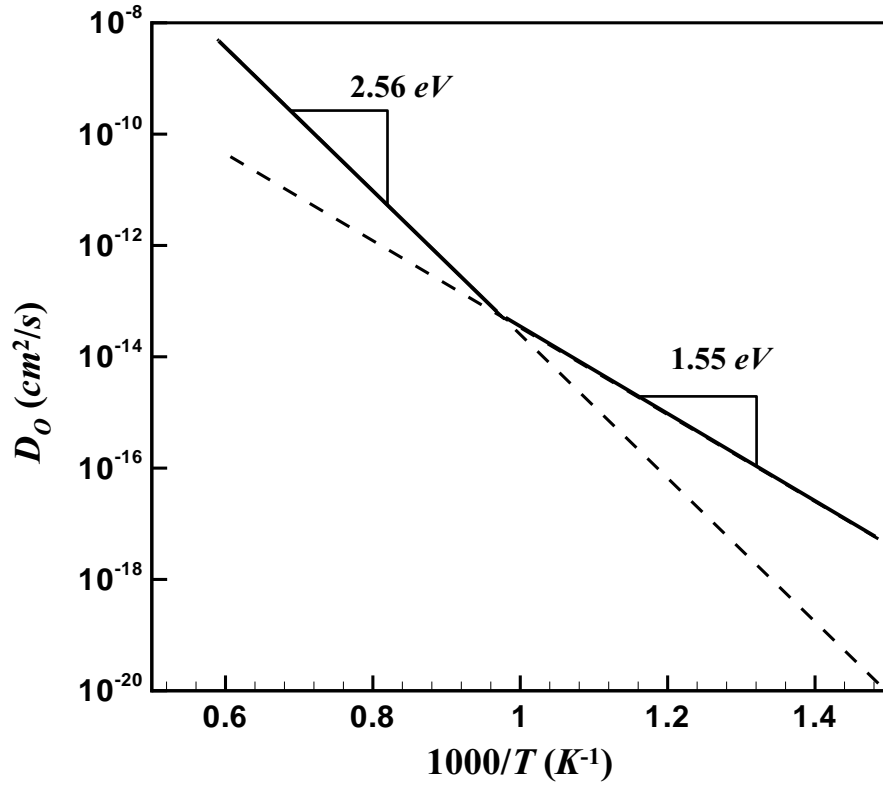
Figure 3.3: The oxygen diffusivity as a function of temperature.

Theoretically the temperature dependence of the surface energy is a direct result of the excess interfacial entropy [158]. For the melt/crystal interface, the surface energy increases with temperature for both mercury and gallium [158]. Fitting oxygen precipitation data in silicon to the model for classical homogeneous nucleation also has predicted the temperature dependence of surface energy σ [34,196]. In this Chapter, the surface energy of oxygen precipitates is chosen as

$$\sigma = 0.51 + 3 \times 10^{-4}(T - 873K) \quad J/m^2 \tag{3.21}$$

which gaves $0.465 J/m^2 \leq \sigma \leq 0.66 J/m^2$ for $450°C \leq T \leq 1100°C$.

3.3.2 Boundary Conditions for CZ Crystal Growth

For one-dimensional simulations along the pulling direction of CZ crystal growth in this Chapter, Dirichlet boundary conditions are used at the melt/crystal interface for all point defects, oxygen, and clusters, and no-flux boundary conditions are used on the top of crystal for all point defects and oxygen. The concentrations of vacancies and interstitials at the melt/crystal interface are set to equilibrium concentrations at the melt temperature while the oxygen concentration at the melt/crystal interface is a constant which is dependent on oxygen transport in the melt. At the melt/crystal interface, the concentrations of all clusters are set to zero.

3.3.3 Boundary Conditions for Wafer Annealing

The governing equations (3.6) - (3.17) are rather general and they also can be used for wafer annealing simply by setting $V = 0$. The one-dimensional simulations for wafer annealing in this Chapter is from the surface to the centerline and along the axial direction of the wafer. No-flux boundary conditions are used for all point defects and oxygen at the center of the wafer due to symmetry.

Dirichlet boundary condition with equilibrium oxygen concentration at the annealing temperature is used for oxygen on the wafer surface. As discussed in Section 1.2, there are two mechanisms for oxygen out-diffusion to the wafer surface. One is the out-diffusion due to evaporation of oxygen at the wafer surface and the other is a very thin surface oxide layer serving as sink for oxygen in the bulk. Dirichlet boundary condition for oxygen at the wafer surface is valid for both cases.

A silicon dioxide layer is so easy to form on the wafer surface that even at room temperature a very thin (about $25 \, \overset{\circ}{A}$) layer of oxide called native oxide layer can formed on the wafer surface when it is exposed to oxidative environment [18]. Because of this thin oxide layer and also the finite surface recombination rate at the annealing temperature

which is much lower than the melting temperature, Robin boundary conditions are appropriate for vacancies and interstitials on the wafer surface. Many researchers [51,129,130,168] experimentally investigate the surface recombination rate and gave different values for k/D where k and D are surface reaction rate and diffusivity of point defect. Robin boundary conditions for vacancies and interstitials on the wafer surface in this Chapter are

$$D\vec{n} \cdot \nabla C - k(C - C^{eq}) = 0 \quad at \ \ wafer \ \ surface \tag{3.22}$$

where

$$k/D = 500 \ \ cm^{-1} \ for \ \ both \ \ I \ \ and \ \ V \tag{3.23}$$

the value of k/D here is within the range of values in the literature [51,129,130,168].

Generally the initial conditions for wafer annealing are taken from the results of CZ crystal growth. However if we only focus on the oxygen precipitates during wafer annealing and there is no significant oxygen precipitates formed during crystal growth, we may choose zero concentrations for oxygen precipitates as initial conditions.

All the numerical methods used to solve the governing equations above will be discussed in Section 3.6.

3.4 Mesoscopic Growth Models

3.4.1 General Framework for Mesoscopic Growth Model

The diffusion-limited growth rate g and dissolution rate d are two important factors in the governing equations (3.9) - (3.17). These factors are determined by mass balances around an individual microdefect. Consider a microdefect of arbitrary shape that grows by diffusion of a monomer from bulk silicon to the precipitate, as shown in Figure 3.4. Monomer maybe vacancies, interstitials, and oxygen.
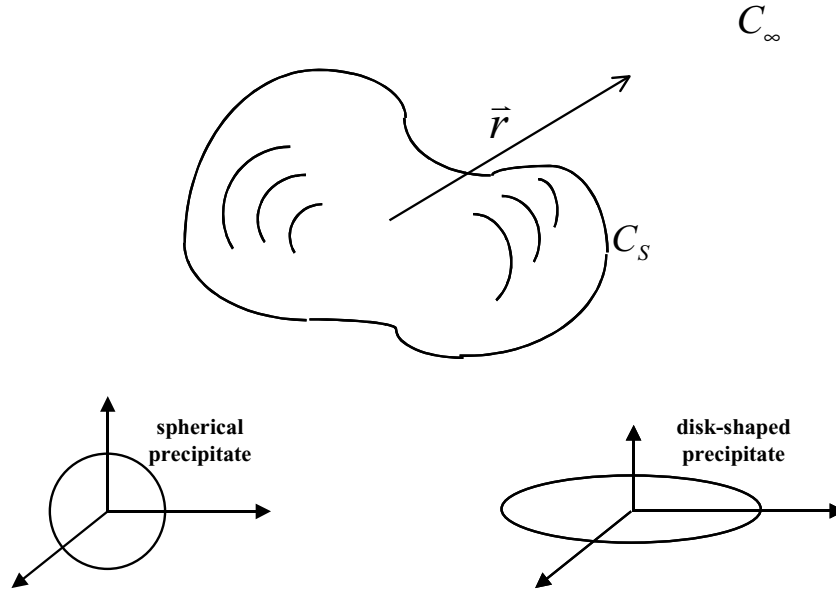
Figure 3.4: Coordinate system for arbitrary shape particle.

The monomer concentration $C(\vec{r})$ in the bulk is governed by the species conservation equation

$$\nabla^2 C = 0 \tag{3.24}$$

where $\vec{r}$ is a position vector measured from the center of the precipitate. Equation (3.24) is solved with the boundary conditions

$$C \to C_\infty \quad as \quad |\vec{r}| \to \infty \tag{3.25}$$

$$C = C_S \quad at \quad \vec{r} = \vec{r}_S \tag{3.26}$$

where C_∞ is the bulk monomer concentration, and $\vec{r}_S$ defines the surface of the precipitate where the concentration is C_S. The surface monomer concentration C_S is determined by a mass balance at the surface of the precipitate as

$$F(n) = g(n) - d(n) \tag{3.27}$$

where $F = F(n)$ is the monomer diffusion flux which is obtained by solving eq. (3.24)

with the boundary conditions (3.25) and (3.26). The growth rate $g(n)$ and dissolution rate $d(n)$ are

$$g(n) = k_r(n)C_S \tag{3.28}$$

$$d(n) = k_r(n)C^{eq}(n) \tag{3.29}$$

where $k_r(n)$ is defect surface reaction rate and $C^{eq}(n)$ is the monomer equilibrium concentration for the precipitate of size n. The equilibrium concentration $C^{eq}(n)$ is related to bulk monomer equilibrium concentration C^{eq} by [138]

$$C^{eq}(n) = C^{eq}\exp\left(\frac{\Delta G^f_{n \to n+1}}{kT}\right) \tag{3.30}$$

where G^f is the non-configurational part of the free energy of formation for a microdefect. This free energy includes surface energy and stress energy. The physical picture for the surface reaction rate is clear by examining the growth of a precipitate. Precipitate is assumed to grow through the 'jump' of monomer within the interfacial layer into the precipitate. Therefore the surface reaction rate is proportional to the number of jump attempts. And the reaction rate $k_r(n)$ is determined by jump rate theory as [138].

$$k_r(n) = V^i\frac{D}{\delta^2}\exp\left(-\frac{\Delta G_{n \to n+1}}{kT}\right) \tag{3.31}$$

where V^i is the volume of the interfacial layer, D/δ^2 is the attachment frequency, D is the monomer diffusivity, δ is the thickness of the interfacial layer which is in the order of the lattice spacing (approximately 0.235 nm), and G is the total free energy of formation for a microdefect.

The formulations above for the growth rate and dissolution rate are general for any defect shape. As already discussed in Section 3.1, a critical feature of oxygen precipitates is the dependence of morphology on the annealing temperature. The effect of precipitate

147

morphology is investigated by modeling the evolution of spherical and disk-shaped precipitates. The elastic energy is the lowest for the disk-shaped and the highest for the spherical precipitate. While the spherical precipitate has the lowest surface energy. The growth models for spherical and disk-shaped precipitates are discussed in the following two sections.

3.4.2 Growth Model for Spherical Precipitate

For spherical defects, eq. (3.24) and the boundary conditions become

$$\frac{\partial}{\partial r}\left(r^2\frac{\partial C}{\partial r}\right) = 0 \tag{3.32}$$

with boundary conditions

$$C(r=\infty) = C_\infty \tag{3.33}$$

$$C(r=r_n) = C_S \tag{3.34}$$

The solution of eqs. (3.32) - (3.34) is

$$C(r) = C_\infty + \frac{r_n(C_S - C_\infty)}{r} \tag{3.35}$$

The monomer diffusion flux at the surface of this spherical defect is therefore

$$F(n) = 4\pi r_n^2 D\frac{\partial C}{\partial r}\bigg|_{r=r_n} = 4\pi r_n D(C_\infty - C_S) \tag{3.36}$$

Substituting eqs. (3.28), (3.29) and (3.36) into eq. (3.27) gives

$$C_S = \frac{k_r(n)C^{eq}(n) + k_d(n)C_\infty}{k_r(n) + k_d(n)} \tag{3.37}$$

where

$$k_d = 4\pi r_n D \tag{3.38}$$

With eq. (3.37) the growth rate and dissolution rate for spherical defect can be determined by eqs. (3.28) and (3.29). The volume of the interfacial layer V^i in eq. (3.31) for spherical defect is $4\pi r_n^2 \delta$.

3.4.3 Growth Model for Disk-shaped Precipitate

For a disk-shaped defect, oblate spheroidal coordinates have to be employed to solve eq. (3.24) with boundary conditions (3.25) and (3.26) [110]. The oblate spheroidal coordinates are shown in Figure 3.4.
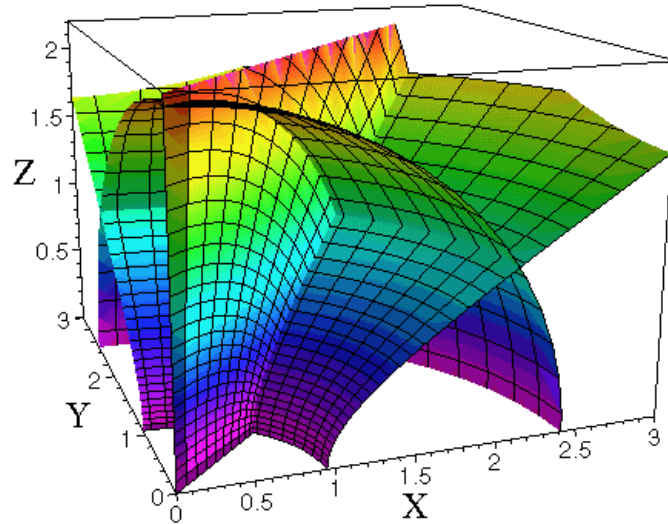

Figure 3.5: Oblate spheroidal coordinates (three surfaces for constant ξ, η, and ϕ are shown).

The relationships between rectangular (*x, y, z*) and oblate spheroidal (ξ, η, ϕ) coordinates are [110]

$$z = r_n \xi \eta \tag{3.39}$$

$$x = r_n \sqrt{(\xi^2 + 1)(1 - \eta^2)} \cos\phi \tag{3.40}$$

$$y = r_n \sqrt{(\xi^2 + 1)(1 - \eta^2)} \sin\phi \tag{3.41}$$

where $0 \le \xi \le \infty$ and $-1 \le \eta \le +1$. The surface $\xi = 0$ is a oblate disk of radius r_n. In oblate spheroidal coordinates

$$\nabla^2 C = \frac{1}{r_n(\xi^2 + \eta^2)} \left[\frac{\partial}{\partial\xi}\left((\xi^2 + 1)\frac{\partial C}{\partial\xi}\right) + \frac{\partial}{\partial\eta}\left((1 - \eta^2)\frac{\partial C}{\partial\eta}\right) + \frac{\xi^2 + \eta^2}{(\xi^2 + 1)(1 - \eta^2)}\frac{\partial^2 C}{\partial\phi^2} \right] \tag{3.42}$$

The solution of eq. (3.24) with boundary conditions (3.25) and (3.26) for a disk-shaped defect in oblate spheroidal coordinates is simply.

$$C(\xi) = C_\infty + \frac{2(C_S - C_\infty)}{\pi} \operatorname{atan}\left(\frac{1}{\xi}\right) \tag{3.43}$$

The monomer diffusion flux at the surface of a disk-shaped defect with radius r_n is

$$F(n) = 2\int_0^{r_n} D\frac{\partial C}{\partial z}\bigg|_{\xi=0} 2\pi r\, dr = 2\pi D\int_0^{r_n^2} \frac{\partial C}{\partial z}\bigg|_{\xi=0} d(r^2) = 2\pi D\int_0^{r_n^2} \frac{\partial C}{\partial z}\bigg|_{\xi=0} d(x^2 + y^2)$$

$$= 2\pi D\int_0^{r_n^2} \frac{\partial C}{\partial z}\bigg|_{\xi=0} d(r_n^2(\xi^2 + 1)(1 - \eta^2)) = 2\pi D\int_0^{r_n^2} \frac{\partial C}{\partial z}\bigg|_{\xi=0} d(r_n^2(1 - \eta^2))$$

$$= 4\pi D r_n^2 \int_0^1 \frac{\partial C}{\partial z}\bigg|_{\xi=0} \eta\, d\eta \tag{3.44}$$

Because $C = C(\xi)$,

$$\frac{\partial C}{\partial z} \equiv \frac{\partial C}{\partial\xi}\frac{\partial\xi}{\partial z} + \frac{\partial C}{\partial\eta}\frac{\partial\eta}{\partial z} + \frac{\partial C}{\partial\phi}\frac{\partial\phi}{\partial z} = \frac{dC}{d\xi}\frac{\partial\xi}{\partial z} \tag{3.45}$$

Using eqs. (3.43), (3.40), and (3.41) yields

$$\frac{dC}{d\xi} = \frac{2(C_\infty - C_S)}{\pi}\frac{1}{\xi^2 + 1} \tag{3.46}$$

$$x^2 + y^2 = r_n^2(\xi^2 + 1)(1 - \eta^2) \tag{3.47}$$

$$\xi(1 - \eta^2)\frac{\partial \xi}{\partial z} - \eta(\xi^2 + 1)\frac{\partial \eta}{\partial z} = 0 \tag{3.48}$$

From eq. (3.39)

$$1 = r_n\eta\frac{\partial \xi}{\partial z} + r_n\xi\frac{\partial \eta}{\partial z} \tag{3.49}$$

Combining eqs. (3.48) and (3.49) gives

$$\frac{\partial \xi}{\partial z} = \frac{1}{r_n\left(\eta + \dfrac{\xi^2(1 - \eta^2)}{\eta(\xi^2 + 1)}\right)} \tag{3.50}$$

The concentration gradient is computed from eqs. (3.45), (3.46), and (3.50) as

$$\left.\frac{\partial C}{\partial z}\right|_{\xi = 0} = \frac{2(C_\infty - C_S)}{\pi}\frac{1}{r_n\eta} \tag{3.51}$$

Substituting eq. (3.51) into (3.44) gives

$$F(n) = 8Dr_n(C_\infty - C_S) \tag{3.52}$$

Substituting eqs. (3.28), (3.29) and (3.52) into (3.27) gives

$$C_S = \frac{k_r(n)C^{eq}(n) + k_d(n)C_\infty}{k_r(n) + k_d(n)} \tag{3.53}$$

The monomer concentration at the surface of disk has the same form as that for a spherical defect as described by eq. (3.37), but with different definitions for k_d and k_r. For the disk-shaped precipitate

$$k_d = 8r_nD \tag{3.54}$$

The volume of interfacial layer V^i in eq. (3.31) for the disk-shaped defect is $2\pi r_n^2\delta$. The growth rate and dissolution rate for disk defect are determined from eqs. (3.53), (3.28) and

151

(3.29).

3.5 Free Energy of Formation for Oxygen Precipitates

3.5.1 General Framework for Free Energy of Formation for Oxygen Precipitates

Oxygen precipitation in silicon can be expressed mechanistically by the formula

$$P_n + (0.5 + \gamma_I)Si + O + \gamma_V V \leftrightarrow P_{n+1} + \gamma_I I + stress \ energy \tag{3.55}$$
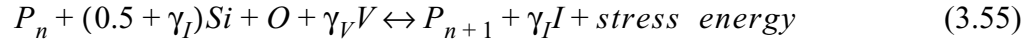
where P_n is an oxygen precipitate of size n which forms by aggregating oxygen (O), sili-con (Si), ejecting interstitials (I) and absorbing vacancies (V). The stoichiometic coeffi-cients γ_I and γ_V give the number of interstitials ejected and vacancies absorbed, respectively, during the reaction. A general free energy of formation for oxygen precipita-tion is described as

$$G(n) = -nkT\ln\frac{C_O}{C_O^{eq}} - \gamma_V nkT\ln\frac{C_V}{C_V^{eq}} + \gamma_I nkT\ln\frac{C_I}{C_I^{eq}} + E_V + E_S \tag{3.56}$$

where the first three terms are configurational contributions from the super-saturations of oxygen, vacancies and interstitials. The term E_V represents the contribution to the free energy from the stress field created by the density mismatch of the particle and matrix, as shown in Figure 3.6. V_m is the volume of the unconstrained cavity created by the precipi-tate in the matrix including the additional volume created by vacancy absorption and inter-stitial ejection. The volume of the unconstrained precipitate is V_p. For a silicon oxide precipitate $V_p > V_m$ and stress is generated in the precipitate and matrix to create the final precipitate volume V_f with compressive stress in the precipitate. E_S is the surface energy of the precipitate/matrix interface. γ_I and γ_V are determined by minimizing the free energy of formation of the individual precipitate [169,170]. The stress energy and surface energy all depend on the shape of the precipitate. The free energy of formation for spheri-cal and disk-shaped precipitates are discussed in the following sections.
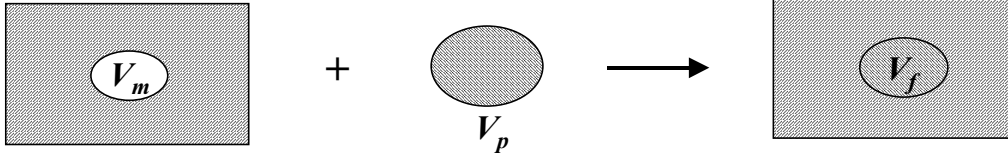
Figure 3.6: Stress energy due to the density mismatch of the particle and matrix.

3.5.2 Free Energy of Formation for Spherical Oxygen Precipitate

The stress energy can be determined by the linear elasticity theory. Consider a spherical oxygen precipitate with unconstrained volume V_p embedded into the spherical matrix cavity with volume V_m to create a final spherical precipitate with volume V_f. The corresponding radii r_p, r_m and r_f are shown in Figure 3.7. The linear misfit e_T is defined as [111]

$$\frac{V_p}{V_m} = (1 + e_T)^3 \tag{3.57}$$

where

$$\frac{V_p}{V_m} = \frac{V_{SiO_2}}{V_{Si}(1 + 2\gamma_I + 2\gamma_V)} \tag{3.58}$$

where V_{SiO_2} and V_{Si} are the volumes of SiO_2 and Si respectively. The volume V_{SiO_2} is approximately equal to two times V_{Si} or

$$V_{SiO_2} \approx 2V_{Si} \tag{3.59}$$

Rearranging eqs. (3.57) and (3.58) gives the expression for γ_I and γ_V

$$\gamma_I + \gamma_V = \frac{1}{2}\left((1 + e_T)^{-3}\frac{V_{SiO_2}}{V_{Si}} - 1\right) \tag{3.60}$$

The constrained strain e_C is defined as [111]

153

$$\frac{V_f}{V_m} = (1 + e_C)^3 \qquad (3.61)$$
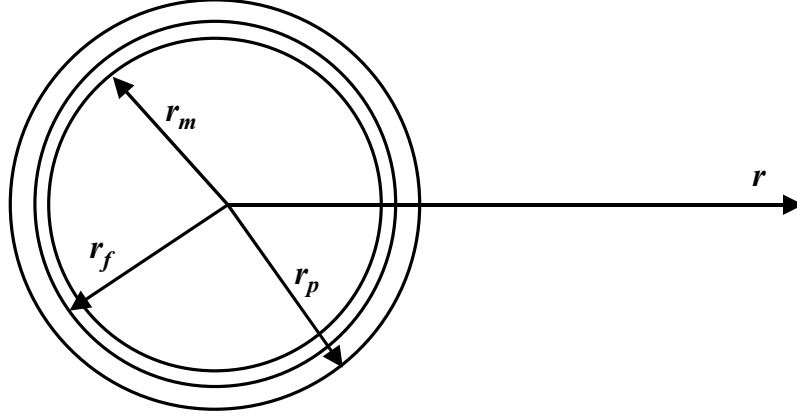
Figure 3.7: Spherical precipitate in the spherical coordinates.

Due to the spherical symmetry, the governing equation for the displacement $u(r)$ of the matrix due to the inclusion of the precipitate is reduced to [156]

$$r^2 \frac{d^2 u}{dr^2} + 2r \frac{du}{dr} - 2u = 0 \qquad (3.62)$$

with boundary conditions

$$u = e_C r_m \quad at \quad r = r_m \qquad (3.63)$$

$$u = 0 \quad at \quad r \rightarrow \infty \qquad (3.64)$$

The solution for $u(r)$ is

$$u(r) = e_C r_m^3 / r^2 \qquad (3.65)$$

In the matrix the radial and tangential strains are [156]

$$\varepsilon_{rr} = \frac{du}{dr} = -\frac{2e_C r_m^3}{r^3} \qquad (3.66)$$

$$\varepsilon_{\theta\theta} = \frac{u}{r} = \frac{e_C r_m^3}{r^3} \tag{3.67}$$

These strains are related to the stress σ as [156]

$$E\varepsilon_{rr} = \sigma_{rr} - 2v\sigma_{\theta\theta} \tag{3.68}$$

$$E\varepsilon_{\theta\theta} = -v\sigma_{rr} + (1-v)\sigma_{\theta\theta} \tag{3.69}$$

where E and v are the Young's modulus and Poisson's ratio of the matrix. The dilatation in the precipitate is a uniform hydrostatic compression $3(e_T - e_C)$, and the pressure p is therefore [111]

$$p = 3K(e_T - e_C) \tag{3.70}$$

where K is the bulk modulus of the precipitate. At the boundary $u(r=r_m) = e_C r_m$,

$$p = -\sigma_{rr} \tag{3.71}$$

Substituting eqs. (3.66), (3.67), (3.70), and (3.71) into eqs. (3.68) and (3.69) at $r = r_m$, and cancelling $\sigma_{\theta\theta}$ gives

$$e_C = \frac{e_T}{X} \tag{3.72}$$

where the constant X is defined as

$$X \equiv 1 + \frac{2E}{3K(1+v)} \tag{3.73}$$

Young's modulus E, Poisson's ratio v, and shear modulus μ of the matrix are related by [156]

$$\mu = \frac{E}{2(1+v)} \tag{3.74}$$

Therefore the constant X is rewritten as

$$X \equiv 1 + \frac{4\mu}{3K} \qquad (3.75)$$

The shear modulus μ of Si (the matrix) is chosen as $6.41 \times 10^{10} Pa$, and the bulk modulus of SiO_2 (the precipitate) is chosen as $3.47 \times 10^{10} Pa$ [205].

Nabarro [112] further proved that the elastic energy of the inclusion of the spherical precipitate into the matrix was given by

$$E_V = 6\mu V_m e_C e_T \qquad (3.76)$$

Therefore the free energy of formation for a spherical oxygen precipitate is described as

$$G(n) = -nkT\ln\frac{C_O}{C_O^{eq}} - \gamma_V nkT\ln\frac{C_V}{C_V^{eq}} + \gamma_I nkT\ln\frac{C_I}{C_I^{eq}} + \left(\frac{4}{3}\pi r_m^3\right) \cdot 6\mu e_C e_T + 4\pi r_f^2 \sigma \qquad (3.77)$$

The free energy of formation of a spherical oxygen precipitate is rewritten based on eqs. (3.57), (3.61) and (3.72) as

$$G(n) = -nkT\ln\frac{C_O}{C_O^{eq}} - \gamma_V nkT\ln\frac{C_V}{C_V^{eq}} + \gamma_I nkT\ln\frac{C_I}{C_I^{eq}} + G^f(n) \qquad (3.78)$$

where the non-configurational part $G^f(n)$ is

$$G^f(n) \equiv \left(\frac{4}{3}\pi r_p^3\right) \cdot \frac{6\mu X e_C^2}{(1 + X e_C)^3} + 4\pi r_p^2 \left(\frac{1 + e_C}{1 + X e_C}\right)^2 \sigma \qquad (3.79)$$

and the unconstrained precipitate radius r_p is related to SiO_2 volume V_{SiO_2} as

$$\frac{4}{3}\pi r_p^3 = \frac{n}{2} V_{SiO_2} \qquad (3.80)$$

The coefficients γ_I and γ_V are determined by minimizing $G(n)$ described by eq. (3.77) or (3.78). The equations for γ_I and γ_V are therefore $\left.\frac{\partial G(n)}{\partial \gamma_I}\right|_{\gamma_V} = 0$ and $\left.\frac{\partial G(n)}{\partial \gamma_V}\right|_{\gamma_I} = 0$ or

$$nkT\ln\frac{C_I}{C_I^{eq}} + \frac{\partial G^f(n)}{\partial e_C}\frac{\partial e_C}{\partial \gamma_I} = 0 \qquad (3.81)$$

$$-nkT\ln\frac{C_V}{C_V^{eq}} + \frac{\partial G^f(n)}{\partial e_C}\frac{\partial e_C}{\partial \gamma_V} = 0 \tag{3.82}$$

From eqs. (3.57), (3.58), and (3.72)

$$\frac{\partial e_C}{\partial \gamma_I} = \frac{\partial e_C}{\partial \gamma_V} \tag{3.83}$$

In order to satisfy both eq. (3.81) and (3.82), the following relationship must hold

$$nkT\ln\frac{C_I}{C_I^{eq}} = -nkT\ln\frac{C_V}{C_V^{eq}} \tag{3.84}$$

Generally the concentrations of vacancy and interstitial do not necessarily satisfy eq. (3.84). This implies that the minimum free formation energy of a spherical oxygen precipitate with respect to γ_I and γ_V are on the domain boundary of (γ_I, γ_V). In other words, either γ_I or γ_V has to be zero. Physically this means that the stress energy associated with a spherical oxygen precipitate is released by either interstitial ejection or vacancy absorption, but not both. When $\gamma_I = 0$, γ_V is determined by minimizing Gibbs free formation energy with respect to γ_V. When $\gamma_V = 0$, γ_I is determined by minimizing Gibbs free formation energy with respect to γ_I. If the free formation energy at $(\gamma_I = 0, \gamma_V)$ is lower than that at $(\gamma_V = 0, \gamma_I)$, the stress is released through vacancy absorption. Otherwise the stress is released through interstitial ejection.

For vacancy absorption $(\gamma_I = 0, \gamma_V \neq 0)$ mechanism, $\gamma_I = 0$ and $\frac{\partial G(n)}{\partial \gamma_V} = 0$

$$-nkT\ln\frac{C_V}{C_V^{eq}} + \frac{\partial G^f(n)}{\partial e_C}\frac{\partial e_C}{\partial \gamma_V} = 0 \tag{3.85}$$

where $\partial G^f(n)/\partial e_C$ is determined from eq. (3.79)

$$\frac{\partial G^f(n)}{\partial e_C} = \frac{4}{3}\pi r_p^3\left(\frac{12\mu X e_C}{(1+Xe_C)^3} - \frac{18\mu X^2 e_C^2}{(1+Xe_C)^4} + \frac{3\sigma}{r_p}\left(\frac{2(1+e_C)}{(1+Xe_C)^2} - \frac{2(1+e_C)^2 X}{(1+Xe_C)^3}\right)\right) \tag{3.86}$$

and $\partial e_C / \partial \gamma_V$ is determined from eq. (3.60)

$$1 = -\frac{3}{2}(1 + Xe_C)^{-4}\frac{XV_{SiO_2}}{V_{Si}}\frac{\partial e_C}{\partial \gamma_V} \tag{3.87}$$

The maximum value for e_C is determined as 0.075 from eqs. (3.60) and (3.72) by setting $\gamma_I = \gamma_V = 0$. Substituting eqs. (3.86) and (3.87) into eq. (3.85) and removing high order terms for e_C taking the limit of $e_C \ll 1$ gives

$$e_C = -\frac{kT}{4\mu V_{Si}}\ln\frac{C_V}{C_V^{eq}} + \frac{\sigma}{2\mu r_p}\left(1 - \frac{1}{X}\right) \tag{3.88}$$

Therefore γ_V and $G(n)$ for a spherical oxygen precipitate through vacancy absorption can be determined as

$$\gamma_V = \frac{1}{2}\left((1 + Xe_C)^{-3}\frac{V_{SiO_2}}{V_{Si}} - 1\right) \tag{3.89}$$

$$G(n) = -nkT\ln\frac{C_O}{C_O^{eq}} - \gamma_V nkT\ln\frac{C_V}{C_V^{eq}} + \left(\frac{4}{3}\pi r_p^3\right) \cdot \frac{6\mu Xe_C^2}{(1 + Xe_C)^3} + 4\pi r_p^2\left(\frac{1 + e_C}{1 + Xe_C}\right)^2 \sigma \tag{3.90}$$

For interstitial ejection ($\gamma_V = 0$, $\gamma_I \neq 0$) mechanism, the same procedure can be applied. The free energy of formation for a spherical oxygen precipitate through interstitial ejection can be calculated by the following three equations:

$$e_C = \frac{kT}{4\mu V_{Si}}\ln\frac{C_I}{C_I^{eq}} + \frac{\sigma}{2\mu r_p}\left(1 - \frac{1}{X}\right) \tag{3.91}$$

$$\gamma_I = \frac{1}{2}\left((1 + Xe_C)^{-3}\frac{V_{SiO_2}}{V_{Si}} - 1\right) \tag{3.92}$$

$$G(n) = -nkT\ln\frac{C_O}{C_O^{eq}} + \gamma_I nkT\ln\frac{C_I}{C_I^{eq}} + \left(\frac{4}{3}\pi r_p^3\right) \cdot \frac{6\mu Xe_C^2}{(1 + Xe_C)^3} + 4\pi r_p^2\left(\frac{1 + e_C}{1 + Xe_C}\right)^2 \sigma \tag{3.93}$$

These two regions for spherical precipitate growth occur at very different rates. When there is a pre-existing high vacancy concentration, as is installed during the MDZ process, precipitate growth occurs at high rates due to stress relief for the spherical precipitate by vacancy absorption. For the growth by the interstitial ejection mechanism to proceed, the ejected interstitials must diffuse from the matrix. Otherwise, a super-saturation of self-interstitials is created leading to high free energies and very low growth rates. When stress relief is only possible by interstitial ejection, low rates for spherical precipitate growth cause disk-shaped precipitates to dominate at low annealing temperatures.

3.5.3 Dominate Shape of Oxygen Precipitate at Low Nucleation Temperature

As shown in Figure 3.2, the stress energy is the largest for sphere. This high stress energy associated with the spherical oxygen precipitate could be released by interstitial ejection at the expense of $\gamma_I kT \ln(C_I / C_I^{eq})$ according to eq. (3.56). However, unless the ejected interstitials can be quickly captured by other sinks, the super-saturation of interstitials could build up instantly and make the growth of spherical oxide energetically unfavorable. The sinks for ejected interstitials may include possible interstitial sink near oxygen precipitate, wafer surface, and interstitial clusters in the bulk. In the following analysis, it will be shown that none of these sinks is rapid enough to significantly decrease the super-saturation of interstitials because of low self-diffusion $D_I C_I^{eq}$ of interstitials at low temperature.

A model problem is examined to illustrate the difficulty for ejected interstitials to be captured by a sink near oxygen precipitate at low annealing temperature. Consider a spherical oxygen precipitate nucleus of size 10^2 shown in Figure 3.8. The interstitial concentration around the oxygen precipitate is governed by the species conservation equation

$$\nabla^2 C_I = 0 \qquad (3.94)$$

The boundary condition for C_I at the surface of the precipitate $r = r_0$ is

$$C_I = C_I^{eq}(T) \quad at \quad r = r_0 \tag{3.95}$$

where T is the annealing temperature. Due to a sink for interstitials at $r = kr_0$ the boundary condition for C_I at the sink is

$$C_I = 0 \quad at \quad r = kr_0 \tag{3.96}$$

where the constant k is a indicator of the difficulty to remove ejected interstitials by a sink near the oxygen precipitate. The higher k, the easier to diffuse interstitials to the sink. When k is approaching 1, the sink has to be very close to the precipitate surface, therefore it implies that the removal of the interstitials by the sink is difficult.
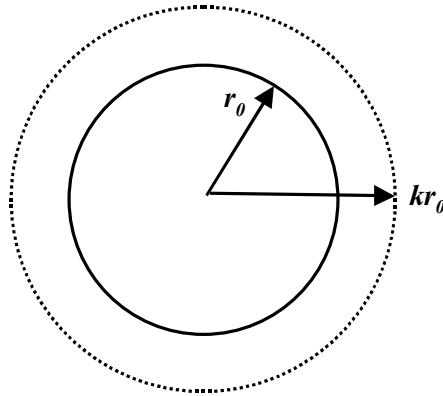
Figure 3.8: Spherical oxygen precipitate of size 10^2 ($r=r_0$) with the sink for interstitials at $r=kr_0$.

The constant k is determined by the mass balance of the interstitials

$$4\pi D_I(T)C_I^{eq}(T)r_0\frac{k}{k-1} = \frac{50}{30 \times 3600} \tag{3.97}$$

The left side of the eq. (3.97) is the diffusion flux determined by solving eq. (3.94) with boundary conditions (3.95) and (3.96). In order for oxide of size 10^2 to form during 30 hours wafer annealing at low temperature $T = 650°C$, about 50 interstitials have to be

ejected to release the high stress energy. The right side of the eq. (3.97) is calculated based on the ejection of 50 interstitials during 30 hours. At $T = 650°C$, $D_I(650°C) = 1.9 \times 10^{-6} cm^2/s$ and $C_I^{eq}(650°C) = 1.5 \times 10^5 cm^{-3}$ based on eqs. (2.30) and (2.32). Solving eq. (3.97) gives $k = 1.0006$ which indicates that the removal of the interstitials by the sink around the oxygen precipitate is difficult due to low self-diffusion $D_I C_I^{eq}$ of interstitials at low temperature.

The interstitials ejected by oxygen precipitates also could diffuse to the wafer surface during the wafer annealing. A simple calculation is performed to investigate this possibility. A cross-section of the wafer is shown in Figure 3.9 with the half thickness of the wafer $\delta = 362.5 \mu m$ and typical thickness of the surface denuded zone $d = 40 \mu m$. The ejected interstitials diffuse to the wafer surface through the diffusion layer in the denuded zone. Suppose the surface recombination rate for interstitials is infinite fast so that the interstitial concentration at the wafer surface is equilibrium interstitial concentration $C_I^{eq}(T)$ at the annealing temperature. The mass balance for the interstitials is used to determine the bulk interstitial concentration C_I which need to be maintained to diffuse ejected interstitials. The higher C_I, the higher super-saturation of the interstitials, and therefore the more difficult for spherical oxygen precipitate to form according to eq. (3.56).
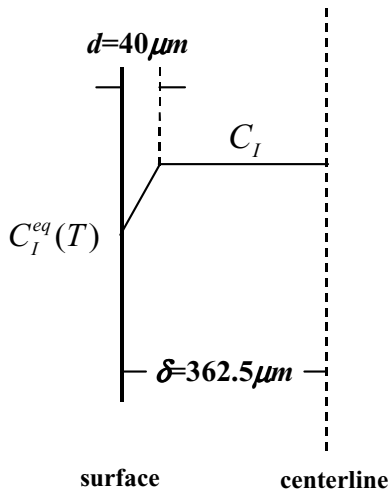
Figure 3.9: Cross-section of the wafer.

In order to form spherical oxide nucleus of size 10^2 with typical density of $O(10^{10})cm^{-3}$ in 30 hours, $O(10^{12})cm^{-3}$ interstitials have to ejected and diffuse to the wafer surface. So the mass balance of the interstitials gives

$$D_I(T)\frac{C_I - C_I^{eq}(T)}{d} = \frac{(\delta - d) \times 10^{12}}{30 \times 3600} \qquad (3.98)$$

Solving eq. (3.98) at $T = 650°C$ gives $C_I = 6 \times 10^8 cm^{-3}$ which is more than three orders-of-magnitude higher than the equilibrium interstitial concentration at $T = 650°C$. This high super-saturation of interstitials makes it impossible to form spherical oxygen precipitates with high density through interstitial ejection at low temperature.

One more possible destiny for the ejected interstitials are the interstitial clusters in the crystal. Interstitial clusters form when the interstitials are supersaturated. The simulation results of oxide size distributions after 32 hours annealing at 650 $°C$ for oxygen level of $C_O = 8.0 \times 10^{17} cm^{-3}$ are shown in Figure 3.10 for spherical oxides under different conditions and disk-shaped oxide whose free energy of formation is the subject of the next Section. As discussed in Section 2.2.2, the surface energy of interstitial cluster

$\sigma_I = 1.2 \ J/m^2$ gives good estimations for interstitial cluster aggregation temperature. With this surface energy, the density of the spherical oxygen precipitates is far below that of the disk-shaped oxygen precipitates which has good agreement with the experiments. The detail comparison between these experiments and the simulations of disk-shaped oxygen precipitate are referred to Section 3.9.2. The lower σ_I, the easier to form interstitial clusters, therefore the easier to remove ejected interstitials and form spherical oxygen precipitates. However, even with much lower surface energy $\sigma_I = 0.4 \ J/m^2$, the density of the spherical oxides is still more than three orders-of-magnitude lower than the experimental results. The simulation results shown in Figure 3.10 demonstrate that the formation of interstitial clusters is still not fast enough at low temperature to form enough spherical oxygen precipitates. To make this point, the size distribution also is shown for a hypothetical model in which the bulk interstitial concentration is held fixed at $C_I = C_I^{eq}(T)$, corresponding to a system where interstitials ejected from precipitates are instantly absorbed into an undefined defect structure. In this case, the density of spherical precipitates is slightly higher than the density for disk-shaped particles
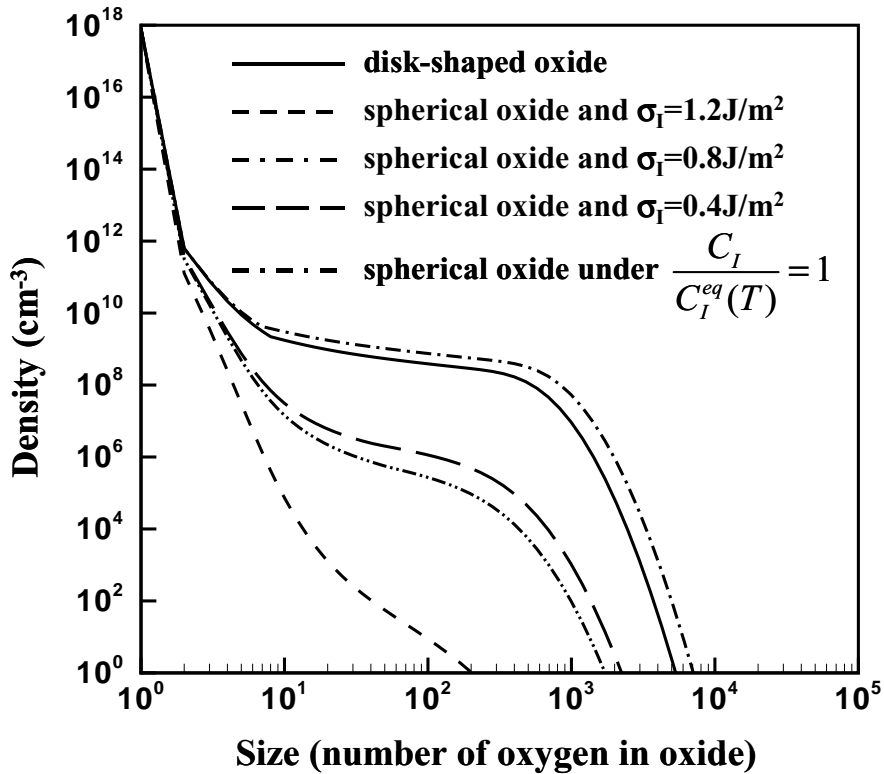
Figure 3.10: Size distributions of spherical oxides and disk-shaped oxides after 32 hours annealing at $650°C$ for $C_O=8.0\times10^{17}cm^{-3}$.

Fortunately, even without interstitial ejection the stress energy could still be considerately reduced by taking different shapes such as disk. As shown in Figure 3.2, the stress energy is lowest for disk-shaped precipitate. The expense for shapes other than sphere is the increased surface energy. But overall the disk-shaped oxygen precipitates are still energetically favorable over spherical precipitates. This may explains why oxygen precipitates always have ribbon or disk shapes during regular low temperature annealing [68]. However there is an exception for this. When there exists a pre-established high vacancy concentration, like in the MDZ process discussed in section 1.2, the oxygen precipitate can keep its minimum surface energy shape - sphere, while the high stress energy of the spherical oxygen precipitate can be efficiently released through vacancy absorption.

3.5.4 Free Energy of Formation for Disk-Shaped Oxygen Precipitate

Hu [62] found that the stress energy of a disk-shaped oxygen precipitate can be treated as a circular dislocation loop with a giant Burgers vector which corresponds to the lattice displacement perpendicular to the disk. By minimizing the free energy including the stress energy and surface energy, Hu [67] reasonably predicted the aspect ratio of disk-shaped oxygen precipitate compared with experimental measurements. Based on Hu's [67] expression of the stress energy for the disk-shaped oxygen precipitate, a general free energy of formation for a disk-shaped oxygen precipitate is expressed as

$$G(n) = -nkT\ln\frac{C_O}{C_O^{eq}} - \gamma_V nkT\ln\frac{C_V}{C_V^{eq}} + \gamma_I nkT\ln\frac{C_I}{C_I^{eq}} + \frac{\mu r(hs)^2}{2(1-v)}\left(\ln\left(\frac{8r}{hs}\right) - 1\right) + 2\pi r^2 \sigma \quad (3.99)$$

where v is the Poisson's ratio, r and h are the radius and thickness of the disk-shaped oxide shown in Figure 3.11. The fourth term in eq. (3.99) is the energy of the dislocation loop with the giant Burgers vector hs. s is the lattice displacement per unit thickness perpendicular to the disk. The last term is the surface energy for the two circular surfaces of the disk.

Figure 3.11: Disk-shaped oxygen precipitate.
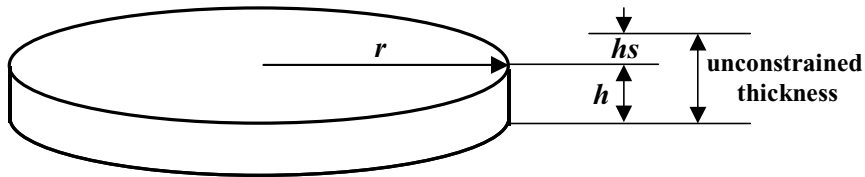
Because the stress energy of the disk-shaped precipitate is low, there is little need to release stress by vacancy absorption and interstitial ejection. This point is made clear by the plot of the free energy $G(n=100)$ as a function of γ_I for disk-shaped oxide with aspect ratio $2r/h = 6$ at $650°C$ and $C_I/C_I^{eq} = 10^2$ in Figure 3.12. The γ_I is determined by

minimizing the free energy. So in this case $\gamma_I < 10^{-5}$ is very small compared with $\gamma_I = 0.37$ corresponding minimum free energy for spherical oxide under the same conditions
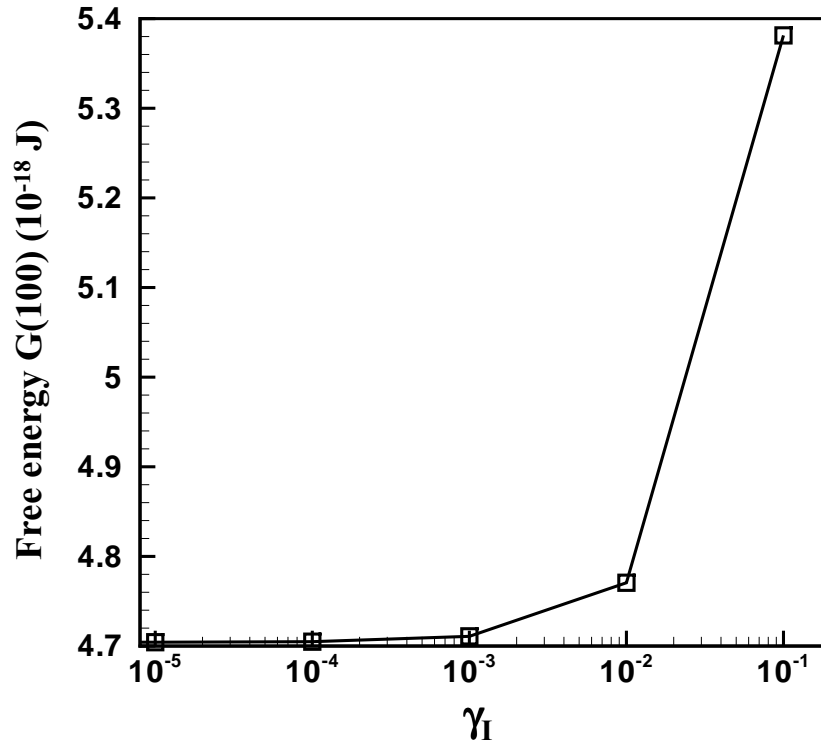
Figure 3.12: Free energy $G(n=100)$ as a function of γ_I for disk-shaped oxide with aspect ratio $2r/h=6$ at $650°C$ and $C_I/C_I^{eq}=10^2$ (compared with $\gamma_I=0.37$ corresponding minimum free energy for spherical oxide under the same conditions).

Accordingly, it is assumed that $\gamma_I = \gamma_V = 0$. The free energy of formation for a disk-shaped oxygen precipitate is expressed simply as

$$G(n) = -nkT\ln\frac{C_O}{C_O^{eq}} + \frac{\mu r(hs)^2}{2(1-v)}\left(\ln\left(\frac{8r}{hs}\right) - 1\right) + 2\pi r^2\sigma \qquad (3.100)$$

Because neither interstitials are ejected nor vacancies are absorbed, the linear misfit e_T can be calculated from eq. (3.60) as

$$e_T = \left(\frac{V_{SiO_2}}{V_{Si}}\right)^{\frac{1}{3}} - 1 \tag{3.101}$$

The constrained strain e_C is therefore given by eq. (3.72) as

$$e_C = e_T/X = \left[\left(\frac{V_{SiO_2}}{V_{Si}}\right)^{\frac{1}{3}} - 1\right]/X \tag{3.102}$$

The radius r and thickness h of the disk-shaped precipitate are related as

$$\pi r^2 h = V_f = V_m(1 + e_C)^3 = \frac{n}{2}V_{Si}(1 + e_C)^3 \tag{3.103}$$

and s, the lattice displacement per unit thickness, is related to e_T and e_C by

$$s = \frac{e_T - e_C}{1 + e_C} \tag{3.104}$$

The aspect ratio of the disk is determined by minimizing the free formation energy described by eq. (3.100) under the constrain of specific volume eq. (3.103) [67]. This leads to

$$\frac{r}{\Gamma} = \frac{\left(\frac{r}{hs}\right)^2}{\ln\left(\frac{8r}{hs}\right) - 2} \tag{3.105}$$

where the constant Γ is

$$\Gamma \equiv \frac{8\pi\sigma(1 - v)}{3\mu} \tag{3.106}$$

The radius and thickness of the plate are obtained by solving eqs. (3.103) and (3.105). The aspect ratio $2r/h$ as a function of size n is shown in Figure 3.13. When $n < 10^2$, the aspect ratio $2r/h < 2$ and is not physically meaningful. The minimum aspect ratio here is set as $2r/h = 6$ and corresponds to the horizontal line in Figure 3.13.
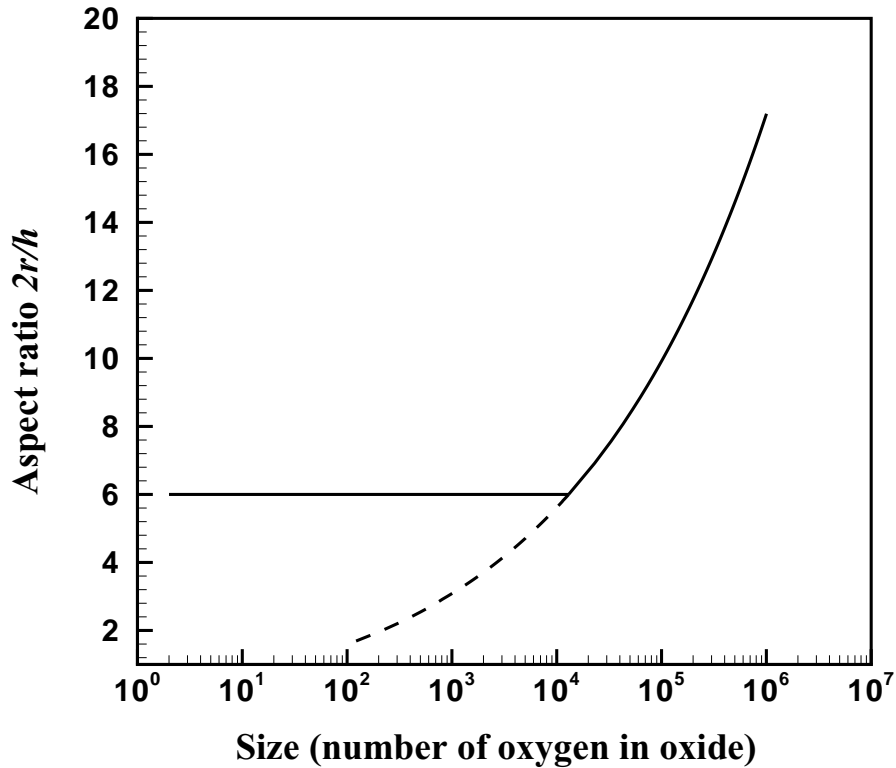
Figure 3.13: The aspect ratio of the disk-shape as a function of size of the oxygen precipitate.

The free energy of formation for disk-shaped oxygen precipitates and spherical oxygen precipitates with different super-saturation of interstitials and vacancies at $650°C$ are shown in Figure 3.14. Clearly, spherical precipitates have the lowest free energy when a super-saturation of vacancies exists. The free energy is always higher when the mechanism shifts to interstitial ejection and $C_I/C_I^{eq} > 1$. The disk-shaped precipitate has a lower free energy than all spherical precipitates except those with pre-existing super-saturations of vacancies.
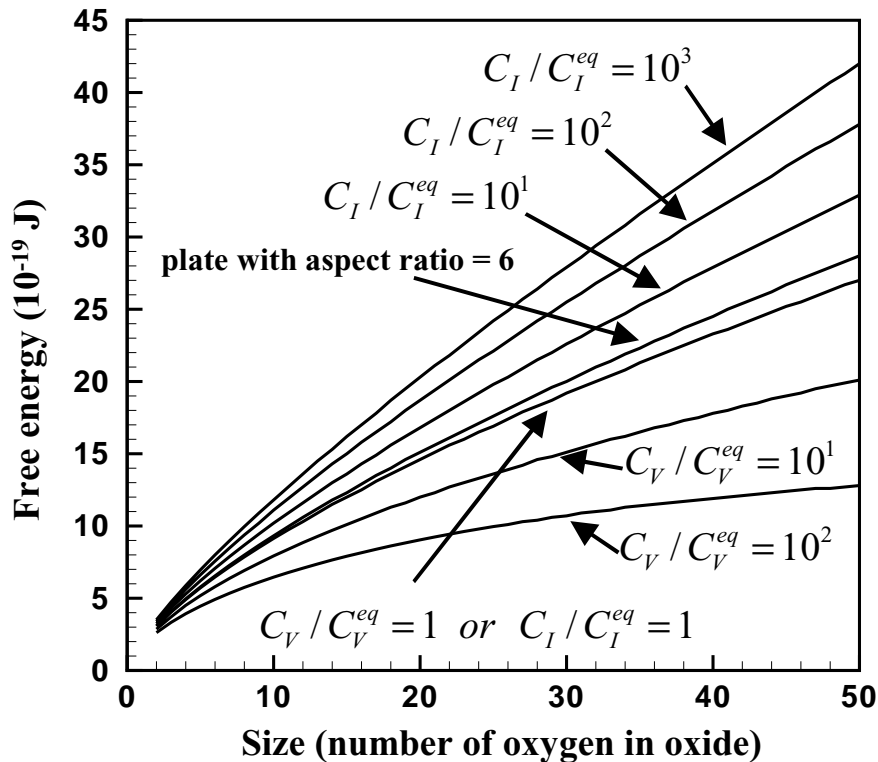
Figure 3.14: The free energy of formation for the disk-shaped oxygen precipitates and the spherical oxygen precipitates with different super-saturation of interstitials and vacancies at $650°C$.

3.6 Numerical Methods

Sinno [150,151,152,154] and Mori [107,108] had successfully developed a framework with hybrid numerical methods to solve the dynamic of native point defects and their clusterings. Sinno developed some numerical methods based on the standard Galerkin method with artificial diffusivities for clusters and CC70 [20] finite difference method to simulate dynamics of vacancies, interstitials and their clusters during steady state crystal growth. Mori further developed a time-dependent simulator to account for dynamics of native point defects and their clusters not only for the steady state but also for the transit state. In Mori's work, the discontinuous Galerkin (DG) method was used in stead of the standard Galerkin method for clusters to avoid artificial diffusivities, maintain the stability of the

solutions, and make the algorithm parallellizable. The local discontinuous Galerkin (LDG) method was used for native point defects and the operating splitting method was used for time integral. For the numerical simulations of vacancies, interstitials, oxygens and all their clusters in this chapter, CC70 is used for the size space of all FPEs, DG is used for the spatial variables of all DREs and FPEs, LDG is used for the spatial variables of governing equations for all point defects including oxygen, time integration involves an operating splitting method and implicit Eular integration in time. The accuracy and efficiency of the simulations are improved by using iteration and adaptive time steps for each operating splitting step. All the numerical methods are only discussed briefly here, some further details can be referred to [108].

3.6.1 CC70 Finite Difference Method

The size components of the Fokker-Planck equations for clusters are discretized by CC70. CC70 is a kind of finite difference scheme which has properties of non-negative solution and particle conserving and may significantly reduce the number of mesh points required with no loss of accuracy [20,31,32,121,122].

$$\left(\frac{\partial}{\partial t} + V\frac{\partial}{\partial z}\right)f_n = \frac{\partial}{\partial n}\left(A(n)f_n + B(n)\frac{\partial}{\partial n}f_n\right) = \frac{I_{m+1/2} - I_{m-1/2}}{\Delta n_m} \qquad (3.107)$$

where

$$I_{m+1/2} = A_{m+1/2}f_{m+1/2} + B_{m+1/2}\left(\frac{\partial}{\partial n}f\right)_{m+1/2} \qquad (3.108)$$

$$A_{m+1/2} = (A_m + A_{m+1})/2 \qquad (3.109)$$

$$B_{m+1/2} = (B_m + B_{m+1})/2 \qquad (3.110)$$

$$\left(\frac{\partial}{\partial n}f\right)_{m+1/2} = \frac{f_{m+1} - f_m}{\Delta n_{m+1/2}} \qquad (3.111)$$

$$\Delta n_{m+1/2} = n_{m+1} - n_m \tag{3.112}$$

$$\Delta n_m = (n_{m+1} - n_{m-1})/2 \tag{3.113}$$

$$f_{m+1/2} = (1 - \delta_m)f_{m+1} + \delta_m f_m \tag{3.114}$$

$0 \le \delta_m \le 1/2$. This scheme becomes centered and forward differencing when δ_m is equal to 1/2 and 0 respectively. If δ_m is fixed, positivity and particle conserving can not be guaranteed. The main idea of CC70 is adjusting δ_m so that the numerical solution is the same as the exact solution.

$$I_{m+1/2} = \left(A_{m+1/2}(1 - \delta_m) + \frac{B_{m+1/2}}{\Delta n_{m+1/2}}\right)f_{m+1} - \left(\frac{B_{m+1/2}}{\Delta n_{m+1/2}} - \delta_m\right)f_m \tag{3.115}$$

The equilibrium solution is

$$I_{m+1/2} = 0 \tag{3.116}$$

$$\frac{f_{m+1}}{f_m} = \frac{\dfrac{B_{m+1/2}}{\Delta n_{m+1/2}} - \delta_m}{A_{m+1/2}(1 - \delta_m) + \dfrac{B_{m+1/2}}{\Delta n_{m+1/2}}} \tag{3.117}$$

The exact equilibrium solution is

$$A(n)f_n + B(n)\frac{\partial}{\partial n}f_n = 0 \tag{3.118}$$

$$\frac{\partial}{\partial n}\ln f_n = -\frac{A(n)}{B(n)} \tag{3.119}$$

$$\frac{f_{m+1}}{f_m} = \exp\left(-\int_{n_m}^{n_{m+1}} \frac{A(n)}{B(n)}dn\right) \approx \exp\left(-\frac{A_{m+1/2}}{B_{m+1/2}}\Delta n_{m+1/2}\right) \tag{3.120}$$

δ_m can be solved by comparing eqs (3.117) and (3.120)

$$\delta_m = \frac{1}{w_{m+1/2}} - \frac{1}{\exp(w_{m+1/2}) - 1} \tag{3.121}$$

where

$$w_{m+1/2} = \frac{A_{m+1/2}}{B_{m+1/2}} \Delta n_{m+1/2} \tag{3.122}$$

substituting eq. (3.121) into eq. (3.115)

$$I_{m+1/2} = \frac{B_{m+1/2}}{\Delta n_{m+1/2}} (W^+_{m+1/2} f_{m+1} - W^-_{m+1/2} f_m) \tag{3.123}$$

where

$$W^\pm_{m+1/2} = \frac{w_{m+1/2}}{2 \sinh \dfrac{w_{m+1/2}}{2}} \exp\left(\pm \frac{w_{m+1/2}}{2}\right) \tag{3.124}$$

Therefore the Fokker-Planck equations can be written in a tri-diagonal form

$$\left(\frac{\partial}{\partial t} + V\frac{\partial}{\partial z}\right) f_m - a_m f_{m-1} + b_m f_m - c_m f_{m+1} = 0 \tag{3.125}$$

where

$$a_m = \frac{1}{\Delta n_m} \frac{B_{m-1/2}}{\Delta n_{m-1/2}} W^-_{m-1/2} \tag{3.126}$$

$$b_m = \frac{1}{\Delta n_m} \left(\frac{B_{m-1/2}}{\Delta n_{m-1/2}} W^+_{m-1/2} + \frac{B_{m+1/2}}{\Delta n_{m+1/2}} W^-_{m+1/2}\right) \tag{3.127}$$

$$c_m = \frac{1}{\Delta n_m} \frac{B_{m+1/2}}{\Delta n_{m+1/2}} W^+_{m+1/2} \tag{3.128}$$

The finite difference mesh for the FPEs is set as

$$n_{m+1} = n_m + (1 + \lambda)^m \tag{3.129}$$

where λ is the adjustable parameter to control the mesh refinement in size space.

3.6.2 Discontinuous Galerkin (DG) Method and Local Discontinuous Galerkin (LDG) Method

The governing equations for all the clusters (both DREs and FPEs) are hyperbolic in spa-

tial space. The traditional methods used to solve hyperbolic equation have numerical diffi-

culties in either stability or accuracy. The discontinuous Galerkin method which draw a lot of attention recently has high order accuracy and good stability at the same time [21,23,81]. The numerical results by different methods compared with exact solution are shown in Figure 3.15 [81]. The difference between the standard Galerkin method and the discontinuous Galerkin method in terms of elements and nodes is illustrated in Figure 3.16.
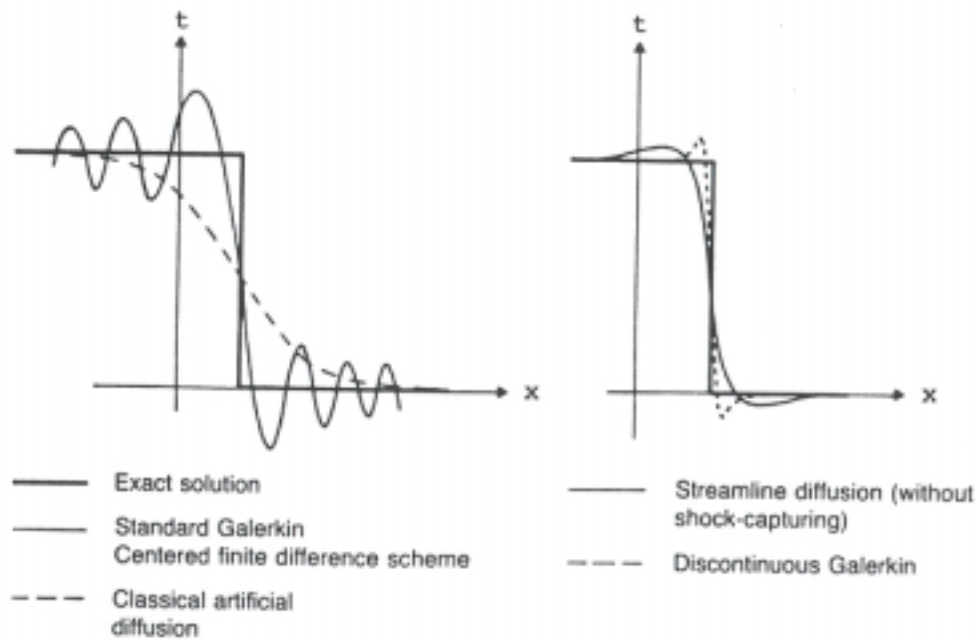

Figure 3.15: The numerical results by different methods compared with exact solution (taken from [81]).

Standard Galerlin (SG)
  space of continuous piecewise
  polynomial functions
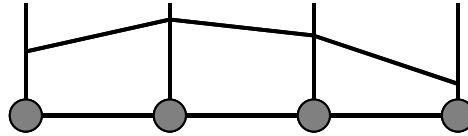
nodes defined at elemental boundaries

Discontinuous Galerkin (DG)
  space of piecewise polynomial functions
  w/o continuity requirement
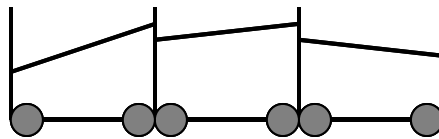
nodes defined inside element

Figure 3.16: The difference between the standard Galerkin method and the discontinuous Galerkin method.

Only a simple example is illustrated here to show how the discontinuous Galerkin method works. Consider a hyperbolic differential equation

$$V\frac{du}{dz} = g(z, u) \tag{3.130}$$

with boundary condition

$$u(z=0) = u_0 \tag{3.131}$$

where V is a positive constant, u is the unknown and $g(z,u)$ is a function of z and u.

Eq. (3.130) may be solved element-by-element. As shown in Figure 3.17, for a given element I_j, the value $u(z_j^-)$ is known and what is needed to be solved is unknown u which satisfies eq. (3.130) in the element I_j.
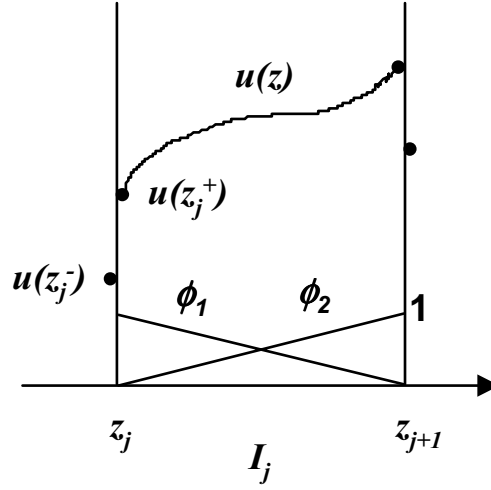
Figure 3.17: The scheme of the discontinuous Galerkin method.

Assuming in the element I_j, the unknown u can be approximated as

$$u = \sum_{i=1}^{K} u_i \phi_i \tag{3.132}$$

where K is an integer, u_i is the unknown coefficient and ϕ_i is basis function in I_j. Taking inner product on eq. (3.130) with ϕ_i gives

$$\int_{\partial I_j^-} V u_z \phi_i dz + \int_{I_j} V u_z \phi_i dz = \int_{I_j} g \phi_i dz \qquad \text{i=1}\ldots K \tag{3.133}$$

$$\int_{\partial I_j^-} V(u(z_j^+) - u(z_j^-))\delta(z_j)\phi_i dz + \int_{I_j} V u_z \phi_i dz = \int_{I_j} g \phi_i dz \qquad \text{i=1}\ldots K \tag{3.134}$$

$$V\phi_i(z_j)(u(z_j^+) - u(z_j^-)) + \int_{I_j} V u_z \phi_i dz = \int_{I_j} g \phi_i dz \qquad \text{i=1}\ldots K \tag{3.135}$$

where ∂I_j^- represents the inflow boundary of the element I_j, and $\delta(z_j)$ is the dirac delta function. Compared with the standard Galerkin method, the first term in eq. (3.135) is an extra term which is the direct result of discontinuity at the element boundary. Because of

the discontinuity, u_z or du/dz is equal to $(u(z_j^+) - u(z_j^-))\delta(z_j)$ at ∂I_j^-. Therefore the integral of $Vu_z\phi_i$ at ∂I_j^- is equal to $V\phi_i(z_j)(u(z_j^+) - u(z_j^-))$. Differentiating eq. (3.132) and substituting it into eq. (3.135) gives

$$V\phi_i(z_j)(u(z_j^+) - u(z_j^-)) + \int_{I_j} V\left(\sum_1^K u_i\phi_{iz}\right)\phi_i dz = \int_{I_j} g\phi_i dz \quad i=1\ldots K \quad (3.136)$$

u_i can be solved from a set of linear equations described by (3.136), and u in I_j can be assembled by using eq. (3.132). In this thesis K is set as 2, and local basis functions ϕ_1 and ϕ_2 are therefore linear and shown in Figure 3.17.

For a function with discontinuity at the element boundary, the first order derivative can be defined at the discontinuous element boundary and it is nothing but the dirac delta function, but the second order derivative can not be defined at the discontinuous element boundary. Therefore the discontinuous Galerkin method can not be directly applied to the governing equations for native point defects and oxygen which have diffusion terms. The way to get around this is to introduce the auxiliary vector. For example, the original governing equation for oxygen is

$$\left(\frac{\partial}{\partial t} + V\frac{\partial}{\partial z}\right)C_O + \nabla \bullet (-D_O(T)\nabla C_O) + \left(\frac{\partial}{\partial t} + V\frac{\partial}{\partial z}\right)\int_2^\infty nf_O dn = 0 \quad (3.137)$$

By introducing the auxiliary vector $\vec{q}_O$, the eq. (3.137) above becomes

$$\left(\frac{\partial}{\partial t} + V\frac{\partial}{\partial z}\right)C_O + \nabla \bullet (-D_O(T)\vec{q}_O) + \left(\frac{\partial}{\partial t} + V\frac{\partial}{\partial z}\right)\int_2^\infty nf_O dn = 0 \quad (3.138)$$

$$\vec{q}_O = \nabla C_O \quad (3.139)$$

Eqs. (3.138) and (3.139) are a set of first order differential equations for C_O and $\vec{q}_O$, therefore the discontinuous Galerkin method can be applied to both C_O and $\vec{q}_O$. The method of applying the discontinuous Galerkin method to the second order differential

equation by introducing the auxiliary vector is called the local discontinuous Galerkin method (LDG) [7,22]. The details of the implementation of the discontinuous Galerkin method and the local discontinuous Galerkin method into the point defects and their clusters can be referred to [108].

3.6.3 Time Integration

An operator splitting method is used to decouple the point defect equations and clusters equations at each time step [108]. The time integration scheme is shown in Figure 3.18. At time t_{m+1}, keep the values of concentrations of point defects $C_X(t_m)$ ($X = I, V, O$) at time t_m and the implicit Eular method is used to solve concentrations of clusters $C_{nX}(t_{m+1})$ and $f_X(t_{m+1})$ first. Then the implicit Eular method is used to solve concentrations of point defects $C_X(t_{m+1})$ at time t_{m+1} by using the $C_{nX}(t_{m+1})$ and $f_X(t_{m+1})$ just solved in the previous step.

Figure 3.18: The time integration scheme: the operating splitting method.
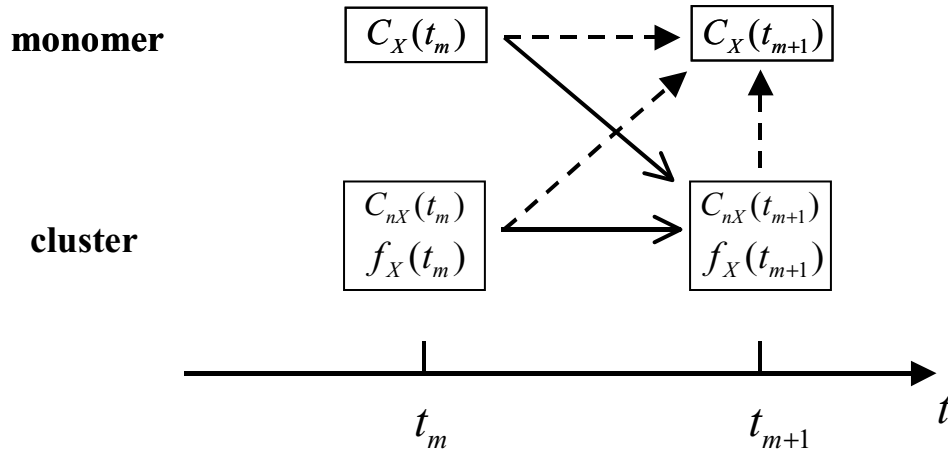
This time integration method is a kind of semi-implicit method. It may be iterated at each time step to get more accurate solutions. Every time when $C_{nX}(t_{m+1})$ and $f_X(t_{m+1})$ to be solved, the newest values of $C_X(t_{m+1})$ are used. Every time when $C_X(t_{m+1})$ to be solved, the newest values of $C_{nX}(t_{m+1})$ and $f_X(t_{m+1})$ are used.

Adaptive time step control can be used to make the numerical simulation more efficient [42]. Let $C_X(\Delta t_m)$ denotes $C_X(t_{m+1})$ computed with one time step of size $\Delta t_m = t_{m+1} - t_m$, $C_X(\Delta t_m/2)$ for $C_X(t_{m+1})$ computed with two time steps of size $\Delta t_m/2$, and C_X^* for $C_X(t_{m+1})$ with zero local error. Since the Eular method used here has the first order accuracy,

$$C_X^* = C_X(\Delta t_m) + K_X \Delta t_m^2 + O(\Delta t_m^3) \tag{3.140}$$

$$C_X^* = C_X(\Delta t_m/2) + 2K_X(\Delta t_m/2)^2 + O(\Delta t_m^3) \tag{3.141}$$

where K_X is constant. Combining eqs. (3.140) and (3.141), and eliminating the second order terms for Δt_m gives

$$C_X^* = [2C_X(\Delta t_m/2) - C_X(\Delta t_m)] + O(\Delta t_m^3) \tag{3.142}$$

Eq. (3.142) indicates that extrapolation from $C_X(\Delta t_m/2)$ and $C_X(\Delta t_m)$ by expression $2C_X(\Delta t_m/2) - C_X(\Delta t_m)$ has higher order accuracy than the Eular method.

Subtracting eq. (3.140) from eq. (3.141) gives

$$\frac{1}{2}K_X\Delta t_m^2 \approx C_X(\Delta t_m/2) - C_X(\Delta t_m) \tag{3.143}$$

Based on eq. (3.143), the next time step Δt_{m+1} is taken as

$$\Delta t_{m+1} = \Delta t_m \, min\left(\left(\frac{\varepsilon}{C_X(\Delta t_m/2) - C_X(\Delta t_m)}\right)^{1/2}, 2\right) \tag{3.144}$$

where ε is the error limit, and X represents native point defects and oxygen. The 2 is to avoid large increases in time step size.

3.7 Enhanced Oxygen Precipitation due to Grown-in Spatial Inhomogeneities in the Oxygen Distribution

3.7.1 Nonuniform Oxygen Distribution in Silicon Crystal
As discussed in Section 3.2, models based on diffusion-limited homogeneous nucleation

have been used extensively in attempts to predict observed oxide precipitate nucleation and growth rates. There are several significant outstanding problems with current models of oxide precipitation. The most notable problem is the apparently anomalous nucleation rate seen experimentally at low temperatures (below about 600 $^{\circ}C$). Simulations predict oxide precipitation kinetics reasonably well across a wide temperature range, but fail dramatically at temperatures below 600 $^{\circ}C$. Many factors could contribute this phenomena. For example, the migration energy for oxygen at low temperature could be 1.5 eV instead of 2.5 eV at high temperature as discussed in Section 3.3.1. That means the oxygen diffusivity at low temperature extrapolated from high temperature oxygen diffusivity is much lower than that predicted from lower migration energy. This anomalous oxygen diffusivity at low temperature together with ramping process could explain anomalous nucleation rate for oxygen precipitates at low temperature.

The role of an inhomogeneous oxygen monomer distribution within the silicon bulk as a potentially important factor in setting the observed nucleation and growth rates during wafer annealing and crystal growth is considered here. The non-uniform incorporation of oxygen into Czochralski silicon is well known [55,199] because of microscopic fluctuations in the solidification rate at the crystal-melt interface, as caused by imperfections in the crystal growth system [197,198] and turbulent fluctuations in the melt. An example of such grown-in spatial inhomogeneities in the oxygen distribution is shown in Figure 3.19. The magnitude of these fluctuations depends on the segregation of oxygen at the melt/solid interface and on the size of the fluctuations in the solidification rate. Marioton and Gosele [101] have postulated this mechanism for enhanced oxygen precipitation, but did not explore it further. The effect of the resulting inhomogeneity in the oxygen concentration is quantitatively investigated through two separate calculations. The first is the analysis of a simple model that shows how a spatially inhomogeneous oxygen concentration,

coupled with the nonlinear kinetics for the nucleation of precipitates, can lead to substantial increases in the apparent nucleation rates. The second calculation is based on a detailed simulation of oxygen precipitation using a self-consistent model of point defect dynamics and oxygen precipitation.
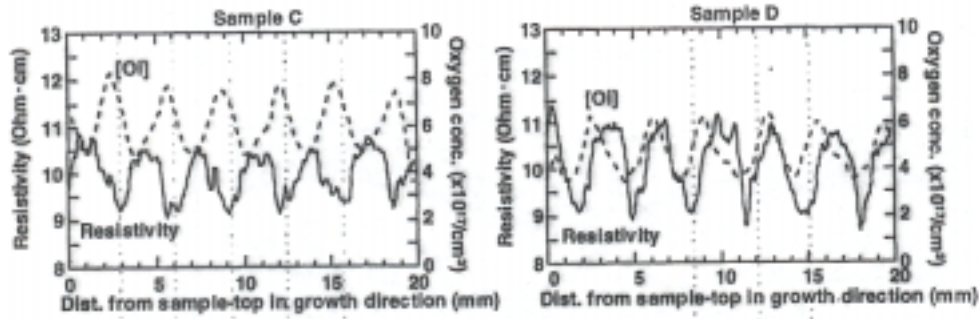
Figure 3.19: Grown-in spatial inhomogeneities in the oxygen distribution (taken from [55]).

3.7.2 Model Problem

In the simple model we consider the evolution in time (τ) of the one-dimensional profile (x) of a species $C(x, \tau)$ that is governed by the simple nonlinear reaction-diffusion equation that models transport of a dilute species, such as oxygen, and consumption of the species into aggregates according to a p-th order reaction:

$$\frac{\partial C}{\partial \tau} = \frac{\partial^2 C}{\partial x^2} - Da C^p \tag{3.145}$$

where Da is the dimensionless reaction rate, or Damkohler number, which scales reaction rate with diffusion. The magnitude of the reaction rate, p, depends on whether nucleation or growth of the precipitates is being considered.

In eq. (3.145) the appropriate length scale λ describes the initial inhomogeniety in the dimensionless monomer concentration:

$$C(x, 0) = 1 + \varepsilon \cos(2\pi x) \tag{3.146}$$

180

where ε sets the amplitude of the fluctuation; $\varepsilon = 0$ corresponds to a uniform initial oxygen concentration. The initial-value problem, eqs. (3.145) and (3.146), is solved with no flux boundary conditions at $x=0$ and $x=1$. When $\varepsilon = 0$, the concentration is always uniform in space and is expressed as $C(x, \tau) = C_u(\tau)$. The governing equation for $C_u(\tau)$ is therefore reduced to ordinary differential equation

$$\frac{\partial C_u}{\partial \tau} = -Da C_u^p \tag{3.147}$$

The solution is

$$C_u(\tau) = \frac{1}{(1 + (p-1)Da\tau)^{\frac{1}{p-1}}} \tag{3.148}$$

A reaction enhancement factor is defined based on the reference state $C_u(\tau)$, so that

$$\eta(\tau) \equiv \frac{1 - \langle C(x, \tau) \rangle}{1 - C_u(\tau)} \tag{3.149}$$

where $\langle . \rangle$ stands for averaging the concentration over $0 \le x \le 1$. Then $\eta(\tau)$ measures the consumption of single oxygen atoms based on homogeneous nucleus formation and growth; for $\varepsilon = 0$, $\eta(\tau) = 1$. The form of η is inspired by the availability of FTIR measurements for the concentration of interstitial single oxygen atoms within bulk silicon [].

The effects of changing Da and p were probed by analytical ($Da \gg 1$) and numerical solution of eqs. (3.145) and (3.146); the results are depicted in Figure 3.20 in terms of the evolution of $\eta(\tau)$ for $\varepsilon = 0.5$. Time is scaled as $Da\tau$ because $C(x, \tau)$ is only a function of $Da\tau$ for $\varepsilon = 0$ as shown in eq. (3.148). For $Da \gg 1$, the diffusion term in eq. (3.145) can be ignored and the time has to be rescaled,

$$\frac{\partial C}{\partial (Da\tau)} = -C^p \tag{3.150}$$

Therefore the analytical solution for $Da \gg 1$ is

$$C(x, \tau) \;=\; \cfrac{1}{\left(\cfrac{1}{C(x,\,0)^{\,p-1}} + (p-1)Da\tau\right)^{\frac{1}{p-1}}} \tag{3.151}$$

And the $\eta(\tau)$ for $Da \gg 1$ is

$$\eta(\tau) \equiv \cfrac{1 - \displaystyle\int_0^1 \cfrac{1}{\left(\cfrac{1}{C(x,\,0)^{\,p-1}} + (p-1)Da\tau\right)^{\frac{1}{p-1}}}\,dx}{1 - \cfrac{1}{(1 + (p-1)Da\tau)^{\frac{1}{p-1}}}} \tag{3.152}$$
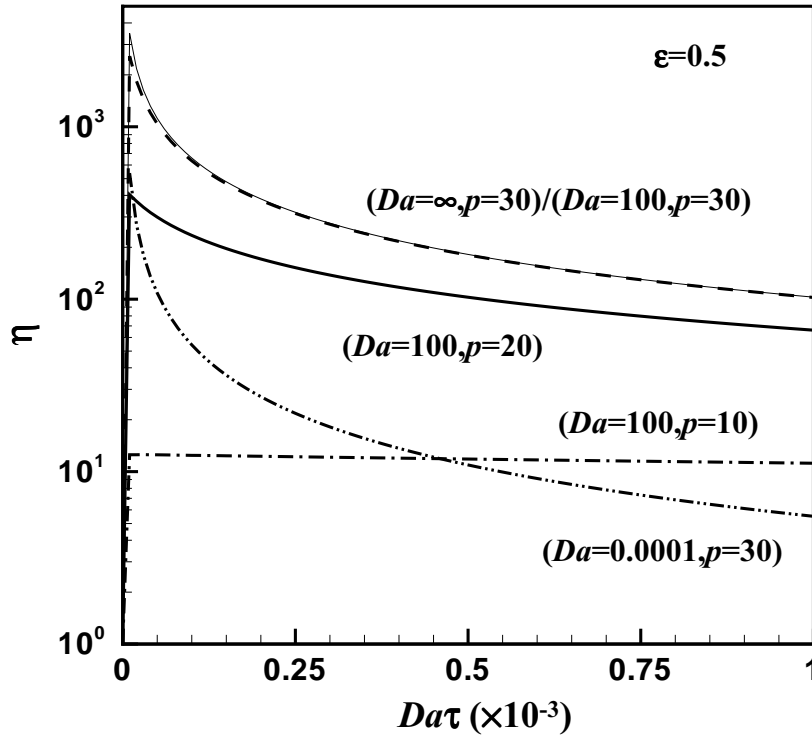

Figure 3.20: Enhancement factor predicted with model described by eq. (3.145) with $\varepsilon=0.5$.

In all cases, $\eta(\tau)$ quickly reaches a maximum and then decays gradually at a rate set by Da. For $Da \gg 1$, the fast reaction rate relative to diffusion allows minimal dispersion of

the initial fluctuation in the oxygen concentration. For slow reaction rates ($Da \ll 1$), diffusion effectively levels the peaks in oxygen concentration before significant reaction can take place. The value of $\eta(\tau)$ at relatively long times is primarily a function of the reaction order, p. As p increases, $\eta(\tau)$ also increases for a given $Da\tau$, while for $p = 1$ $\eta(\tau) = 1$ for any value of ε. When $p = 1$, eq. (3.145) becomes

$$\frac{\partial C}{\partial \tau} = \frac{\partial^2 C}{\partial x^2} - DaC \tag{3.153}$$

Integrating from $x = 0$ to $x = 1$

$$\frac{\partial \int_0^1 Cdx}{\partial \tau} = \int_0^1 \frac{\partial^2 C}{\partial x^2}dx - Da\int_0^1 Cdx \tag{3.154}$$

Rewriting the first term on the right-hand side

$$\frac{\partial \int_0^1 Cdx}{\partial \tau} = \frac{\partial C}{\partial x}\bigg|_{x=0}^{x=1} - Da\int_0^1 Cdx \tag{3.155}$$

Employing the no-flux boundary conditions on both ends

$$\frac{\partial \langle C \rangle}{\partial \tau} = -Da\langle C \rangle \tag{3.156}$$

The equation about for $\langle C \rangle$ is the same as equation for C_u when $p = 1$, which implies $\eta(\tau) = 1$ for $p = 1$. This fact is easily understood by noting that for $p = 1$ eq. (3.145) is linear and the regions of higher reaction rate caused by increased initial values of $C(x, \tau)$ are exactly balanced by lower reaction rates in regions with lower concentrations. The apparent value of the reaction order can be connected to the processes of nucleation and growth. For precipitate growth, the reaction rate is first-order in the oxygen concentration, $C(x, \tau)$, $p = 1$. For the nucleation process, the reaction rate scales as a power of C roughly equal to the number of oxygen atoms in a critically sized precipitate at a given

temperature.

The results of the simple model, eq. (3.145), suggest that an initially nonhomogeneous oxygen concentration will lead to an enhanced nucleation rate of oxide clusters. The extent of the enhancement is a function of the amplitude and frequency of the initial oxygen fluctuations. Increasing the fluctuation frequency is equivalent to decreasing λ or to decreasing Da and thus leads to enhanced oxygen diffusion and to decreasing $\eta(\tau)$. The effect of increasing ε is shown in Figure 3.21 and is dramatic. Enhancements range from $O(10^1)$ for $\varepsilon = 0.2$ to $O(10^2)$ for $\varepsilon = 0.5$.
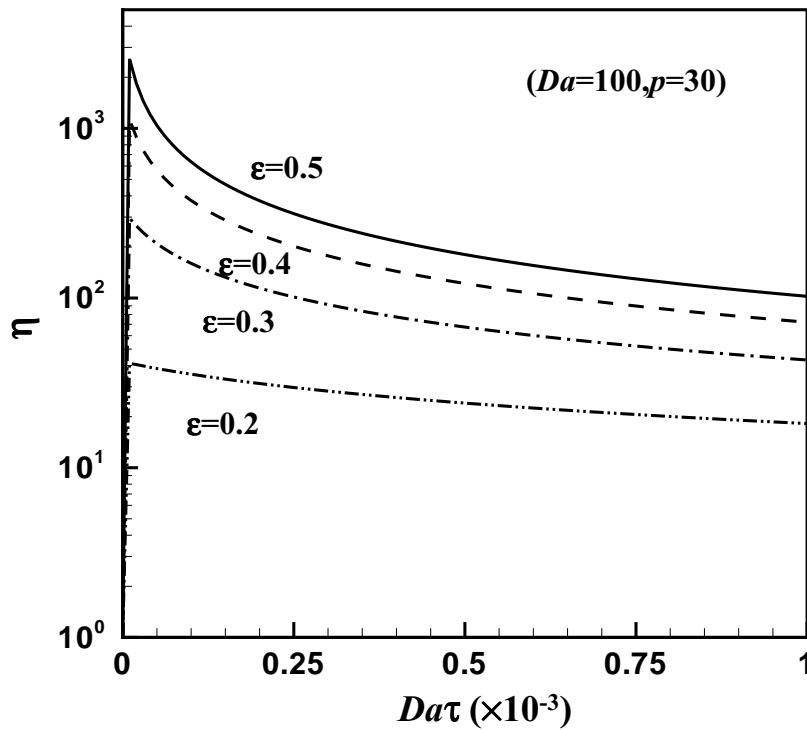

Figure 3.21: Enhancement factor predicted with model described by eq. (3.145) for varying amplitude ε; $Da=100$ and $p=30$.

3.7.3 Simulation Results of Enhanced Oxygen Precipitation

Prediction of the effect of spatial fluctuations in the oxygen concentration on the precipitate size distribution has been made by direct time-dependent simulation of a Low-Hi

wafer annealing using a defect dynamics model for disk-shaped oxygen precipitates which is discussed in Section 3.3 - 3.5. The Low-Hi wafer annealing procedure includes 450 $°C$ anneal for 32 hours (the nucleation phase) followed by 800 $°C$ anneal for 4 hours and then 1000 $°C$ anneal for 16 hours (the precipitate growth phase). The ramping rate is $5°C$/min which is an industry standard. There is no pre-anneal at very high temperature, so there is no enough pre-established vacancy to release high stress energy associated with spherical oxygen precipitates, therefore disk-shaped oxygen precipitates dominate. It is assumed that the oxygen concentration in the wafer is non-uniform with a spatial frequency given by eq. (3.146) with spatial wavelength $\lambda = 100\mu m$ and that there are initially no precipitates in the wafer. The average oxygen concentration is taken to be $6 \times 10^{17} cm^{-3}$. A no-flux boundary condition for oxygen is assumed in order to separate the effects of the nonhomogeneous oxygen concentration from the effects of the surface denuded zone. The results of the wafer annealing simulations with varying ε are presented in terms of the average oxide precipitate size distribution over the wavelength and the enhancement factor η. The enhancement factor is computed using eq. (3.149) by averaging the total loss of oxygen monomer over the wavelength.

The resulting size distribution of oxide is shown in Figure 3.22 for different values of ε. The unit for size of oxygen precipitate is the amount of oxygen in the precipitate. The case of a uniform oxygen distribution, $\varepsilon = 0$, produced the smallest number of precipitates and results in a size distribution with the smallest precipitates. When $\varepsilon = 0.5$, the number of clusters is approximately two orders-of-magnitude larger and larger clusters are grown. The total concentration of oxide clusters bigger than 5nm and the total number of oxygen atoms in these clusters are listed in Table 3.2. The enhancement factors relative to the base case are estimated by computing the total number of oxygen atoms represented

185

by each of the size distributions; $\eta = 1.13 \times 10^1$ for $\varepsilon = 0.2$ and $\eta = 3.51 \times 10^2$ for $\varepsilon = 0.5$.
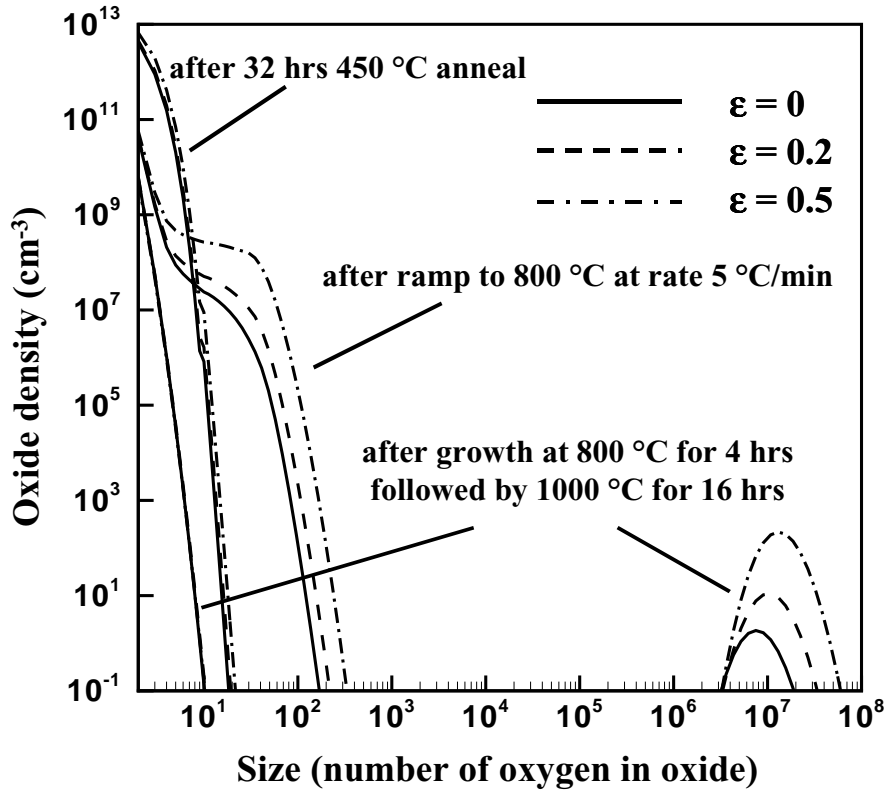
Figure 3.22: Average size distribution of oxygen precipitates predicted with simulations of Low-Hi wafer annealing for values of ε of 0, 0.2, and 0.5.

Oxygen Field	Oxide Density (cm^{-3})	Total Oxygen in the Oxide (cm^{-3})	Enhancement Factor
Uniform $\varepsilon = 0$	1.42×10^7	1.35×10^{14}	1
Nonuniform $\varepsilon = 0.2$	1.18×10^8	1.52×10^{15}	1.13×10^1
Nonuniform $\varepsilon = 0.5$	2.89×10^9	4.74×10^{16}	3.51×10^2

Table 3.2: Results for annealing simulations after Low-Hi wafer annealing: total concentration of oxide clusters larger than 5nm, total oxygen atoms in these clusters, and the enhancement factor.

These results demonstrate that the microscopic fluctuations in the oxygen concentration profile that are typically seen in silicon grown by the Czochralski method can have a significant effect on the number and size distribution of oxide precipitates in annealed wafers. In particular, the non-homogeneous oxygen distributions lead to faster nucleation rates at low temperatures because of the impact of the highly nonlinear kinetics during this phase. The effect of this spatial inhomogeneities could be very general. For any non-linear system with the spatial fluctuation, the enhancement of apparent kinetic could be observed.

3.8 Perfect Silicon

3.8.1 Concept of Perfect Silicon

As discussed in section 2.1, roughly the OSF-ring separates the vacancy-rich core, which is populated by voids, from the self-interstitial-rich outer annulus, which contains stacking faults. However, strictly speaking OSF-ring is close to but inside the radial position where interstitial and vacancy recombine exactly with each other. This spatial pattern is displayed in Figure 3.23 for an as-grown crystal wafer. A very interesting region of the crystal lies just outside the OSF-ring. The silicon in this region is almost defect-free except some small oxide precipitates which are created during crystal growth and can be dissolved by a high temperature annealing afterward. The existence of this region is an indication of the crystal growth conditions where almost perfect silicon can be grown. The detail of this structure also can be described as $R_{OSF} < R_{free} < R_{\Delta = 0}$, where R is radius, and subscripts *OSF*, *free* and $\Delta = 0$ correspond to OSF-ring, defect-free region, and the region where interstitial and vacancy recombine exactly with each other. Others have recognized the quality of this material [41] and silicon wafer suppliers have begun producing this "perfect silicon" [40].
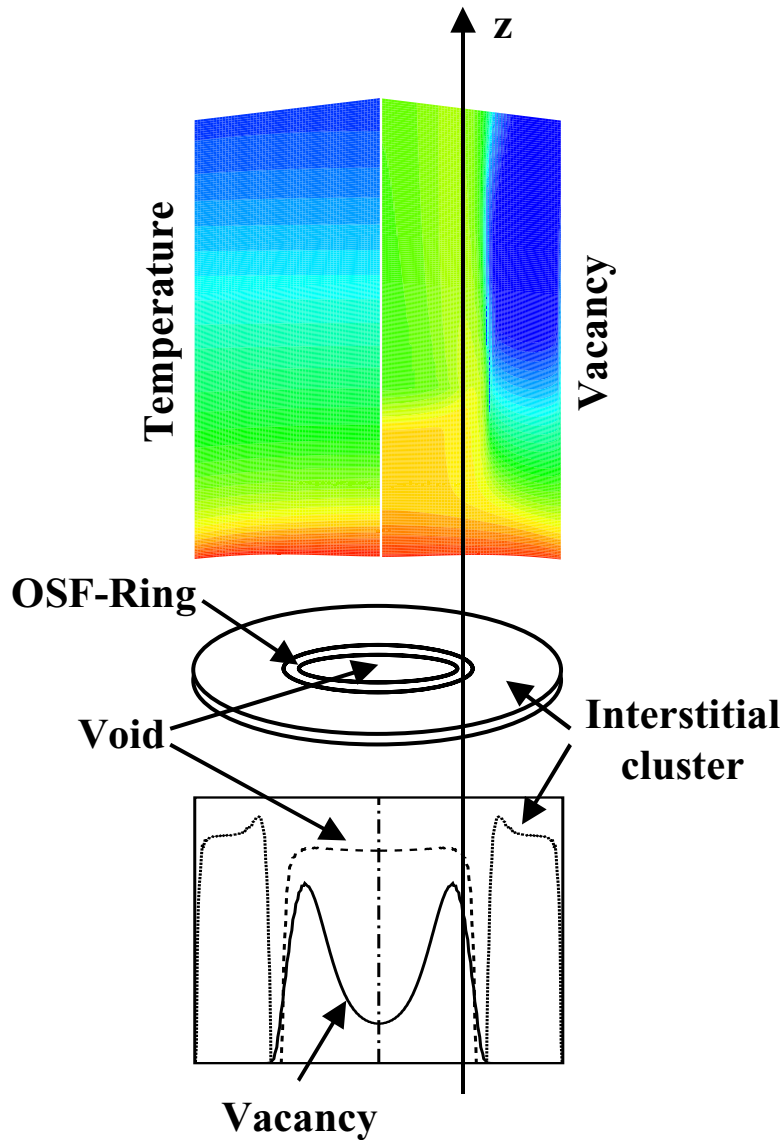
Figure 3.23: Qualitative picture of the asymmetric defect dynamics in the CZ crystal growth. The temperature profile and vacancy distribution are shown throughout the crystal for growth conditions with the OSF-ring inside the crystal. The distribution of point defects and aggregates in a wafer from this crystal are shown in the bottom graph.

Just inside $R_{\Delta = 0}$, there is no significant interstitials and their clusters since it is in vacancy-rich region. The intermediate vacancy concentration is relative low and therefore the void aggregation temperature is relative low. Without other impurity such as oxygen involved, significant voids can still form but at lower temperature. However with appro-

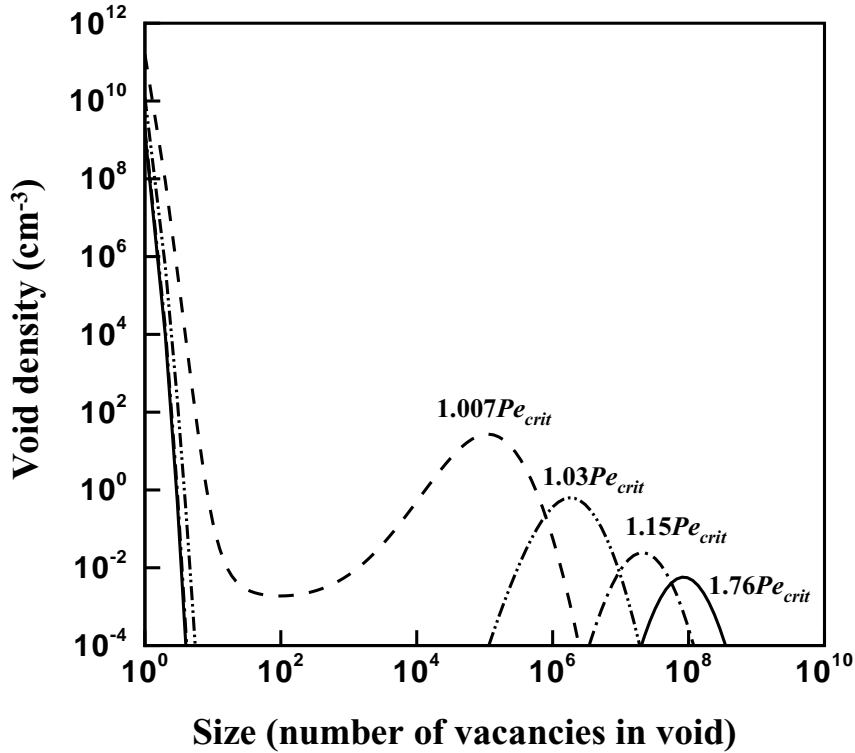priate oxygen present, vacancy can be consumed by small oxygen precipitates before the low void aggregation temperature leaving no driving force for void formation. These small oxygen precipitates can be then dissolved by a high temperature anneal. So the oxygen with appropriate concentration in silicon widens the operating windows for defect-free or perfect silicon.

3.8.2 Simulation Results

The simulation results of CZ-crystal growth with and without oxygen are compared in this section to illustrate the effect of oxygen and 'prefect' silicon. One-dimensional (neglecting radial diffusion) simulations of point defect dynamics and microdefect formation in crystal growth without oxygen are shown in Figure 3.24 for several growth rates. The axial temperature profile used in the calculations also is shown in Figure 3.24(a). The vacancy profile in Figure 3.24(a) is typical for growth of a vacancy-rich crystal. After rapid recombination, the intermediate vacancy concentration C_V^{int} is established and persists until the temperature decreases to the void aggregation temperature for $C_V = C_V^{int}$. The density of voids rapidly rises and vacancy concentration begins to decrease as the vacancies are absorbed into the voids. The void aggregation temperature is not a constant, but dependent on the intermediate vacancy concentration. For lower intermediate concentration only at lower temperature the super-saturation of vacancy can be high enough to drive the void formation. Lowering the pull rate so that $Pe/Pe_{crit} \to 1$ decreases C_V^{int}, as predicted by eq. (2.109) and shifts void aggregation to lower temperatures. The size distribution of voids predicted for these values of Pe are shown in Figure 3.24(b). For Pe much bigger than Pe_{crit} the voids are large, as is characteristic of CZ-silicon. The profile for $Pe = 1.76 Pe_{crit}$ corresponds to a average void diameter of 145 nm and a total density of voids larger than 50 nm of $6.9 \times 10^5 \ cm^{-3}$.

C_V

Total void density

1.76Pe_{crit}

1.15Pe_{crit}

1.03Pe_{crit}

1.007Pe_{crit}
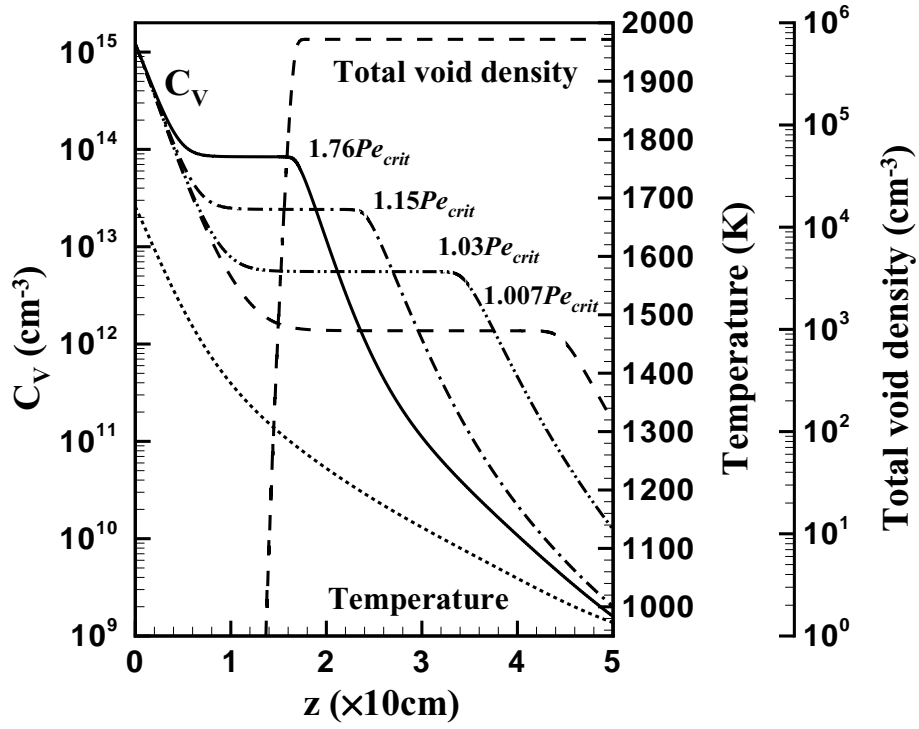
Temperature

(a)

(b)

Figure 3.24: One-dimensional simulation results of CZ-crystal without oxygen: (a) Vacancy profiles during crystal growth under the same temperature field but different Pe. Total void density is shown for $Pe=1.76Pe_{crit}$. (b) Void size distributions for different Pe.

The presence of oxygen in CZ silicon improves the quality of the as-grown material. As the temperature decreases in the crystal the super-saturation of oxygen causes small clusters of oxide to form that consume a portion of the intermediate vacancy concentration and make these vacancies unavailable for aggregation into voids. This effect is enhanced by the delay of the nucleation of voids; as a result, the final voids become smaller as $Pe \rightarrow Pe_{crit}$. This effect is demonstrated in the simulations shown from Figure 3.25 to Figure 3.28 for $Pe = 1.76Pe_{crit}$ and $Pe = 1.007Pe_{crit}$ for crystals without oxygen and with an oxygen concentration of $C_O = 6.0 \times 10^{17} \ cm^{-3}$ introduced at melt/crystal interface.

For $Pe = 1.76Pe_{crit}$ the presence of oxygen has no effect on the vacancy concentration until a temperature much lower than the void aggregation temperature under this growth condition, as shown in Figure 3.25. At $z > 3.4$ where most of the intermediate vacancies are already depleted by void formation, the vacancy concentration with oxygen present is lower than that without oxygen because these residual vacancies are consumed by oxygen precipitates at low temperature. The final size distributions of voids and oxygen precipitates at the top of the crystal are shown in Figure 3.26. There is essentially no effect of the oxygen on the void distribution and only very small oxygen precipitates are predicted to be present.
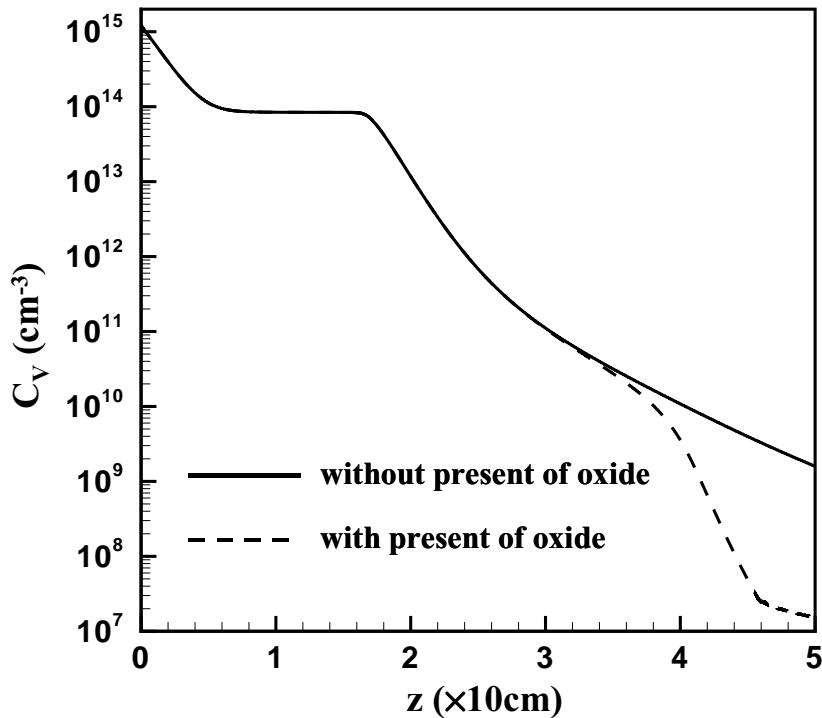

Figure 3.25: Vacancy profiles for $Pe=1.76Pe_{crit}$ with and without oxygen.
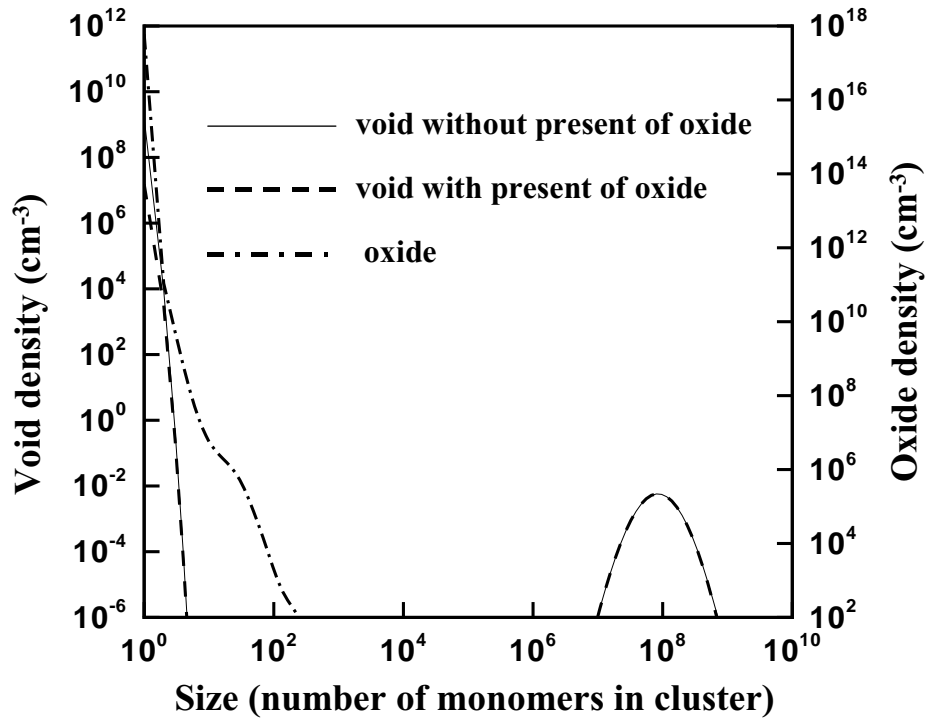
Figure 3.26: Void size distributions with and without oxygen, and oxygen precipitate size distribution for $Pe=1.76Pe_{crit}$.

For $Pe = 1.007Pe_{crit}$, the profiles of vacancy are shown in Figure 3.27, and the size distributions of voids and oxygen precipitates are shown in Figure 3.28. The predictions are drastically different for $Pe = 1.007Pe_{crit}$. Under this growth condition, the intermediate vacancy concentration is relative low compared with that under high Pe. Therefore the void aggregation temperature is also low. The vacancy profiles with and without oxygen in Figure 3.27 clearly show that vacancies are already consumed by oxygen precipitates significantly before they can be consumed by voids. The delay in the aggregation of voids to a lower temperature caused by the decrease in the intermediate vacancy concentration leads to much more growth of small oxide precipitates and to substantial depletion of the already smaller reservoir of vacancies. As a result, void density is significantly

decreased with oxygen present, as shown in Figure 3.28. Slightly larger oxygen precipitates are predicted but are only barely visible; essentially there is no oxygen precipitate bigger than 50 nm in diameter which is roughly the detection limit. The density of oxygen precipitates above the 5 nm is only $8.6 \times 10^5 \ cm^{-3}$. Fortunately these small oxygen precipitates could be dissolved during a high temperature annealing which is normally the first step of traditional Hi-Low-Hi wafer annealing. It should be also noted that oxygen concentration barely changes during the crystal growth. Only a very small faction of oxygen exists in the form of oxygen precipitates. The silicon crystal grown under this condition is essentially defect-free or prefect: there is no interstitials and their clusters since it is in vacancy-rich region; there is no significant voids since the void formation is suppressed by oxygen precipitation; there is only some small oxygen precipitates which can be dissolved by a high temperature anneal afterward.
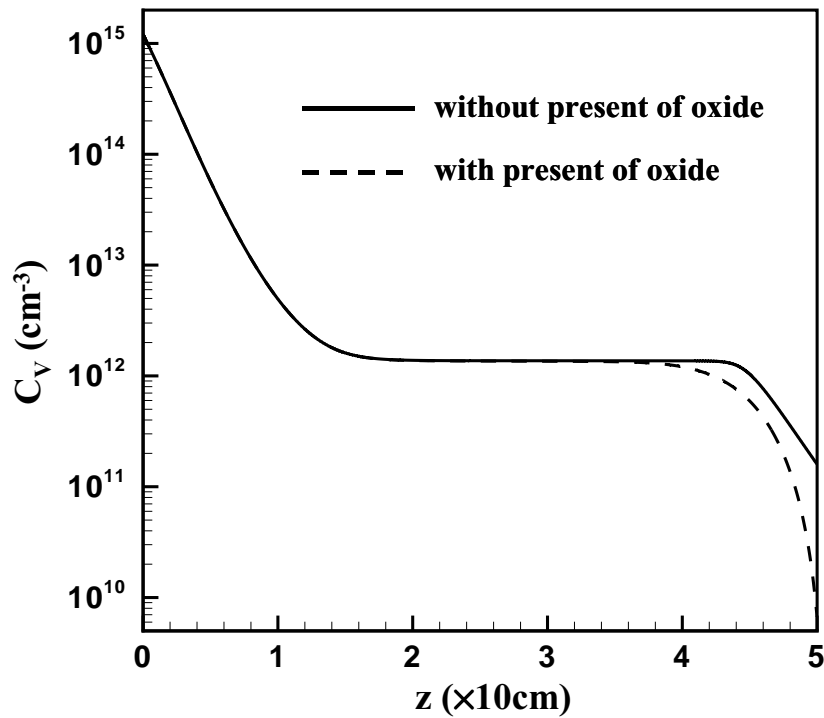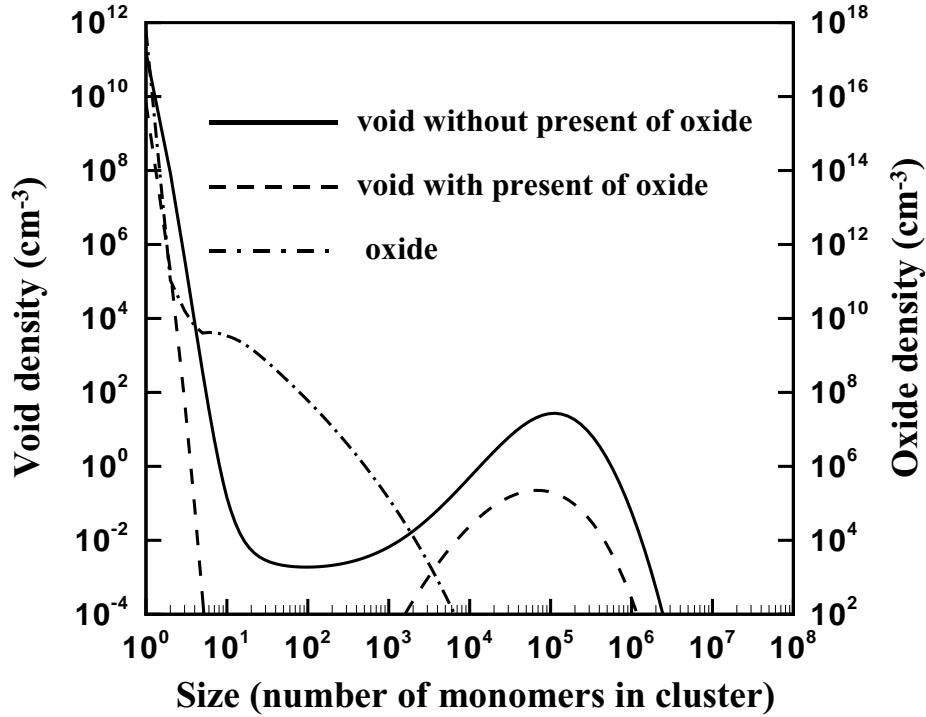
Figure 3.28: Void size distributions with and without oxygen, and oxygen precipitate size distribution for $Pe=1.007Pe_{crit}$.

The simulations of point defect dynamics and aggregation described here demonstrate theoretically that almost defect-free or perfect silicon can be produced by melt crystal growth at the precise conditions where the intermediate point defect concentrations caused by rapid point defect recombination at high temperatures are approximately equal. The presence of oxygen reduces the sensitivity of this operating window to the exact value of pull rate (or temperature gradient) and essentially opens the operating window making growth of this material more feasible. Control of the final oxide precipitate distribution in the material is still achieved using conventional annealing cycles.

3.9 Wafer Annealing

3.9.1 Typical Hi-Low-Hi Wafer Annealing

Oxides or oxygen precipitates with appropriate size and density can serve as gettering sites for metallic impurities which are introduced during fabrication processes, and they may be only concentrated in the middle of the wafer, leaving a defect-free surface section or denuded zone (DZ) where devices can be fabricated. This spatially nonuniform distribution of oxygen precipitates within wafer can be achieved by a traditional Hi-Low-Hi wafer annealing process.

The physics of Hi-Low-Hi wafer annealing can be illustrated by one-dimensional simulation along axial direction. The computational domain is shown in Figure 3.29. The wafer thickness is 725 μm which is typical for 8-inch wafer. Because of symmetry the computational domain is the half thickness of the wafer. The dimensionless axial position $z = 0$ (length scale is chosen as 100 μm) corresponds to wafer surface and $z = 3.625$ corresponds to centerline of the wafer thickness. The initial oxygen concentration of Hi-Low-Hi wafer annealing is set to $8 \times 10^{17} cm^{-3}$ uniformly distributed across the wafer. The boundary conditions for oxygen are equilibrium oxygen concentration at annealing temperature at $z = 0$ and no-flux boundary conditions at $z = 3.625$. Some small oxygen precipitates formed during crystal growth can be dissolved quickly (within seconds) during the first high temperature and this dissolution process is called the removal of the 'thermal history'. So it is reasonable to set zero concentration for all oxygen precipitates as initial condition of Hi-Low-Hi wafer annealing. Unless the temperature of the first step is very high (for example, higher than 1200 $°C$) and the cooling rate after this step is very fast (for example, about $100°C/s$), the vacancy established after the first high temperature anneal is not high enough to form significant spherical oxygen precipitates through vacancy absorption mechanism. As already discussed in Section 3.5.3, the spherical oxy-

gen precipitation through interstitial injection is also slow due to the inefficient removal of interstitials ejected by spherical oxygen precipitates. So the majority of oxygen precipitates are disk-shaped oxygen precipitates for a typical Hi-Low-Hi wafer annealing. The wafer annealing processes simulated here is 1100 $^\circ C$ anneal for 16 hours followed by 650 $^\circ C$ anneal for 16 hours and then 1000 $^\circ C$ anneal for 16 hours.

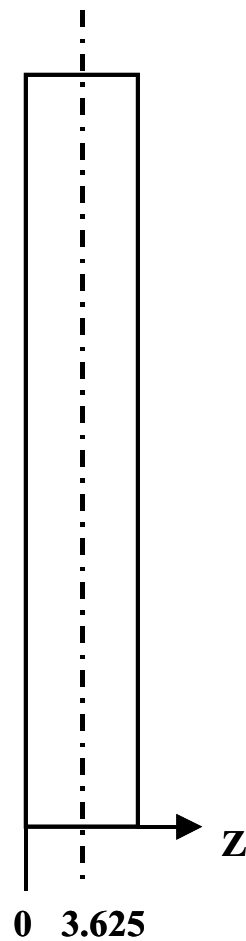**Figure 3.29:** Wafer cross-section and computational domain.

The oxygen profile after the first high temperature anneal at 1100 $^\circ C$ for 16 hours is shown in Figure 3.30. Oxygen concentration near the wafer surface is significantly reduced due to out-diffusion of oxygen, however the oxygen concentration in the bulk of wafer barely changes because of low diffusivity of oxygen with respect to length scale of

wafer thickness, for example $D_O = 8.03 \times 10^{-11} cm^2/s$ at $1100 \, ^\circ C$. This spatially non-uniform oxygen pattern is the root cause of the low density of oxygen precipitates near wafer surface and the high density of oxygen precipitates in the middle section of the wafer. During the second low temperature anneal at $650 \, ^\circ C$ for 16 hours, the super-saturation of oxygen is not high enough near the wafer surface to drive the oxygen precipitation. However, small oxide nuclei are generated by the high super-saturation of oxygen in the bulk of the wafer, but it is difficult for these nuclei to grow bigger because the temperature is too low for oxygen diffusion even in short range. The last step is the growth of the oxygen precipitates in the bulk of the wafer at $1000 \, ^\circ C$ for 16 hours. At this stage, nuclei generated during the second low temperature anneal grow rapidly due to the relative high oxygen diffusivity at high temperature. The nucleation and growth of oxygen precipitates in the bulk of the wafer are clearly illustrated in the simulation results of the size distributions of oxygen precipitates at the center of the wafer after each annealing step shown in Figure 3.31. The final distribution of total oxide density across the wafer is shown in Figure 3.32. The oxide density in the bulk is about 10^{10} cm^{-3} and they can serve as effective gettering sites for metallic impurities which are introduced during the device fabrication. The near surface region with low density of oxygen precipitates is called denuded zone where devices are fabricated.
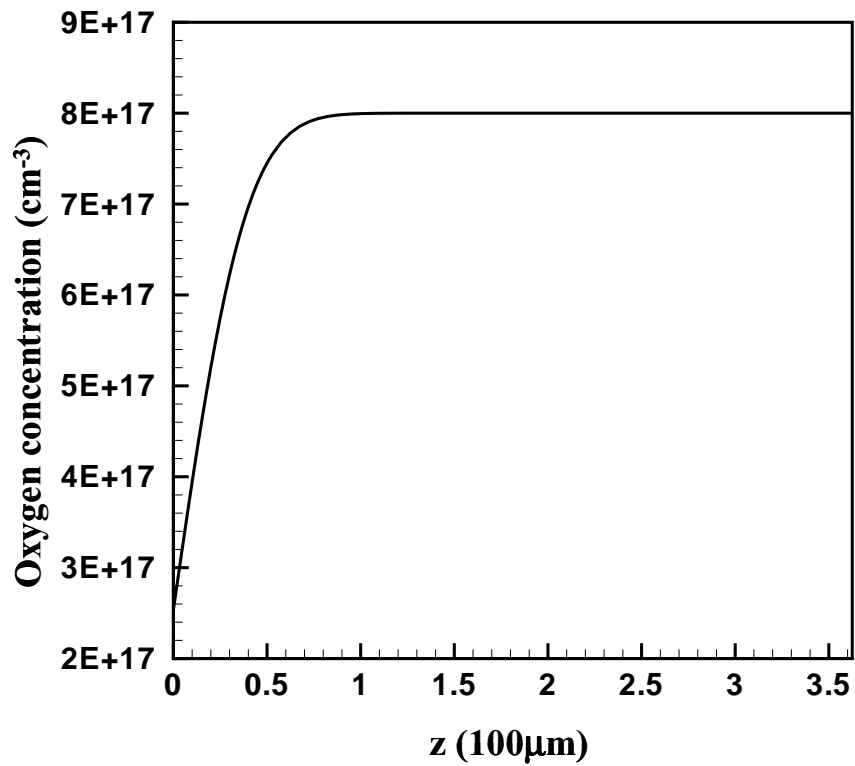
Figure 3.30: Oxygen profile after the first high temperature anneal at 1100 $°C°C$ for 16 hours.
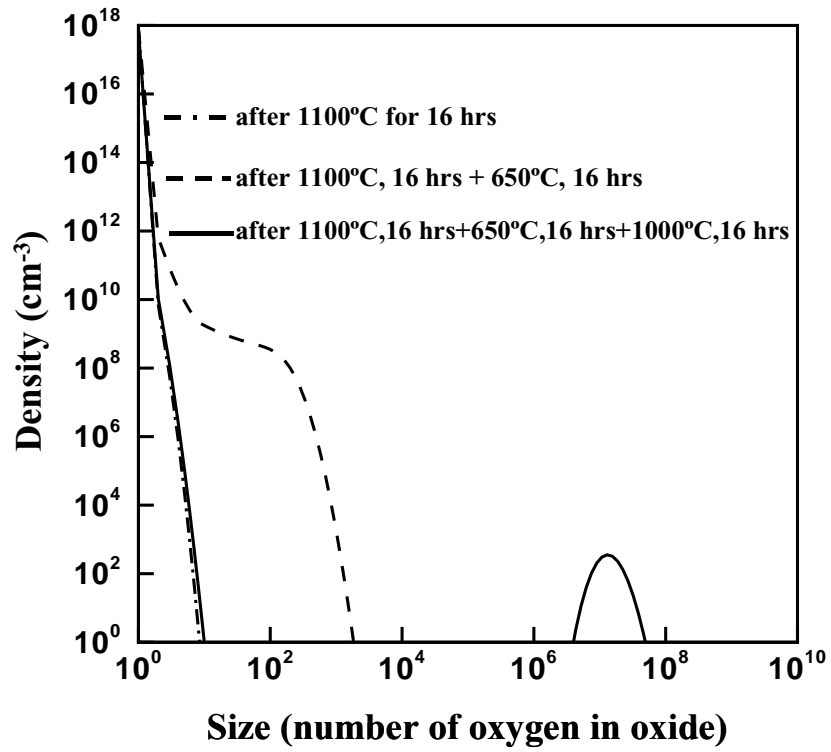
Figure 3.31: Size distributions of oxygen precipitates at the center of the wafer after each annealing step.
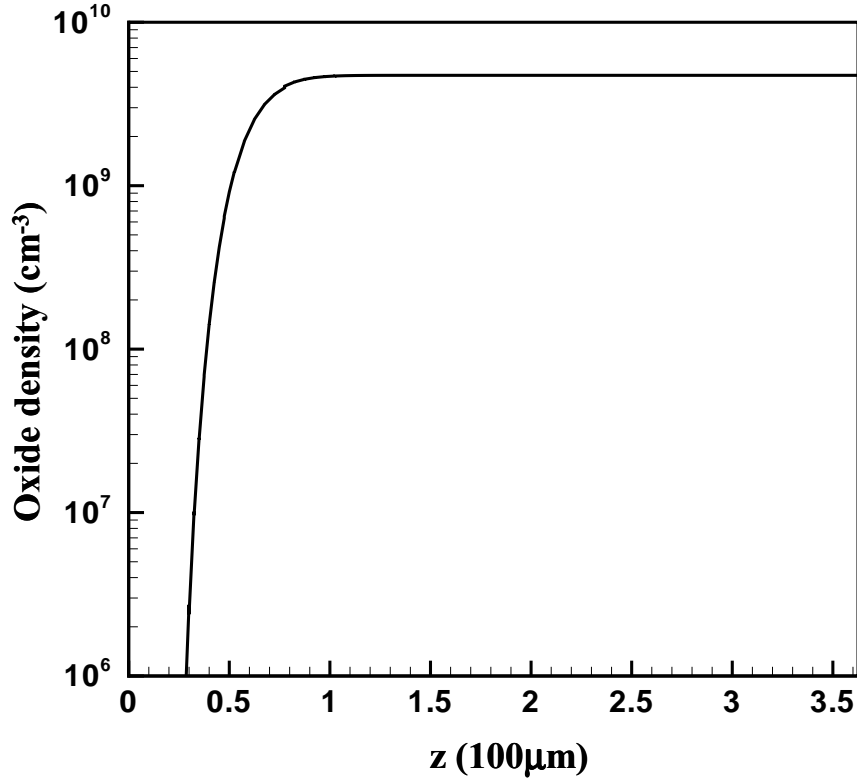
Figure 3.32: Final distribution of oxide density across the wafer.

3.9.2 Simulation of Traditional Wafer Annealing Compared with Experimental Data

The experimental results of oxygen precipitation during wafer annealing done by MEMC and referred in several papers by Kelton et al. [87,196] are the most systematic results published so far. The simulation results of oxygen precipitation based on the model described in Section 3.3 - 3.5 are compared with these experimental results. The experiment procedure is shown in Figure 3.33. The silicon wafers with three different oxygen concentration - $6.0 \times 10^{17} cm^{-3}$, $7.0 \times 10^{17} cm^{-3}$ and $8.0 \times 10^{17} cm^{-3}$ - were studied. The purpose of the first step is to dissolve the grown-in oxide or erase the 'thermal history' of the silicon wafer so that the initial oxide distribution in the wafer can be normalized and scatter of experimental data due to grown-in oxide can be prevented. The second step is the nucleation of oxygen precipitates at different nucleation temperature T_{nucl} for differ-

ent annealing time t_{nucl}. The last step is the growth of some small oxygen precipitates formed during the nucleation stage. The higher growth temperature, the higher oxygen diffusivity, and therefore the faster growth of oxygen precipitates. However the higher growth temperature, the bigger critical size of oxygen precipitates, and therefore the fewer oxide nucleus can grow and the lower final oxide density. The high temperature growth with an intermediate temperature pre-growth can generate high final oxide density in shorter time. During the annealing at 800 $°C$ for 4 hours, the oxides between critical sizes at 800 $°C$ and 1000 $°C$ can grow to bigger oxides to survive the anneal at 1000 $°C$. These oxides will dissolve during the annealing at 1000 $°C$ otherwise.
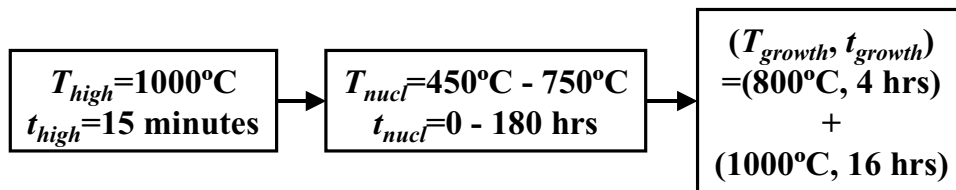
Figure 3.33: Annealing procedure (taken from [87]).

Since the first annealing step at 1000 $°C$ is only 15 minute, there is essentially no oxygen out-diffusion and oxygen is uniformly distributed across the wafer. The temperature of the first annealing step is only 1000 $°C$ and not high enough to establish high vacancy concentration needed for the formation of spherical oxygen precipitates, so the majority of oxygen precipitates formed during the second low temperature anneal are disk-shaped oxides and there is essentially no interaction between these disk-shaped oxides and native point defects. Therefore the simulation of oxygen precipitates under this annealing circle is zero dimensional in spatial space and the initial oxide distribution can be taken as zero concentrations for all oxides. In the experimental procedure described in Kelton's paper [87], ramping rate between different annealing steps, especially the ramping rate between

nucleation step and growth step, was not reported. The sensitivity of final oxide density on the ramping rate is studied in the following simulations.

The simulation results of oxygen precipitates for different nucleation temperatures and different initial oxygen concentrations are shown in Figure 3.34 (for $C_O = 8.0 \times 10^{17} cm^{-3}$), Figure 3.35 (for $C_O = 7.0 \times 10^{17} cm^{-3}$), and Figure 3.36 (for $C_O = 6.0 \times 10^{17} cm^{-3}$). The experiment procedure is 1000 $°C$ anneal for 15 minutes followed by 32 hours anneal at different nucleation temperatures, and then 800 $°C$ anneal for 4 hours and 1000 $°C$ anneal for 16 hours. The industry standard ramping rate is 5 $°C/$ min. In the Figure 3.34, simulation results of the final oxide density vs. different nucleation temperatures for initial oxygen concentration of $8.0 \times 10^{17} cm^{-3}$ are shown for three different ramping rate - infinite ramping rate, 5 $°C/$min and 3 $°C/$min. All the simulation results show the same trend as the experimental data - there is a peak around 600 $°C$. When nucleation temperature is higher than this, the super-saturation of oxygen at nucleation temperature is lower and therefore the oxide density is lower. This is an equilibrium limitation. When nucleation temperature is lower than this, the oxygen diffusivity is too low to generate enough nuclei for a given time which can grow during the following growth steps. This is a dynamics limitation. Because of this, the results of oxide density at low nucleation temperatures are sensitive to the ramping rate. During the ramping process between low temperature nucleation step and growth step, some small oxide nuclei, which will dissolve during the growth step otherwise, can grow bigger and survive the growth step. The slower ramping process, the more time for small nuclei to grow, and therefore the higher oxide density. For standard ramping rate which is 5 $°C/$min, the simulation results reasonably agree with the experimental results. For the rest of simulations in this section, the ramping rate is chosen as 5 $°C/$min. The simulations results of oxide density

as a function of nucleation temperature for other oxygen levels in Figure 3.35 and Figure 3.36 also show reasonable agreement with the experimental data.
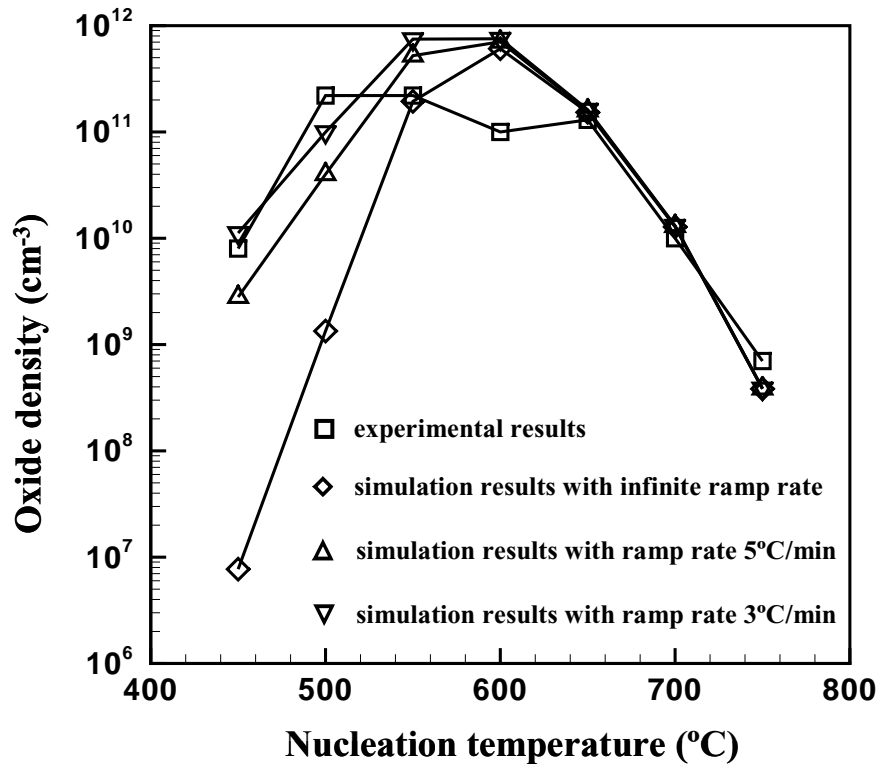
Figure 3.34: Oxide density as a function of nucleation temperature for C_O=8.0×10^{17}cm^{-3}.
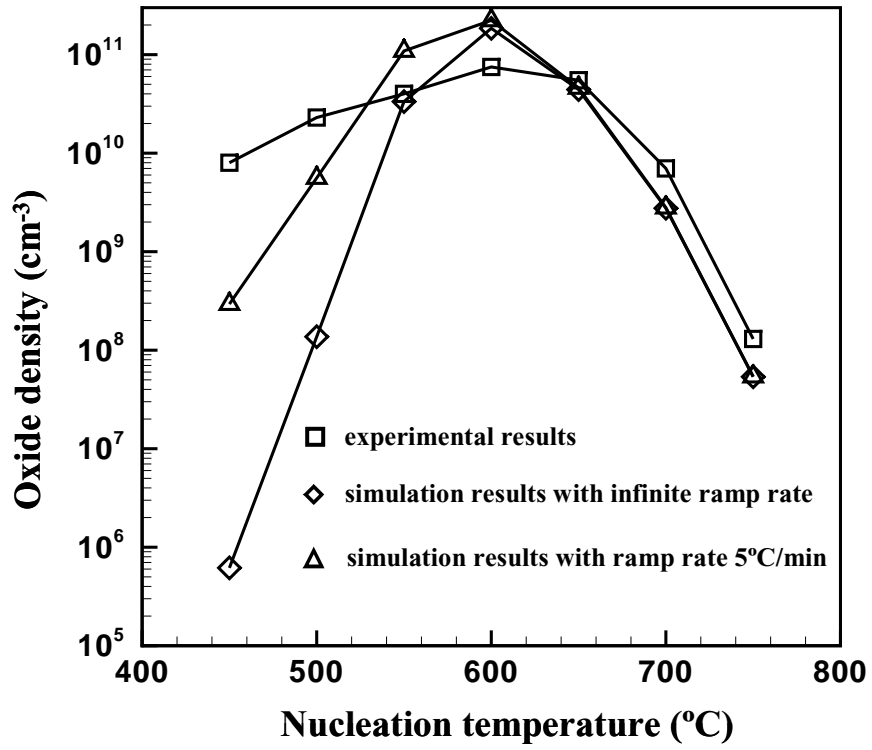
Figure 3.35: Oxide density as a function of nucleation temperature for C_O=7.0×10^{17} cm^{-3}.
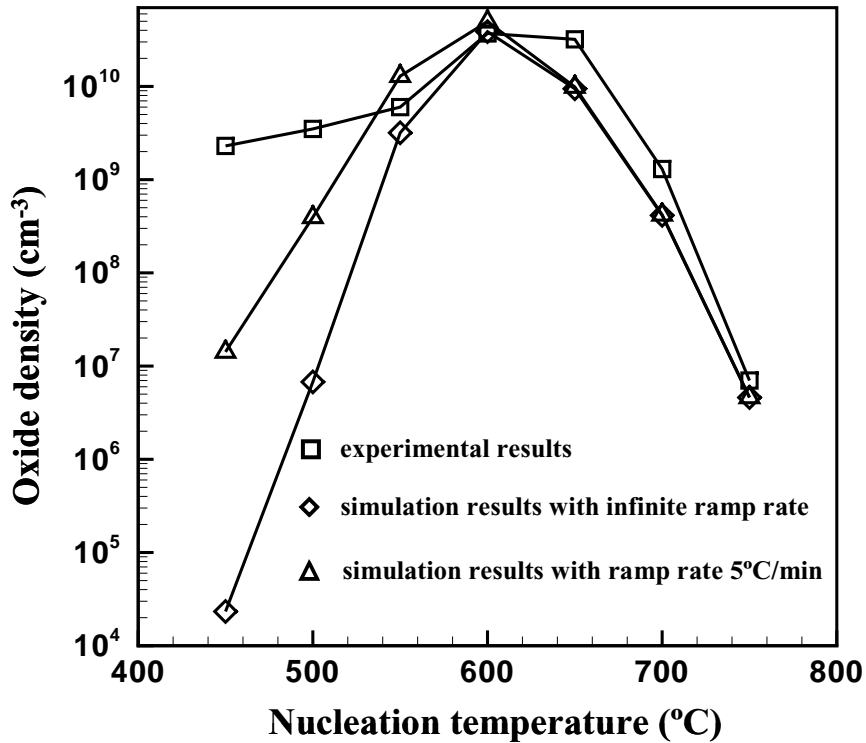
Figure 3.36: Oxide density as a function of nucleation temperature for C_O=6.0×$10^{17}cm^{-3}$.

The simulation results of oxide density for different nucleation time are shown in Figure 3.37. The experimental procedure is 1000 $°C$ anneal for 15 minutes followed by 650 $°C$ anneal for different nucleation time, and then 800 $°C$ anneal for 4 hours and 1000 $°C$ anneal for 16 hours. The initial oxygen concentration is $7.0 \times 10^{17} cm^{-3}$. The simulation results reasonably agree with experimental data and some important concepts can be inferred from this figure. The oxide density is approximately linear to nucleation time with an intercept on the time axial. The slope of the linear part is called nucleation rate and the interception on the time axial is called induction time [87]. In this case the induction time is the time needed for oxide size distribution to establish beyond the critical size for 800 $°C$. After that the nucleation of oxide bigger than the critical size for 800 $°C$ is at a constant rate. Generally this induction time is dependent on both the nucleation temperature

and the growth temperature. The lower nucleation temperature, the lower oxygen diffusivity, and the longer time for oxide size distribution to reach certain critical size and therefore the longer induction time. The higher growth temperature, the bigger critical size, and the longer time for oxide size distribution to reach that critical size and therefore the longer induction time.
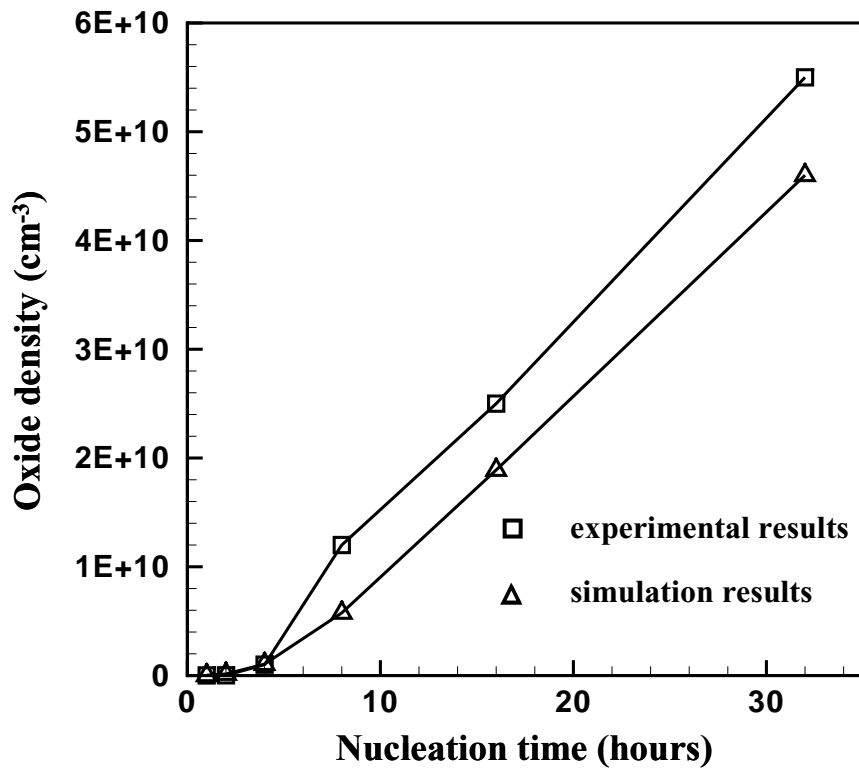
(a)
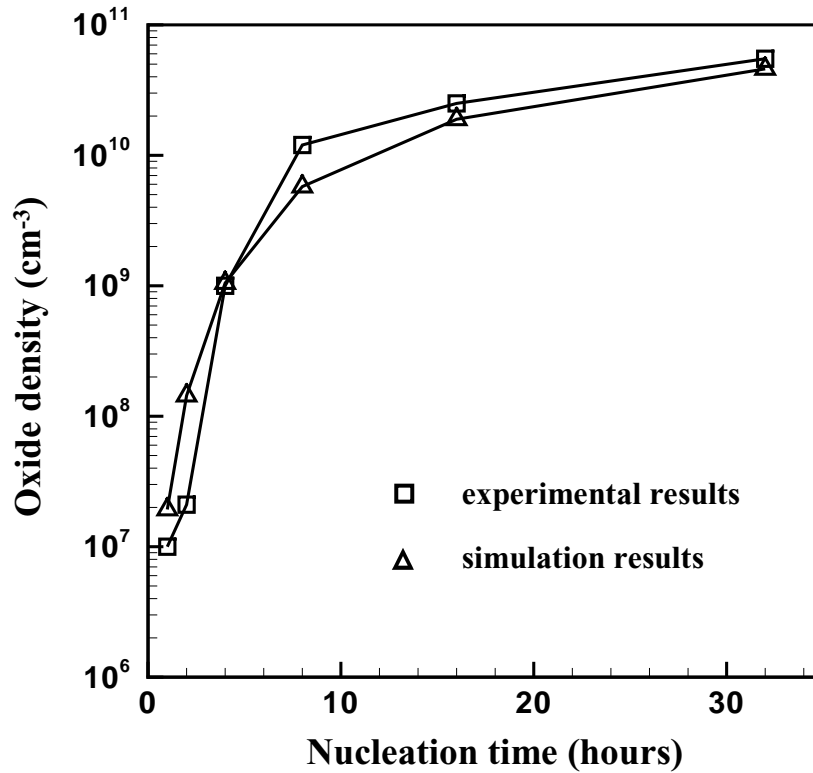
(b)

Figure 3.37: Oxide density as a function of nucleation time at 650 $°C$ for C_O=7.0×10^{17}cm^{-3} plotted on linear (a) and logarithmic (b) scales.

The dependence of oxide density on the nucleation time and nucleation temperature predicted by the model together with a single set of physical parameters described in Section 3.3 - 3.5 reasonably agree with the experimental results. This is an indication that the model may capture the right physics of the oxygen precipitation. It should be emphasized that spherical oxygen precipitates coexist with disk-shaped oxygen precipitates and they are competing species. However disk-shaped oxygen precipitates dominate during the low temperature annealing without a pre-anneal at very high temperature. The size distributions of spherical oxides and disk-shaped oxides after 32 hours annealing at 650 $°C$ for $C_O = 8.0 \times 10^{17} cm^{-3}$ are compared in Figure 3.38. The density of disk-shaped oxides is

more than four orders-of-magnitude higher than that of spherical oxides. The spherical oxide distribution under the condition of $C_I/C_I^{eq} = 1$ (corresponding a system where all self-interstitials ejected by spherical oxides are instantly consumed by some undefined sinks) is also shown for comparison. The density of the spherical oxide distribution under the condition of $C_I/C_I^{eq} = 1$ is slightly higher than that of disk-shaped oxide. These three oxide distributions are consistent with the free energy curves shown in Figure 3.14.
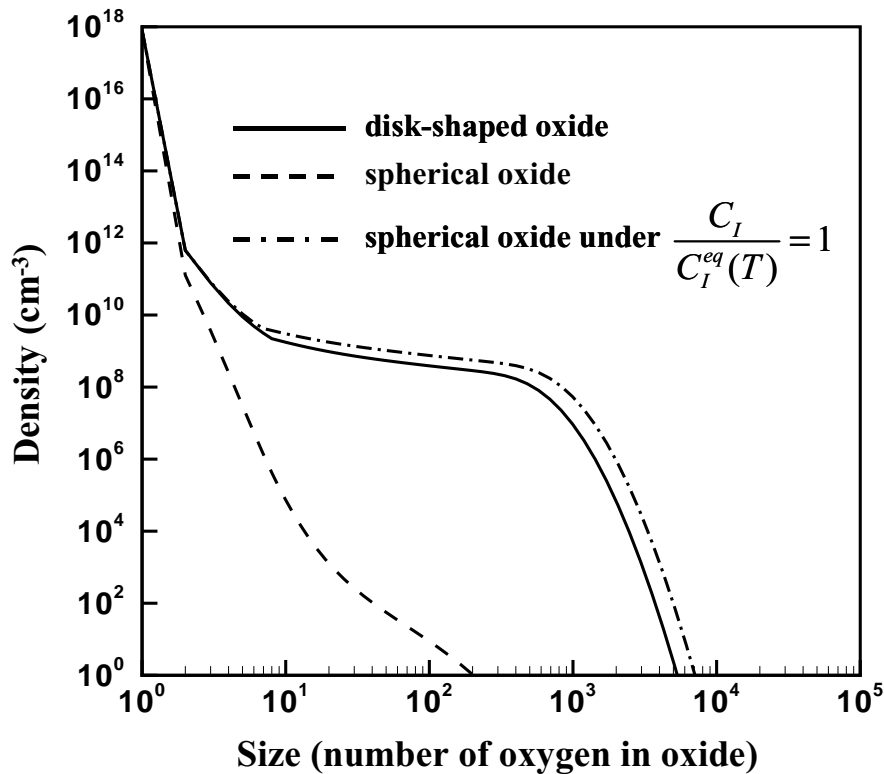
Figure 3.38: Size distributions of spherical oxides and disk-shaped oxides after 32 hours annealing at $650°C$ for $C_O=8.0\times10^{17}cm^{-3}$.

3.9.3 Vacancy Assisted Oxygen Precipitation

One important characteristic of the typical Hi-Low-Hi wafer annealing is the high thermal budget. Since the surface denuded zone is formed by oxygen out-diffusion during the first high temperature anneal, the annealing time has to be long to make surface out-diffusion

layer thick enough. Without the assistant of enough vacancy, nucleation rate of oxygen precipitation at the second low temperature anneal is low and there also is considerable induction time. So the annealing time for the first two steps must be long enough, normally at least more than a dozen hours.

Modern VLSI fabrication requires less and less thermal budget, and a technology called the 'Magic Denuded Zone' (MDZ) and developed by MEMC [39] can be used to make a wafer with oxygen precipitates in the middle section and a surface denuded zone, but with low thermal budget. The mechanism to achieve the spatially nonuniform oxide distribution is totally different between the traditional Hi-Low-Hi wafer annealing and MDZ. The MDZ also has three steps: the first step is rapid thermal anneal at very high temperature; the second step is low temperature anneal but with very short annealing time; the last step is basically the same as that of the traditional Hi-Low-Hi wafer anneal. Typically in MDZ process, the wafer is first heated rapidly (with a ramp rate of $50°C/s$) from room temperature to $1250°C$ and held there for 10 seconds before being cooled to room temperature at a cooling rate of approximately $100°C/s$. No out-diffusion of oxygen occurs during the very short first step; however, very small oxygen precipitates that may have existed in the crystal are dissolved. More importantly, the equilibrium vacancy concentration corresponding to $T = 1250°C$ is created during this step, and diffuses to the surface only in a thin surface layer because of fast cooling after this step. As a result, there is a high vacancy concentration in the bulk of the wafer. With the assistance of vacancy, nucleation of oxygen precipitates during the second low temperature anneal occurs preferentially in the bulk of wafer, leaving the surface of wafer essentially free of oxygen precipitates, although with high oxygen concentration. It should be emphasized that the annealing time for the second low temperature anneal in MDZ process has to be short, normally only a couple hours. The nucleation rate of oxygen precipitation at low tempera-

ture anneal is very fast with the assistance of vacancy due to low free energy described in eq. (3.77), so in short anneal time oxygen can only precipitate in the middle section of wafer where vacancy concentration is very high. However if the annealing time of the second low temperature is as long as that of traditional Hi-Low-Hi wafer anneal, oxygen can also precipitate near the surface of the wafer and there is no surface denuded zone anymore because of high oxygen concentration even in the surface area for MDZ process. Apparently the annealing time for the first two steps in MDZ process are much shorter than these in traditional Hi-Low-Hi wafer annealing, so the thermal budget of the MDZ process is greatly reduced.

The predictions for precipitate density as a function of t_{nucl}, with and without vacancy assistance, are shown in Figure 3.39 and Figure 3.40 and compared with experimental measurements for $C_O = 7 \times 10^{17} cm^{-3}$. Results are shown for the traditional Hi-Low-Hi process and for the MDZ annealing cycle with $T_{high} = 1250°C$ for 10 seconds. In both cases, $T_{nucl} = 650°C$ and $T_{growth} = 1000°C$ for 16 hours. The thermal ramp-rate between $650°C$ and $1000°C$ was not reported in the experiments and is crucial for prediction of the results. The sensitivity of the final oxide density to the ramp rate is shown in Figure 3.39 for classical Hi-Low-Hi annealing. The experimental results are best matched with a ramp rate of $20°C/min$, which has been used in the remainder of the calculations. The match between experiments and simulations is reasonable, considering that the detection limit for measuring the oxide density is approximately $1 \times 10^7 cm^{-3}$. The effect of the MDZ treatment on the oxide density in both experiments and simulations is shown in Figure 3.40. The impact of the implanted vacancy distribution on the higher nucleation rate of spherical precipitates is clearly seen. Also the agreement between experiments and simulations is excellent.
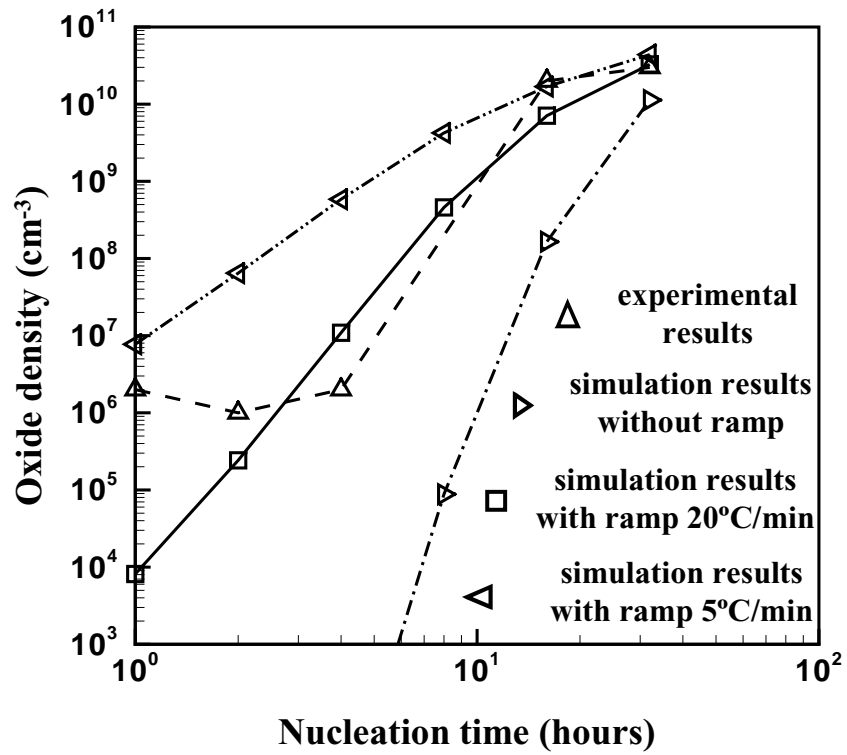
Figure 3.39: Sensitivity of oxide density on the ramping rate for traditional annealing process without vacancy assistance.
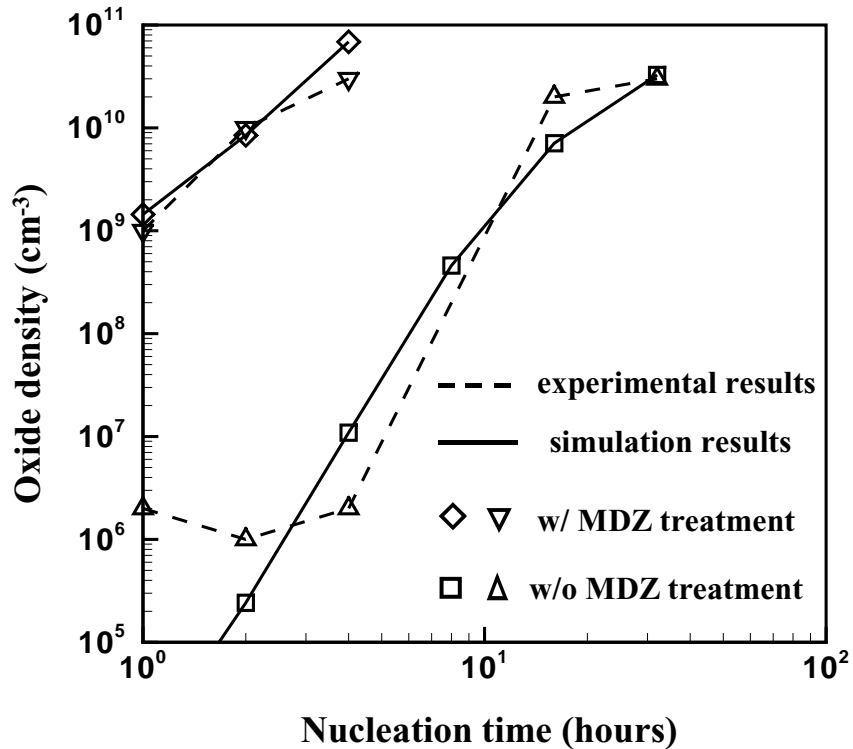
Figure 3.40: Oxide density as a function of the nucleation time with and without vacancy assistance.

3.10 Conclusion

The oxygen concentration that is inherent to CZ-grown silicon wafers is crucial to the mechanical and electrical properties of silicon wafers. The oxide precipitates that form from the oxygen super-saturation and their associated stacking faults and dislocation loops serve as getting sites for metallic impurities. An internally consistent model for quantitative prediction of oxygen precipitation is presented. The model includes the dynamics of oxygen precipitation and the influence of point defects on this precipitation. Most importantly, the effect of precipitate morphology is included by modeling the evolution of spherical and disk-shaped precipitates.

Point defect dynamics plays a critical role in oxide precipitation. Because the density of the precipitate is approximately half that of the matrix, elastic stress energy is created that can be dissipated by vacancy absorption into the precipitate or self-interstitial ejection into the matrix. At low annealing temperature spherical precipitates which have the lowest surface energy grow preferentially when there is ample vacancy concentration in the crystal to supply the free volume required to release the high elastic stress. The removal of the ejected interstitials is not fast enough to release the high stress energy associated with the spherical oxides because of low self-diffusion of the interstitials at low temperature. Therefore disk-shaped precipitates which has the lowest stress energy are favor at low nucleation temperature when stress relief is only possible by interstitial ejection.

The imperfections in the crystal growth system and turbulent fluctuations in the melt may lead to non-uniform incorporation of oxygen into CZ silicon. The role of an inhomogeneous oxygen distribution was quantitatively investigated as a potential factor through two separate calculations. The first is the analysis of a simple model that shows how a spatially inhomogeneous oxygen concentration, coupled with the nonlinear kinetics for the nucleation of precipitates, can lead to substantial increases in the apparent nucleation rates. The second calculation is based on a detailed simulation of oxygen precipitation using a self-consistent model of oxygen precipitation. The simulation results show that for a non-uniform oxygen distribution with wavelength of $100 \mu m$ and fluctuation magnitude of 0.2, average oxide density could be one order-of-magnitude higher than that for uniform oxygen distribution.

The self-consistent model can be used to explore a variety of processes including CZ crystal growth and different annealing strategies such as traditional Hi-Low-Hi and MDZ wafer annealing. The simulations of point defects dynamics and oxygen precipitation during CZ crystal growth reveal dramatically different effect of oxygen on the microdefects

dynamics under different Pe. At high Pe, the void aggregation temperature is high and the intermediate vacancies are already depleted by void formation before they can be significantly consumed by oxygen precipitates. In this case, there is essentially no effect of the oxygen on the void distribution and only very small oxygen precipitates are predicted to be present. When $Pe \rightarrow Pe_{crit}$, the delay in the aggregation of voids to a lower temperature caused by the decrease in the intermediate vacancy concentration leads to much more growth of small oxide precipitates and to substantial depletion of the already smaller reservoir of vacancies. As a result, void density is significantly decreased with oxygen present and slightly larger oxygen precipitates which could be dissolved during a high temperature anneal afterward are predicted. The 'perfect silicon' can be produced at the conditions around Pe_{crit} where interstitials and vacancies almost completely recombine with each other. The present of oxygen widens this operating window making growth of this material more feasible.

The physics of wafer annealing is clearly demonstrated by the simulations of oxygen precipitation in this Chapter. The ramping rate between different annealing steps, especially the ramping rate between the nucleation step and growth step, was not reported in the experimental data. The simulation results show that ramping rate is an important factor especially for annealing at very low temperature or for short annealing time. This is because during the ramping process between the nucleation step and growth step, some small oxide nuclei, which will dissolve during the growth step otherwise, can grow bigger and survive the growth step. The sensitivity of final oxide density on the ramping rate is studied. It should be emphasized that the effect of the ramping process could not be modeled without accounting for the oxide size distribution. With a reasonable ramping rate, simulation results successfully predict oxide densities and the effects of nucleation temperature and time during traditionally Hi-Low-Hi annealing. The simulation results show

a peak in oxide density as a function of nucleation temperatures. This maximum repre-sents a balance between the driving force of the oxygen super-saturation and inhibition of oxygen diffusion at low temperature where too few nuclei are formed in the set time. The same self-consistent model also captures the vacancy-assisted oxygen precipitation in the MDZ annealing process whose mechanism is different from that of the traditional Hi-Low-Hi wafer annealing. The agreement between simulation results and experimental data is excellent.

Chapter 4

Conclusions

Most microelectronic devices are fabricated on substrates made of single crystal silicon. In order to make more powerful microelectronic devices with high quality and yield, the microdefects in single silicon crystal must be well controlled. Therefore the understanding of microdefects formation in silicon crystal is crucial and this thesis is devoted to it. The mechanisms of microdefects formation are investigated by both theoretical and computational approaches. This thesis provides deeper physical insight into the defect formation in silicon crystal from crystal growth through wafer annealing, and a comprehensive framework to model the defect formation in single crystal silicon. Both theoretical and computational results agree with experimental data.

The theoretical analysis of the native point defects and formation of their clusters in CZ crystal growth is performed from the melt/crystal interface through the clusters formation at lower temperature. A rigorous asymptotic analysis is carried out first to get the expression for the critical value of V/G which separates the vacancies-rich core and interstitials-rich annular regions. The critical value of V/G is a function of physical properties of native point defects at silicon melting temperature only. This analysis is then extended to the intermediate point defect concentration at arbitrary V/G and the effect of impurity such as Boron on the critical V/G. The cluster formation is further analyzed by examining discrete and continuous forms of rate equations to get useful scalings and quantitative prediction of important variables such as aggregation temperature, total void density, and average size of void.

A framework is presented for modeling oxygen precipitation in silicon by including the details of the growth of oxygen precipitates and the important roles of self-interstitials

and vacancies in this process. The framework also includes the role of precipitate morphology by including micro-mechanical models for both spherical and disk-shaped precipitates. Spherical shaped precipitates grow preferentially when there is ample vacancy concentration in the crystal to supply the free volume required to release elastic stress. Disk-shaped precipitates are favor at low nucleation temperature when stress relief is only possible by interstitial ejection. The model successfully predicts a variety of annealing strategies including traditional Hi-Low-Hi wafer annealing and MDZ annealing process.

4.1 Summary

4.1.1 Theoretical Analysis on Native Point Defects and Point Defect Clusters

The theoretical analysis on native point defects and point defect clusters includes two steps. In the first step, intermediate point defect concentration is determined by analyzing point defects balance in the boundary layer near melt/crystal interface without any clustering since super-saturation of point defect is not high enough to drive significant clustering in this thin boundary layer. Then in the second step, nucleation of point defect clusters is analyzed based on the intermediate point defect concentration obtained in the first step and temperature field around aggregation temperature.

The asymptotic analysis on critical V/G, intermediate vacancy concentration, intermediate interstitial concentration, and effect of boron on critical V/G are performed in the region close to the melt/crystal interface. The asymptotic analysis is based on two important characteristics - large Damkohler number Da and small ω (ratio of axial and radial length scales) - about the CZ silicon crystal growth. The large Da is due to the high recombination rate near the melt/crystal interface and leads to mass law for vacancies and interstitials. The small ω is due to the high activation energy for the equilibrium concentrations of native point defects and leads to a thin recombination layer near the melt/crystal interface and negligible radial contribution of diffusion.

Point defect clusters formation is modeled by combination of discrete rate equation for small n and its continuous representation for large n with matching between them. The analysis on various scales shows that for small n, the time-dependent term in the governing equation can be ignored and the corresponding equation is called inner equation. The discrete form of inner equation is employed since continuous form is not valid for small n. The inner equation is also called stationary solution because there is no time-dependent term. The reason why the time-dependent term is negligible for small n is that the time scale to reach the stationary size distribution for small n is much smaller than the system time scale. For large n, the second order terms for n can be ignored and the corresponding equation is called outer equation. The outer equation has continuous form and it is a first order partial derivative equation. For large n, the cluster size distribution propagate with a drift velocity. At matching point between the inner and outer equations, both concentration and flux are matched.

Based on the analysis of the inner and outer equations with the appropriate model for growth rate and dissolution rate, two important scalings for total void concentration and average void size are obtained. Total void concentration is proportional to $\langle G \rangle^{3/2} (C_V^{int})^{-1/2}$ and the average void size is proportional to $(C_V^{int} / \langle G \rangle)^{3/2}$. The quantitative theoretical estimations of void aggregation temperature, total void concentration, and average void size also reasonably agree with the simulation results.

4.1.2 Modeling of Oxygen Precipitation
The oxygen precipitates and their associated stacking faults and dislocation loops, if confined in the middle of the wafer and with appropriate size and density, can serve as getting sites for metallic impurities introduced during device fabrication. An internally consistent model for quantitative prediction of oxygen precipitation is presented. The model includes the dynamics of oxygen precipitation and the influence of point defects on this precipita-

tion. Most importantly, the effect of precipitate morphology is included by modeling the evolution of spherical and disk-shaped precipitates.

Point defect dynamics plays a critical role in oxide precipitation. Because the density of the precipitate is approximately half that of the matrix, elastic stress energy is created that can be dissipated by vacancy absorption into the precipitate or self-interstitial ejection into the matrix. At low annealing temperature spherical precipitates which have the lowest surface energy grow preferentially when there is ample vacancy concentration in the crystal to supply the free volume required to release the high elastic stress. The removal of the ejected interstitials is not fast enough to release the high stress energy associated with the spherical oxides because of low self-diffusion of the interstitials at low temperature. Therefore disk-shaped precipitates which has the lowest stress energy are favor at low nucleation temperature when stress relief is only possible by interstitial ejection.

The model is used to explore a variety of processes including CZ crystal growth and different annealing strategies such as traditional Hi-Low-Hi and MDZ wafer annealing. The substantial increase in the apparent nucleation rates due to an inhomogeneous oxygen distribution is quantitatively investigated. The simulations of point defects dynamics and oxygen precipitation during CZ crystal growth reveal the operating conditions under which the 'perfect silicon' can be produced.

The physics of wafer annealing is clearly demonstrated by the simulations of oxygen precipitation. The sensitivity of final oxide density on the ramping rate is studied. With a reasonable ramping rate, simulation results successfully predict oxide densities and the effects of nucleation temperature and time during traditionally Hi-Low-Hi annealing. The simulation results show a peak in oxide density as a function of nucleation temperatures. This maximum represents a balance between the driving force of the oxygen super-saturation and inhibition of oxygen diffusion at low temperature where too few nuclei are

formed in the set time. The same self-consistent model also captures the vacancy-assisted oxygen precipitation in the MDZ annealing process whose mechanism is different from that of the traditional Hi-Low-Hi wafer annealing.

4.2 Directions for Future Work

4.2.3 Application of the Theoretical Analysis to the Simulation of Native Point Defects and Point Defect Clusters

The two-dimensional (both axial and radial directions) profiles of native point defects and point defect clusters during crystal growth can be approximated by a series of one-dimensional simulation results along axial direction but at different radial positions. However a more rigorous approach is to run two-dimensional simulations. Currently one-dimensional simulation of native point defects and point defect clusters takes hours to finish while two-dimensional simulation takes weeks. Mori [108] was able to run two-dimensional simulations on a parallel computer clusters with 8 nodes and finish in days. In order to make two-dimensional simulator for native point defects and their clusters deliverable to industry, we need to speed up the simulator so that it can be done in days on a single node.

Currently the discrete rate equations are solved for small clusters and the Fokker-Planck equations are solved for big clusters. About 90% of the computational time is spent on the calculation of the clusters. The CC70 finite difference method used to solve the Fokker-Planck equations involves many exponential calculations which are very computationally intensive. The theoretical analysis in Section 2.5 provides the formula for both small clusters (the solution of the inner equation) and large clusters (the solution of the outer equation). Therefore there is no need to numerically solve the discrete rate equations and Fokker-Planck equations. If the solutions of the discrete rate equations and Fokker-Planck equations are replaced by the formula based on the theoretical analysis, most of the computational time will be spent on the monomer calculations which account less than

10% of the computational time in the current simulator. So the simulator for native point defects and point defect clusters during the CZ crystal growth could be a factor of 10 faster. Two-dimensional simulations could be routinely performed.

4.2.4 Oxygen Precipitation at Very Low Temperatures

In the simulations of the traditional Hi-Low-Hi wafer annealing in Section 3.9.2, the simulation results of disk-shaped oxide densities at $T_{nucl} < 500°C$ could be one or two order-of-magnitude lower than experimental data. This discrepancy could be addressed in three aspects: thermodynamics, transport, and the assistance of some small defect complexes.

As discussed in Section 3.1, experimental observation showed that rod-shaped oxygen precipitates dominate at $T_{nucl} < 500°C$. However as shown in Figure 3.2, in isotropic environment the stress energy of a rod-shaped precipitate is at least three quarter of that of a spherical precipitate with the same volume, and it could be much higher than that of a disk-shaped precipitate. So rod-shaped particle is not thermodynamically favorable compared with disk-shaped particle in isotropic sense. The fact that the rod-shaped oxide orientates along <110> direction [10] implies the stress energy and surface energy of rod-shaped oxide need to be addressed anisotropically. The rod-shaped oxide may be thermodynamically favorable in anisotropic sense.

Another factor could be transport or oxygen diffusion to the oxide. Ham [53] showed that in the limit of high aspect ratio, the diffusion flux to a rod-shaped particle at entire surface is in the order of $D(C_\infty - C_S)L/\ln(L/r)$ where L and r are the length and radius of the rod, and the diffusion flux to a rod-shaped particle only at two ends is in the order of $Dr(C_\infty - C_S)$. The flux to a rod-shaped particle only at two ends is smaller than that for a disk-shaped particle described by eq. (3.52). Even for the flux to a rod at entire surface, it is not significantly higher than that for a disk-shaped particle unless the aspect ratio of the rod is very high. So the normal transport of oxygen to the oxide can not explain why the

simulation results underpredict oxide densities at very low nucleation temperature. However the oxygen concentration in the region close to the oxide could be higher than the bulk oxygen concentration because this region is the transit between silicon matrix and oxide where the oxygen concentration is in the order of 10^{21}cm^{-3}. The higher oxygen concentration near the oxide leads to higher oxygen transport to oxide. This effect may only work for oxygen precipitation at very low temperature because the high oxygen concentration close to the oxide may not be sustained with relatively high oxygen diffusivity at medium nucleation temperature.

Thermal donors, which are small clusters of oxygen atoms, silicon atoms and point defects and electrically active, are formed in the temperate range 300-500$°C$ and rapidly annihilated above 600$°C$ [104]. The temperature range for the formation of thermal donors is the same as the temperature range where discrepancy between experimental and simulation results for oxide density occurs. This indicates that some small oxygen complexes such as thermal donors which are only formed at very low temperature may play an important role in oxygen precipitation.

References

[1]   Abe, T., and Harada, H., *Mat. Res. Soc. Symp. Proc.*, **14** (1983), 1.

[2]   Abe, T., and Kimura, M., *Electrochem. Soc. Proc.*, **90-** (1990), 105.

[3]   Abe, T., *Electrochem. Soc. Proc.*, **98-1** (1998), 157.

[4]   Aihara, K., Takeno, H., Hayamizu, Y., Tamatsuka, M., and Masui, T., *J. Appl. Phys.*, **88** (2000), 3705.

[5]   Ataka, M. and Ogawa, T., *J. Mater. Res.*, **8** (1993), 2889.

[6]   Baldan, A., *J. Mater. Sci.*, **37** (2002), 2171.

[7]   Bassi, F., and Rebay, S., *J. Comput. Phys.*, **131** (1997), 267.

[8]   Braggins, T. T. and Thomas, R. N., *Electrochem. Soc. Meet. Ext. Abstr.*, **169** (1986), 354.

[9]   Ataka, M. and Ogawa, T., *J. Mater. Res.*, **8** (1993), 2889.

[10] Bergholz, W., *Semiconductors and Semimetals*, **42** (1994), 513.

[11] Bongiorno, A., and Colombo, L., *Phys. Rev. B*, **57** (1998), 8767.

[12] Bornside, D., Brown, R.A., Fujiwara, T., Fujiwara, H. and Kubo, T., *J. Electrochem. Soc.*, **142** (1995), 2790.

[13] Bourret, A., *Inst. Phys. Conf. Ser.*, **87** (1987), 39.

[14] Brown, R. A., *AIChE J.*, **34** (1988), 881.

[15] Brown, R. A., Maroudas, D., and Sinno, T., *J. Crystal Growth*, **137** (1994), 12.

[16] Brown, R. A., Wang, Z., and Mori, T., *J. Crystal Growth*, **225** (2001), 97.

[17] Bullis, W. M., *Mater. Sci. and Eng.*, **B72** (2000), 93.

[18] Campbell, S. A., *The Science and Engineering of Microelectronic Fabrication*, Oxford University Press, 1996.

[19] Campbell, S. A., *Materials Science and Engineering*, **R20** (1997), 1.

[20] Chang, J. S. and Cooper, G., *J. Comp. Phys.*, **6** (1970), 1.

[21] Cockburn, B., *Advanced Numerical Approximation of Nonlinear Hyperbolic Equations*, ed. A. Quarteroni, Springer-Verlag, Berlin, (1998), 151.

[22] Cockburn, B., and Shu, C-W., *SIAM J. Numer. Anal.*, **35** (1998) 2440.

[23] Cockburn, B., and Shu, C-W., *J. Comput. Phys.*, **141** (1998) 199.

[24] Corbett, J. W., McDonald, R. S., and Watkins, G. D., *J. Phys. Chem. Solids*, **25** (1964), 873.

[25] Craven, R. A., *Mat. Res. Soc. Symp. Proc.*, **36** (1985), 159.

[26] Dash, W., Gardner, E. and Tice, W., *J. Appl. Phys.*, **29** (1958), 736.

[27] Dornberger, E., Esfandyari, J., Graf, D., Vanhellemont, J., Lambert, U., Dupret, F. and von Ammon, W., *Electrochem. Soc. Proc.*, **97** (1996), 40.

[28] Dornberger, E. and von Ammon, W., *J. Electrochem. Soc.*, **143** (1996), 1648.

[29] Dornberger, E., Graf, D., Suhren, M., Lambert, U., Wagner, P., Dupret, F., and von Ammon, W., *J. Crystal Growth*, **180** (1997), 343.

[30] Drozdov, A. N. and Morillo, M., *Phys. Rev. E*, **54** (1996), 931.

[31] Epperlein, E. M., *J. Comp. Phys.*, **112** (1994), 291.

[32] Epperlein, E. M., *Laser and Particle Beams*, **12** (1994), 257.

[33] Esfandyari, J., Schmeiser, C., Senkader, S., Hobler, G. and Murphy, B., *J. Electrochem. Soc.*, **143** (1996), 995.

[34] Esfandyari, J., Vanhellemont, J., and Obermeier, G., *Electrochem. Soc. Proc.*, **99-1** (1999), 437.

[35] Fahey, P. M., Griffin, P. B. and Plummer, J. D., *Rev. Mod. Phys.*, **61** (1989), 289.

[36] Fair, R. B., *J. Electrochem. Soc.*, **122** (1975), 80.

[37] Falster, R., Pagani, M., Gambaro, D., Cornara, M., Olmo, M., Ferrero, G., Pichler, P. and Jacob, M., *Solid State Phenom.*, **57-58** (1997), 129.

[38] Falster, R., Voronkov, V. V., Holzer, J. C., Markgraf, S., McQuaid, S. and Mule'Stagno, L., *Electrochem. Soc. Proc.*, **98-1** (1998), 468.

[39] Falster, R., Gambaro, D., Olmo, M., Cornara, M. and Korb, H., *Electrochem. Soc. Proc.*, **98-13** (1998), 135.

[40] Falster, R., Holzer, J. C., Markgraf, S. A., Mutti, P., McQuaid, S. A., and Johnson, B. K., *United States Patent*, 5,919,302 (1999).

[41] Falster, R., and Voronkov, V. V., *MRS Bulletin*, **25-6** (2000), 28.

[42] Finlayson, B. A., *Nonlinear Analysis in Chemical Engineering*, McGraw Hill Book Company, New York, (1980).

[43] Freeland, P. E., Jackson, K. A., Lowe, C. W. and Patel, J. R., *Appl. Phys. Lett.*, **30** (1977), 32.

[44] Gall, P., Fillard, J., Bonnafe, J., Rakotomvo, T., Rufer, H. and Schwenk, H., *Defect Controll in Semiconductors* (1990), 255.

[45] Ghandhi, S. K., *VLSI Fabrication Principles: Silicon and Gallium Arsenide*, Wiley, New York, (1983).

[46] Gilles, D., Weber, E. R. and Hahn, S. K., *Phys. Rev. Lett.*, **64** (1990), 196.

[47] Girifalco, L. A., *Statistical Physics of Materials*, Wiley, New York, (1973).

[48] Gräf, D., Lambert, U., Brohl, M., Ehlert, A., Wahlich, R. and Wagner, P., *J. Electrochem. Soc.*, **142** (1995), 3189.

[49] Gräf, D., Lambert, U., Brohl, M., Ehlert, A., Wahlich, R. and Wagner, P., *Mater. Sci. and Eng.*, **B36** (1996), 50.

[50] Gräf, D., Suhren, M., Lambert, U., Schmolke, R., Ehlert, A., von Ammon, W. and Wagner, P., *J. Electrochem. Soc.*, **145** (1998), 275.

[51] Griffin, P. B., and Plummer, J. D., *Mater. Res. Soc. Symp. Proc.*, **71** (1986), .

[52] Ham, F. S., *J. Phys. Chem. Solids*, **6** (1958), 335.

[53] Ham, F. S., *J. Appl. Phys.*, **30** (1959), 1518.

[54] Hasebe, M., Takeoka, Y., Shinoyama, S. and Naito, S., *Jpn. J. Appl. Phys.*, **28** (1989), L1999.

[55] Hasebe, M., Fukuda, J., Iwasaki, T., Harada, H., and Tanaka, M., *Electrochem. Soc. Proc.*, **2000-17** (2000), 54.

[56] Holzl, R., Fabry, L., and Range, K. J., *Appl. Phys. A*, **73** (2001), 137.

[57] Hoshi, K., Suzuki, T., Okubo, Y., and Isawa, N., *Electrochem. Soc. Meet. Ext. Abstr.*, **157** (1980), 811.

[58] Hoshi, K., Isawa, N., Suzuki, T., and Okubo, Y., *J. Electrochem. Soc.*, **132** (1985), 693.

[59] Hourai, M., Kelly, G. P., Tanaka, T., Umeno, S., and Ogushi, S., *Electrochem. Soc. Proc.*, **99-1** (1999), 372.

[60] http://www.egg.or.jp/MSIL/english/index-e.html

[61] Hu, S. M., *J. Appl. Phys.*, **45** (1974), 1567.

[62] Hu, S. M., *Appl. Phys. Lett.*, **31** (1977), 139.

[63] Hu, S. M., *J. Appl. Phys.*, **52** (1981), 3974.

[64] Hu, S. M., *J. Appl. Phys.*, **57** (1985), 1069.

[65] Hu, S. M., *J. Appl. Phys.*, **57** (1985), 4527.

[66] Hu, S. M., *Appl. Phys. Lett.*, **48** (1986), 115.

[67] Hu, S. M., *Mat. Res. Soc. Symp. Proc.*, **59** (1986), 249.

[68] Hu, S. M., *Mater. Sci. and Eng.*, **R13** (1994), 105.

[69] Huh, J.-Y., Tan, T. Y. and Gosele, U., *J. Appl. Phys.*, **77** (1995), 5563.

[70] Huff, H. R. and Goodall, R. K., *Solid State Phenom.*, **47-48** (1996), 65.

[71] Hwang, G. S., and Goddard III, W. A., *Phys. Rev. B*, **65** (2002), 233205.

[72] Iida, M., Kusaki, W., Tamatsuka, M., Iino, E., Kimura, M., and Muraoka, S., *Electrochem. Soc. Proc.*, **99-1** (1999), 499.

[73] Inoue, N., Osaka., J. and Wada, K., *J. Electrochem. Soc.*, **129** (1982), 2780.

[74] Inoue, N., Watanabe, K., Wada, K., and Osaka, J., *J. Crystal Growth*, **84** (1987), 21.

[75] The International Technology Roadmap for Semiconductor, 2001.

[76] Isomae, S., *J. Appl. Phys.*, **70** (1991), 4217.

[77] Itsumi, M., Akiya, H. and Ueki, T., *J. Appl. Phys.*, **78** (1995), 5984.

[78] Itsumi, M., Akiya, H., Ueki, T., Tomita, M. and Yamawaki, M., *Jpn. J. Appl. Phys.*, **35** (1996), 812.

[79] Jastrzebski, L., *Mat. Sci. and Eng.*, **B4** (1989), 113.

[80] John, J. P., and Law, M. E., *Appl. Phys. Lett.,* **62** (1993), 1388.

[81] Johnson, C., *Numerical Solution of Partial Differential Equations by the Finite Element Method*, Cambridge University Press, (1987).

[82] Kageshima, H., Taguchi, A., and Wada, K., *Appl. Phys. Lett.*, **76** (2000), 3718.

[83] Karoui, A., Karoui, F. S., Yang, D., and Rozgonyi, G. A., *Solid State Phenom.*, **82-84** (2002), 69.

[84] Kashchiev, D., *Nucleation: Basic Theory with Applications*, Butterworth-Heinemann, Oxford, (2000).

[85] Kato, M., Yoshida, Y., Ikeda, Y. and Kitagawara, Y., *Jpn. J. Appl. Phys.*, **35** (1996), 5597.

[86] Keller, W. and Muhlbauer, A., *Floating-Zone Silicon*, Marcel Dekker, Inc., New York, (1981).

[87] Kelton, K. F., Falster, R., Gambaro, D., Olmo, M., Cornara, M., and Wei, P. F., *J. Appl. Phys.*, **85** (1999), 8097.

[88] Kim, S. S. and Wijaranakula, W., *J. Electrochem. Soc.*, **142** (1995), 553.

[89] Kimerling, L. C., *Radiation Effects in Semiconductors*, ed. N. B. Urli, The Institute of Physics Conference Series **31** (1976), 221.

[90] Kimerling, L. C., Blood, P., and Gibson, W. M., *Defects and Radiation Effects in Semiconductors*, ed. J. H. Albany, The Institute of Physics Conference Series **46** (1979), 273.

[91] Kinney, T. A., and Brown, R. A., *J. Crystal Growth*, **132** (1993), 551.

[92] La Magna, A., and Coffa, S., *Phys. Rev. Lett.*, **82** (1999), 1720.

[93] Leray, J. L., Paillet, P., and Autran, J. L., *Journal de Physique III*, **6** (1996), 1625.

[94] Lin, W. and Benson, K. E., *Ann. Rev. Mater. Sci.*, **17** (1987), 273.

[95] Lin, W., *Semiconductors and Semimetals*, **42** (1994), 9.

[96] Lipchin, A., and Brown, R. A., *J. Crystal Growth*, **216** (2000), 192.

[97] Lipchin, A., and Brown, R. A., *J. Crystal Growth*, **205** (1999), 71.

[98] Luo, W., Rasband, P. B., Clancy, P., and Roberts, B. W., *J. Appl. Phys.*, **84** (1998), 2476.

[99] Maddalon-Vinante, C., Ehret, E. and Barbier, D., *J. Appl. Phys.*, **79** (1996), 2707.

[100] Maraden, K., Sadamitsu, S., Yamamoto, T. and Shigematsu, T., *Jpn. J. Appl. Phys.*,

34 (1995), 2977.

[101] Marioton, B. P. R., Gosele, U., *J. Appl. Phys.*, **63** (1988), 4661.

[102] Maroudas, D. and Brown, R.A., *J. Mater. Res.*, **6** (1991), 2337.

[103] Mathiot, D., and Pfister, J. C., *J. Appl. Phys.*, **55** (1984), 3518.

[104] Michel, J. and Kimerling, L. C., *Semiconductors and Semimetals*, **42** (1994), 251.

[105] Miyazaki, M., Miyazaki, S., Yanase, Y. and Ochiai, T., *Jpn. J. Appl. Phys.*, **34** (1995), 6304.

[106] Miyazaki, M., Miyazaki, S., Yanase, Y. and Kitamura, T., *Jpn. J. Appl. Phys.*, **36** (1997), 6187.

[107] Mori, T., Wang, Z., and Brown, R. A., *Electrochem. Soc., Proc.*, **17** (2000), 118.

[108] Mori, T., *Modeling the Linkages between Heat Transfer and Microdefect Formation in Crystal Growth: Examples of Czochralski Growth of Silicon and Vertical Bridgman Growth of Bismuth Germanate*, PhD thesis, Massachusetts Institute of Technology, (2000).

[109] Mori, T., Sinno, T. and Brown, R. A., to be published (1998).

[110] Morse, P. M., and Feshbach, H., *Methods of Theoretical Physics*, McGraw-Hill Book Company, New York, (1953).

[111] Mott, N. F., and Nabarro, F. R. N., *Proc. Phys. Soc.*, **52** (1940), 86.

[112] Nabarro, F. R. N., *Proc. R. Soc. A*, **175** (1940), 519.

[113] Nabarro, F. R. N., *Theory of Crystal Dislocations*, Oxford, (1967).

[114] Nakamura, K., Saishoji, T., Kubota, T., Iida, T., Shimanuki, Y., Kotooka, T. and Tomioka, J., *J. Crystal Growth*, **180** (1997), 61.

[115] Newman, R. C., and Jones, R., *Semiconductors and Semimetals*, **42** (1994), 289.

[116] Pagani, M., Falster, R., Fisher, G. R., Ferrero, G. C. and Olmo, M., *Appl. Phys. Lett.*, **70** (1997),1572.

[117] Plummer, J. D., Deal, M. D., and Griffin P. B., *Silicon VLSI Technology*, Prentice Hall, (2000).

[118] Popov, V. P., Antonova, I. V., Stas, V. F., Gutakovskii, A. K., Spesivtsev, E. V., Mardegzhov, A. S., Franznusov, A. A., and Feofanov, G. N., *Mater. Sci. Eng. B*, **73** (2000), 82.

[119] Orr Arienzo, W. A., Glang, R., Lever, R. F., Lewis, R. K., and Morehead F. F., *J. Appl. Phys.*, **63** (1988), 116.

[120] Osaka, J., Inoue, N. and Wada, K., *Appl. Phys. Lett.,* **36** (1980), 288.

[121] Park, B. T. and Petrosian, V., *Astrophys. J.*, **446** (1995), 699.

[122] Park, B. T. and Petrosian, V., *Astrophys. J. Suppl. Ser.*, **103** (1996), 255.

[123] Rasband, P. B., Clancy, P., and Thompson, M. O., *J. Appl. Phys.*, **79** (1996), 8998.

[124] Peibst, H. and Raidt, H., *Phys. Stat. Sol.*, **68** (1981), 253.

[125] Pellegrino, P., Leveque, P., Lalita, J., Hallen, A., Jagadish, C., Svensson, B. G., *Phys. Rev. B*, **64** (2001), 195221.

[126] Ramm, J., Beck, E., Dommann, A., Eisele, I., and Kruger, D., *Thin Solid Films*, **246** (1994) 158.

[127] Ravi, K. V., *J. Electrochem. Soc.*, **121** (1974), 1090.

[128] Ravi, K. V., *Imperfections and Impurities in Semiconductor Silicon*, John Wiley and Sons, New York, (1981).

[129] Rogers, W. B., and Massoud, H. Z., *J. Electrochem. Soc.*, **138** (1991), 3483.

[130] Rogers, W. B., and Massoud, H. Z., *J. Electrochem. Soc.*, **138** (1991), 3492.

[131] Rozgonyi, G. A., Deysher, R. P. and Pearce, C. W., *J. Electrochem. Soc.*, **123** (1976), 1910.

[132] Ryuta, J., Morita, E., Tanaka, T. and Shimanuki, Y., *Jpn. J. Appl. Phys.*, **29** (1990), L1947.

[133] Sasaki, H., Kadoi, M., Furuya, H., Shingyouji, T. and Shimanuki, Y., *Jpn. J. Appl. Phys.*, **33** (1994), L5.

[134] Satoh, Y., Shiota, T., Murakami, Y., Shingyouji, T. and Furuya, H., *J. Appl. Phys.*, **79** (1996), 7947.

[135] Schrems, M., Brabec, T., Budil, M., Potzl, H., Guerrero, E., Huber, D. and Pongratz, P., *Mat. Sci. and Eng.*, **B4** (1989), 393.

[136] Schrems, M., Brabec, T., Budil, M., Pötzl, H., Guerrero, E., Huber, D. and Pongratz, P., *Defect Control in Semiconductors*, (1990), 245.

[137] Schrems, M., *Mat. Sci. Forum.*, **117-118** (1993), 231.

[138] Schrems, M., *Semiconductors and Semimetals*, **42** (1994), 391.

[139] Senkader, S., Wilshaw, P. R., and Falster, R., *J. Appl. Phys.*, **89** (2001), 4803.

[140] Shimura, F., Tsuya, H. and Kawamura, T., *J. Appl. Phys.*, **51** (1980a), 269.

[141] Shimura, F., Tsuya, H. and Kawamura, T., *Appl. Phys. Lett.*, **37** (1980b), 483.

[142] Shimura, F. and Tsuya, H., *J. Electrochem. Soc.*, **129** (1982), 1062.

[143] Shimura, F. and Hockett, R. S., *Appl. Phys. Lett.*, **48** (1986), 224.

[144] Shimura, F., *J. Appl. Phys.*, **59** (1986), 3251.

[145] Shimura, F., *Semiconductor Silicon Crystal Technology*, Acdemic Press, San Diego, (1989).

[146] Shimura, F., *Solid State Phenom.*, **19-20** (1991), 1.

[147] Shimura, F., *Semiconductors and Semimetals*, **42** (1994), 1.

[148] Shimura, F., *Semiconductors and Semimetals*, **42** (1994), 577.

[149] Sin, G. H., *Modeling of Microdefects in Czochralski Growth Silicon*, Ph.D thesis, Massachusetts Institute of Technology, (2000).

[150] Sinno, T., *Defects in Crystalline Silicon: Integrated Atomistic and Continuum Modeling*, Ph.D thesis, Massachusetts Institute of Technology, (1998).

[151] Sinno, T., Brown, R. A., von Ammon, W., and Dornberger, E., *J. Electrochem. Soc.*, **145** (1998), 302.

[152] Sinno, T., Brown, R. A., von Ammon, W., and Dornberger, E., *J. Electrochem. Soc.*, **146** (1999), 2300.

[153] Sinno, T., Susanto, H., Brown, R. A., von Ammon, W., and Dornberger, E., *Appl. Phys. Lett.*, **75** (1999), 1544.

[154] Sinno, T., Dornberger, E., von Ammon, W., Brown, R. A., and Dupret, F., *Mater. Sci. Eng.*, **243** (2000), 1.

[155] Sinno, T., *Electrochem. Soc. Proc.*, 2002-2 (2002),.

[156] Slaughter, W. S., *The Linearized Theory of Elasticity*, Birkhäuser, (2002).

[157] Song, L. W., Benson, B. W., and Watkins, G. D., *Phys. Rev. B*, **33** (1986), 1452.

[158] Spaepen, F., *Solid State Phys.*, **47** (1994), 1.

[159] Sueoka, K., Ikeda, N., Yamamoto, T., and Kobayashi, S., *J. Appl. Phys.*, **74** (1993), 5437.

[160] Sueoka, K., Akatsuka, M., Nishihara, K., Yamamoto, T., and Kobayashi, S., *Mater. Sci. Forum*, **196-201** (1995), 1737.

[161] Sueoka, K., Akatsuka, M., Ono, T., Asayama, E., Koike, Y., Adachi, N., Sadamitsu, S., and Katahama, H., *Electrochem. Soc. Proc.*, **2000-17** (2000), 164.

[162] Sueoka, K., Akatsuka, M., Okui, M., and Katahama, H., *Electrochem. Soc. Proc.*, **2002-2** (2002), 541.

[163] Sumino, K. and Yonenaga, I., *Semiconductors and Semimetals*, **42** (1994), 449.

[164] Susanto, H., *Modeling the Effect of Boron on Microdefect Formation*, Engineer thesis, Massachusetts Institute of Technology, (1998).

[165] Tan, T. Y., Gardner, E. E., and Tice, W. K., *Appl. Phys. Lett.*, **30** (1977), 175.

[166] Tan, T. Y. and Gösele, U. M., *Appl. Phys. Lett.*, **40** (1982), 616.

[167] Tan, T. Y. and Taylor, W. J., *Semiconductors and Semimetals*, **42** (1994), 353.

[168] Taniguchi, K., Antoniadis, D. A., and Matsushita, Y., *Appl. Phys. Lett.*, **42** (1983), 961.

[169] Taylor, W. J., Tan, T. Y. and Gösele, U. M., *Appl. Phys. Lett.*, **59** (1991), 2007.

[170] Taylor, W. J., Gösele, U. M. and Tan, T. Y., *Mater. Chem. and Phys.*, **34** (1993), 166.

[171] Tersoff, J., *Phys. Rev. Lett.*, **64** (1990), 1757.

[172] Ueki, T., Itsumi, M. and Takeda, T., *Appl. Phys. Lett.*, **70** (1997), 1248.

[173] Usami, T., Matsushita, Y., and Ogino, M., *J. Crystal Growth*, **70** (1984), 319.

[174] Vandenbossche, E., and Baccus, B., *J. Appl. Phys.*, **73** (1993), 7322.

[175] Vanhellemont, J. and Claeys, C., *J. Appl. Phys.*, **62** (1987), 3960.

[176] Vanhellemont, J., *J. Appl. Phys.*, **78** (1995), 4297.

[177] Vanhellemont, J., *Appl. Phys. Lett.*, **68** (1996), 3413.

[178] Vanhellemont, J., Esfandyari, J., Obermeier, G., Dornberger, E., Graf, D., Lambert, U. and Kissinger, G., *Electrochem. Soc. Proc.*, **98-13** (1998), 101.

[179] von Ammon, W., *Soid State Phen.*, **47** (1996), 97.

[180] von Ammon, W., Dreier, P., Hensel, W., Lambert, U., and Koster, L., *Mater. Sci. Eng. B*, **36** (1996), 33.

[181] von Ammon, W., Holzl, R., Virbulis, J., Dornberger, E., Schmolke, R., and Graf, D., *J. Crystal Growth*, **226** (2001), 19.

[182] von Ammon, W., Holzl, R., Virbulis, J., Dornberger, E., Schmolke, R., and Graf, D., *Soid State Phen.*, **82-84** (2002), 17.

[183] Voronkov, V. V., *J. Crystal Growth*, **59** (1982), 625.

[184] Voronkov, V. V., Mil'vidskii, M. G., Grinshtein, P. M. and Babitskii, Yu. M., *Sov. Phys. Crystallogr.*, **34** (1989), 115.

[185] Voronkov, V. V., and Falster, R., *J. Crystal Growth*, **194** (1998), 76.

[186] Voronkov, V. V., and Falster, R., *J. Crystal Growth*, **204** (1999), 462.

[187] Voronkov, V. V., and Falster, R., *J. Appl. Phys.*, **87** (2000), 4126.

[188] Voronkov, V. V., and Falster, R., *Microelectronic Eng.*, **56** (2001), 165.

[189] Wada, K., Inoue, N., and Kohra, K., *J. Crystal Growth*, **49** (1980), 749.

[190] Wada, K., and Inoue, N., *J. Crystal Growth*, **71** (1985), 111.

[191] Wada, K. and Inoue, N., *Electrochem. Soc. Proc.*, **86-4** (1986), 778.

[192] Wang, Z., Sinno, T., and Brown, R. A., *Appl. Phys. Lett.*, **78** (2001), 180.

[193] Wang, Z., and Brown, R. A., *J. Crystal Growth*, **231** (2001), 442.

[194] Watkins, G. D., and Troxell, J. R., *Phys. Rev. Lett.*, **44** (1980), 593.

[195] Watkins, G. D., *Materials Science in Semiconductor Processings*, **3** (2000), 227.

[196] Wei, P. F., Kelton, K. F., and Falster, R., *J. Appl. Phys.*, **88** (2000), 5062.

[197] Wilson, L. O., *J. Crystal Growth*, **48** (1980), 435.

[198] Wilson, L. O., *J. Crystal Growth*, **48** (1980), 451.

[199] Witt, A. F., Lichtensteiger, M., and Gatos, H. C., *J. Electrochem. Soc.*, **120** (1983), 1119.

[200] Wolf, D., and Tauber, R. N., *Silicon Processing for the VLSI Era, Volume 1 - Process*

Technology, Lattice Press, California, (1986).

[201] Yamada, N. and Yamada-Kaneta, H., *J. Electrochem. Soc.*, **145** (1998), 3628.

[202] Yamagishi, H., Fusegawa, I., Fujimaki, N. and Katayama, M., *Semicond. Sci. Technol.*, **7** (1992), A135.

[203] Yanase, Y., Ono, T., Kitamura, T., Horie, H. and Ochiai, T., *Jpn. J. Appl. Phys.*, **36** (1997), 6200.

[204] Yang, K., Carle, J., and Kleinhenz, R., *J. Appl. Phys.*, **62** (1987), 4890.

[205] Yasutake, K., Umeno, M., and Kawabe, H., *Phys. Stat. Sol. (a)*, **83** (1984), 207.

[206] Zauderer, E., *Partical Differential Equations of Applied Mathematics*, John Wiley & Sons, New York, (1983).

[207] Zimmermann, H. and Falster, R., *Appl. Phys. Lett.*, **60** (1992), 3250.

[208] Zulehner, W., *Semiconductor Silicon*, eds. G. C. Harbeke and M. J. Schilz, (1989), 127.

[209] Zulehner, W. and Huber, D., *"Czochralski-Grown Silicon," Crystals: Growth, Properties and Applications*, 8 J. Grabmaier, ed., Springer, new York, (1982).